PERFORMANCE EVALUATION OF THE CELESCOPE EXPERIMENT

Contract NAS 5-1535

Prepared for

National Aeronautics and Space Administration
Goddard Space Flight Center
Greenbelt, Maryland

July 1971

Smithsonian Institution
Astrophysical Observatory
Cambridge, Massachusetts 02138

TABLE OF CONTENTS

TABLE OF CONTENTS (Cont.)

PERFORMANCE EVALUATION OF THE CELESCOPE EXPERIMENT

Contract NAS 5-1535

Principal Investigator

F. L. Whipple

Project Scientist

Robert J. Davis

Deputy Project Scientist

W. A. Deutschman

Project Manager

R. T. Ayer

July 1971

Smithsonian Institution
Astrophysical Observatory
Cambridge, Massachusetts 02138

106-043

TABLE OF CONTENTS (Cont.)

SECTION I

HIGHLIGHTS OF THE CELESCOPE EXPERIMENT

C. A. Lundquist

HIGHLIGHTS OF THE CELESCOPE EXPERIMENT

The principal objective of the Celescope experiment is to measure the ultraviolet magnitudes of very many stars in a statistically significant fraction of the sky (see, for example, Davis (1965); Whipple and Davis (1960)). During its operational life on the Orbiting Astronomical Observatory (OAO II), the four ultraviolet-sensitive television cameras carried by the experiment indeed achieved the desired statistical sky survey by recording some 8500 television pictures of stellar fields, each $2° \times 2°$, covering a total of 10% of the sky (see, for example, Davis (1970)). The stellar data will soon be cataloged in other documents. Recorded here are the pertinent engineering experience and the performance evaluation of the Celescope experiment, in the hope that this information will be useful to later experimenters.

The design, fabrication, and operation of the Celescope experiment manifest its astronomical objectives. Because the objective is observation of a significant fraction of the sky, image tubes that view an adequate area at each exposure were the natural choice for detectors on the telescopes. But there were no ultraviolet-sensitive television canera tubes in existence when Celescope was initiated in 1959, and there was no design of a system to use them in a laboratory photometer, let alone a stellar photometer for spaceflight. Nor was there an Orbiting Astronomical Observatory with well-defined characteristics into which the photometer must fit. Thus, the engineering experience of Project Celescope started from scratch, evolved through most of the first decade of the space age, and culminated in OAO II.

Within the sky area observed, magnitude measurement of some several thousand stars is a reasonable statistical sample. Because stars become increasingly more numerous with decreasing apparent brightness, the television cameras must record stars 10^4 times dimmer than the brightest ultraviolet stars. This requirement sets the sensitivity threshold and the dynamic range required and satisfied by the Celescope hardware.

The sensitivity is achieved by specially produced ultraviolet-sensitive television tubes that employ the secondary electron conduction (SEC) principle in an electron-image storage target. The development of these Westinghouse Uvicon tubes from a starting point where the SEC principle was a new laboratory discovery, to final successful flight operation, is a technological triumph of Celescope.

As must be expected, this pioneering development of the first SEC television cameras had its share of perplexing hurdles, and the resulting tubes have characteristics that make stringent demands on interface engineering, orbital operations, and data processing. The ultimate success of the Celescope experiment demonstrates that engineering solutions in a total-system context were found for all problems that arose. The Celescope experience supports the subsequent selection of tubes based on the SEC principle for other space missions, particularly in as much as later applications of such tubes benefit from continuing development by their manufacturers.

As a stellar photometer, the Uvicon with its electronics derives its remarkable dynamic range from the property that the brightness of a star is registered on the target as an electron image that increases in both charge density and spatial extent as a function of the brightness of the star. Thus, in its digitized format, the image of a star is a matrix of charge-density values. The brighter the star, the more elements the matrix contains.

The digitization of the television picture requires special circuitry because the OAO spacecraft systems cannot accommodate rapid transmission of a television picture. This design consideration is satisfactorily met by a technique labeled superscan by EMR, in which the readout electron beam is off the remaining image most of the time. When the system is ready for data input, the beam is swiftly deflected to the next image point to be sampled, the charge is measured for a small region around the point, and the beam swings back off the image to wait for the next cycle.

The arithmetic sum (Sigma) of the values above background for the matrix elements of a star image is taken as the primary Celescope measure

that can generate inconsistent Sigma values and magnitudes. That this does not happen appreciably is a validation of the mechanical and thermal design of the telescope systems.

The Celescope experiment incorporates many engineering concepts to enhance reliability. Much of the electronic circuitry is quad-redundant at the module level; these systems were operating normally when checked 26 months after launch. The high-voltage power supplies in the flight package give no indication of arcing problems; the adopted design and potting procedures can be recommended for future uses. Although there are four telescopes in the experiment and four ultraviolet spectral bands to be covered, these are not related in a one-to-one fashion. Instead, a filter configuration bisects the camera field so that each half responds to a different spectral band; thus, for redundancy each spectral band is observed by two camera tubes. However, this concept is not an unqualified success, because star images overlapping the dividing line cannot be used.

The most troublesome problem involving reliability concerns protection of the Uvicon target from accumulating a charge of such size that electrostatic forces puncture or rupture the target material. (Fortunately, recent SEC tube designs avoid this phenomenon.) The Celescope project had to use tubes susceptible to this limitation and therefore had to compensate for it by circuitry design and operational procedures. Even so, one tube suffered target damage early in orbital operations. Although this caused a decrease in operational efficiency, no qualitative loss resulted. Because of the redundant filter configuration, data continued to be taken in all four spectral bands until observations were discontinued.

After 17 months of operation (40% longer than the nominal objective) Celescope sensitivity reached a level below which further routine observations were unjustified. On April 26, 1970, Celescope was turned off, while still in operable condition. It was turned on again briefly on February 2, 1971, and found to be in the same condition as 9 months earlier. It may still be operated and take further data if objectives arise for which its sensitivity is adequate.

of the ultraviolet magnitude of the star. The processing of the Celescope observations then requires that the correspondence between Sigma and stellar magnitude be accurately known as a function of image position on the camera photocathode and target, of time, and of temperature and other system parameters. This is equivalently a description of the full Celescope system response and hence is a vital aspect of the engineering.

The correspondence between Sigma and ultraviolet magnitude is far from linear. An initial mathematical model for it was generated from extensive laboratory measurements made before the OAO launch. When the experiment was in orbital operation, most parameters in the model were redetermined, and their temporal evolution derived from the stellar observations themselves. For this purpose, the telescopes were periodically directed toward standard star areas. Procedures for differential improvement of model parameters were implemented with the condition that multiple observations of the same star at different epochs, at different exposure times, and at different positions on the television picture should yield the same magnitude within expected system accuracies.

These mathematical procedures not only generate the parameters needed for data processing but also yield retrospective engineering information on the time dependence of system sensitivity. The photometric sensitivity decreases with time, as was generally anticipated before launch.

The most useful indication of the accuracy of the processed stellar data comes from the scatter in the magnitude values for multiple observations for each of some 1500 stars. For the different cameras and spectral bands, the standard deviation of this scatter ranges between 0.1 and 0.2 mag. This is in substantial agreement with the 0.1-mag accuracy goal established early in the Celescope design. Such accuracy over a dynamic range of 10^4 is a noteworthy engineering feat.

Image focus might have profoundly degraded this accuracy but did not. A change in the optical or electronic focus affects the image size in a way

The subsequent sections of this report relate in some detail the aspects of Celescope engineering and performance that seemed most significant to their authors. Section II, by Dr. Yasushi Nozawa, addresses particularly the engineering problems and their solutions for the benefit of later experiments. A tabulation of the major engineering conclusions can be found in the first paragraphs of Dr. Nozawa's paper, and other conclusions are collected at the end of each chapter.

Section III, by the staff of EMR, summarizes broadly their viewpoints on Celescope engineering. EMR was the major design and fabrication contractor for the experiment package and supporting ground equipment.

Section IV, by Dr. William Deutschman, describes briefly the data-processing procedures implemented for Celescope observations. His paper recognizes that the production and application of appropriate procedures and computer software are an integral part of the total engineering picture of an enterprise such as Celescope.

Finally, Section V identifies the very many people who over the years contributed to the final success of the project.

References

DAVIS, R. J., Ed.

1968. The Celescope experiment. Smithsonian Astrophys. Obs. Spec. Rep. No. 282, 132 pp.

1970. Ultraviolet photometry of stars obtained with the Celescope experiment in the Orbiting Astronomical Observatory. In IAU Symp. No. 36, Ultraviolet Stellar Spectra and Ground-Based Observations, ed. by L. Houziaux and H. E. Butler, D. Reidel, Dordrecht, Holland, pp. 109-119.

WHIPPLE, F. L., and DAVIS, R. J.

1960. Proposed stellar and interstellar survey. Astron. Journ., vol. 65, pp. 285-290.

SECTION II

ENGINEERING REVIEW OF THE CELESCOPE TELEVISION PHOTOMETER

Y. Nozawa

CHAPTER 1

INTRÓDUCTION

1.1 General

The purposes of this report are:

1. To provide a commentary on the engineering experience gained with Project Celescope in television mapping of the celestial sphere in the ultraviolet.

2. To discuss some problem areas encountered and the actions taken to overcome them.

3. To present information of value to similar future endeavors.

For the reader who is not familiar with Project Celescope, a brief description of this experiment and of the capabilities of the OAO satellite is included as Appendix A. Details of the Celescope experiment are given in the text wherever pertinent and useful.

Many internal Celescope reports were prepared during the project performance. They give the results of specific tests and investigations and contain a wealth of useful information on the instrumentation. Because they are not easily accessible, we have avoided referencing them here. We have included in this report, however, sufficient information from them so that the reader need not consult the originals. (A list of these internal reports is included as Appendix B.) Published Celescope reports, on the contrary, are freely cited.

It is not our intention here to undertake a scientific discussion on the astrophysical data obtained by Celescope (that aspect of the project will be presented elsewhere by staff scientists). Nor is it intended to provide a systematic description of the instrumentation used. Published accounts exist, and the interested reader is referred to them.

For convenience, this section is divided into parts A and B. In general, part A deals with characteristics of hardware, and part B describes supplementary characteristics of the total system, consisting of spacecraft hardware and computer software. The distinction between characteristics of hardware and software is somewhat arbitrary, since our knowledge of the hardware depends upon information displayed and printed out by the software. Nevertheless, we distinguish between them for convenience. The main role of the data-processing system (software) is to transform the data generated by the hardware into a format convenient to the user. In order to perform this function, any anomalies or temporal changes in hardware characteristics must be compensated for in the software. When there are complicated nonlinearities and temporal changes, a major software effort may have to be devoted to compensating for them.

1.2 Summary and Conclusion

Before proceeding to the principal text of Section II, we summarize the highlights of the engineering experience gained with Project Celescope. For the reader who is familiar with this Project, the terms used and the issues addressed are understandable. Those who are not familiar with Celescope will find an explanation of the terms and issues in the chapters that follow.

Celescope has accomplished a great deal, and some of its engineering concepts are as advanced today as 10 years ago, when they were first conceived by the Project staff and its industrial contractors. There have been problems, as always there are in complex electronic-optical systems that push technological frontiers in a space environment.

The following points highlight our experience with the performance of the Celescope experiment:

1. Optical, mechanical, and thermal design of the telescopes proved fully satisfactory in terms of image quality and stability.

2. Contamination-control procedures during ground operations were fully successful.

3. Positional stability of star images in the final television pictures was not completely satisfactory, and careful attention to factors affecting it, such as magnetic fields, is necessary.

4. The lack of an opaque shutter as opposed to the electronic shutter we employed prevented us from using a significant number of dark experimentation periods.

5. High-voltage power supplies, ion traps, and associated circuitry (anti-arcing) performed perfectly.

6. Quad-redundancy design in Celescope produced a reliable operation of the electronic package, but at the cost of some increase in power and weight.

7. Superscan readout performed well.

8. The calibrator lamps proved to be valuable for providing a record of Celescope performance from the time the flight telescopes were first assembled, through all phases of subsystem and system testing, to well after launch.

9. The calibrator lamps carried initial calibration data into orbit, but did not provide thereafter sufficient data for accurately establishing the time dependence of the photometer response.

10. Protection against target-material breakdown (crossover) is a critical requirement. The Celescope techniques proved to be satisfactory for three of our four cameras.

11. For some methods of preventing target-material breakdown and, in particular, the method used in Celescope, the output signal becomes critically dependent on the focus of a stellar image on the target.

12. Uvicon sensitivity during orbital operations decreased with time. Nevertheless, the useful life of the Celescope experiment significantly exceeded the prelaunch goal of 1 year in orbit for gathering scientific data.

13. Scattered sunlight severely limited Celescope's opportunities for daylight observations.

14. Geocorona seriously interfered with Celescope measurements in the spectral band that includes 1216 Å.

The following conclusions based on experience with analyses of the data from orbit are included for completeness.

1. Calibration of the Uvicons in orbit was possible and necessary.

2. Our photometric accuracy, after orbital calibration, is better than 0.2 mag.

3. The use of two filters, one for each half of the field of view, posed significant data-reduction problems. It also required us to reject many stars that were observed near the dividing line.

4. Excessive manual intervention in the data-reduction system was necessary because the housekeeping data were on a different data channel from the video data and the camera number was not included with the video data.

Our overall conclusion is that the Celescope experiment system successfully demonstrated the capability of a versatile and precise, space-borne astronomical television photometer.

CHAPTER 2

TARGET-MATERIAL BREAKDOWN IN UVICON IMAGE TUBES

2.1 Introduction

The Uvicon image tubes, which are the main sensors of the Celescope experiment, were the first operational television camera tubes to use the Secondary Electron Conduction* (SEC) principle. As the Uvicon tubes were innovative in many ways, in the course of the project we experienced the usual unavoidable difficulties that are encountered in extending a technological frontier. Among many problems, the most critical and time consuming was what we sometimes called plague, or destructive crossover, or simply crossover. Since the word "crossover" does not give an accurate description of the phenomenon and is very confusing, the problem will be referred to hereafter as target-material breakdown.

The Uvicon program began in 1960 with SAO's issuing of a subcontract to Westinghouse Research Laboratories for development of television camera tubes having the characteristics required for the Celescope experiment: two ultraviolet spectral responses, with sharp long-wavelength cutoffs near 2000 and 3000 Å; photometric accuracy of 10% for measuring the brightnesses of stars between 0 and 10th mag with exposure times of 60 sec; clear separation of star images 0.6 mm apart on the photocathode; a fully usable field of view 2° square; and satisfactory operation throughout the specified prelaunch testing sequence, leading to prediction of survival through the launch phase and of satisfactory operation during 1 year in orbit.

The photometric requirement could not be met by any type of television camera tube available in 1960. Westinghouse originally hoped that satisfactory

*Also read as Secondary Electron Conductivity or Secondary Emission Conductivity.

Uvicons could be built using the EBIC principle (Electron Bombardment Induced Conductivity). By the end of 1961, Westinghouse had built and tested several Ebic-type Uvicons, none of which had satisfactory photometric sensitivity. By that time, engineers at the Research Laboratory had sufficiently investigated the phenomenon of secondary electron conduction to become convinced that Uvicons utilizing the SEC principle could meet the SAO specifications.

The first Uvicon tube based on the SEC principle was manufactured in February 1962. Probably the first experience of target-material breakdown occurred on May 22, 1962, during the acceptance test at Electro-Mechanical Research, Inc., which was the prime contractor for the Celescope experiment. The target was completely ruptured, and the Uvicon tube became unusable. We suffered many similar failures, but each failure gave us some new insight into the problem. We also undertook a special investigation specifically aimed at preventing the recurrence of the phenomenon. By the time of system assembly of the Celescope experiment, the principal modes of target-material breakdown were well understood, and methods for its prevention were incorporated into the system design and operational principles of Celescope.

Despite precautions, in the early period of orbital operation the Celescope experiment suffered a series of target-material breakdowns, and, as a result, camera 2 finally ceased functioning.

The objective of this chapter is to review all related information on target-material breakdown and to serve as reference for future enterprises. In the first three sections, the basic principles of the SEC target and Uvicon, which are necessary for an understanding of the target-material breakdown, will be explained. The following sections describe methods of prevention and their effects. The last sections describe some actual experiences of target-material breakdown and discuss their causes.

2.2 Uvicon Structure and Operational Principles

The Uvicon tube is a type of SEC image tube. It consists of two major parts as shown in Figure 1: an imaging section and a readout-gun (or scanning) section. The faceplate (the front end of the imaging section) is made of lithium fluoride (LiF), which is transparent to ultraviolet light. The inner surface of the faceplate is the photocathode. It is backed by a semi-transparent film of metal used in the generation of the electrical field, which is an essential part of the electron optics. When photons enter through the faceplate, they form an image on the photocathode surface. The photocathode produces photoelectrons from the photon image. When high voltage is applied to the electron lenses in the imaging section, these photoelectrons are accelerated toward the target plane. If no high voltage is applied to the electron lenses, photoelectrons will not be directed toward the target; therefore, the high voltage acts as a shutter to control image formation at the target. The photoelectron image formed at the target is similar to the optical image but reduced in size by half. The photoelectrons, which have an energy of about 7 keV, penetrate the target support structure and produce an image of positive charge on the target, according to the SEC principle. The process of generating a positive-charge image on the target is called an exposure. After completion of the exposure, readout is begun. Readout is the process of discharging the target by use of the readout electron beam from the readout gun. The discharge current from the signal plate in the target is the output signal, which is a measure of the original number of incident photons. The readout-gun section is identical to the normal Vidicon gun except that it has been made more rugged for space application. The low-energy electron beam generated by the cathode in the gun section is directed toward the target by a set of electron lenses in the gun section. It is made to scan the target surface by the application of deflection voltages across the deflection plates in the gun.

From its conception, the Uvicon was intended for space applications. Therefore, some features not essential for ground use are incorporated. One of them is all-electrostatic operation. The imaging of photoelectrons on the target surface is accomplished by electrostatic means, and the readout beam

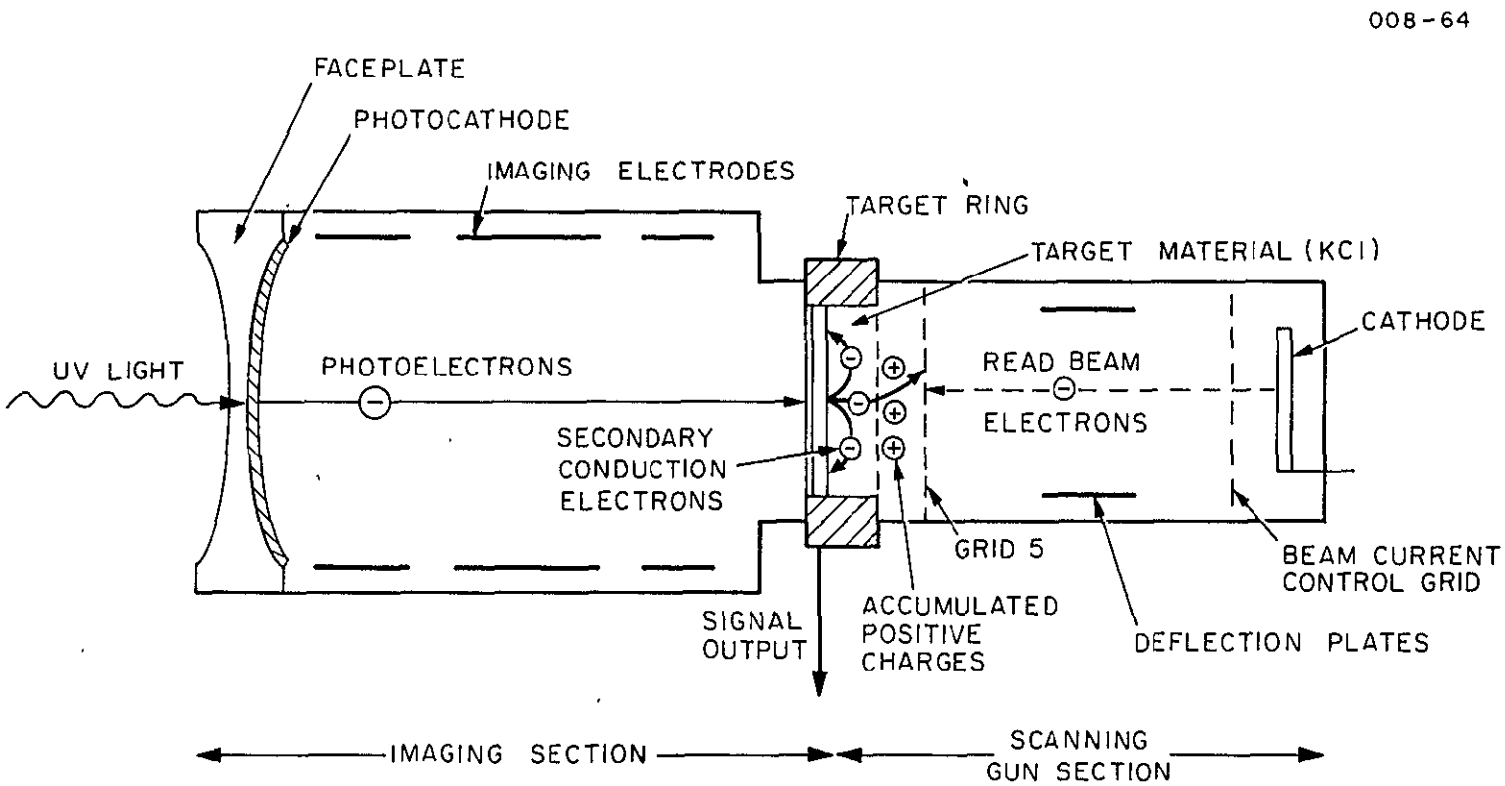

Figure 1. Schematic diagram of Uvicon tube.

is focused and deflected electrostatically. All-electrostatic operation meets the requirements of limited electrical power and stringent magnetic cleanness. One of the disadvantages of an all-electrostatic tube is that the stability of the image position is susceptible to external magnetic disturbances, which include the earth's magnetic field, despite careful magnetic shielding. The other disadvantage is the need for a high-curvature faceplate, which introduced problems in design and manufacturing of the tube. Figure 2 shows a photograph of the Uvicon.

The necessity of utilizing electrostatic rather than electromagnetic focusing and deflection should be carefully reviewed before these requirements are imposed for future space flights.

The operation of the Uvicon follows a fixed sequence of four major phases: priming, exposure, readout, and standby. Priming brings the exit surface of the target to the equilibrium potential of the cathode by means of a low-energy electron beam from the cathode. In this process, at least 10 to 20 frames of scanning of the entire target surface are required. Also, to avoid dangerous transients of potential charge, the potential of the target is gradually changed in several steps. The priming process also eliminates any residual charges from the previous exposure or any other operation. After priming, the potential distribution in the tube is set in such a way that the Uvicon can be exposed to the light with high voltage on without any danger to it. At exposure time, the high voltage is applied to the electron lenses in the imaging section of the Uvicon. After exposure, i.e., after the high voltage is turned off, the readout process begins. It extracts the positive charge from the target in the form of a discharge current. Since the readout process erases the charge pattern, only the first frame contains useful data. After readout, the Uvicon is ready for another cycle of priming or for the standby mode.

Each phase of the operation cycle is distinguished by a particular voltage configuration in the Uvicon tubes. We defined five different modes of camera

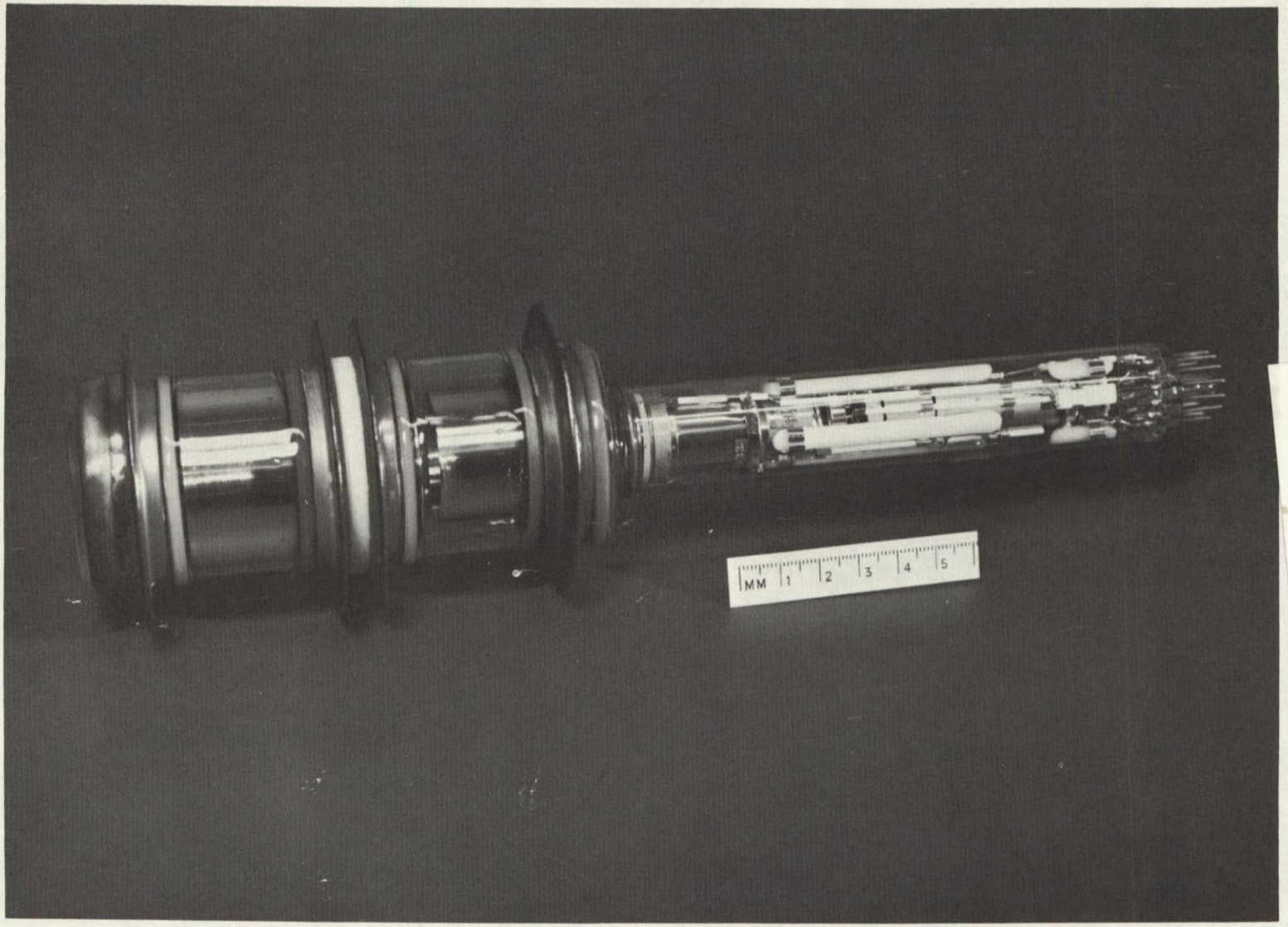

Figure 2. Photograph of Uvicon tube.

status, corresponding to the different voltage configurations: high velocity, polarize low, polarize high, expose, and readout. The actual voltage configurations in polarize high and readout are identical; the distinction made is one of function only, and the names are often used interchangeably. These distinctions in camera mode refer to the status of the electron-gun (scanning) section. For the imaging section, there are two different modes; high-voltage on and high-voltage off. Normally, the imaging section is kept on high-voltage off. Only during exposure is high-voltage on applied, and it must be used with the expose mode in the electron-gun section. Because of the fixed nature of its use, the mode of the imaging section is seldom mentioned explicitly.

Table 1 indicates the voltage configurations in the Uvicon tube during different camera modes. Table 2 indicates the actual status of the camera in different phases of operation. The Uvicon tubes in the Celescope experiment are controlled through telemetered commands. Table 3 lists the representative commands for Celescope operation, and Tables 4 and 5 show an example of one operational cycle for one Uvicon tube. The basic structure of the operational sequence in Celescope depends mainly on the timing requirement of scanning and the voltage constraints of techniques for preventing target-material breakdown. In the following section, the scanning method, which is unique, will be described in detail. Then, in succeeding sections, the prevention of target-material breakdown will be discussed.

2.3 Digital Scanning System in Celescope*

Video data from Celescope can be transmitted in real time in two different ways through the OAO communications channels. One is real-time analog transmission with a system bandwidth of 62.5 kHz. The other is real-time digital transmission with a rate of 5×10^4 bits/sec in the form of PCM NRZ.

*See, Nozawa, Y. A digital television system for satellite-borne ultraviolet photometer, Advances in Electronics and Electron Physics, ed. by J. D. McGee, D. McMullan, and E. Kahan, vol. 22, pp. 865-874, Academic Press, New York, 1966.

Table 1. Target-G5 voltage configuration.

Camera mode	Voltage (GND = 0 V)		Potential difference from cathode	
	G5 (V)	Target (V)	G5 (V)	Target (V)
High velocity	+180	+180	+430	+430
Polarize low	+180	-250	+430	0
Polarize high	+180	-241	+430	+ 9
Expose	-241	-241	+ 9	+ 9
Readout	+180	-241	+430	+ 9

Table 2. Operation phase and status of camera.

Operation phase	Camera mode	Imaging section	Readout beam	Filament
Camera off	High velocity	High-voltage off	Off	Off
Turn on	High velocity	High-voltage off	On	Off
	High velocity	High-voltage off	On	On
Standby	High velocity	High-voltage off	Off	On
Priming	High velocity	High-voltage off	On	On
	High velocity	High-voltage off	Off	On
	Polarize low	High-voltage off	Off	On
	Polarize low	High-voltage off	On	On
	Polarize low	High-voltage off	Off	On
	Polarize high	High-voltage off	Off	On
	Polarize high	High-voltage off	On	On
	Polarize high	High-voltage off	Off	On
	Expose	High-voltage off	Off	On
Expose	Expose	High-voltage on	Off	On
Readout	Expose	High-voltage off	Off	On
	Readout	High-voltage off	Off	On
	Readout	High-voltage off	On	On
	Readout	High-voltage off	Off	On
	High velocity	High-voltage off	Off	On
Turn off	High velocity	High-voltage off	Off	On
	High velocity	High-voltage off	On	On
	High velocity	High-voltage off	On	Off
	High velocity	High-voltage off	Off	Off
Power off	Prime power (+28 V) is off			

Table 3. List of control commands for Celescope.

Functional classification of commands		Command format		
		Syllable 1	Syllable 2	Syllable 3
Individual camera-control commands	Camera-mode selection	Camera N (N=1,2,3,or 4	High velocity, polarize low readout, or mode expose	(Blank)
	Sweep-mode selection		Sweep	Analog or digital
	Gun-voltage on/off control		Beam, filament, or medium-voltage power supply	On or off
	Imaging-section control		Expose	
	Calibrator control		Calibration lamp	
	Gun-voltage-level adjustment		Beam focus adjustor	1, 2, 3, or 4
			Astigmatism	1,2,3,4,5,6,7,or 8
System-configuration selection commands	Redundant power supply	Select	+6, +18, or -12 V	A or B
	Redundant digital-sweep generator		Horizontal BC, vertical BC, horizontal out, or vertical out	
	Redundant analog-to-digital convertor		ADC	
	Data-transmission mode		System-operation mode	PCM, analog, store or off
	Data-output channel		Video	Cameras 1,2,3,or 4
	Threshold-level setting for store-mode operation		Threshold	0,1,2,3,---,14,or 15

Table 4. Command sequence for camera operation used during ground testing.

Operation phases	Command sequence for camera x (x = 1, 2, 3, or 4)		
Camera turn on	Select	Operating mode	Off
	Select	Video	Cx
	Camera x	High velocity	
	Camera x	MVPS	On
	Wait	15	Sec
	Select	Operating mode	Analog
	Camera x	Beam	On
	Camera x	Filament	On
	Wait	60	Sec
	Camera x	Beam	Off
Priming	Camera x	Calibration lamp	On
	Wait	y	Sec
	Camera x	Beam	On
	Wait	5	Sec
	Camera x	Beam	Off
	Wait	1	Sec
	Camera x	Polarize low	
	Wait	20	Sec
	Camera x	Beam	On
	Wait	10	Sec
	Camera x	Beam	Off
	Wait	1	Sec
	Camera x	Readout	
	Wait	20	Sec
	Camera x	Beam	On
	Wait	30	Sec
	Camera x	Beam	Off
	Wait	1	Sec
	Camera x	Mode expose	
	Wait	1	Sec (Minimum)
Expose	Camera x	Expose	On
	Wait	60	Sec (Standard)
	Camera x	Expose	Off
	Camera x	Calibration lamp	Off
	Wait	1	Sec

Table 4. (Cont.)

Operation phases	Command sequence for camera x (x = 1, 2, 3, or 4)		
Readout	Select	Operating mode	PCM
	Select	Video	Cx
	Camera x	Readout	
	Wait	5	Sec
	Camera x	Beam	On
	Wait	22	Sec
	Camera x	Beam	Off
	Wait	1	Sec
	Camera x	High velocity	
	Wait	15	Sec
Camera turn off	Select	Operating mode	Analog
	Select	Video	Cx
	Camera x	Beam	On
	Camera x	Filament	Off
	Wait	60	Sec
	Camera x	Beam	Off
	Wait	1	Sec
	Camera x	MVPS	Off
	Select	Operating mode	Off

Note: (1) y = 300 sec for cameras 1 and 3 and 60 sec for cameras 2 and 4. (2) It is assumed that electron package E-4 was properly turned on before camera turn-on process was started. (3) Timing of command sequence used in orbit is different from this table. See Table 5 for details.

The Celescope television system should not only take full advantage of the spacecraft's capability, but should also fulfill the following basic requirements: (a) a square raster, (b) a noninterlaced scan, (c) an equal horizontal and vertical resolution, set at about 300 television lines in the analog mode and at $2^8 = 256$ television lines in the digital mode, in order to meet the angular resolution requirements in conjunction with the Celescope optical system (Davis and Godfredson, 1961), (d) a 1% accuracy in signal amplitude, met by digitizing to $2^7 = 128$ levels or, in the analog mode, by maintaining a 40-db signal-to-noise ratio in the communications link, (e) a real-time digital transmission, required as the primary operating mode because of practical limitations on the size of onboard data storage and on transmitter power, and because of the desired accuracy and data-handling capacity, backed up by both a digital store mode and a real-time analog-transmission mode, and (f) a dynamic range of 10^4.

The main reason for the adoption of a digital transmission system as the prime mode of operation is its accuracy — an almost negligible error rate of 10^{-6} in normal operating condition. Another factor is the ease of direct coupling to a digital computer for data processing and star cataloging.

Direct transmission of video data in digital form at the rate specified for the OAO spacecraft (5×10^4 bits/sec) requires the very slow scanning time of 1 frame in 10.5 sec, and the various parameters of the television system become those shown in Table 6. For comparison purposes, Table 6 also shows these same parameters for the analog backup mode of operation.

The digital system has a square raster of 256 lines, each having 256 picture elements. Eight bits (including one for parity check) are required to express the video-signal amplitude for each element. Since the pulse width for 1 bit is 20 μsec, 160 μsec are necessary for transmission of the video-amplitude data from each element. Therefore, 10.5 sec are required for transmission of one television frame (about 5×10^5 bits). At such a slow rate, a digital-scan system is easier to build than an analog system, within certain restrictions. The digital-scanning system utilizes the element-to-element scan shown in Figure 3 to provide more accurate beam positioning

Table 5. Command list for priming, expose, and readout used in orbit.

Operation phases	Command sequence for camera x (x = 1, 2, 3, or 4)		
Priming	Camera x	Cal.lamp	On
	Wait	y	Sec
	Camera x	Beam	On
	Wait	3	Sec
	Camera x	Beam	Off
	Camera x	Pol.low	
	Wait	11	Sec
	Camera x	Beam	On
	Wait	3	Sec
	Camera x	Beam	Off
	Camera x	Readout	
	Camera x	Beam	On
	Wait	10	Sec
	Camera x	Beam	Off
	Camera x	Mode expose	
	Wait	1	Sec
Expose	Camera x	Expose	On
	Wait	60	Sec (Standard)
	Camera x	Expose	Off
	Camera x	Cal.lamp	Off
Readout	Select and	Operating mode Video	PCM Cx (combined command)
	Wait	5	Sec
	Camera x	Readout	
	Wait	1	Sec
	Camera x	Beam	On
	Wait	21	Sec
	Camera x	Beam	Off
	Wait	1	Sec
	Camera x	High velocity	

Note: (1) y = 0 to 300 or more, depending on available time and requirement of warmup time. (2) Turn-on and turn-off sequence used in orbit are essentially identical to the ground sequences.

Table 6. Basic parameters for real-time transmission Celescope television system.

		Digital transmission	Analog transmission
Number of	Picture elements in a line	256	~300
	Lines in a frame	256	~300
	Picture elements in a frame	65,536	~90,000
	Bits in a picture element	8	—
	Bits in a frame	524,288	—
Transmission time or scanning time	Bit	20 μsec	—
	Element	160 μsec	5 μsec
	Line	40.1 msec	1.6 msec
	Frame	10.5 sec	0.48 sec

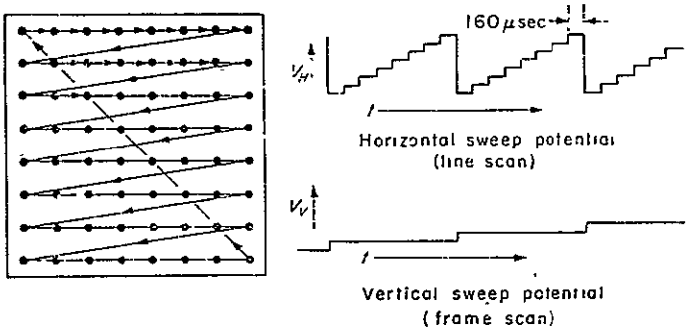

Figure 3. Illustration of digital scan.

than would be possible at these speeds if analog-sweep generators were used. Because of the fast rise and fall times of the staircase sweep potentials (of the order of 1 μsec) compared to the sweep speed (160 μsec per element), retrace blanking is not used in the Celescope system.

A disadvantage of this digital-scan system is the reduction of video-signal amplitude when long beam dwell times were used. In the Uvicon, as in other television camera tubes, the video signal is generated by discharging a charge pattern stored on the target. The longer the time that is utilized in reading out a given charge, the lower will be the peak value of signal current. This effect is shown in Figure 4, where the upper trace indicates beam dwell time and the lower trace indicates signal output. Since the analog scan employs 5-μsec dwell time and the digital scan uses 160 μsec, the peak value of the signal in the digital scan is roughly 1/80 of the analog-scan signal. It is a problem for video-amplifier gain and signal detection, especially if we bear in mind that design limitations force us to use a single video amplifier having the wide bandwidth, and therefore the high noise, appropriate to the analog signal. Under these conditions, the signal-to-noise ratio would be 10 db lower in digital than in analog scan.

To overcome this problem, Electro-Mechanical Research, Inc. (EMR), developed the special scanning scheme called "superscan" to achieve short beam dwell time under slow-scan conditions (Nozawa and Tucker, 1966; Nozawa, 1966). This superscan technique is actually a sample-scanning system, utilizing the scanning pattern shown in Figure 5. During most of the 160-μsec interval between scans, the beam is directed toward a part of the raster previously scanned. The superscan deflection, superposed on the element-by-element digital scan, causes the beam to dart into the unscanned portion of the raster so as to dwell on the unscanned picture element for only 5 μsec. The output video signal, therefore, contains useful information during only 5/160, or ~3%, of the total time, and the signal level is the same as that for the comparable analog scan. The sample-and-hold circuit isolates this useful portion of the video signal, which is then digitized by an analog-to-digital converter.

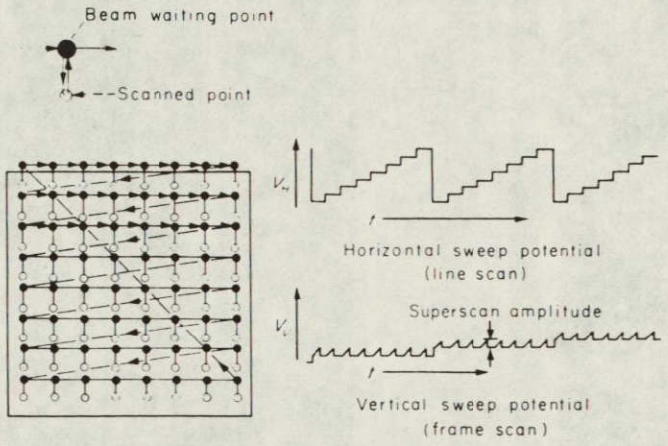

Figure 5. Illustration of superscan.

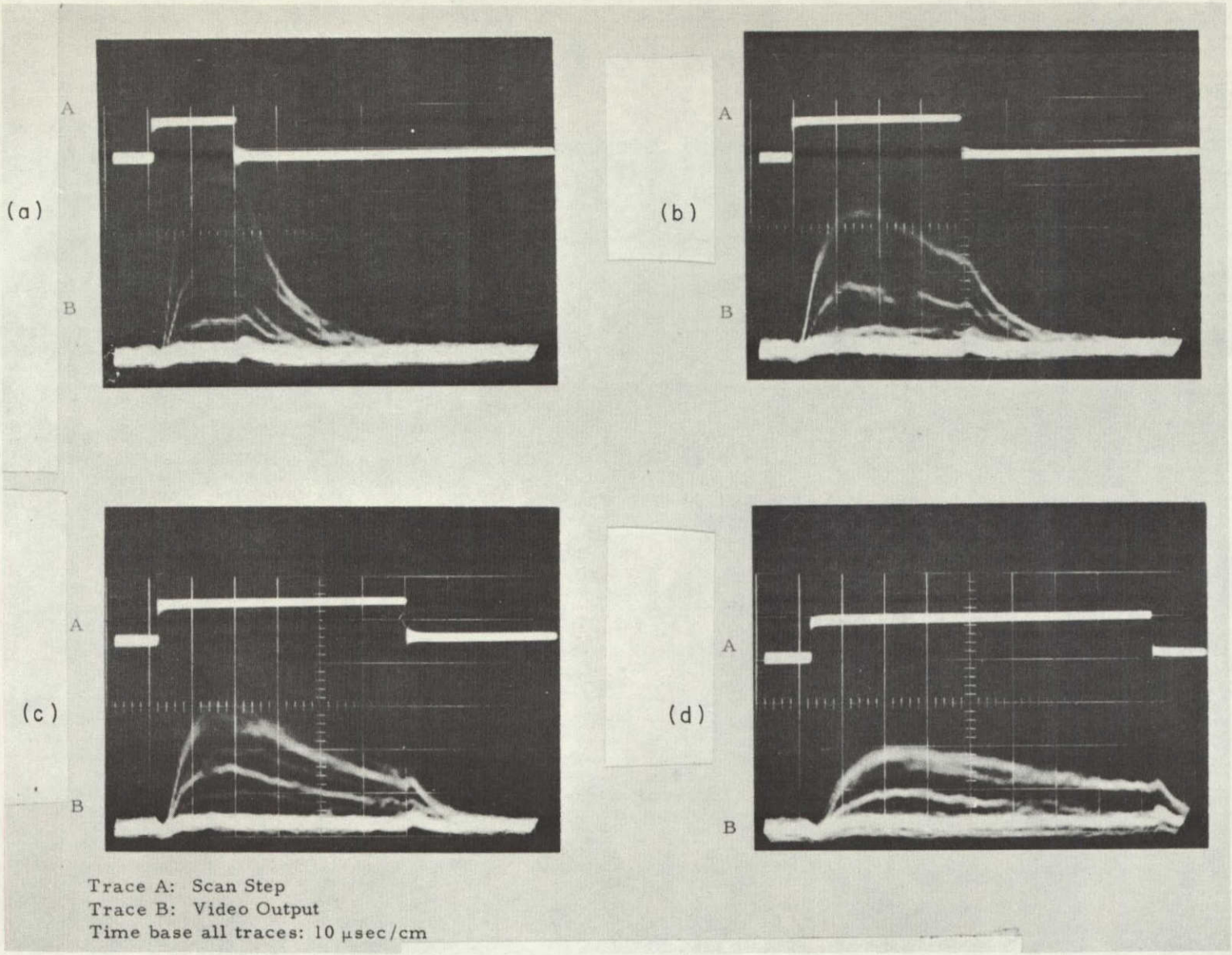

Figure 4. Output amplitude reduction due to beam dwell time. Target readout response of Uvicon S 34-A showing the fall in signal current as the beam dwell time is increased. Beam dwell time: (a) 20 μsec, (b) 80 μsec, (c) 120 μsec, (d) 160 μsec.

2.4 Principles of the SEC Target

The application of the SEC phenomenon to image tubes was developed mainly by Goetze and his group at Westinghouse (Goetze, 1962; Goetze, Boerio, and Green, 1964; Goetze and Boerio, 1964; Goetze, 1966; Boerio, Beyer, and Goetze, 1966). Before their study, there were several (direct view) image tubes that used a potassium chloride target (or, more correctly, dynode) (Wachtel et al., 1960; Wachtel, Doughty, and Anderson, 1960; Wilcock, Emberson, and Weekley, 1960; Emberson, Todkill, and Wilcock, 1962; Slark and Woolgar, 1962). But these tubes used solid potassium chloride, which produced secondary electron yields of 5 to 6 at most. The real breakthrough was the adoption of a low-density (or spongy) potassium chloride target, which produces up to 200 secondary electrons for every incident primary electron. Television image tubes using the low-density KCl target, which were later called SEC image tubes (Goetze and Boerio, 1964; Goetze, 1966), were developed at Westinghouse as a part of Uvicon development (Doughty, 1966). SEC television tubes were also developed in England (Filby et al., 1964; Filby, Mende, and Twiddy, 1965, 1966).

In an earlier era of development, Uvicon tubes were based on an EBIC principle (Schneeberger et al., 1962) rather than the SEC principle. But EBIC Uvicons could not produce the required sensitivity, so SEC Uvicons were adopted instead.

The structure of the target in these SEC tubes consists of three layers of membrane as shown in Figure 6. Aluminum foil, which is attached to the support ring, is oxidized to form aluminum oxide (Al_2O_3). The aluminum oxide membrane, which is transparent, is the main support structure for mechanical strength. Then the aluminum that becomes the signal plate for the target is vacuum deposited on the aluminum oxide. Finally, powdered potassium chloride is vacuum deposited on the signal plate in an argon atmosphere at a pressure of a few millimeters of mercury.

In operation, the SEC target is bombarded from the aluminum oxide side by primary electrons with energies of 5 to 10 keV (about 7 keV in the case

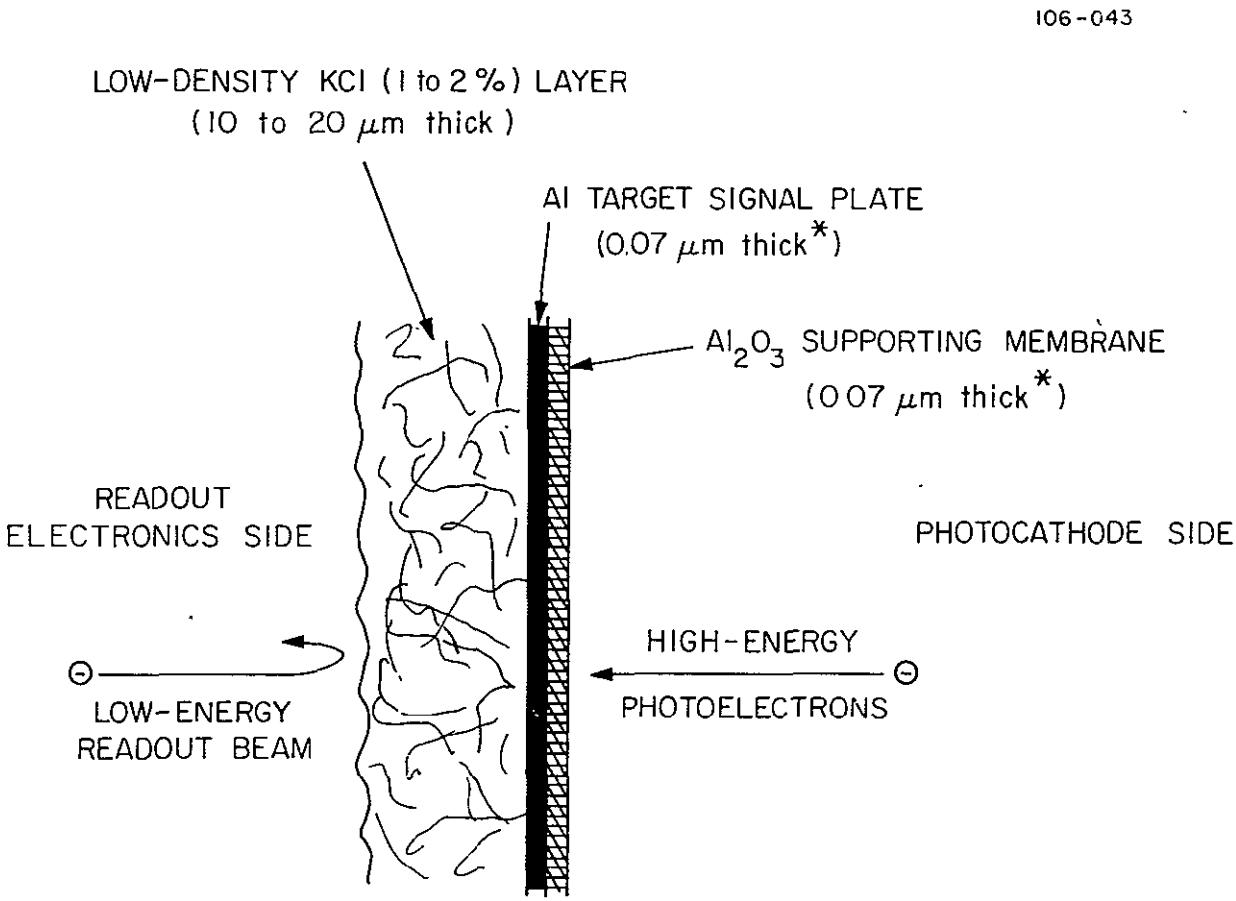

Figure 6. Structure of SEC target. Note: Thickness is not to scale. *British target is 0.05 μm thick. (Based on Filby et al. (1966).)

of the Uvicon). After penetrating the aluminum oxide and aluminum membranes, these high-energy primary electrons pass through the potassium chloride and produce secondary electrons in large numbers. The freed secondary electrons escape in the vacuum between the potassium chloride fibers (the low-density potassium chloride has a fibrous structure) and are eventually captured by nearby electrodes, the signal plate, or ionized atoms. Residual positive charges, which are not so mobile as the electrons, remain in the potassium chloride target.

If an electrical field is applied across the membrane of potassium chloride in the direction of its thickness, the freed electrons become more mobile and the yield of secondary electrons and residual positive charge is increased.

The electrical field is applied by creating a difference in electrical potential between the aluminum signal plate and the exit surface (the side of the potassium chloride membrane away from the signal plate). The potential difference is generated before electron bombardment by scanning the exit surface with an electron beam. Sometimes a distinction is made between SEC (Secondary Electron Conduction) and TSE (Transmission Secondary Electron) target operation, depending upon the direction of the applied electrical field. When the signal plate or entrance side for the primary electrons is positive, then it is called SEC; when the signal plate is negative, it is called TSE. But the operation is often referred to as SEC regardless of the direction of the electrical field. In the case of Uvicon, the signal plate is about 9 V positive with respect to the equilibrium target exit surface; it is therefore a true SEC operation. The yield of the secondary electrons and therefore the resultant residual positive charge depend on the energy of the incoming primary electrons and the intensity of the electrical field. Figures 7 and 8 illustrate examples of these relations. As shown in Figure 8, the yield of secondary electrons in the SEC mode is generally higher than that of TSE, except in a very weak field.

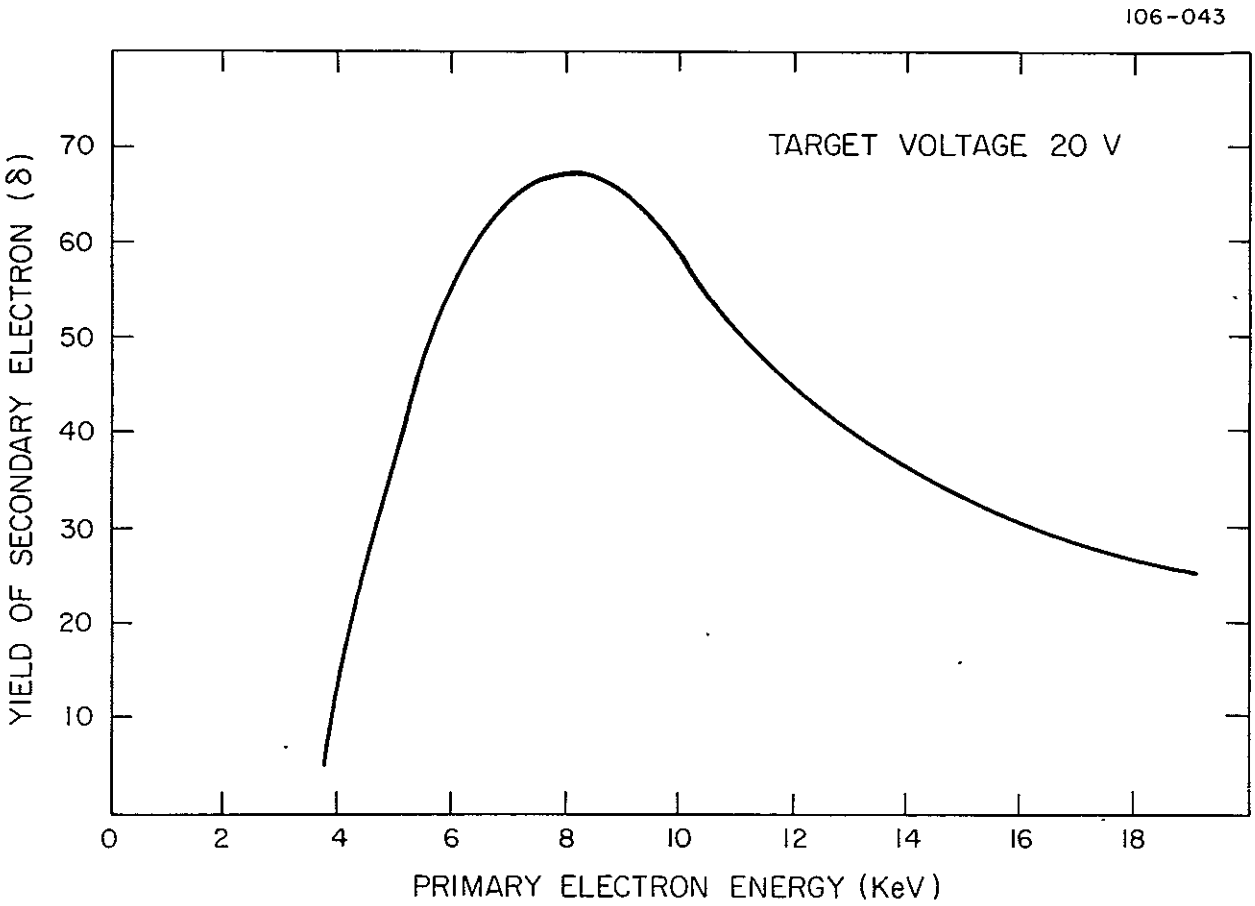

Figure 7. Yield of secondary electrons vs. energy of primary electrons. (Based on Boerio et al. (1966).)

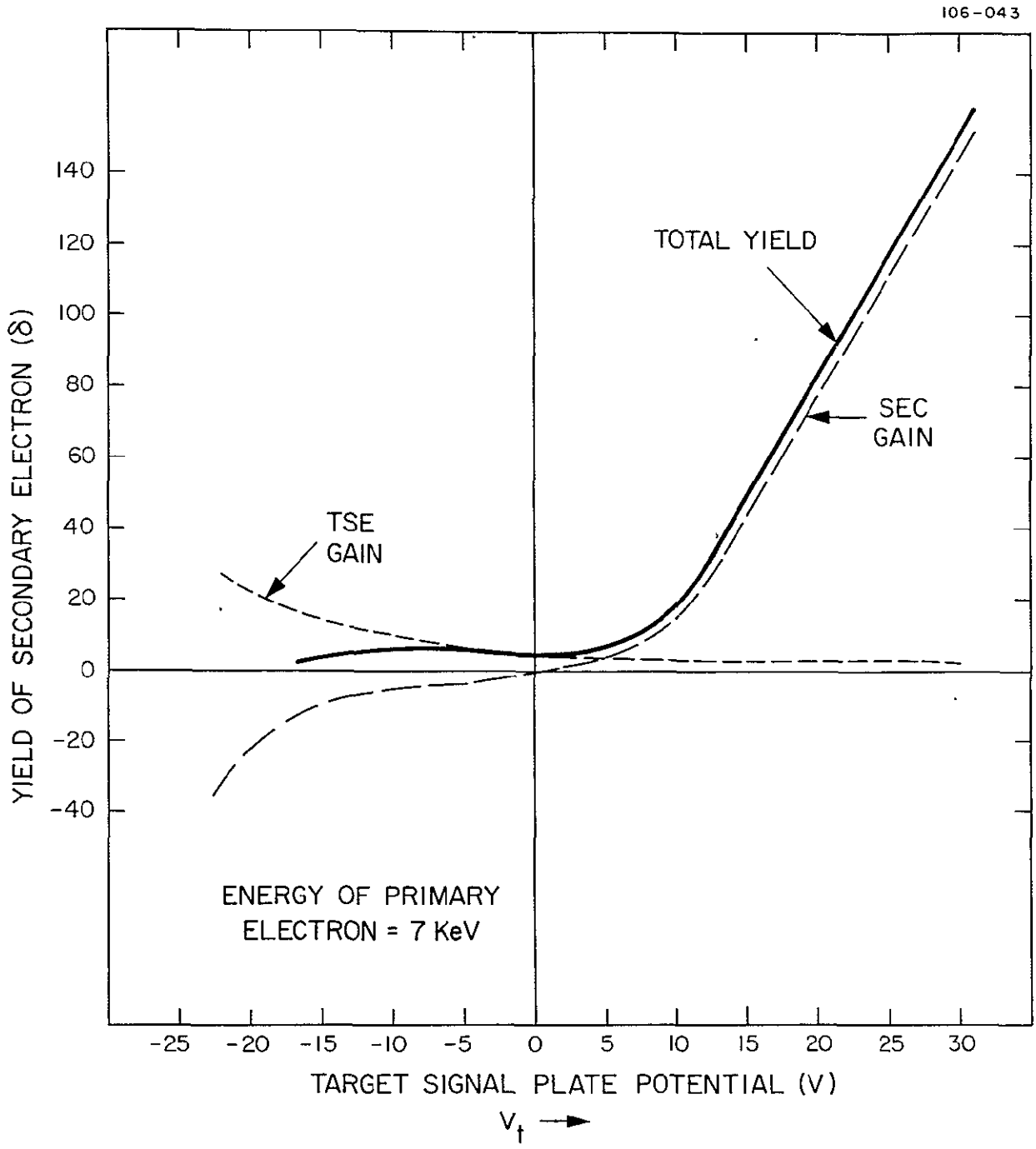

Figure 8. Yield of secondary electrons vs. electrical field in target.

2.5 Circumstances Inducing Target-Material Breakdown

The actual circumstances under which target-material breakdown occurs vary considerably. The following list represents most of the circumstances encountered during test and evaluation. Those marked with an asterisk were also encountered in orbit.

1. Excessive exposure to input light,*
2. Repeated underscanning,
3. Readout without proper priming,
4. Incomplete sequence of priming,
5. Partial (portion of target only) priming,
6. Uneven priming of target,
7. Too long beam dwell time,
8. Error in operational sequence,*
9. Error in gun-voltage setup,
10. Excessive exposure to radiation,
11. Defective tube.

Also, it was observed that target-material breakdown tends to occur more often in the digital mode than in the analog mode. Or, in a more general sense, the slower the scan, the likelier is the experience of target-material breakdown.

Beam current is another important factor in target-material breakdown. The greater the beam current, the likelier target-material breakdown is for the same scanning speed. Therefore, the Celescope experiment used the minimum level of beam current that is compatible with a safe operation.

The probability of target-material breakdown can be reduced by adoption of operating procedures to avoid the conditions listed above. The following provisions were taken in the Celescope system to minimize the risk of target-material breakdown.

1. Automatic switching of scanned area — In order to accomodate system-design requirements for reduced-size scanning (underscan), and the priming requirement for scanning the entire target area (overscan), an automatic-scan switching was adopted. After expose-on and -off commands are

issued, the automatic-scan switching logic is armed. Then, the next beam-on command automatically creates an underscan readout frame. To ensure the correct camera data readout, the camera-select command is incorporated as part of the logic. When the readout of the underscan frame has been completed, the beam is automatically turned off. The priming sequence, therefore, must start by the explicit command of "beam on." The switching of the scan area is accomplished by changing the gain of deflection amplifiers through logic circuits.

2. Automatic control of beam starting position — If the beam is turned on for readout or priming, the command frequently occurs at the middle of the frame. During readout this may result in the partial loss of data, and during priming, uneven (or, more accurately, uncontrolled) priming of the target surface. Since the deflection-voltage sequence and beam-on command are under the control of different, unsynchronized clocks, deflection voltage being controlled by a clock onboard the satellite, and beam-on command being controlled by a clock at the ground station, it is necessary to inhibit the execution of the beam-on command until both horizontal and vertical deflection voltages correspond to the beginning of the frame.

3. Manual switching of scan mode (digital and analog) — Even with the use of the superscan technique, the cumulative beam dwell time is 160 μsec in digital scan, because superscan deflects the beam to a previously scanned portion of the target during idle time (the total deflection space being only 10 elements or so during the superscan sweep). In analog scan, the total beam dwell time is only 5 μsec. Therefore, analog scan is employed for priming (polarization) purposes. Switching between digital and analog scans is manual and is usually preprogramed in accordance with fixed timing intervals.

4. No electron beam during standby — The Uvicon target can support a charge in excess of that required to produce target-material breakdown, provided that the condition is not aggravated by release of additional secondary electrons created by the scanning beam. Therefore, the electron beam is always suppressed except during priming and readout (data frame). The

chance of target-material breakdown is thus reduced considerably, because the electron beam is off during 90% of the orbital time.

5. Prevention of operation error — Rigid operational procedures have been established for preventing the target-material breakdown condition in the electrode potentials in the Uvicon. To avoid human error in operation, command sequences are generated as a file of punched cards, and special programing checks the validity of the command sequence. The valid command sequence is fed to a computer, which issues commands for transmission in real time or for loading the command memory.

6. Rigid tests and inspection — The last listed cause of target-material breakdown is a defective tube. If the vacuum of the Uvicon is not good and there is some residual gas in the tube envelope, then the gas will be ionized during exposure and readout. Positive ions from residual gas may accumulate on the target surface and increase the target-surface potential, thus creating target-material breakdown. Therefore, rigid testing and inspection of the tube were performed to eliminate faulty tubes.

These modifications may lessen the chance of target-material breakdown; but this possibility could not be eliminated until the mechanism was understood and a fundamental method that prevents it was adopted.

2.6 Theory and Prevention of Target-Material Breakdown

Target-material breakdown is the process of dielectric breakdown of the potassium chloride target membrane. This is a problem inherent in the SEC target (Filby, Mende, and Twiddy, 1965). Sometimes the potassium chloride destruction will be accompanied by destruction of the aluminum oxide support. In this case, the target becomes completely useless. Complete destruction of the target was very common in the early development of the Uvicon. Later, the destruction of very limited areas of the target was more commonly observed. It involves removal of part of the potassium chloride

from the supporting structure, which means that the supporting structure or signal plate is directly exposed to the readout beam. The bare spots on the signal plate are referred to as false stars. In analog mode, these false stars appear as point images resembling stars; in digital mode, because the scanning does not erase the false star on the first pass, the superscan elongates them to streaks.

The first type of target-material breakdown happens during the high voltage in the expose mode. The positive charge generated at the target by incoming photoelectrons continues to increase during exposure so long as light is incident on the photocathode and the high voltage is on. If not limited, this positive charge can increase to the point where it directly causes the dielectric breakdown of the target material.

The second mode occurs during readout. During normal readout, the yield of secondary electrons on the potassium chloride must be less than one. This is equivalent to saying that the discharge of the positive charge is complete. When the yield of secondary electrons exceeds unity, the process ceases to be readout; on the contrary, as in the original imaging process, the secondary electrons generated will be lost from the target material and the positive charge on the target will be increased.

The yield of secondary electrons is a function of the potential difference between the readout beam and the surface of the potassium chloride. Figure 9 illustrates this function. The yield of secondary electrons increases as the potential difference increases and at some point, 10 V or so, the yield exceeds unity. The voltage at this point is called the first crossover potential. At higher voltage, the amount of positive charge accumulated on the target increases rapidly and finally reaches the point of dielectric breakdown of the target material. Thus, the second mode of target-material breakdown may be caused indirectly by the accumulation of positive charge on the target in excess of the first crossover potential. It is therefore dangerous to accumulate a positive charge sufficient to cause the second mode of target-material breakdown, even though the amount is not sufficient to cause the first. If

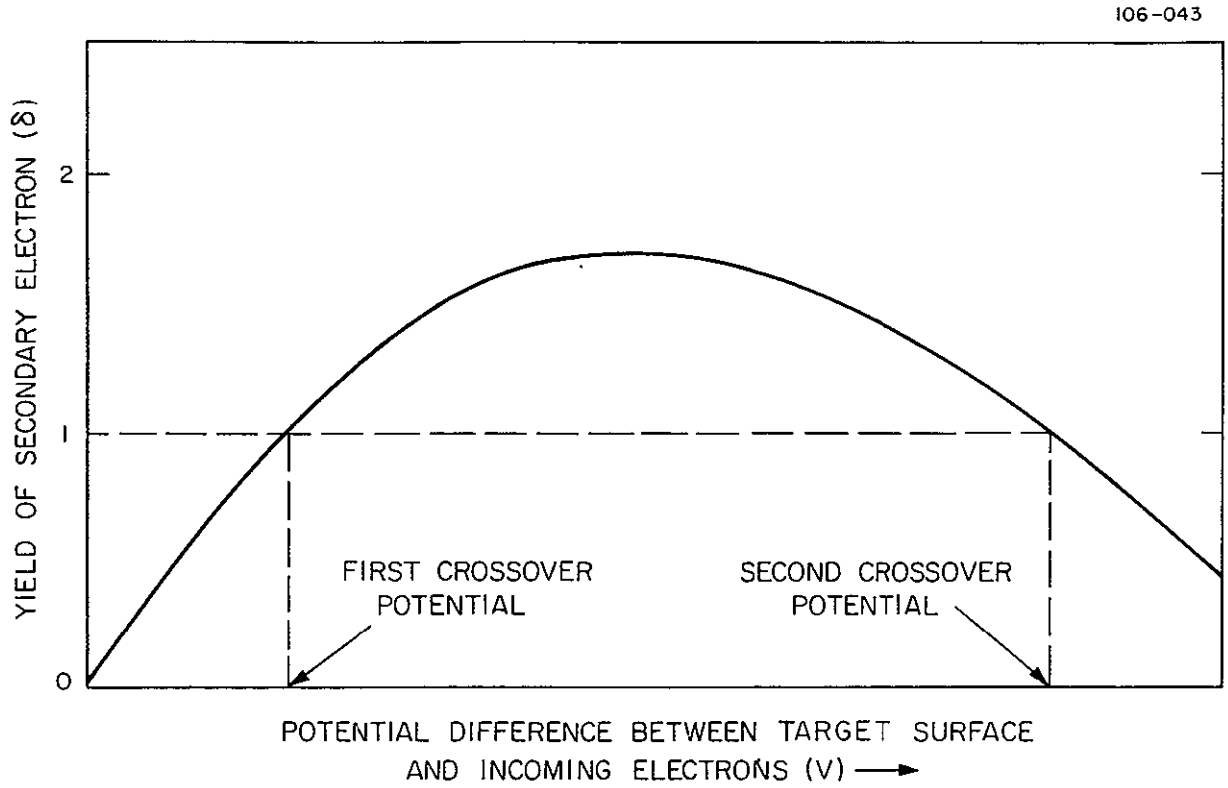

Figure 9. Yield of secondary electrons due to low-energy primary electrons.

the maximum allowable potential of the cumulative positive charge is limited to less than the first crossover potential, target-material breakdown will effectively be prevented. To accomplish this, there are several approaches:

1. Increase the first crossover potential of the target.

2. Limit the maximum potential of the positive charge during high-voltage on period.

3. Reduce the potential differences between the accumulated positive charge and the read-out low-energy electron beam.

The first method can be accomplished by improved manufacture. For instance, Uvicon tubes manufactured in Pittsburgh have a higher potential of first crossover than the tubes from Elmira. However, methods of controlling the first crossover potential were not developed in time. Recent studies indicate that coating the target surface with some other material considerably increases the first crossover potential of the target (McMullan and Towler, 1969). A second method, limiting the maximum allowable potential of the accumulated charge, was actually adopted for the Uvicon. The simplest way is to limit the input of the photons. If the intensity of the input is high, then the integration time of the input must be limited. In the case of Celescope, a list of prohibitively bright objects in the sky was compiled. Since Celescope explores the unknown heaven of the ultraviolet, heavy reliance on this method is not really appropriate. The best way to limit the maximum potential of the accumulated charge is to limit it electrically by inserting an electrode near the target. This method was adopted for almost all other SEC vidicons, but it has some drawbacks. For instance, image resolution suffers by insertion of the extra electrode. Because of the loss of the resolution, it has been suggested that the suppressor grid be eliminated from future SEC vidicons for astronomical application (Lowrance and Zucchina, 1961). In the case of Celescope, the final design was frozen before a suppressor grid was even considered. Concern about damaging the structural integrity prevented the insertion later of a new suppressor grid. Instead, the available grid in the Uvicon was used as a substitute. (Structural integrity is very important for

the survival of the Uvicon. Because of the severe launch environment, changes of mechanical configuration in the tubes that may diminish the structural integrity may jeopardize tube ruggedization.)

The closest electrode to the target in the Uvicon is the normalizing grid (number 5 or G5). Its function is to correct the direction of the readout beam to normal to the target surface for readout or priming. The difference of potential between the target and G5 is on the order of 500 V. Therefore, the maximum allowable potential for the accumulated charges on the target will be close to the 500 V determined by the G5, if the grid is kept at normal potential during expose. That was the case during the previous experiences that ended in target-material breakdown. But G5 is not needed during the exposure mode, and its voltage may be varied from the normal 500 V when the Uvicon is in the expose mode. Therefore, G5 can be used as a suppressor grid during the expose mode or high-voltage-on period. As explained before, if the maximum allowable potential is limited to less than the first crossover potential, then the readout process will not cause target-material breakdown even though the G5 potential is raised to a normal 500 V during readout. The maximum allowable potential during expose is determined by both the signal-plate potential and the suppressor (or G5) potential. If both potentials are kept below the first crossover potential of the target, the potential of the accumulated charges will be less than the first crossover potential in any circumstances. In Celescope, the difference between the signal-plate potential and G5 potential was kept at 9 V with respect to target-exit surface during expose mode, which includes the high-voltage-on period. The potentials of the G5 and target signal plate are switched back to their nominal values during priming and readout. Switching of the potential is accomplished by the logic circuit shown in Figure 10. The use of G5 as a suppressor grid made mandatory the separation of expose and readout cycles, because the same grid has different uses during the different phases of operation. A SEC Vidicon with a suppressor grid separated from G5 does not need a separate cycle of readout and expose, even though it may help to reduce the chance of the target-material breakdown. The danger in limiting the maximum potential of the accumulated charge is the introduction of nonlinearity into the transfer relationship of the image tube. Limiting the

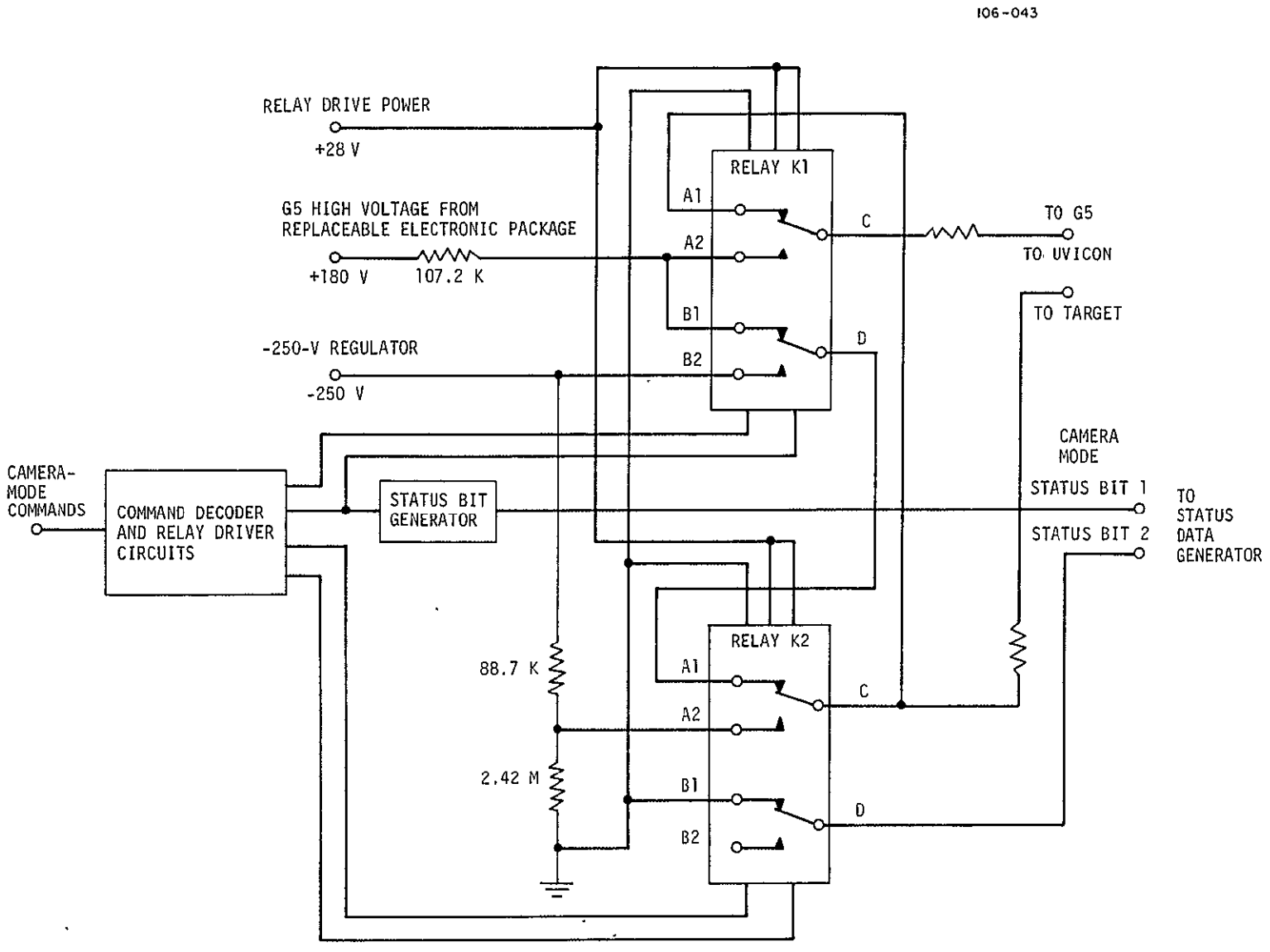

Figure 10. Logic circuit for switching potential of G5 and target. Note: All values are nominal. Each camera has separate circuits.

maximum potential of the charge is equivalent to the introduction of a saturation level to the output charge. Once the potential of the output charge reaches the limited potential, the relationship between the number of input photoelectrons and the amount of positive charge becomes nonlinear. These saturation effects occur in the case both of amplitude output and of total charge output (in Celescope, the total charge output used). Once nonlinearity between the input of electrons and the output of positive charge is introduced, the image size becomes a very important factor. If there is no limitation on the accumulated charge, the total number of accumulated positive charges will be proportional to the number of photoelectrons input. Limiting the maximum potential truncates the output charge; the truncation introduces size effects. To explain the effects, let us consider two solid bodies of equal volume, say, cone shaped. One has a base area of 10 in.^{2}, and the other, 100 in.^{2}. The heights of both cones are, respectively, 50 in. and 5 in. If we truncate these cones at a height of 1 in., the remaining volumes of these cones are no longer equal. The truncation effect or the image-size effect is common to all types of SEC vidicons with a suppressor grid and to the Uvicon with a substitute suppressor grid.

The third method of preventing target-material breakdown is to limit the differences of potential between the readout beam and the accumulated charge on the target. This can be accomplished in several ways. One is by changing the potential of the signal plate in such a way that the difference between the potential of the positive charge and that of the readout electron beam is always less than the first crossover potential. This technique can be adopted regardless of the potential of the accumulated charge of the target. However, it may require more than one readout to discharge completely the accumulated charge.

An EMR study, discussed in more detail in Chapter 3, examined the effect of image size on output signal for images of the same total intensity. It was found that for image sizes in the general range from 0.2 to 2 times the picture-element size, output depended strongly on image size, thus

requiring great stability of optical and electronic focus in order to preserve instrument calibration. The report implies that this effect is at least partly due to the operating mode, which was strongly influenced by the need for protection against target-material breakdown.

2.7 Target-Material Breakdown During Ground Testing

At the time of launch, the false stars in the Celescope equipment that were an indication of a history of target-material breakdown totaled 11 for all four tubes. The details are shown in Table 7. The four false stars in camera 2 were created before system tests. Since this camera suffered catastrophic failure in orbit, the false stars might have been early symptoms of the future. Uvicon 050D, a product of the Elmira Electronic Tube Division of Westinghouse was initially without any recognizable false stars except one adjacent to the target ring. But during an acceptance test at EMR, the first two of the false stars were created. Details of the circumstances are not clear, but they appeared during a uniformity test or field emission test, which required general illumination and higher-than-normal voltage applied to the imaging section of the Uvicon tubes. Another false star was created during calibration of the Uvicon with a 26-hole pattern. This test also included a very high level of input illumination.

In the case of camera 4, two of the false stars existed immediately after the production of the tube.

After the experiment package, incorporating techniques for prevention of target-material breakdown, was completed, the Celescope system was tested on the ground as a part of system acceptance and integration tests for almost 2 years (details of the tests are listed in Table 8). During this period, only one target-material breakdown occurred. On October 12, 1967, during a vacuum optical bench (VOB) test, which is the system calibration test, a whole optical package had been placed in a vacuum chamber. After

Table 7. List of false stars at the time of launch.

Telescope	Uvicon tube	False-star designation	Approximate position K	Approximate position L	Approximate size ΔK	Approximate size ΔL	Approximate intensity Peak	Approximate intensity Sigma	Date of creation	Remarks
Camera 1	R19A	(none)	221	247	3	3	17	120	?	Rarely seen because of improper beam landing; adjacent to target ring.
Camera 2	65-35-050D	A	108	87	16	6	127	4500	10/27/65	Created during acceptance test; double false star
		B	174	141	16	5	127	4000	7/66	Created during ambient calibration
		C	218	192	16	7	127	4000	10/27/64	Created during acceptance test
		G	58	148	12	5	127	4500	10/10/67	Created during VOB test
		H	90	176	14	4	127	3000	10/10/67	Created during VOB test
		I	100	188	14	4	100	800	10/10/67	Created during VOB test
		J	131	136	14	2	95	800	10/10/67	Created during VOB test
		(none)	252	237	9	6	127	3000	before 10/18/65	Probably created during manufacturing; adjacent to target ring
*Camera 3	R29A									
Camera 4	R42D	D	78	139	8	3	32	400	before 9/1/64	Probably created during manufacturing
		E	157	173	10	3	46	800	before 9/1/64	Probably created during manufacturing

*There is no false star in camera 3. K, L are vertical and horizontal coordinates, respectively.

Table 8. List of major system tests on the ground.

Test period	Name of test
2/ 1/67 – 2/24/67	Postshipment system inspection and functional check
3/16/67 – 3/17/67	Baseline functional test
3/18/67 – 4/ 4/67	Vibration test and mass-property test
4/10/67 – 4/12/67	Postvibration functional test and alignment check
4/20/67 – 5/24/67	E-4 repair and vibration test
5/25/67 – 5/26/67	Postvibration functional test
5/29/67 – 6/ 1/67	SAO/WEP integration test
7/18/67	Prethermal vacuum functional test
7/18/67 – 8/14/67	Thermal vacuum test
8/17/67 – 8/18/67	Postthermal vacuum functional test and inspection
8/23/67	Optical-package alignment check
9/21/67 – 10/23/67	VOB test (system calibration)
11/ 4/67 – 1/18/68	Spacecraft/SAO integration tests
1/27/68 – 2/25/68	Electromagnetic compatibility (EMC) test
3/ 6/68 – 3/21/68	Early thermal-vacuum test
5/ 9/68 – 5/16/68	EMC test
6/25/68 – 6/28/68	Radio frequency interference test
7/ 3/68 – 7/17/68	Aliveness tests and vibration tests
8/ 4/68 – 8/23/68	Thermal-vacuum acceptance test
9/18/68 – 9/20/68	Workmanship vibration test
10/8/68	Postshipment functional test
10/30/68 – 12/ 7/68	Prelaunch aliveness test and practice

completion of a series of tests, all three cameras were being turned off (Test Run No. 122). Since early during the VOB test, camera 2 channel electronics failed, that camera was connected to the channel of camera 4 to allow continuation of VOB testing before repair of the failed part. Because camera 2 and camera 4 channels are interchangeable, this swapping of electronic channels should not have caused any troubles. During turn-off, we experienced an operator error. All operational commands are issued by an IBM 1401 computer by using groups of commands for each stage of testing. The turn-off process is the last sequence of each cycle of testing; after it has been completed, the computer becomes inactive to permit time for rearranging other test setups. As shown in Table 9, the turn-off sequence contains a 60-sec waiting period. A computer operator mistook the waiting period for completion of the whole sequence and depressed the "end" button on the computer. Consequently, the computer immediately stopped all activity, including timing of the 60-sec wait, thus leaving the computer frozen. Detecting this abnormal condition of the Celescope experiment, operational personnel present tried to resume the turn-off sequence but were unsuccessful. They also attempted to introduce emergency commands supposed to recover the Uvicon from any abnormal condition; but these were also fruitless, since the computer was under the control of the inactive condition. Manual command to turn off the Celescope main power supply from the simulated spacecraft could not be issued, again because in the "inactive" state the computer blocks the command route between the Celescope experiment and the experiment test and control unit (ETCU), which, in normal circumstances, is capable of issuing any command by means of a manual pushbutton. Finally, Celescope was shut down by removing manually the cable connection to the power supply. Examination of all Uvicons after this accident revealed four new false stars in camera 2 and no detectable change in the other cameras.

The mechanism of target-material breakdown in this incident is explained as follows: since the methods of preventing target-material breakdown that were adopted limit the maximum potential of accumulated charges on target only during the expose and readout modes — that is, in the steady-state condition of the target and surrounding electrode potential — the prevention method

Table 9. Turnoff sequence used during vacuum optical bench test.

Initial status of system:

System Op mode off, all filaments on, all beam on, all expose off, all camera high velocity.

Command number	Command	
1	System op mode off	
2	Camera 1	beam off and expose off*
3	Camera 2	beam off and expose off*
4	Camera 3	beam off and expose off*
5	Camera 4	beam off and expose off*
6	EDHE	Real time noncyclic
7	Wait	1 sec
8	Status check	
9	Camera 1	beam off and expose off*
10	Camera 2	beam off and expose off*
11	Camera 3	beam off and expose off*
12	Camera 4	beam off and expose off*
13	Camera 1	filament off
14	Camera 2	filament off
15	Camera 3	filament off
16	Camera 4	filament off
17	Camera 1	calibration lamp off
18	Camera 2	calibration lamp off
19	Camera 3	calibration lamp off
20	Camera 4	calibration lamp off
21	EDHE	Real-time noncyclic
22	Wait	1 sec
23	Wait	60 sec
24	Camera 1	Medium-voltage power supply off
25	Camera 2	Medium-voltage power supply off
26	Camera 3	Medium-voltage power supply off
27	Camera 4	Medium-voltage power supply off
28	SAO	experiment off

*Combined command.

is not effective during periods of changing electric field, in particular during turn-on or turn-off or during switching of camera modes. To prevent target-material breakdown during these periods of change, a very rigidly controlled sequence of operations with ample calm-down periods between changes of state was adopted. Failure to follow this predetermined sequence increases the chance of target-material breakdown. Also, to lessen the chance of exposure to dangerous transient conditions, we adopted the policy of a minimum number of camera turn-on and turn-off operations. This policy was also carried on when Celescope was in orbit; for the first 3 months, the Uvicon cameras were never turned off between consecutive SAO operating periods, which spanned 1 to 2 weeks in standby status. Later, this policy was abandoned and cameras were turned off at the end of each SAO operating period for other prevailing reasons: (a) to prevent camera deterioration, especially cathode emission; (b) to lessen the chance of target-material breakdown because of reduced sensitivity of the Uvicon; (c) because the risk of failure during turn-on was reevaluated on the basis of orbital experience and judged to be less than the risk of failure from wear out; (d) on the basis of actual temperature measurement in orbit; it was determined that the Uvicon cameras would not overcool with filament off.

2.8 Experiences in Orbital Operation

The Celescope experiment package was launched as a part of Orbiting Astronomical Observatory (OAO A2) spacecraft, which, on December 7, 1968, was successfully injected into the expected orbit. After spacecraft checkout, the E-4 electronics package was turned on to monitor the status and temperature of the experiment. Then the sunshade covering the Celescope end was opened to allow outgassing before the high voltage in Celescope was turned on. During orbit 101, real-time contact was made with Rosman station; camera 3 was turned on; and the first picture of an ultraviolet star field was taken in the analog mode.

Camera 3 was then tested for 1 day before attempting to turn on the other cameras. The exposure time was increased from 5 to 15 sec. After testing the PCM operation mode, we scheduled a series of daylight exposures with

camera 3. The first 5-sec exposure proved that camera 3 could not operate in the daylight at the orientation of the satellite. The next day at the Rosman dark contacts we turned cameras 4, 1, and 2 on.

Camera 4 passed the 5-sec daylight exposure test at the last available Rosman contact. The following day, we tested the cameras operating together and tested camera 4 in daylight with a 20-sec exposure. Extrapolating from the 5- and 20-sec exposure tests, we decided that it would be safe to expose camera 2 and 4 for 60 sec in the daylight.

At the next Rosman contact, R141, camera 2 had 27 new false stars. These were obviously the results of daytime observation. Camera 4 apparently did not suffer any ill effects from the same daytime observation; but an operational policy was set to avoid thereafter any daytime observation. Therefore, all observations after orbit 155 were dark (night) observations; some dawn and dusk observations were included in the later period after camera sensitivity had decreased. These later observations were also all exposures looking near the antisun direction; in contrast, earlier daytime observations were all looking toward the sun, but more than 45° away from it. The failure of camera 2 was caused by daylight observations — that is, by overexposure to light — despite our techniques for preventing target-material breakdown. Probably the limiting voltage imposed by the substitute suppressor grid was not sufficiently low to prevent some portion of the target reaching the first crossover voltage.

The next contacts (R121 through R258), which included 1 week of an inactive period of Celescope, were performed successfully without any difficulties. All active contacts in this period were real-time dark Rosman contacts. Then the next set of remote contacts started. These operations were intended to make maximum use of the data-gathering opportunities. The priming was performed during one of the remote contacts, which was in daylight. Then expose was performed during a dark period by commands stored in the spacecraft command memory. Readout was executed in the next available contact which was in daylight. After completion of readout, the priming sequence could be started for the succeeding exposure, and so on. The first available real-time contact, R268, following the set of remote operations disclosed 26 additional false stars

in camera 2. There were no indications of additional false stars in the other cameras.

The immediate cause of the second instance of target-material breakdown was determined by an experiment during orbit 296. Since the target-material breakdown occurred during semi-back-orbit operation, in which priming and readout were performed during real-time operation, but the actual expose was done in back orbit, expose mode was suspected as the cause. Expose mode will be abbreviated as XMO to avoid confusion with expose, which is the actual application of high voltage to the imaging section and which is designated HVON. During the orbital experiment, camera 3 was left in expose mode with the high-voltage off for the entire 100 min of orbital period except for a very short HVON for resetting of the electronic logic. The readout picture showed a very high background, which indicates some kind of signal integration was going on when the camera is in the expose mode. The true nature of the incoming signal was later determined as light input from the sun, scattered sunshine, air glow caused by sunshine, or earthshine. From these experiences, the duration in XMO for each camera was limited to at most 5 min at first, then later increased to 15 min; also, during inactive periods, the Celescope end of the sunshade was kept closed to avoid unnecessary input of daylight.

Later, at R1344, camera 2 ceased to function completely. The direct cause of the failure is attributed to (a) the video preamplifier or (b) the filament. In either case, the failure could easily have been caused by degraded vacuum in the Uvicon tube, which may be induced by frequent target-material breakdown. The detailed history of camera 2 is shown in Table 10 and Figure 11.

A primary cause of failure in camera 2 was our assumption that tests conducted on one Uvicon could be used to determine the performance of another.

Camera 4 also suffered minor target-material breakdown that created two additional false stars. This breakdown was caused by a readout without prior priming (and also expose). The normal operating sequence gradually raises the target potential from high-velocity to polarize-low, polarize-low to polarize-high, and each step allows sufficient time to equalize the target

Table 10. Brief history of camera 2 operation.

Contact station and orbit number	Operation	Remarks
R115	Turn on, 5-sec exposure, analog readout	No change in number of false stars (= 8)
R128	4-camera operation, 60-sec exposure, pulse-coded modulation (PCM) readout	
R129	4-camera operation, 180-sec exposure, store readout, only part of picture received	Probably target-material breakdown occurred
R130	4-camera operation, 60-sec exposure, analog readout	No change in number of false stars (= 8)
Q132, S133, S134, S135, S136, S137, Q138, Q139	Camera 2 - camera 4 operation, 60-sec exposure to daylight, PCM readout	Almost all cases experienced target-material breakdown
R141A, R141B	4-camera operation, 60-sec exposure, PCM readout	Found 27 new false stars (total = 35)
R143, R144, R155, R255, R256A, R256B, R257A, R257B R258	4-camera operation, 60-sec exposure, PCM readout	No change in number of false stars (= 35)
S260, S261, S262, S263, S264, S265, O266, R268, O268	Prime during the previous contact, 63-sec exposure in back orbit, PCM readout in this contact	Almost all cases had target-material breakdown; at S261, at least one extra false star, at O266, 20 new false stars found (total = 56)
R269	4-camera operation, 60-sec exposure, PCM readout	Found 8 additional false stars (total = 66)
R271A	Turned off	
R664	Turn on	
R748	5-sec exposure, analog readout	
R762, R763	5-sec exposure, PCM readout	No change in number of false stars (= 66)
R776	30-sec exposure, analog readout	
R777	30-sec exposure, PCM readout	
R790	60-sec exposure, PCM readout	
R990	5-min XMO	
R991, R992	5-min XMO	
R1006	10-sec exposure, 8-min XMO, PCM readout	
R1017	4-camera operation, 60-sec exposure, PCM readout	
R1018A through R1103	Normal operation, typically, 4-camera operation, 60-sec exposure, PCM readout	
R1105A	4-camera operation, 60-sec exposure, PCM readout	Small target-material breakdown in central region
R1105B	4-camera operation, 60-sec exposure, PCM readout	Target-material breakdown in center and lower right-side regions
R1117	Priming attempt causes target-material breakdown	
R1301	Target-quality check performed	
R1344	No video output detected, turn off	
R1358 to M1359	Turn on and pumping performed; turn off	
R1370 to R1371	Turn on and pumping performed, turn off	Ceased camera 2 operation

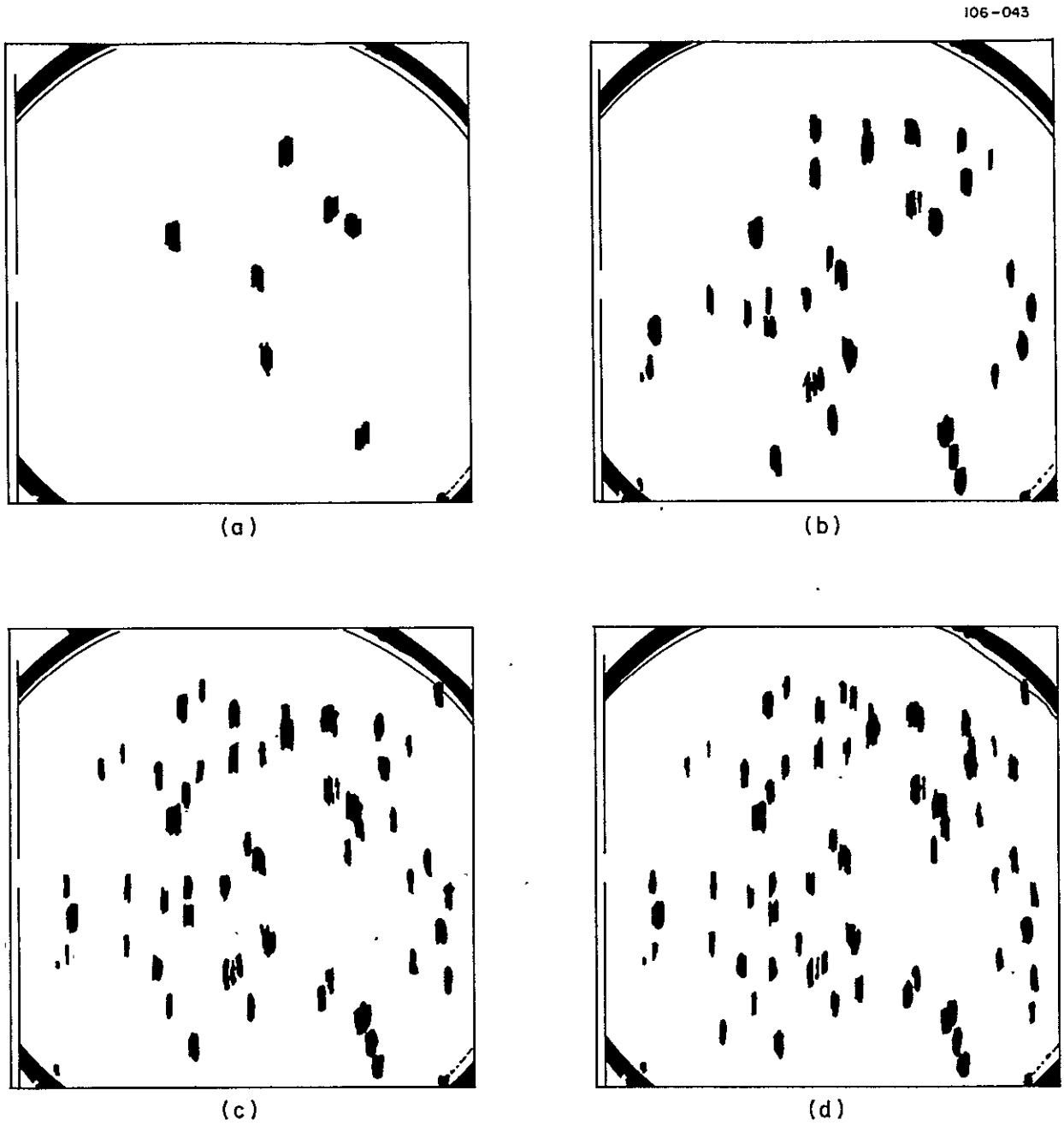

Figure 11. Appearance of camera 2 picture without real star images: (a) at the time of launch through R130, (b) R141 through R258, (c) at O266, (d) R269 through R1104.

potential by the priming process, in order to avoid disruptive transient conditions. The unexpected readout cycle started in the polarize-high mode, initiating a sudden large change in voltage and target-material breakdown.

2.9 Causes of Orbital Target-Material Breakdown

In the second incidence of target-material breakdown in camera 2, the prolonged period of XMO caused an excess charge accumulation on the target. To discover the source of excess charge accumulation, additional experiments were performed on the ground. A fairly common source of background noise in TV tubes is internal light from the filament. For example, filament-photocathode coupling is observed in the SEC Vidicon, and it is standard operational procedure to turn off the filament during long exposures to avoid internally generated extraneous light. However, since filament light contains only the visible and infrared, and the Uvicon is not sensitive to either, no filament-photocathode coupling was expected. This expectation was confirmed by experiments.

In one experiment, a D-type Uvicon, the same type as camera 2, was left in XMO in bright daylight with the faceplate uncovered. The output frame displayed very high background noise, duplicating the result of a similar orbital experiment. Then, the faceplate of the Uvicon was covered completely to prevent external light from reaching the photocathode, and the Uvicon was left in bright daylight again for up to 6 hours. The readout frame did not indicate any increase of background above normal dark-exposed pictures. This proves that residual sensitivity in XMO is caused by external input, not from internal light.

Mechanisms suggested for the generation of a charge from external signals are the following: (a) direct generation of photoelectrons by potassium chloride (the target material), (b) stray photoelectrons from the photocathode to the target, or (c) space radiation.

To examine the possible effects of space radiation (high-energy particles or gamma rays), special ground tests were performed with the cooperation of Goddard Space Flight Center (GSFC). The results indicate the following (Nozawa, Newman, and Wallgren, 1970):

1. Gamma and beta rays easily cause excessive charge accumulation on the target if their intensity is sufficiently high.

2. The rate of charge accumulation on the target in HVON is 100 to 1000 times greater than in XMO.

3. The mechanism of charge accumulation by radiation in HVON is the fluorescence of the lithium fluoride faceplate. When it is excited by radiation, the fluorescent photons generate photoelectrons at the photocathode.

4. In the case of XMO, fluorescent light from the faceplate seems to stimulate photoelectron production in the potassium chloride target.

5. Actual space radiation is not strong enough to produce any noticeable increased, in background even when the Uvicon is left for a full 60 sec in HVON in the most intense region of the OAO orbit.

6. If there were enough space radiation to produce a high background, then it could be detected in the Celescope picture, since the radiation shield provided by the telescope structure is not sufficient to reduce such intense radiation.

Considering the results of this experiment and the energy required to penetrate aluminum oxide target support structure, for the photoelectrons the first mechanism is most likely to be the cause of charge accumulation.

Since camera 2 has been the only one to suffer catastrophic target-material breakdown, there must be something different about it. The difference may be the result of manufacturing methods. As shown in Table 11, it was the only camera manufactured in the Elmira tube division. The rest of the cameras were manufactured in Pittsburgh, where a research-and-development type of manufacture was followed. Even during the assembly of the camera module and the camera-calibration period, Elmira tubes suffered target-material breakdown more easily than Pittsburgh tubes. Also, the first crossover potential for Elmira tubes was about 10 to 13 V; for Pittsburgh tubes, 15 to 19 V. The system was designed such that the electronic channels of all cameras were interchangeable. Therefore, the electronic setup favored Pittsburgh tubes over Elmira tubes because the former had a greater margin of safety before reaching the first crossover potential. Interpretation of this fact is not yet clear, but we can postulate the following: The first crossover

2 A

Table 11. List of flight Uvicon.

	Camera 1	Camera 2	Camera 3	Camera 4
Uvicon serial number	R19A	65-35-050D	R29A	R42D
Manufacture	Pittsburgh	Elmira	Pittsburgh	Pittsburgh
Tip-off date	5/15/64	10/19/65	8/7/64	8/31/64
Final potting date	5/10/66	7/15/66	6/16/66	9/24/66
Completion date of telescope assembly	6/28/66	8/1/66	8/25/66	10/18/66
Electron threshold	5000+	7300+	4600+	3400+
Peak quantum efficiency (%)	2.23	7.8	2.17	7.6
Mechanical fault	Raster oriented 15° clockwise from Z_c axis	None	Cracked target insulator	Internal short G4-G5, corrected
Target-material breakdown before system test	None	During ambient calibration at EMR	None	None
Past history of repair in camera module	Intermittent ground connection in electronic package repaired	None	None	Excessive noise problem corrected

potential varies across the target surface. Then, even if the peak amplitude of the signal as limited by the G5 voltage is constant across the target surface, the signal potential may exceed a local first crossover potential in some region. By the same token, the limiting voltage determined by the G5 may vary as a function of position on the target surface. On the basis of measured saturation voltages of video peak-amplitude output as a function of target position (shown in Figure 12), Elmira tubes display a larger variation of peak (limited) amplitude than do Pittsburgh tubes. The combination of both positional variations makes some tubes more susceptible to target-material breakdown than others, since the safety margin that was supposed to take care of these variations is smaller in some tubes. In the case of Pittsburgh tubes, the safety margin may be 5 to 10 V, but Elmira tubes may have only 1 to 5 V. Therefore, it is conceivable that the limiting potential determined by G5 in Elmira tubes may exceed the first crossover potential in some regions. The reason for the difference in the first crossover potential between both types of Uvicon is not known. It may correspond to differences in the detailed structure (thickness of each membrane, density of potassium chloride, etc.). Another possibility is that the differences in susceptibility to target-material breakdown are caused by the difference in electrode structure between the two groups of tubes.

Target-material breakdown is not easy to observe, because the necessary degree of destruction is rare. Figure 13 is one of these rare pictures. This is the target-material breakdown in camera 2 during Rosman 1105B, which was the last known picture from that camera. The center and lower regions, which indicate adjacent black signal and high white signal, show the target-material breakdown during readout. The black area in the top portion of the picture is not caused by target-material breakdown but is part of the normal behavior of the tube called "shadow." Numerous white spots in the picture are false stars. The white arcs in the four corners are part of the target ring. No star image appears in this picture. The bright glow in the upper portion of the picture is the Lyman-α radiation from the geocorona; the black arcs near the center of the Lyman α are probably regions where the signal level exceeded the first crossover potential. Figure 32(b) shows an earlier occurrence of target-material breakdown in camera 2.

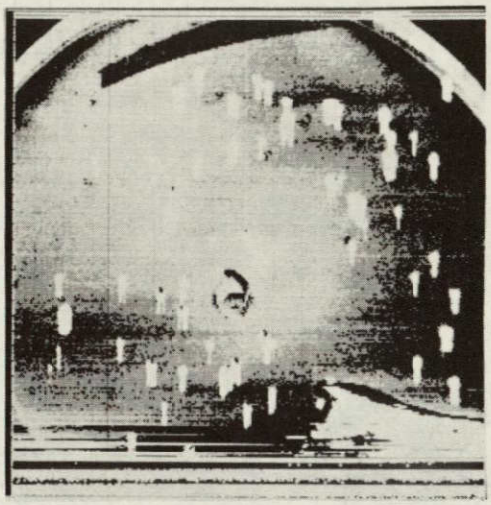

Figure 13. Picture of target-material breakdown: R1105B, the last known picture for camera 2.

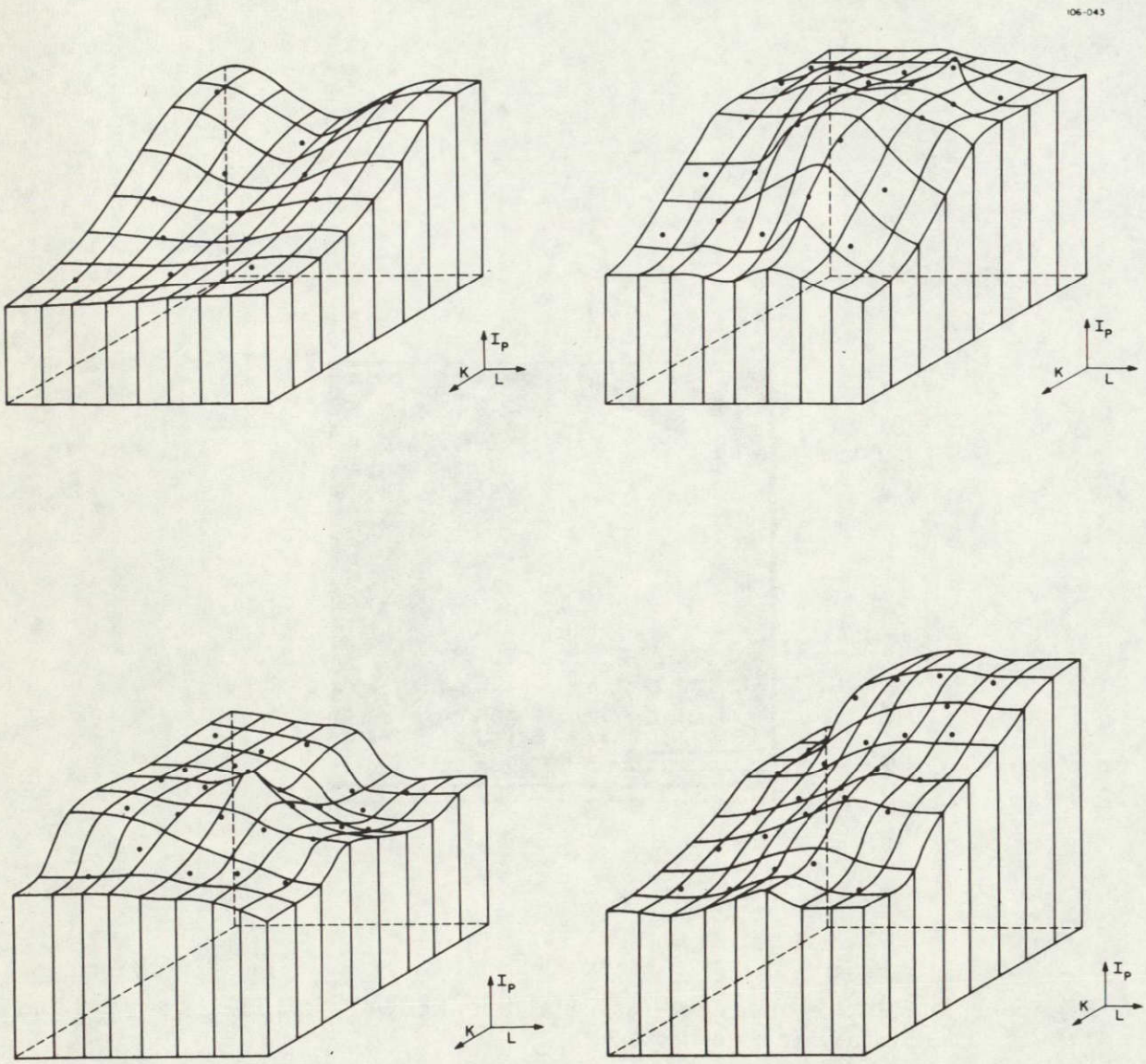

Figure 12. Distribution of limited signal potential on target (relative values). Dots indicate positions of actual amplitude measurements.

2.10 Conclusions

1. Protection against target-material breakdown (crossover) is a critical requirement. The Celescope techniques proved to be satisfactory for three of our four cameras. Improved techniques are now available.

2. Superscan readout used in Celescope was satisfactory.

3. The use of electrostatic rather than electromagnetic focusing/deflection eliminated significant problems but created some new ones. The relative merits of these available alternatives should be reassessed for future experiments.

4. In the case of devices such as the Uvicon, for which it has not been demonstrated by test of a large number of appropriately selected samples that individual items have closely similar characteristics, tests performed on one item should not be used as the basis for determining what operating procedures are proper for another. The Uvicon in Celescope's camera 2 was severely damaged as a result of our not realizing how significantly it differed from the other Uvicons in the experiment.

5. For some methods of preventing target-material breakdown, in particular that used in Celescope, the output signal becomes critically dependent on the focus of a stellar image on the target.

CHAPTER 3

IMAGE QUALITY, EXPECTED AND OBSERVED

3.1 Introduction

In very broad terms, the objectives of the Celescope experiment are the measurement of stellar intensities and the identification of stars for cataloging. To achieve these objectives, the general requirements of the optical system are the formation of high-quality images and the preservation of incoming optical fluxes. In this chapter, the quality of star images will be discussed. Image size, image resolution, and the intensity distribution of an image will be discussed in detail. Some aspects of flux preservation will also be presented, but a detailed discussion of the effects of the electro-optical systems on the measurement of star intensity will be deferred.

In general, the quality of the images returned by Celescope are satisfactory and similar to that expected. On some occasions, however, the quality has fallen below expectations, even though observational results are not seriously affected. In part, this image degradation was due to obstacles to the optimization of image quality that are inherent in the equipment. Instrument design was based on the assumption that the objects observed are point sources; to the extent that they are not, image quality suffers. In addition, interference from extended sources seriously degrades the apparent quality of superimposed point-source images.

Testing and adjusting of the ultraviolet-sensitive equipment presented special difficulties that are not experienced with visible-light systems. Some routine tests for visible optics became major tasks for Celescope. Some kinds of test data common for visible systems may not even be available for the Celescope experiment. These difficulties are a potential source of image degradation, even though actual orbital data indicate no particular problems in this regard.

One important effect of image quality on the Celescope experiment was examined by the EMR Telemetry Division of Weston Instruments, Inc., as part of a study they conducted late in 1970 to assist us in our refinement of the Celescope observational results. They found that, for a Westhinghouse WL30691 SEC Vidicon operated in the same manner as the Uvicons in Celescope, the system output (Sigma) for an artificial star of constant intensity depended critically on the size of the star image on the target. Since the SEC target in the WL30691 is essentially the same as that in the Uvicon, we conclude that defocusing in our Schwarzschild telescope by more than 0.001 in. would have affected our calibration curves to such an extent that we could have easily detected the effect. In Chapter 4, we discuss calibration; the effects described there are considerably smaller than those that would be expected from a relative shift of 0.001 in. between the position of the best optical image surface and the photocathode.

The primary aim of this chapter is to examine when and why the quality of the observed images deviated from our expectations. It is significant to note that we are discussing two different types of images, namely, optical and electro-optical. Optical images can be measured directly by optical or photographic methods.

3.2 Basic Configuration of Optics

There are four identically constructed telescopes in the Celescope experiment package. All four are mounted in parallel with the optical axis of the spacecraft as shown in Figures 14 and 15. Each is provided with different optical filters and Uvicon tubes for a distinct band of spectral sensitivity. To increase system reliability, each camera module (or Uvicon assembly) is equipped with two different filters and is sensitive in two spectral regions. Table 12 defines the spectral regions and sensor configuration.

Celescope uses a Schwarzschild configuration for its telescopes. The Schwarzschild telescope consists of two reflective surfaces: a primary mirror and a secondary mirror. The figure of the primary mirror is hyperbolic, and that of the secondary is an oblate ellipsoidal surface.

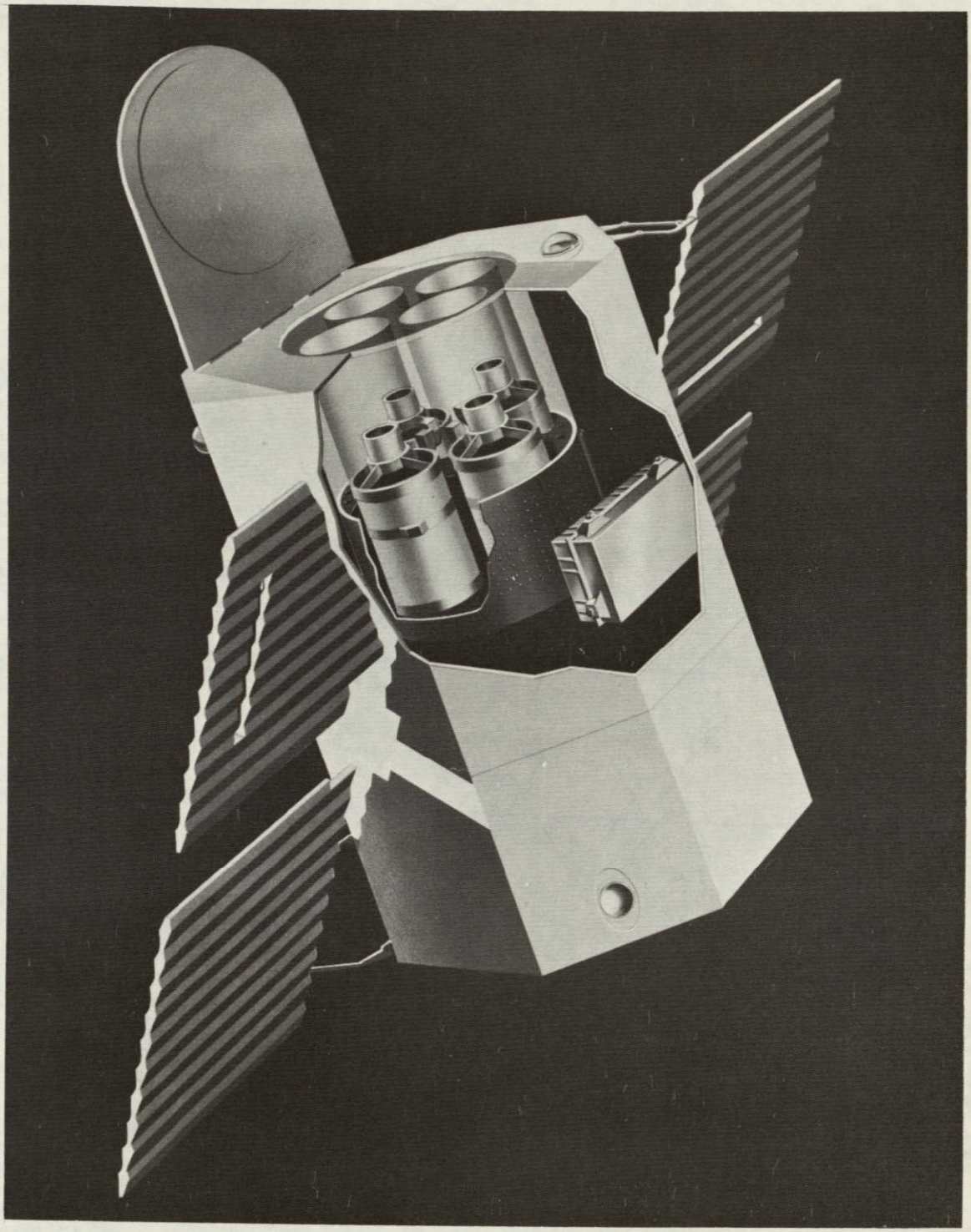

Figure 14. OAO spacecraft with cutaway showing the Celescope experiment.

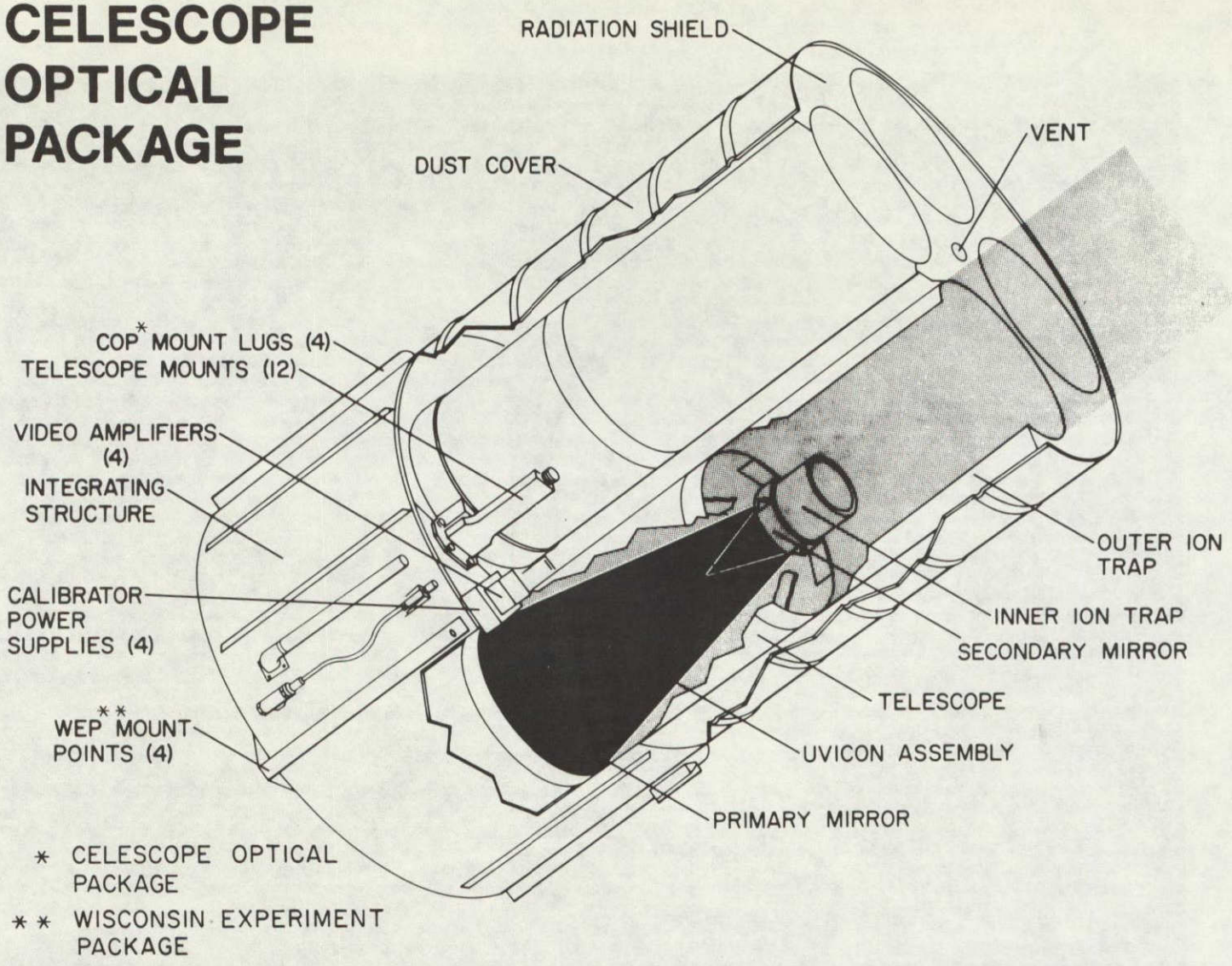

Figure 15. Cutaway of the Celescope optical package.

Table 12. Ultraviolet spectral bands for Celescope.

Camera	Uvicon type Serial no.	Type	Photocathode material	Filters	Ultraviolet spectral bands	Cutoff wavelength (Å)
1	R 19	A	Cs_2Te	Corning 7910	U_1	2100 – 3200
			Cs_2Te	Suprasil quartz	U_2	1550 – 3200
2	65-35-050	D	CsI	BaF_2	U_3	1350 – 2150
			CsI	LiF	U_4	1050 – 2150
3	R 29	A	Cs_2Te	Corning 7910	U_1	2100 – 3200
			Cs_2Te	Suprasil quartz	U_2	1550 – 3200
4	R 42	D	CsI	BaF_2	U_3	1350 – 2150
			CsI	LiF	U_4	1050 – 2150

This configuration was chosen because it is the most compact telescope that could meet the image-quality requirements and provide the space necessary for installing the Uvicon as a detector. It has not been popular in ordinary astronomical applications because of the superior image quality provided by the Schmidt configuration and because of the difficulty of figuring the optical surfaces.

The intrinsic advantage of the Schwarzschild telescope is the quality of the images, which are free from spherical aberration, coma, and curvature of fields. Schwarzschild telescopes used in Celescope differ from the classical ones in order to provide optimum performance for imaging onto the strongly curved Uvicon photocathode. The "basic" two-mirror system was subject to field curvature, coma, and spherical aberration to compensate for these aberrations in the faceplate lens. The system was optimized for a refraction index of 1.46 for the faceplate, corresponding to a wavelength of 1800 Å for lithium fluoride. During optical design, it became evident that a system of the length that the Scwharzschild specified for minimum astigmatism was unnecessary to meet our optical imaging requirements. The physical length of the system was therefore shortened as far as the imaging requirements would allow, in order to make a smaller, more rugged system suitable for space applications. Figure 16 shows the general construction of the telescope. Details of the surface figure are shown in Table 13.

Each mirror was constructed of fused silica with an aluminum-coated reflecting surface with a magnesium fluoride protective coating to ensure long-lasting, high ultraviolet reflectance. Since details of the telescope structure will be described elsewhere, this discussion will be kept brief.

The major concern in the structural design of the telescope is survival during and after launch. During launch, there are severe vibrations and acoustic effects. The nitrogen atmosphere that protects the experiment on the ground must be rapidly released during ascent from the launch pad. Structural integrity must be maintained during launch, despite strict weight

TELESCOPE ASSEMBLY

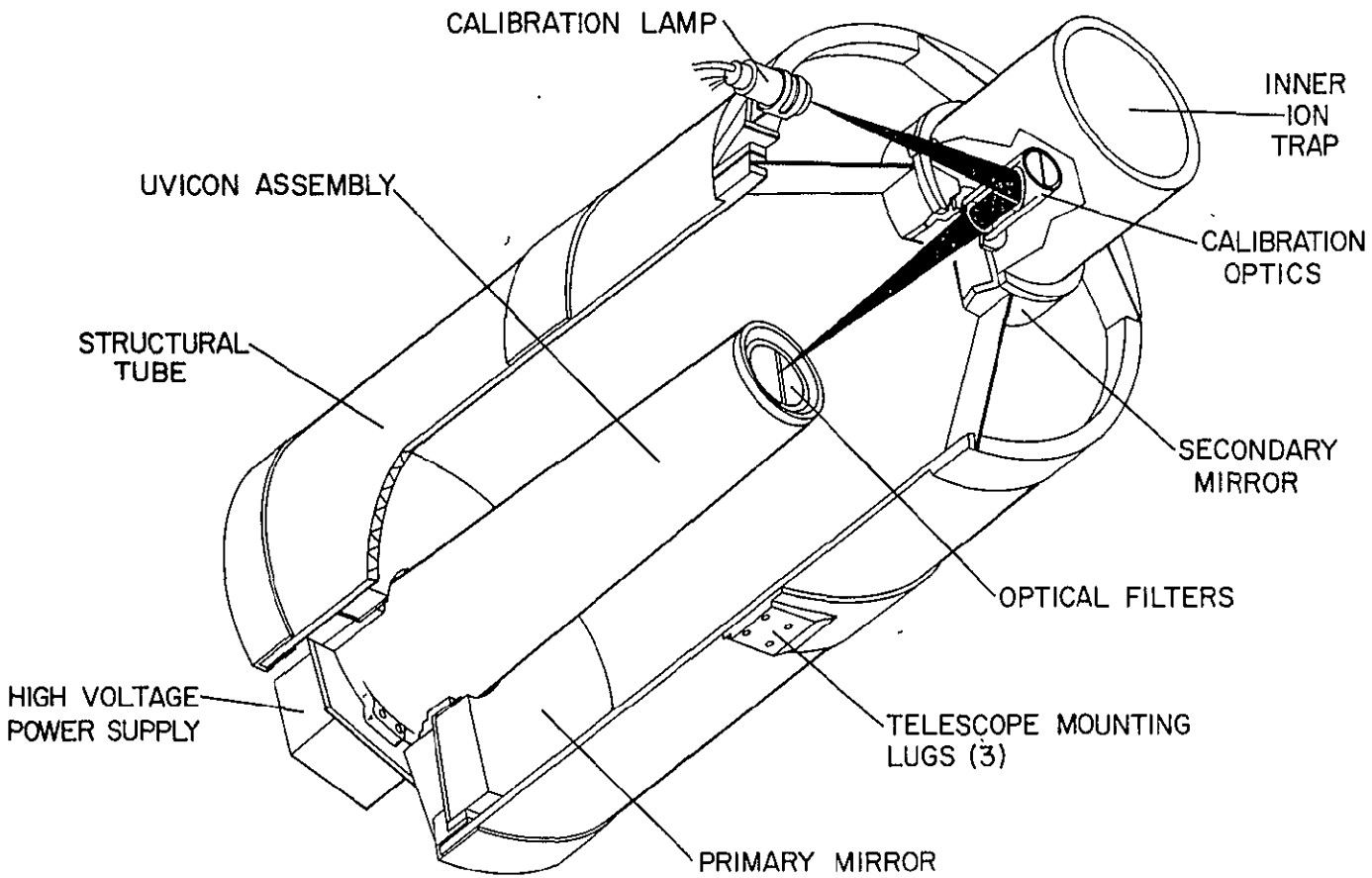

Figure 16. Cutaway of the telescope assembly.

Table 13. Aspheric-surface equation.

Standard form:

$$Z = \frac{C y^2}{1 + \sqrt{1 - (K+1) C^2 y^2}}$$

C = curvature = $\frac{1}{R}$

K = conic constant

Surface	C	K
Primary mirror	-1.38888×10^{-2}	-4.6288
Secondary mirror	$+1.73611 \times 10^{-2}$	+38.955

Z: Height from reference plane (Z = 0).

y: Radial distance from reference axis (y = 0).

limitations on the structure. To meet this challenge, several innovations were adopted: For example, a corrugated telescope tube, a 4-vane secondary mirror support, a 3-point telescope mount, and a torsion-bar shock-absorbing telescope mount were adopted. A related problem is the wide temperature variation in space. Expected or design values of the temperature range are shown in Table 14, along with the actual measured values in orbit. A temperature-compensating structure was used in Celescope to cope with the defocusing effect due to the temperature change in space. The residual defocusing effect is small but it still exists. It was minimized by setting the optimal focus to -20°C, which was the expected average temperature of the telescope in space.

Another problem in space is the high vacuum, which causes outgassing of many materials. Coupled with the temperature gradient within the telescope structure, this may lead to the condensation of outgassed material on the surfaces of optical components. Should this occur, the reflectivity or transmissivity of the optical components would be severely degraded and inaccurate measurements would result. To avoid outgassing, no paint nor paint-like finishes were used inside the telescope. The usual interior surface of nonreflecting paint was replaced by an interior of aluminum and titanium sandblasted to a rough surface by means of pressurized dry nitrogen gas and clean silica sand. Ground-based reflectance measurements justify the elimination of black paint, at least in the ultraviolet region. The telescope structural design was also important for minimizing the effects of reflections from structural surfaces.

Dimensions of the telescope are given in Table 15.

3.3 Calculated Quality of the Optical Image

Since there are refractive components in the Celescope optical system, chromatic aberration must be considered. Actually, the chromatic aberration is the biggest contributor to the optical-image degradation and the

Table 14. Temperature variation in telescope.

	Design values		Observed values	
	Maximum	Minimum	Maximum	Minimum
At primary mirror	+25°0 C	-55°C	+ 9°3 C	-48°0 C
At secondary mirror	+25°0	-55°	+13°0	-51°5

Table 15. Telescope physical and optical parameters.

Total length (without hood)	35 in.
Total length (with hood*)	54.5 in.
Overall length**	55.5 in.
Diameter (without mount)	14.5 in.
Effective aperture diameter of primary mirror	12 in.
Effective aperture diameter of secondary mirror	6 in.
Effective light-gathering area	84.2 $in.^2$
Nominal field of view	2°
Nominal focal length	24 in.
Nominal aperture stop	f/2
Effective aperture stop	f/2.39
Weight	75 lb

*Called the outer radiation shield.

**With radiation shield end plate.

ultimate determinant of optical-image quality. We were willing to accept this amount of chromatic aberration as the limiting factor in optical performance because of our decision to require electrostatic focus in the Uvicon image section, which in turn required strong curvature to the optical image surface (photocathode).

The optical adjustment was specified to provide optimum focus for the D-type cameras at 1600 Å in U_3, and for the A-type cameras at 2050 Å in U_2. According to our computations, such adjustment would provide images less than 125 μ in diameter in U_4 between 1320 and 1470 Å, in U_3 between 1470 and 1800 Å, in U_2 between 1800 and 2600 Å, and in U_1 between 2100 and 2600 Å. For normal early-type stars of the kind primarily observed by Celescope, chromatic aberration would increase the image sizes to 150 μ for U_1, U_2, and U_3 and to 200 μ for U_4. Defocusing by a few thousandths of an inch would not increase the image sizes beyond these values, since it would merely change slightly the wavelength of best focus. These hand computations were done by means of first-order optical theory. They were later checked by ray tracing. Performance of Celescope in orbit in general appears to support the above conclusions.

The calculated quality of images for the Celescope-Schwarzschild telescope was investigated by Dr. A. Shatzel in Ferson Optics, Inc., and presented in an internal report (CER-22) by Mr. W. Wagner of EMR. Some of the material in this section is based on that report. In that investigation, the basic optical system, which includes only a primary mirror and a secondary mirror, and the Celescope optical system, which also includes an optical filter and Uvicon faceplate, were studied. Since the optical filter is part of the optical system, there are four different variations of the system, one for each type of optical filter. (A-type and D-type Uvicon tubes have an identical optical configuration; they differ in the spectral sensitivity of the photocathode.) Only two variations were investigated. These are: (a) the A-type Uvicon with a Suprasil quartz filter

(which corresponds to the U2 filter and is called A1), and (b) the D-type Uvicon with a barium fluoride filter (which corresponds to the U_3 filter and is called D1). Actual ray traces were performed for monochromatic light at 2537 Å for U_2, and 1470 Å for U_3.

Figure 17 shows the change of image sizes as a function of image position. The image size is defined as the diameter of blur circle, which contains 90% of the energy. As shown in Figure 17, the insertion of the filter and faceplate improves the image quality. The specified image size is 125 μ for a field of view 0.6-in. in radius, which is about 1°4 from the optical axis. The size of one television picture element is about 140 μ in diameter. Therefore, the expected image size of stars in the television picture is 1 to 4 elements at optimum focus if there is no image size increase due to the electro-optical mechanism. If the focus is less than optimum but still within the specified limit, then the output image size will be 4 to 9 elements large, provided electro-optical degradation is negligible.

Intensity distribution in an image is quite different for different locations. Figure 18 indicates the intensity distribution for different positions. Since the curves in Figure 18 are cumulative intensities, we can determine the intensity at a picture element located a radial distance r from the center of the image by taking the slope of the curve at r. Also, we can determine from Figure 18 what percentage of energy is included in a detected signal image when a particular value of the intensity is chosen as the cutoff level for the signal. It is obvious that if we choose a fixed level of intensity as the threshold that separates the signal from the background noise, the energy included in the detected signal image varies as a function of image position.

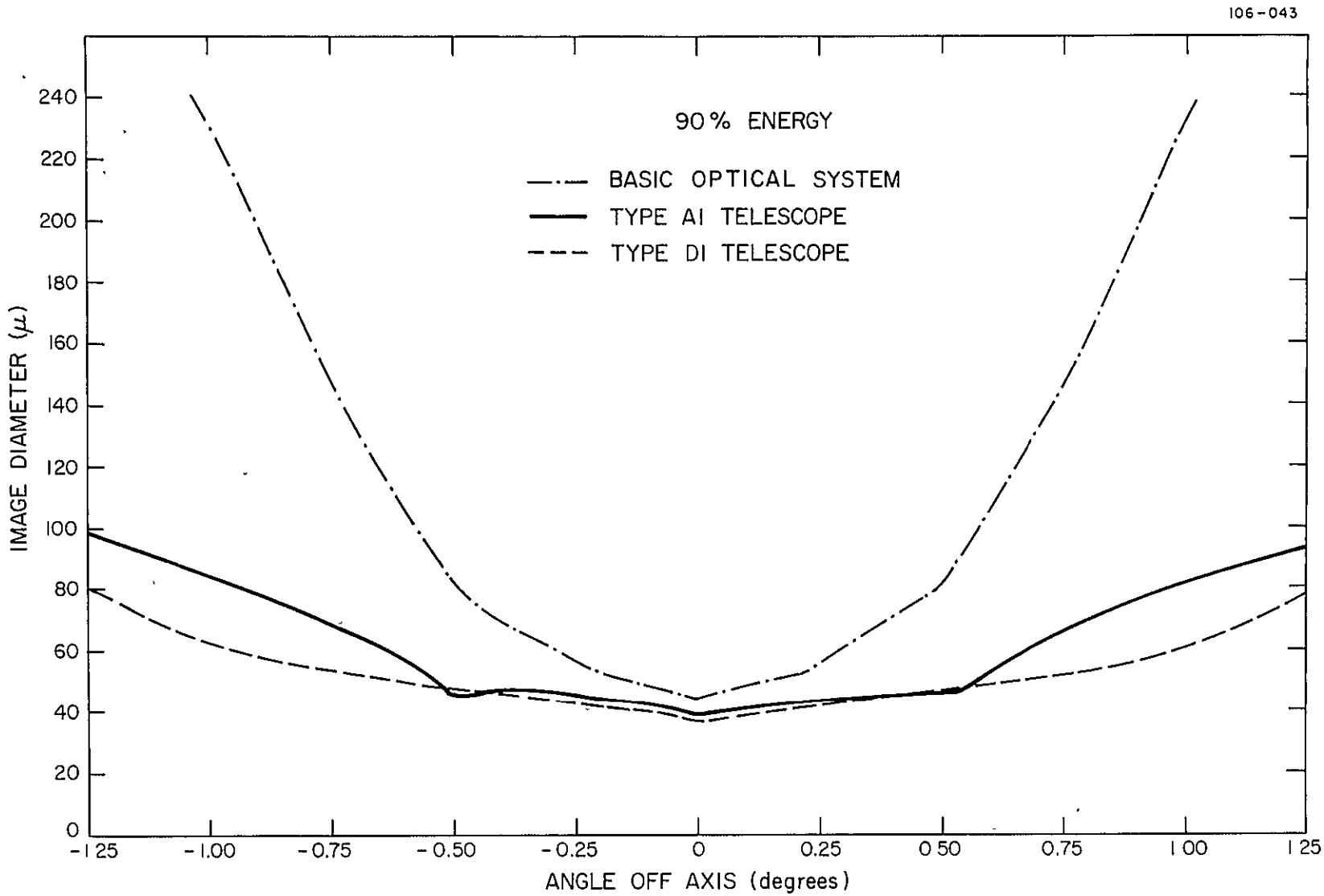

Figure 17. Calculated image diameters as a function of the off-axis distance.

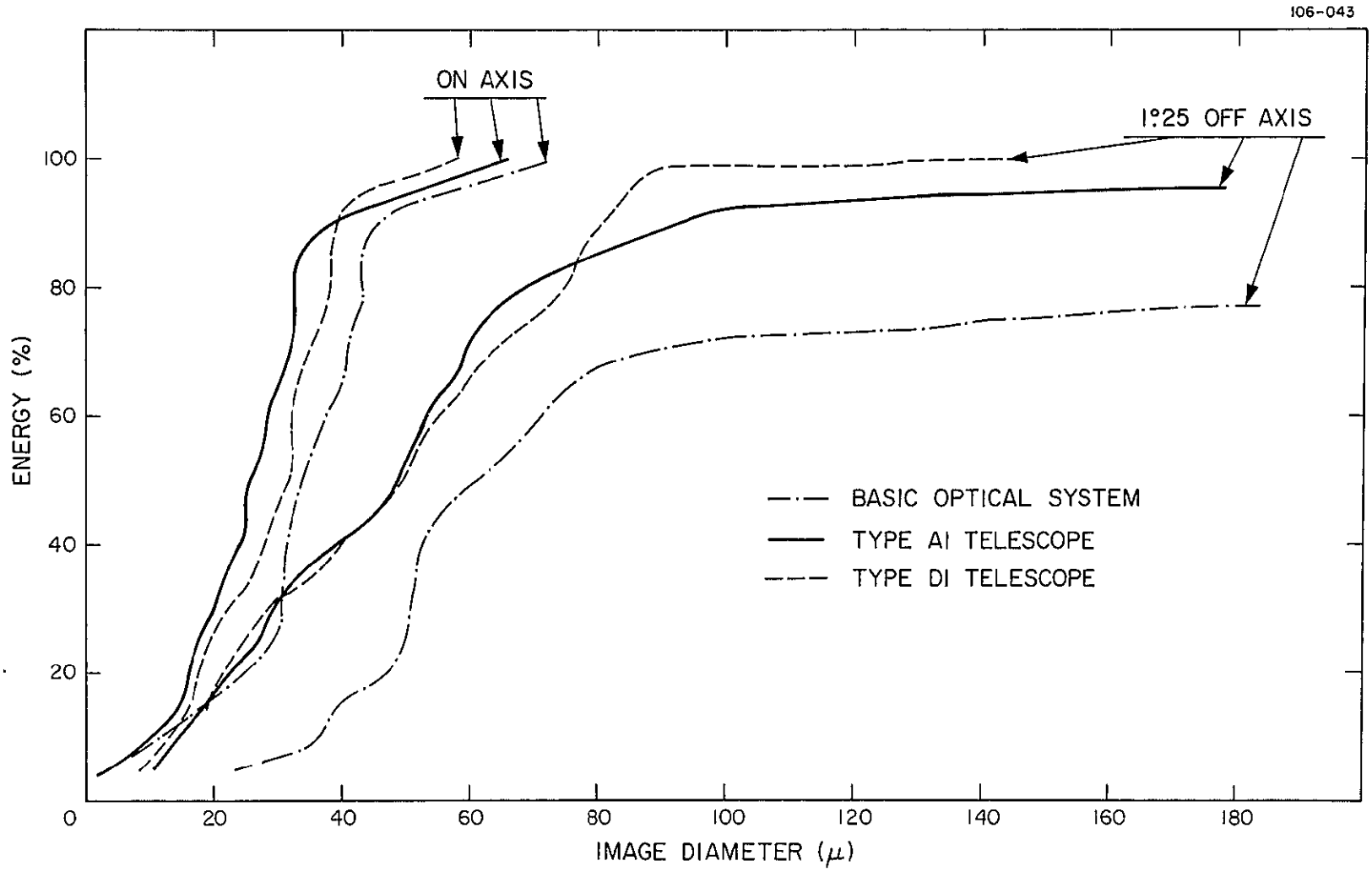

Figure 18. Internal energy distribution in the optical images.

The following is a brief summary of some other findings of this investigation. The Celescope-Schwarzschild telescope displays considerable spherical aberration, coma, and curvature of field. Its performance deteriorates rapidly off axis, and the best off-axis focal surface does not correspond to the best on-axis focus. The system is relatively insensitive to changes in mirror separation, provided the system is refocused. The on-axis image diameter increases by approximately 10.5 μ per 0.001 in. for defocusing in the direction of the secondary mirror and by about 13.5 μ per 0.001 in. in the direction of the primary mirror. It is therefore preferable that any defocusing take place in the direction of the secondary mirror. Within a tolerance of ± 0.005 in. from best focus, the diameter at 90% energy increases from ~40 μ (best focus) to ~ 100 μ. The diameter at 95% energy is within ~ 120 μ for a ± 0.005-in. tolerance on the focal-surface location.

The effect of defocusing off axis is similar to that on axis, although the best image diameter is considerably larger and the best focal-surface location for the diameter at 90% energy is about 0.0025 in. from the best on-axis focus. If the focal surface is located for best on-axis focus, then the 90% energy diameter 1°25 off axis may be as large as 150 μ for a focal-plane tolerance of ± 0.005 in. Compromise between the best on-axis and off-axis focus results in the maximum off-axis image diameter being held to ~ 130 μ. The 95% energy diameter off axis is considerably worse than the 90% diameters and in some instances is as large as 170 μ. Because of the importance of defocusing, the exact position of the focal plane for each telescope is determined experimentally by using a simulated Uvicon and photographic films. Figure 19 shows such a measurement for each telescope.

The image diameter increases on the average ~ 5 μ per change of 0.001 in. in mirror separation if the system is not refocused. The mirror separation was varied ± 0.025 in. from the nominal separation, and the best focus image diameter for the type A1 system changed ~5%, while the type D1 system changed ~15%. There was no significant change in off-axis performance for a change in mirror separation if the system was refocused. Table 16 (with Figure 20) indicates the distance of mirror separation and related dimensions for each telescope. The values indicated in Table 16 include the compensation for chromatic aberration.

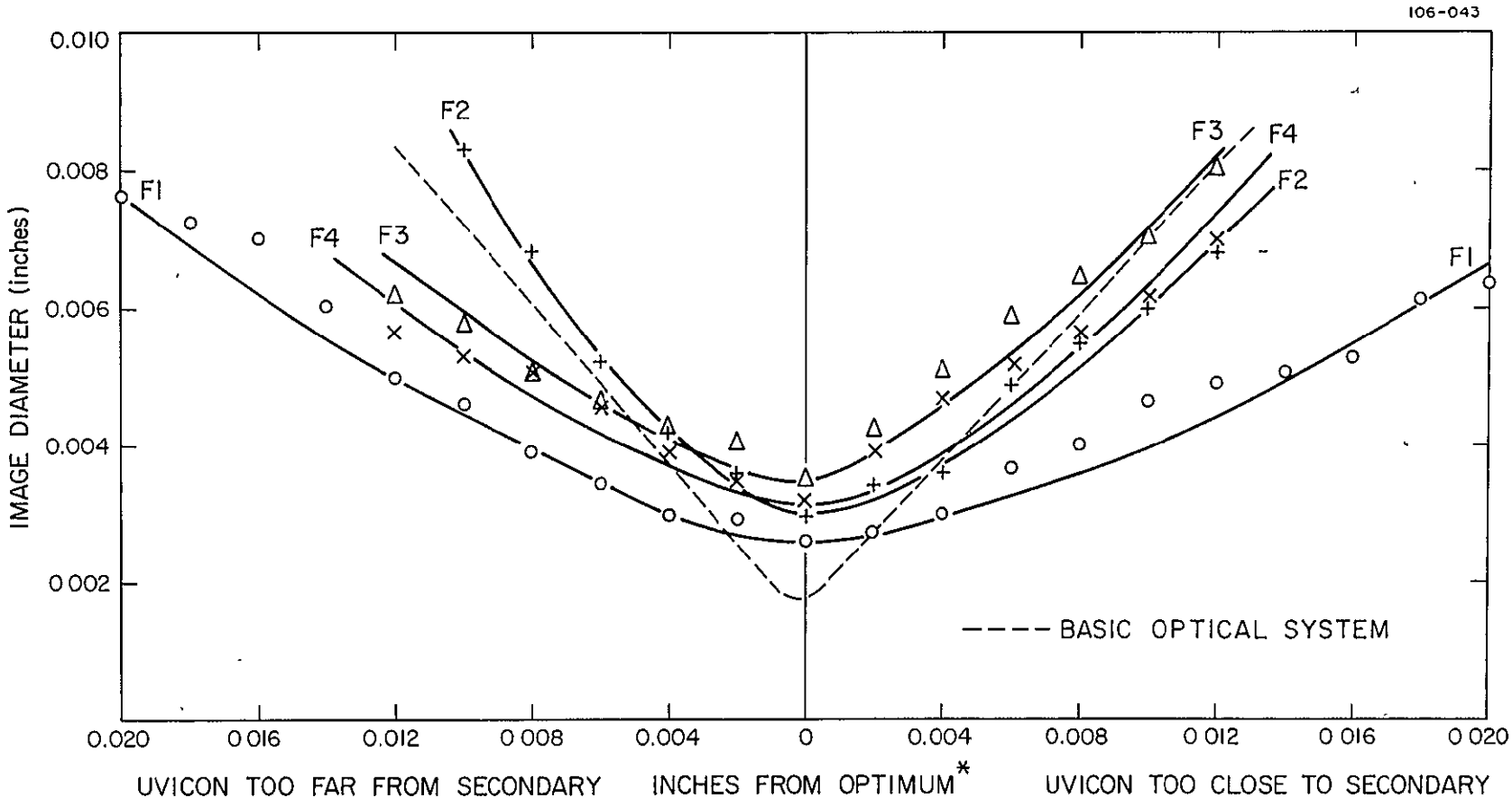

Figure 19. Telescope performance as a function of Uvicon faceplate displacement. *For optimum primary to secondary spacing (which will be achieved under orbital conditions at -20°C).

Table 16. Alignment of flight telescope.

Camera	A Primary rim to secondary rim (in.)	Primary rim to secondary rim at -20°C (in.)	B Secondary rim to Uvicon facepiece vertex (in.)	Angle between filter split and Z_c axis (°)	C Angle between raster line and Z_c axis (°)	D Angle between control fin and Z_c axis (°)	E Outer diameter of telescope (in.)
1	21.240	21.230	9.306	0	15	22.5	14.500
2	21.300	21.290	9.349	0	0	112.5	14.500
3	21.277	21.267	9.373	0	0	22.5	14.500
4	21.236	21.226	9.435	0	0	112.5	14.500

Note: Definitions of A, B, C, D, and E, are shown in Figure 20.

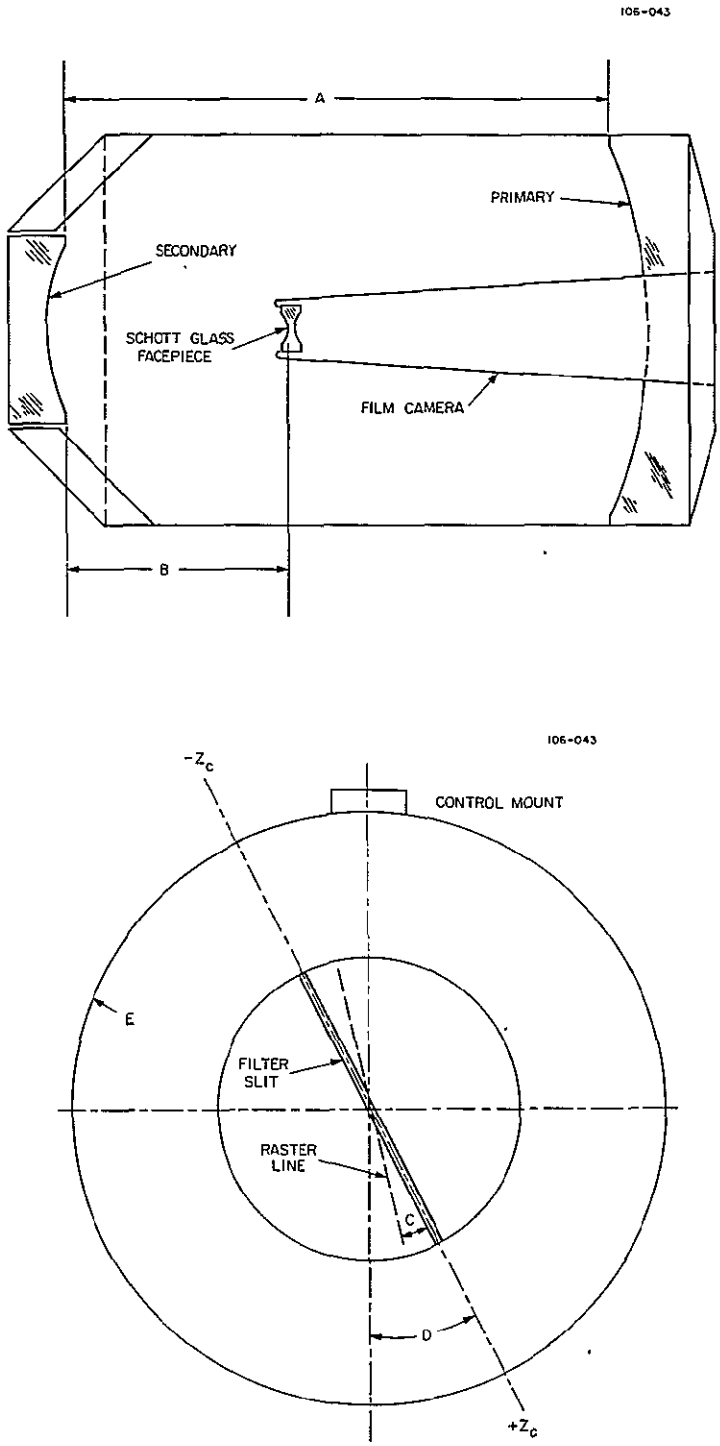

Figure 20. Definition of telescope dimensions used in Table 16: (a) telescope side view, (b) view looking into telescope.

The primary effect of changing filter thickness is to change the position of the best focal plane in accordance with well-known geometrical optical principles. A 0.010-in. change in filter thickness for the Suprasil filter at 2537 Å changes the location of best focus by only 0.0065 in. This change is highly significant, however, because of the use of split filters in the Celescope system. One-half the field uses one type of filter, while the other half uses a second. If the thicknesses of the two filters are chosen with due consideration to the differences in the index of refraction at particular wavelengths, then the two halves of the field will both be in focus (or equally out of focus) at the same wavelength. Because of the differences in dispersion of the filter materials, the two halves of the field will be simultaneously in focus at only one wavelength and will in some degree differ in focus at all other wavelengths. Likewise, if the filter thicknesses are not correct, then one-half the field may be in focus while the other half of the field is defocused. For example, if the tolerance on the Suprasil filter thickness is ± 0.005 in. and the companion filter (Corning 7910) tolerance is ± 0.005 in., then the total change in thickness could be as much as 0.010 in., which in turn could result in approximately 0.006 in. defocusing. This amount of defocusing could, of course, increase the image diameter by 60 to 80 μ. This could be a serious problem since controlling the thickness of the thin filters employed is difficult, and it is not inconceivable that the two halves of the field could differ in focus by 0.005 to 0.015 in. Under these conditions, it is entirely possible that the best average on-axis resolution would not be better than 100 to 125 μ. Variations in filter thickness would also have the same deleterious effects on the off-axis image.

There were at least three followup studies on the effects of filter thickness. Careful selection of filters solved the problem. In the actual observations, U_4 images seem out of focus relative to U_3 images. The main cause of the defocused images is considered to be chromatic aberration.

Since no attempt has been made to evaluate errors in the mirror figures, the data presented in this report represent an idealized situation. Fabrication

of the mirrors, particularly the secondary mirror, is difficult because of the aspheric surfaces, and it is quite possible for the figures to depart somewhat from the theoretical values. This is particularly true for the secondary mirror since the outer zonal radii change more rapidly than the widths of the zones. Changes in figure will obviously alter the system resolution, most likely degrading the resolution.

From examination of radial energy distribution, it is apparent that in many cases the area containing the remaining 10% of the energy is as large as or larger than the area containing the central 90% energy. It is improbable, therefore, that any more than the central 90% image diameter would be detected by using film or the Uvicon as a detector.

One should also note the effect of optical-image degradation on the final system output. As mentioned in Chapter 2 (it will also be discussed later in more detail in part B), the output is sensitive to the image size. Therefore, defocusing or any other factors affecting image size will alter the system output for the same input.

3.4 Image Degradation in Uvicon Image Tubes

The discussion of image quality in the previous section referred only to the optical images, which are on the photocathode. The photocathode produces photoelectrons from the optical image. These are focused onto the target by the electron optics. Therefore, the quality of output images from the television tubes is controlled by nonoptical image degradation. In the Uvicon, three things affect the quality of images: (a) the electron optics in the imaging section, (b) the SEC signal-amplification mechanism in the target, and (c) the readout process.

The electron optics consist of three electrostatic lenses. Aberration in the electron optics is not well documented, but in general the quality of the image is affected by the fluctuation of supply voltages and by the external electromagnetic environment. The electron optics form a half-sized electron image on the target. The quality of this image is optimized by selecting the proper voltage ratio for each element of the electron optics. Figure 21

R19A - CAMERA 1

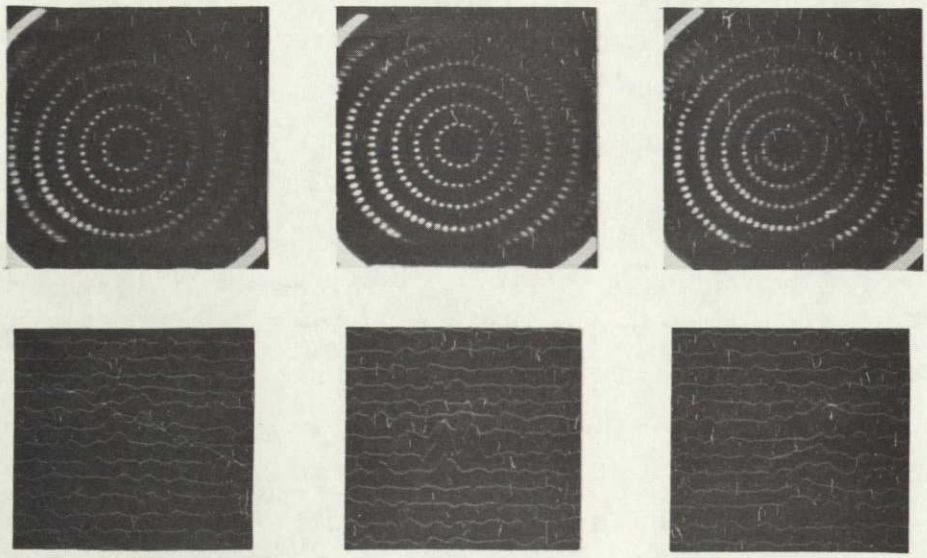

F1 = 8000 V
F2 = 97.759% F1
F3 = 77.4% F1
F4 = 0 V

F1 = 8000 V
F2 = 97.480% F1
F3 = 77.4% F1
F4 = 0 V

F1 = 8000 V
F2 = 97.108% F1
F3 = 77.4% F1
F4 = 0 V

O50D - CAMERA 2

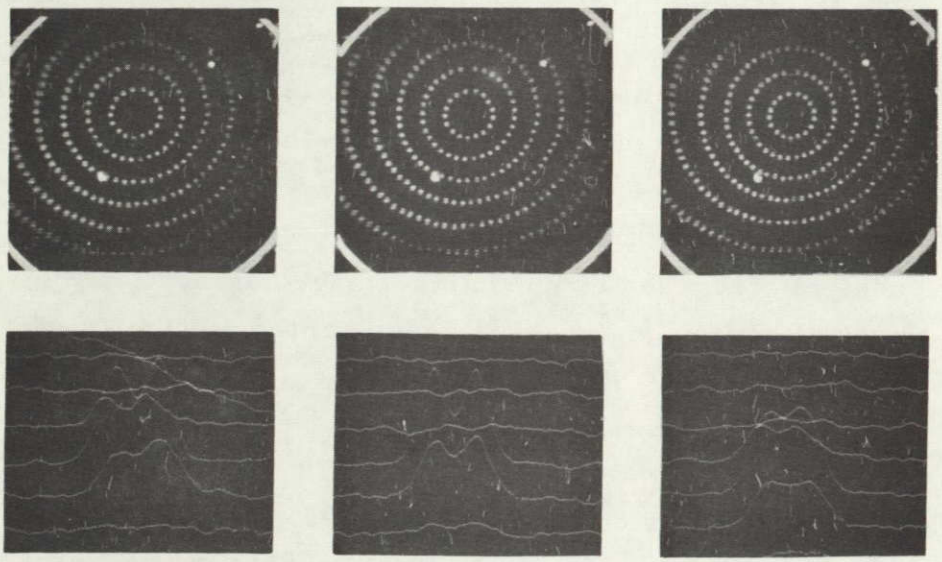

F1 = 8000 V
F2 = 97.759% F1
F3 = 77.4% F1
F4 = 0 V

F1 = 8000 V
F2 = 97.480% F1
F3 = 77.4% F1
F4 = 0 V

F1 = 8000 V
F2 = 97.108% F1
F3 = 77.4% F1
F4 = 0 V

Figure 21. Effect of voltage selection on the electron optics in the imaging section.

illustrates the effect of such a voltage selection. Fluctuations in the voltage ratio between the two lens elements and in the supply voltage are shown in Table 17. The effect of supply-voltage fluctuation is rather small and insignificant; image quality is most sensitive to a change in voltage ratio. To minimize fluctuation in voltage ratio, voltages to both elements are supplied by a fixed-resistor voltage divider. The calculated possible change in voltage ratio is 0.001%, which corresponds to a fluctuation of about 1% in Sigma. The fluctuation of total voltage is expected to be less than 5%, which is equivalent to a 1 to 2% change in Sigma.

The quality of the image formed on the target is not directly measurable, but we can make some assumptions based on an investigation of an optically readable SEC target (Beyer and Goetze, 1966). The resolution of the target is far better than the overall resolution of the Uvicon tube. Therefore, the SEC target is not the limiting factor for resolution in the Uvicon tube (provided all SEC targets manufactured in WEC have similar characteristics); resolution is limited either by the electron optics or by the readout beam.

The final image in the Celescope experiment package is produced by discharging accumulated charges on the target by means of the readout electron beam. In the ideal case, the spread of the readout beam should be exactly equal to the size of one television-picture element, and the beam scan should cover the entire area of the raster without leaving any spot unread and without any overlapping. Furthermore, the scanned position should be equally spaced as in a perfect-square grid. In Celescope, the scan pattern is 256×256 elements, which ideally requires a scanning beam with the same size as one element, uniform in intensity, and square in shape. In practice, it is not possible to generate such a beam. The actual readout beam is larger than one element, has nonuniform distribution of intensity, and is nearly circular. Despite this, the beam can be adjusted in such a way that the result of readout is very similar to the result of an ideal beam for the image of a uniformly illuminated source of very large area.

In the Celescope experiment, the spread of the readout beam is on the order of several elements, based on the observed output image of false stars

Table 17. Effects of variation of high voltage to the imaging section.

a) Fluctuation of Sigma due to variation of ratio between two elements of electron lenses.

		Average Sigma*										
Star coordinates	Hor.	195	95	189	139	48	186	92	137	47	189	92
	Vert.	37	38	80	79	76	119	115	154	151	201	193
Deviation of voltage ratio from the value of best focus (%)	-0.3	654	1624	1446	1509	1645	1055	900	1011	923	633	961
	-0.2	860	1548	1479	1192	1262	1056	771	844	790	744	894
	-0.1	1043	1415	1430	1058	1049	961	880	797	655	876	875
	0	1135	1120	1271	1049	1046	837	913	709	613	922	718
	+0.1	1144	1065	1090	1265	1365	664	1225	832	758	1004	674
	+0.2†	1236	1211	1122	1448	1692	847	1283	897	866	1037	730
	+0.3	1153	1614	1229**	1628	1293	949	1194	1093**	873**	898**	858**

*Average of 3 measurements.

†Only one measurement.

**Average of 2 measurements.

b) Fluctuation of the Sigma due to variation in high-voltage supply.

		Average Sigma*													
Star coordinates	Hor.	203	118	34	200	157	79	199	118	39	158	80	203	120	36
	Vert.	51	56	50	93	95	95	131	132	131	168	168	210	206	209
Supply voltages (Kv)	9.5	3631	943	3792	1191	558	527	770	517	904	421	455	1531	523	1201
	8.8	3218	926	3454	1084	513	517	677	496	823	396	426	1115	469	1068
	8.5	2422	1013	2922	1038	533	632	692	478	453	354	462	839	455	886
	8.2	2486	798	2721	804	422	487	560	381	718	330	319	678	354	683
	7.5	1891	643	2052	632	383	417	499	283	586	265	283	434	267	443

*Average of 3 measurements.

and target rings. If the beam spread is less than one element, the size of the output image produced by a point charge on the target will be one to four elements large, depending on the location of the image with respect to the registration of the scanning pattern. If there is beam spread, then the size of the output image increases and the position of the output image centroid shifts slightly.

The major problem in determining the effect of the readout process on the image quality is the difficulty in producing a good point charge image on the target. However, there is an indirect way to estimate the extent of image degradation during readout. In Celescope, a ruggedized Vidicon gun was used; the readout characteristics of the Uvicon can be expected to be similar to those of other Vidicon tubes. Usually, these Vidicons have a resolution of 300 to 500 lines. We may assume, therefore, that the limiting factor in Uvicon resolution is the electron optics in the imaging section. The effect of superscanning on the image quality has not yet been established. It may also contribute to image degradation.

The effects discussed above are independent of the input intensity. Some image-degrading effects are intensity dependent. One of the most dominant and important effects of this type occurs at the SEC target. To reduce the dangers of target-material breakdown in the Uvicon tube, we imposed a limit on the peak voltage for accumulated charge on the target. Unfortunately, this makes the image vulnerable to a saturation effect at a relatively weak input intensity. When input exceeds the saturation level, the SEC mechanism displays a nonlinear relation between the number of input photoelectrons and the accumulated charge. Since additional incoming photoelectrons can no longer increase the potential at the original position of the image, the image spreads. Figure 22 shows the relationship of image size to input intensity. System output (Sigma) depends critically on the intensity distribution in the optical image and therefore on the stability of optical and electronic focus.

Another phenomenon that causes degradation of image quality is beam bending during readout of very strong signals. If a large charge accumulates on the target, the readout beam being aimed at an adjacent vacant spot is attracted toward the strong charge. As a result, the apparent image size

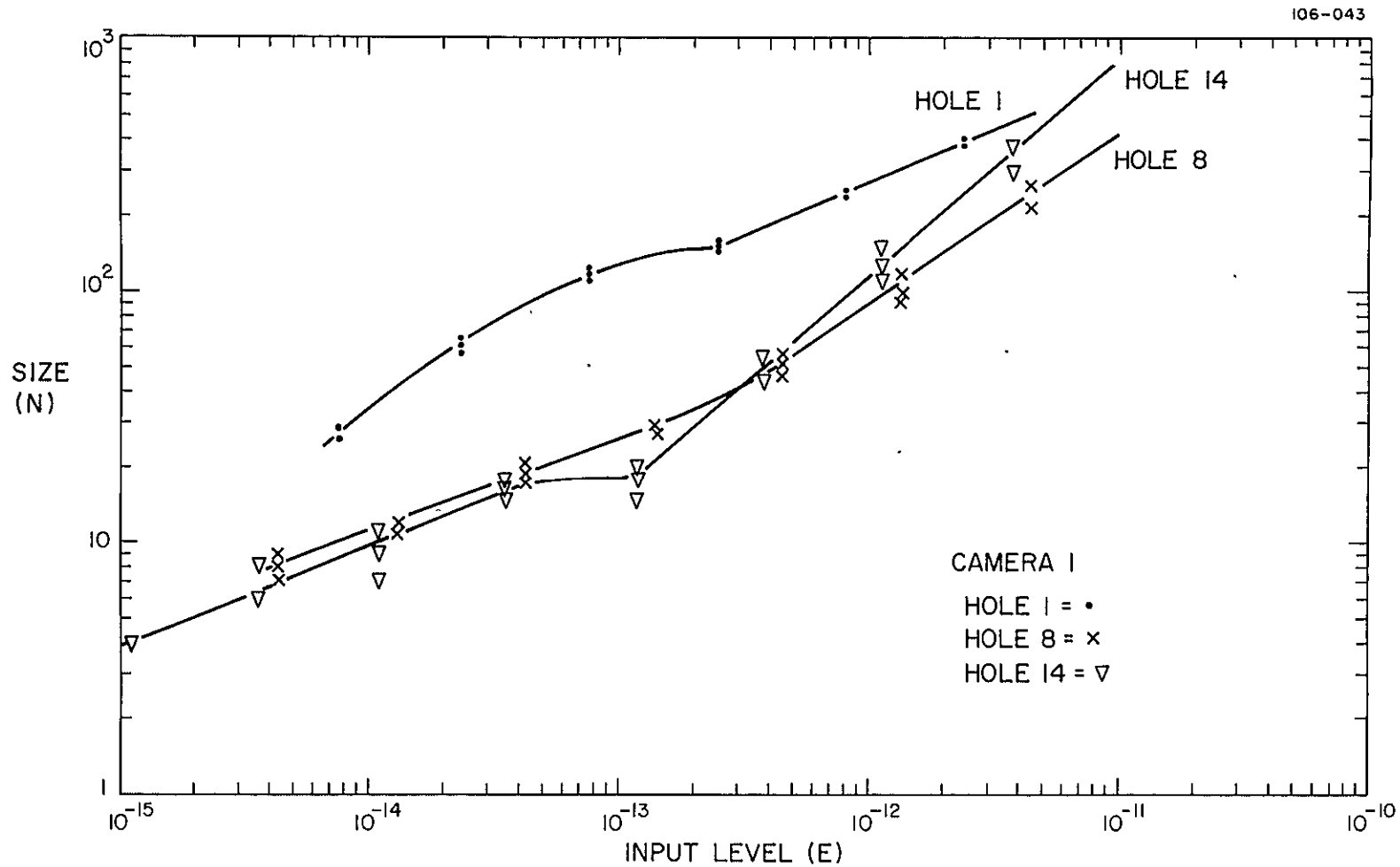

Figure 22. Size change as a function of input level. N: number of TV elements; E: coulombs.

increases and resolution is lost. When this beam bending occurs, the peak intensity of the readout image is less than it should be, so the peak-size curve falls off in high-intensity regions.

Adjustment of gun voltages also affects image quality. In the gun section, the beam, focus, and astigmatism control voltages are adjustable. Generally speaking, any nonoptimal adjustment setting causes larger images and increases Sigma. The effect is shown in Figures 23 and 24.

3.5 Geometrical Stability

In reducing the Celescope data, we use pattern-recognition techniques to determine positions for the observed objects: Our ability to recognize our observed star patterns depends on the suitability of our search catalog, on the accuracy with which we know the raster position of the optic axis, on the accuracy with which we know our distortion correction, and on the stability of our system against changes in distortion. Our first step in pattern recognition is a computer comparison of the observed pattern against the pattern contained in the corresponding area in a search catalog created before launch especially for Celescope identification purposes. This step successfully identifies the stars observed in about 25% of our pictures. It requires a knowledge of the raster position of the optic axis to an accuracy of 0°.25 and of distortion to an accuracy of 0°.04. This step fails to identify the stars in about 25% of our pictures because of errors in the distortion correction, which have an average scatter of about 0°.04. The 0°.25 accuracy of optical-axis position is met. In the case of Celescope, we have found it necessary to follow the automatic pattern recognition with a manual one, not only to eliminate the effects of errors in the distortion correction, but also to supplement our identification catalog with other catalogs and atlases and to identify stars in pictures having too few objects to permit computer identification with our available programs. In this manner, we achieve satisfactory pattern recognition for essentially all of our pictures. Errors and fluctuations in our position and distortion corrections do not affect the accuracy with which Celescope can measure position, because the pattern recognition compensates for these errors.

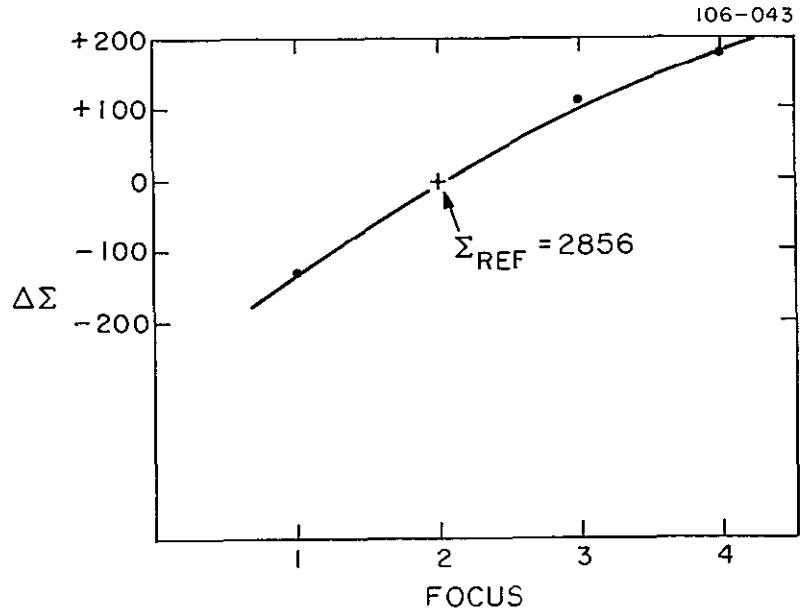

Figure 23. Change of Sigma as a function of the gun focus voltage adjustment. $\Delta\Sigma$ = change of Sigma from Σ_{ref}.

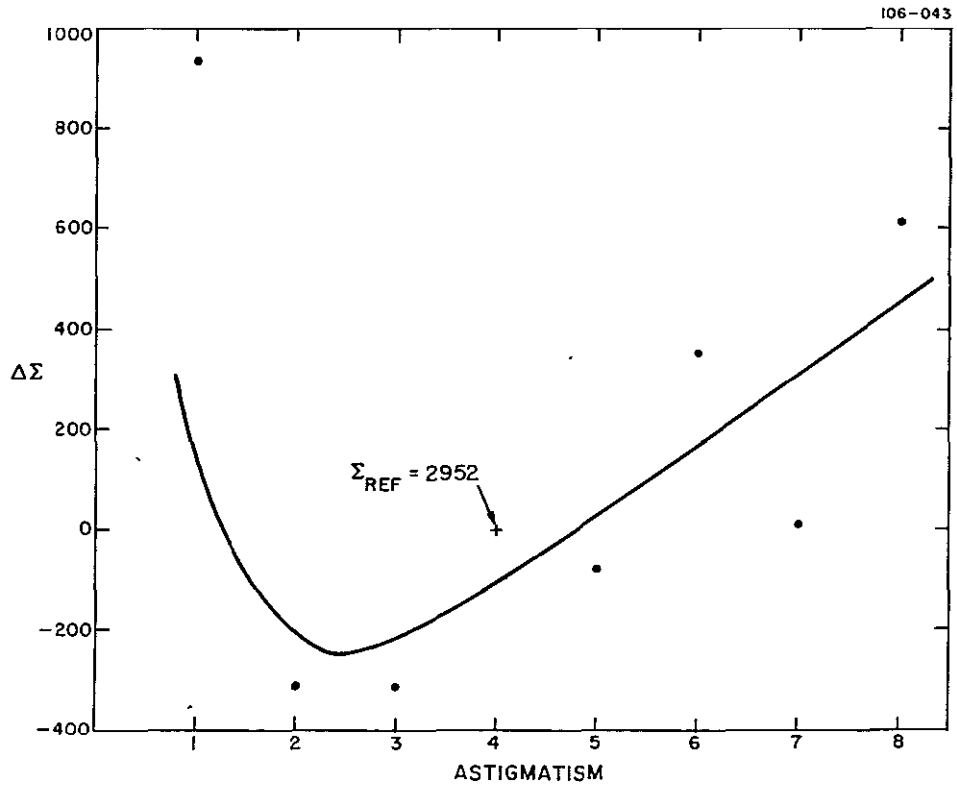

Figure 24. Change of Sigma as a function of astigmatism adjustment. $\Delta\Sigma$ = change of Sigma from Σ_{ref}.

106-043

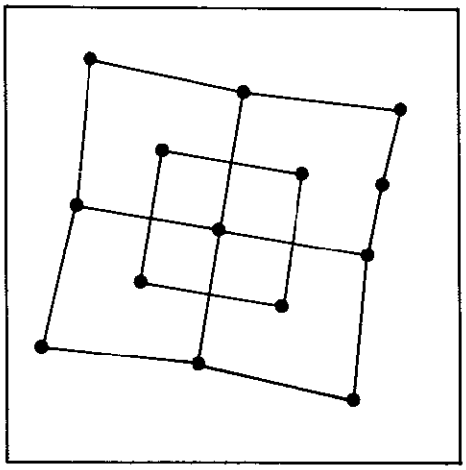

CAMERA 1

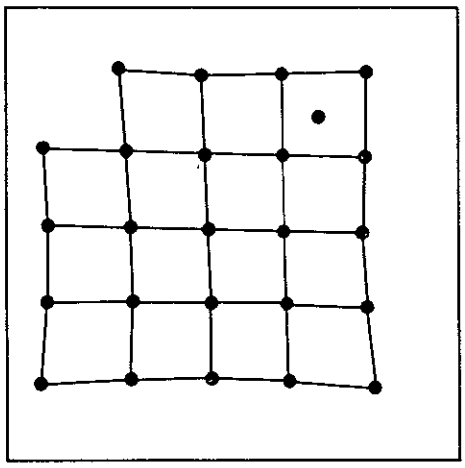

CAMERA 2

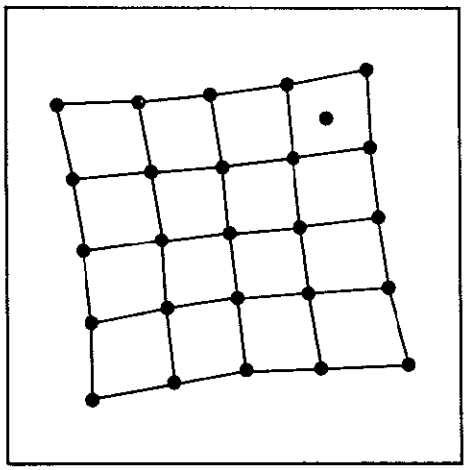

CAMERA 3

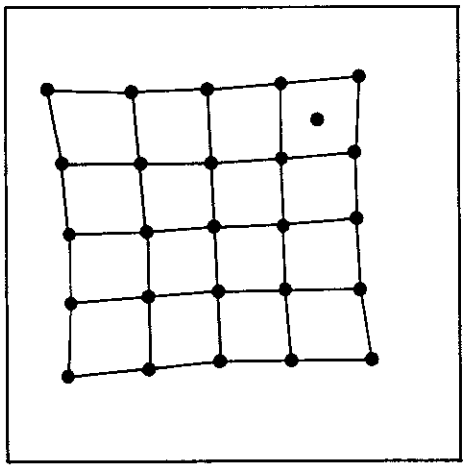

CAMERA 4

Figure 25a. Examples of image distortion in Uvicon output picture. Note: Input pattern is square grids or similar pattern with one additional point.

Instability of image position can be classified into the following three groups: (a) shift of images, (b) distortion, and (c) fluctuation of shift or of distortion. A shift of the optical axis or shifts of an entire frame are mainly caused by external magnetic fields. The susceptible phases of operation are exposure and readout. The effect of the magnetic field during these two phases seems to work in an opposite direction; therefore, the net shift is smaller if the magnetic field is present during both phases than if it is present during only one. The apparent effect of a quickly changing magnetic field is much larger in readout, since exposure is an averaging process. Figure 40(a) in Chapter 4 illustrates this effect during readout. The presence of a changing magnetic field during exposure will produce slightly enlarged images. Since Sigma is very dependent on image size, there is a danger of inaccurate measurement of star intensity. The exact amount of shift varies from camera to camera. Since there is also hysteresis in the shift of position, it is not easy to determine a positional correction factor for each frame. Sensitivity is on the order of a 10-element shift per 1 oersted of field change. In addition, there appears to be a long-term shift of images. Table 18 shows shifts of the calibrator-lamp image position in the raster. The calibrator lamps have fixed positions with respect to the optical axis of the telescope.

When the geometrical stability of images is discussed, there is an implied assumption that the position of an image is clearly and easily determined. In actuality, this is not the case. Actual image sizes are frequently on the order of 10 to 100 elements or more; therefore, determination of the exact image position is not a trivial task. The most commonly used methods define the center as the center of intensity, the peak-intensity position, or the geometrical center of the image. There is also a problem of energy concentration. If a major portion of energy is not concentrated within a small region, the position determined is not reliable. Despite the differences in positions computed by different methods, computed positions may be expected to be consistent since all images in a frame will be treated by the same method.

Table 18. Shift of calibrator image position in the raster.

Image tube	Horizontal		Vertical	
	Average position	Maximum shift from average position	Average position	Maximum shift from average position
Camera 1	134	11	156	9
Camera 3	134	11	145	16

Raster consists of 256 × 256 points. Position is measured by horizontal and vertical element numbers (H, V). H, V = 1 to 256.

Although the Celescope-Schwarzschild telescope displays some amount of coma, the determination of position is not difficult.

Once the method of positional determination is adopted, discussion of geometrical stability becomes more meaningful. The distortion of Uvicon tubes was determined during camera-module calibration. Figure 25 shows output image patterns for the Uvicon and the Celescope system. The distinct pincushion-type distortion is not compensated for in the telescope.

3.6 Conclusions

Not all subjects related to image quality were covered in this chapter, some being deferred to Part B. Based on the material presented here, the following conclusions are drawn.

1. Optical, mechanical, and thermal design of the telescope proved fully satisfactory in terms of image quality and stability.

2. Contamination-control procedures during ground operations were fully successful.

3. Positional stability of star images in the final television picture was not completely satisfactory, and careful attention to factors affecting it, such as the magnetic fields, is necessary.

4. The spacecraft's magnetic unloading system blurred the Celescope images significantly; it had to be turned off during Uvicon expose and readout operations in order to provide pictures of satisfactory photometric quality.

5. For some methods of preventing target-material breakdown, in particular that used in Celescope, the output signal becomes critically dependent on the focus of the stellar image on the target.

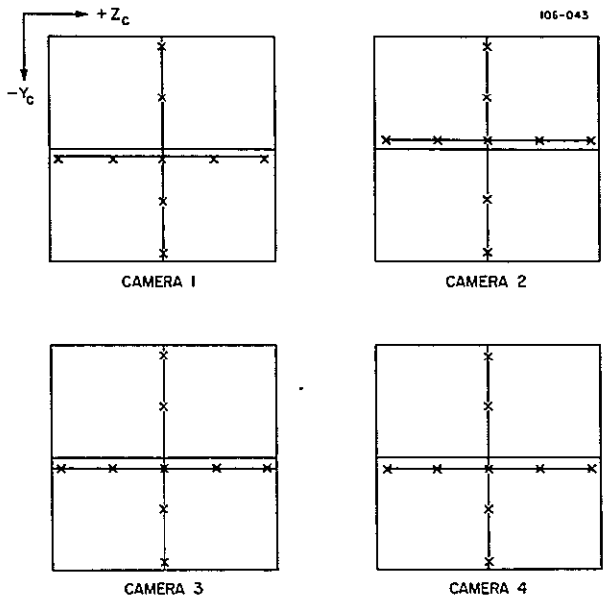

(b) Input

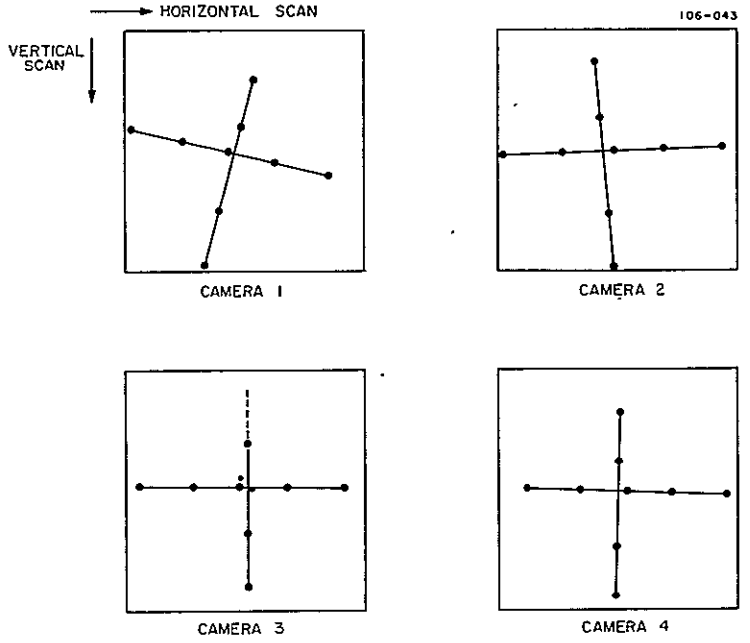

(c) Output

Figure 25 (Cont.). Distortion of Celescope system image.

CHAPTER 4

ENGINEERING INTERPRETATION OF ORBITAL DATA

4.1 Introduction

This chapter interprets orbital data from an engineering point of view and extracts information pertinent to the design of future systems, the extension of system capability (source material for future systems), etc. For the most part, our observations confirm our original design assumptions, but some cases have provided new or unexpected information.

4.2 Daytime Observation

Scientific observation of stars from the ground in daytime, even when possible, poses many difficult problems. In space, because of the lack of an atmosphere, which causes diffusion of light, daytime observation of stars is more likely to be feasible. A portion of Celescope observing time was used for daytime observations, and some useful information was obtained.

In the early period of orbital operation, several daytime observations were attempted (Table 19). The considerable amount of scattered sunlight made it impossible to observe stars. The relative intensity of scattered light for different spectral bands is

$$U_2 > U_1 > U_4 > U_3 \quad .$$

This generally agrees with the intensity of solar flux, provided the Lyman-α emission from the geocorona is included. Three geometrical quantities of possible importance to determining scattered-light levels are also listed in Table 19. These are beta angle (the angle between the Celescope optic axis and the sun line, equal to the angular distance from the target to the sun), solar zenith angle (the angle between the earth line and the sun line, equal to the angular distance between the geocentric position of the satellite and the

Table 19. Daylight observations.

a) Geometrical relation of daytime observations

Contact	Beta angle	Solar zenith angle	Target zenith angle	Camera	Exposure
R102	78	113	82	3	5
R117	78	94	81	4	5
R131	78	103	84	4	20
Q132	78	65	82	2,4	60
S133	78	65	82	2,4	60
S134	78	8	86	2,4	60
S135	77	25	88	2,4	60
S136	77	47	90	2,4	60
S137	77	72	94	2,4	60
Q138	78	99	96	2,4	60
O139	78	14	86	2,4	60
M3310	122	91	32	1,3,4	5
M3311	122	109	14	1,3,4	15
M3325	135	101	34	1,3,4	30
S3329	153	87	66	1,3,4	30
Q3330	153	106	50	1,3,4	5

b) Observed intensities of daylight

Contact	Camera	Exposure	Upper area (16×16)		Lower area (16×16)	
			Average	S.D.	Average	S.D.
R102	3	5	55.6	12.00	39.8	10.50
R117	4	5	19.6	2.13	4.3	0.95
R131	4	20	41.4	8.88	4.5	1.05
Q132	4	60	45.2	2.70	15.9	2.17
S134	4	60	38.2	16.21	21.7	6.11
Q138	4	60	37.3	11.19	5.9	1.20

Note: 1) Upper area corresponds to U_2 in camera 3 and U_4 in camera 4.

2) Lower area corresponds to U_1 in camera 3 and U_3 in camera 4.

3) Intensities were determined by averaging of area of 16×16 elements.

geocentric position of the sun at the time of observation), and the target zenith angle (the supplement of the angle between the earth line and the Celescope optic axis, equal to the angular distance from the geocentric position of the satellite and the geocentric position of the target at the time of observation).

The numerical value of scattered light for U_1, U_2, and U_4 cannot be measured because the intensity exceeds the useful range of Celescope. For U_3, the intensity of scattered light varies with the solar zenith angle, as shown below, when the instrument is pointing away from the sun at a constant beta angle of 78° (see Figure 26 also):

$$I = a \cos \theta + b \quad ,$$

where

- I intensity of scattered light in U_3 (arbitrary unit),
- a a constant (14.7),
- b a constant (8.0),
- θ solar zenith angle.

Possible sources of scattering are the spacecraft structure and the residual atmosphere; the scattered light is probably either sunlight or earthshine. Considering the geometry of spacecraft-sun orientation (Figure 27), we cannot exclude the possibility of scattering by residual atmosphere. However, the most likely cause, considering the form of the above equation, is earthshine.

4.3 Effects of Space Radiation

There are many high-energy particles in space outside the shield of the earth's atmosphere. The effects of these particles on the Celescope experiment package were studied in considerable detail. These effects may be either temporary or permanent. An example of a temporary effect is an increase in background noise in the television picture caused by gamma rays. Examples of permanent effects are a change in the transmittance of filters and target-material breakdown.

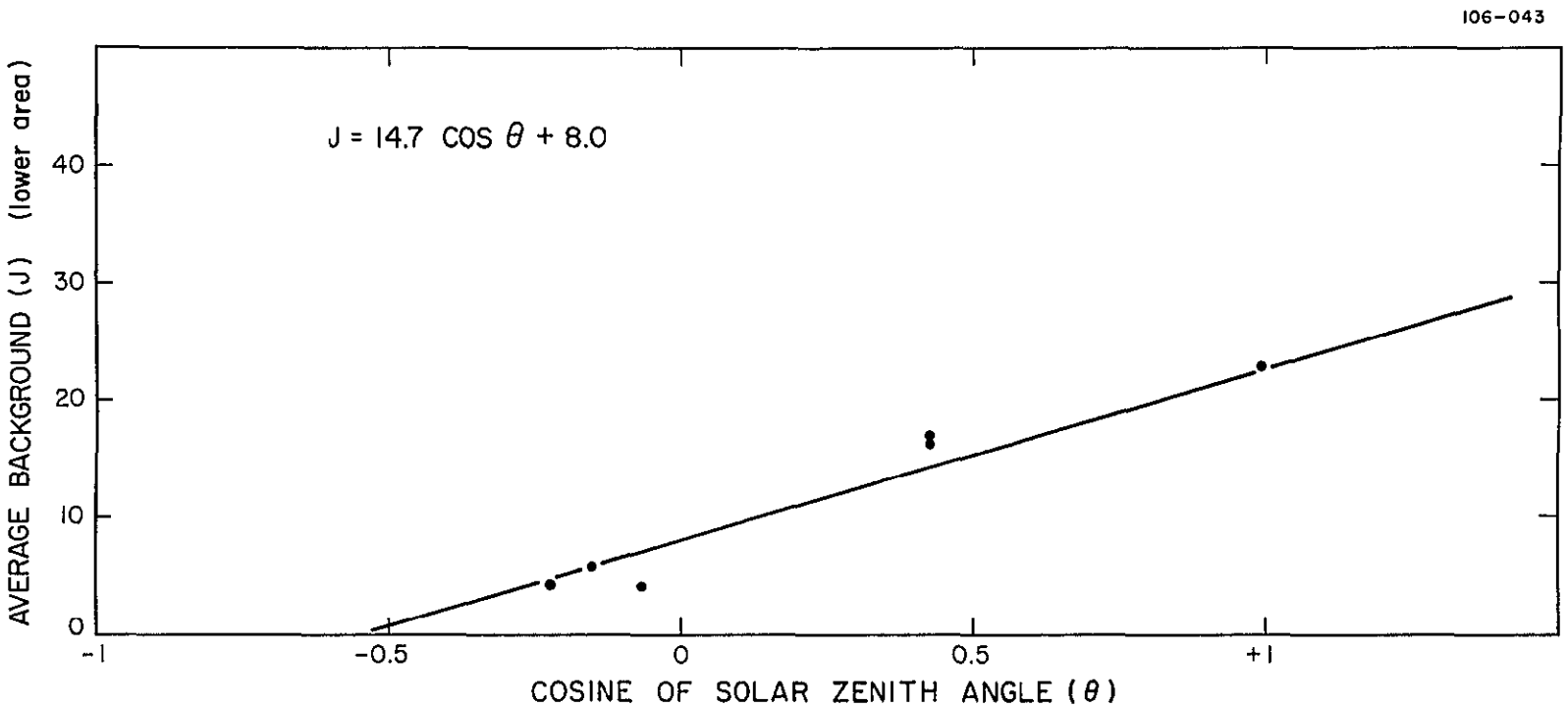

Figure 26. U_3 daylight intensity vs. solar zenith angle.

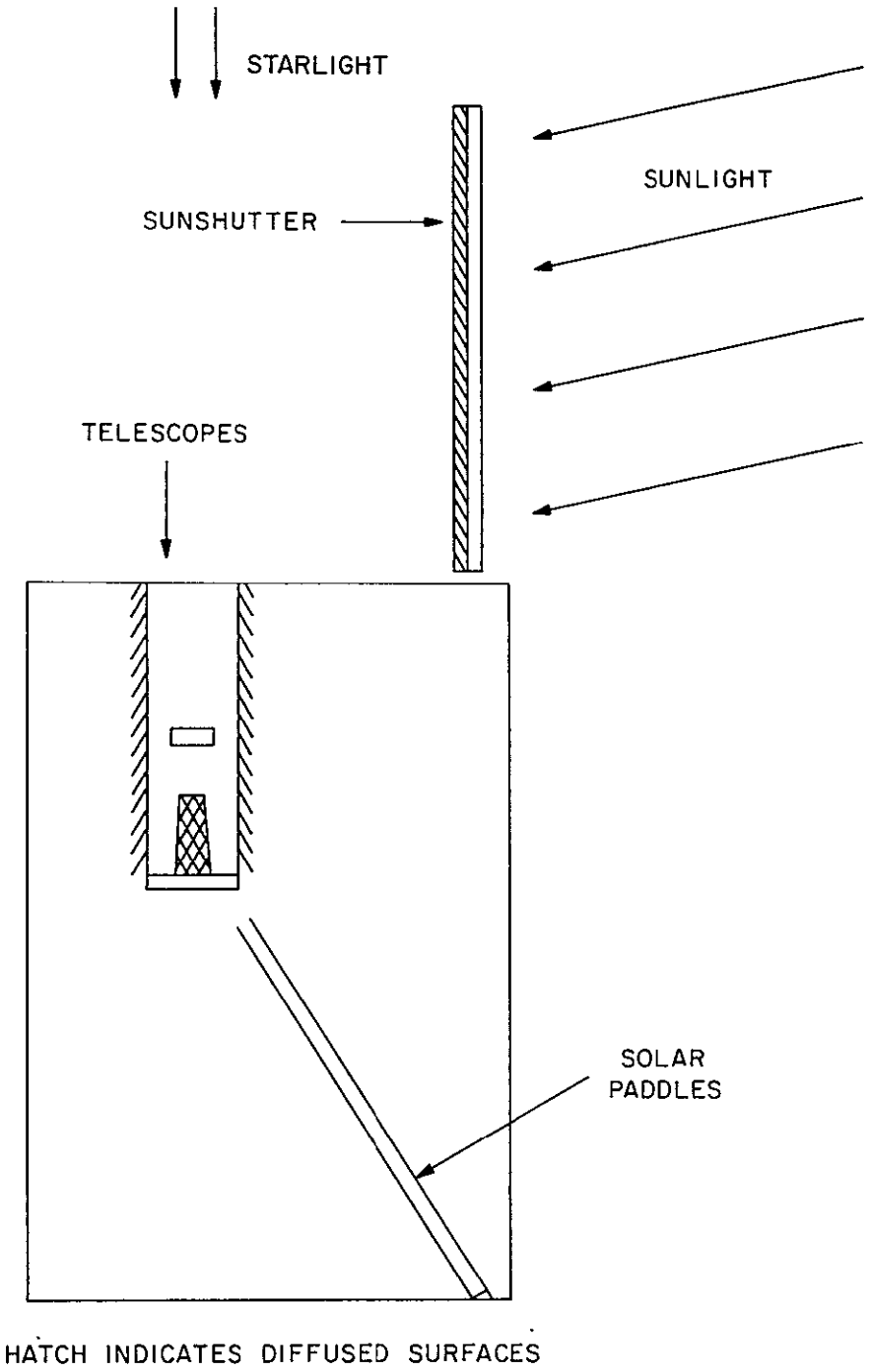

Figure 27. Geometry of daytime observation.

The temporary effects of space radiation were studied on the ground. To simulate them, a small dosage of gamma rays from cobalt 60 and electron beams from the 2-MeV Van de Graaff electron accelerator at GSFC were used. A noticeable effect of these radiations is a rise in the background level (Figure 28). This causes a loss of contrast in the output television pictures, a decrease in the signal-to-noise ratio, and a reduction of the dynamic range. The relation between the average increase in background and the radiation dosage is shown in Figure 29. We see that there is no significant difference, except in sensitivity, between the expose mode and the high-voltage-on mode, nor between the different types of input (gamma ray and electron beam). Table 20 lists the sensitivity of the background noise level to radiation.

From Table 20, it is seen that 1-sec of the high-voltage-on mode is equivalent in effect to $1 \times 10^3 - 5 \times 10^4$ sec (16 min to 14 hr) in the expose mode. Since the orbital period of OAO is approximately 100 min, one full orbit in the expose mode is equivalent to 6 sec in the high-voltage-on mode. Therefore, we can say that if the tube is exposed to radiation in high-voltage on for 6 sec in the most concentrated radiation zone without significant degradation, the Uvicon tube can be left in its expose mode for a full orbit. Decreases of SNR and of dynamic range are illustrated in Table 21.

What mechanism may cause the increase of background level? There are three possibilities:

1. Faceplate scintillation. The faceplate is excited by radiation and becomes an illuminator. Light from the faceplate then acts as regular input to the photocathode and accumulates positive charges on the target.

2. Direct charge generation in the target material. Potassium chloride itself generates electrons from the direct bombardment of radiation.

3. Field emission in the tube. When radiation particles hit the tube wall, they may generate electrons or photons. These may create charges on the target through normal tube operation.

To determine which case is dominant in raising the background, a lead shield with a 0.25-in. hole was placed at the front of the image tube. The tube

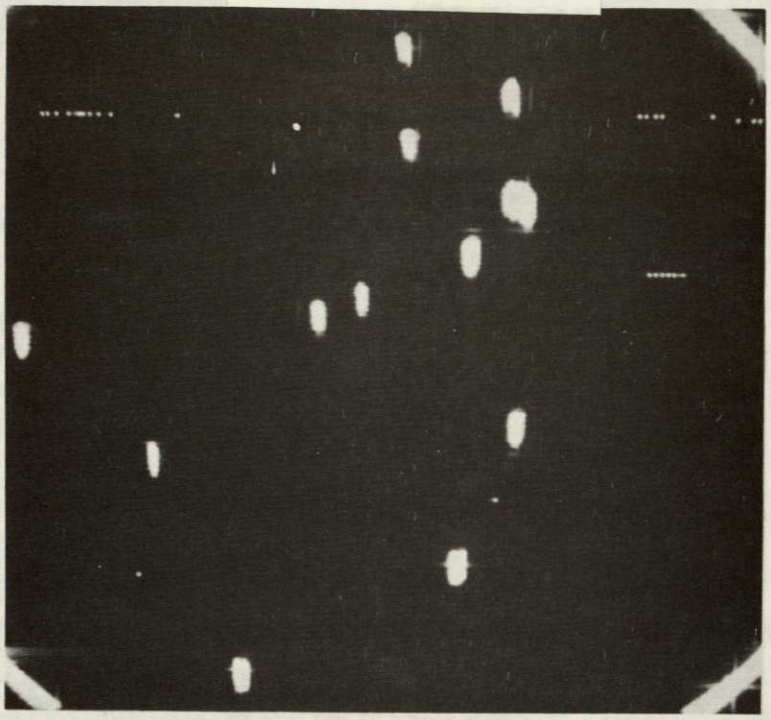

(a)

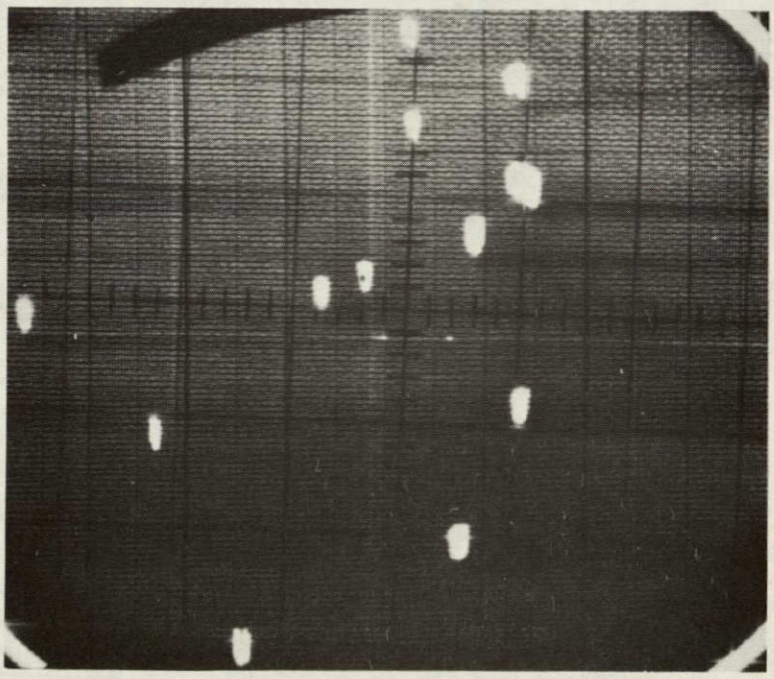

(b)

Figure 28. Apparent effect of radiation on television pictures: (a) without radiation, (b) with radiation.

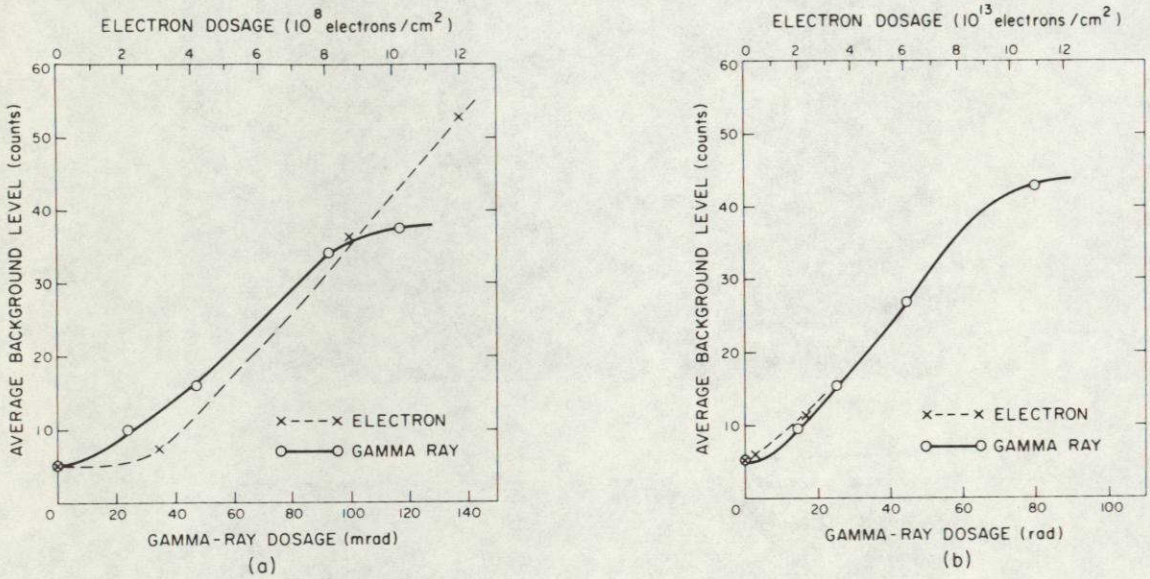

Figure 29. Quantitative relation between increase of background and radiation level: (a) high-voltage-on mode, (b) expose mode.

Table 20. Sensitivity to radiation: increase in background.

Operating mode	Radiation source	
	Gamma ray (count/mrad)*	Electron beam (count/electron/cm^2)*
High-voltage-on	0.38	5.1×10^{-8}
Expose	0.34×10^{-3}	2.4×10^{-13}

*The count is the standardized output amplitude; 1 count $\cong 6 \times 10^{18}$ coulombs.

Table 21. Examples of decrease of SNR and of output dynamic range.

Maximum signal	80 counts
Nominal background level (offset value)	5 counts
Background fluctuation (rms)	0.75 count
SNR without radiation	(80-5)/0.75 = 100
Background with 100 mrad in high-voltage-on mode	35 counts
Fluctuation of background	3.5 counts
SNR with radiation	(80-35)/3.5 = 12.8
Dynamic range without radiation	80-5 = 75 counts
Dynamic range with radiation	80-35 = 45 counts

is then exposed to radiation in the expose mode and the high-voltage-on mode separately. The results are shown in Figure 30.

The presence of the hole in the picture of the high-voltage-on mode and its absence in the expose-mode picture indicate that the increase of the charge in the target is caused by scintillation of the faceplate. The extent of field emission is determined by the following: (a) replacing the holed shield with a solid block, and (b) irradiating the Uvicon from the side. Both cases indicate that field emission contributes 20 to 50% of the increase of background in the high-voltage-on mode and a much higher ratio in the expose mode (up to 100%). When SEC Vidicons other than the Uvicon are used, this temporary degradation may not be so severe as for the latter, the spectral response of which covers the range 1100 to 2500 Å. The amount of field emission may not be substantially different, because the tube body and the Uvicon are constructed of similar material. (Uvicon does not have a coating inside the wall of the tube to reduce field emission.)

The expected peak intensities of electron fluxes (0.5 MeV and up) for OAO are approximately 3.4×10^9 electrons cm^{-2} per orbit. Similarly, peak proton fluxes (5 MeV and higher) are 1.8×10^8 protons cm^{-2} per orbit. The effects of proton radiation on the Uvicon were not investigated, but we can make the assumption that 1 proton is equivalent to 10 electrons for temporary degradation effects. The equivalent peak electron flux then becomes 5.5×10^9 electrons cm^{-2} per orbit. Actually, this peak flux is concentrated in the South Atlantic anomaly and occurs for periods of $\sim$ 10 min. The actual high-voltage-on mode lasts 60 sec at most. Therefore, the peak input radiation to the OAO is 5.4×10^8 electrons cm^{-2}. The shielding effect due to optical components in the experiment is approximately 50 (experimental results). Then the expected peak inputs to the Uvicon are 1.1×10^7 electrons cm^{-2} per exposure. This input should cause approximately 1 to 2 counts of background increase.

A careful review of all orbital data reveals that the background increase of some frames may be attributed to radiation effects. The amount of increase, however, is not more than 0.5 count, far below the level of easy detection. Considering the uncertainty of the expected value of radiation (up to a factor of 5)

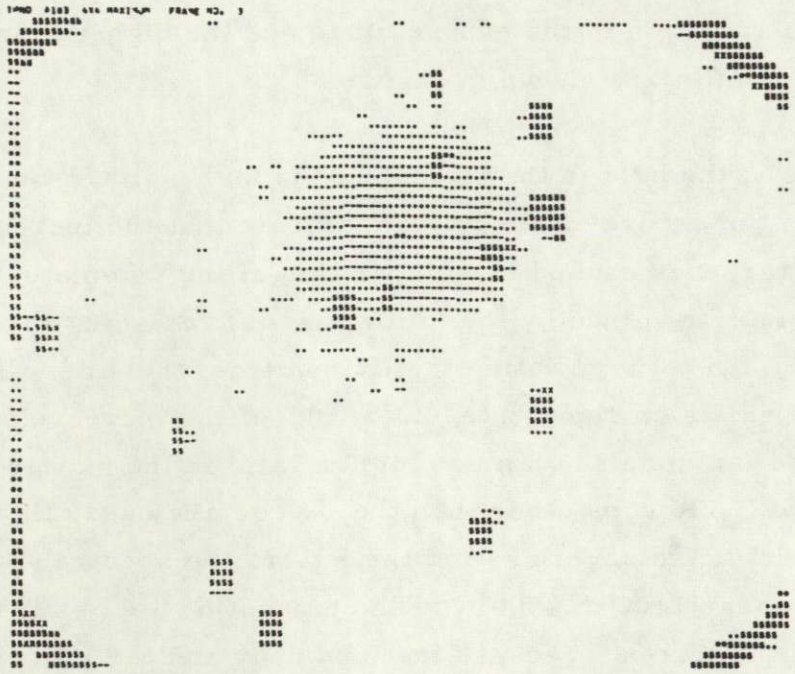

(a)

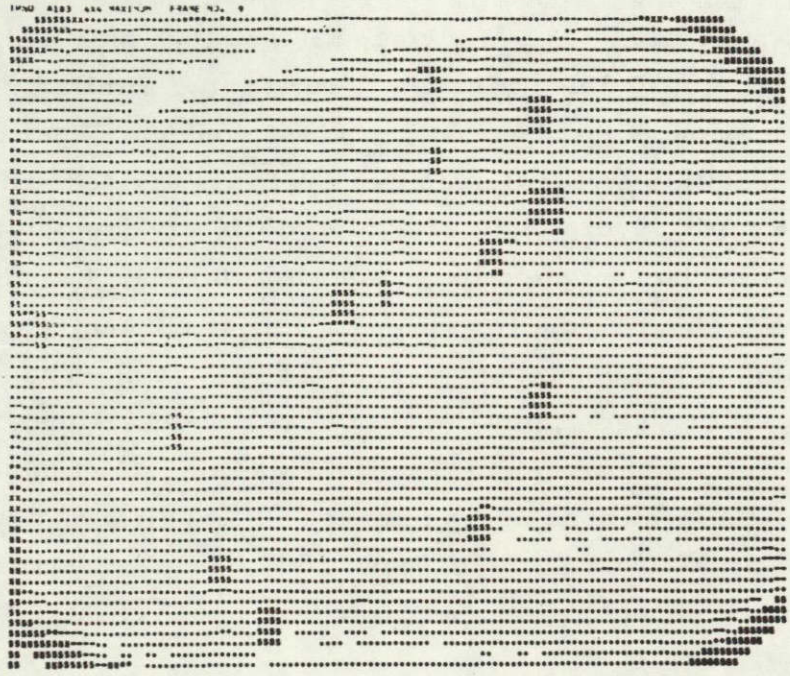

(b)

Figure 30. Television pictures (in computer printout form) when holed shield is placed in front of tube: (a) high-voltage-on mode, (b) expose mode.

and the difference in sensitivity of the tubes (up to a factor 6), this result appears to be in good agreement with the limits of experimental error.

There are two types of permanent damage in the Uvicon: target-material breakdown and a change of optical sensitivity. As mentioned in Chapter 2, target-material breakdown may be caused by overexposure to radiation. This was demonstrated during ground tests. From these tests, the threshold of target-material breakdown is determined (Table 22). The breakdown starts at 60 counts of average background. (Isolated light input may generate up to 80 counts of peak signal without any problems.) The maximum electron flux that OAO will encounter is 5.5×10^{9} electrons cm^{-2} per orbit, concentrated in periods of ~8 to 10 min. Therefore, if the Uvicon is operated in high-voltage-on mode ~10 min in the zone of highest concentrated radiation, the tube may suffer target-material breakdown. Maximum duration of high-voltage on is usually 1 min in normal operation. There is, therefore, no danger of target-material breakdown in the Uvicon due to radiation. Furthermore, Uvicon sensitivity was continuously decreasing and part of the sensitivity reduction is attributed to the target sensitivity; the danger of radiation-induced target-material breakdown is reduced still further as time elapses.

The other type of permanent damage in Celescope, namely, change of optical sensitivity, can be classified further into change of transmittance of filters and Uvicon faceplate and change of reflectance of the mirrors. In 1963, GSFC assisted SAO in conducting a series of tests to determine the effects of space radiation on Uvicon faceplates. Fifteen lithium fluoride Uvicon faceplates were irradiated with various intensities and energies of electrons and protons; their transmittances were measured before and after irradiation. More extensive measurements performed by Heath and Sacher (1965) on typical ultraviolet optical materials demonstrated that lithium fluoride is about 100 times as sensitive to radiation damage as are the other optical materials used in Celescope. If radiation damage affected the performance of Celescope optical materials in orbit, the first effects should appear as the typical wavelength-dependent absorption changes in lithium fluoride.

Figure 31 shows an example of the change of LiF transmittance measure by SAO. A dosage of 10^{12} electrons cm^{-2} at 1 MeV causes a loss of ~ 7% in

Table 22. Threshold radiation level for target-material breakdown.

Operating mode	Radiation source	
	Gamma ray (rad)	Electron beam (electrons cm^{-2})
High-voltage on	0.16	1.2×10^9
Expose	46	not available

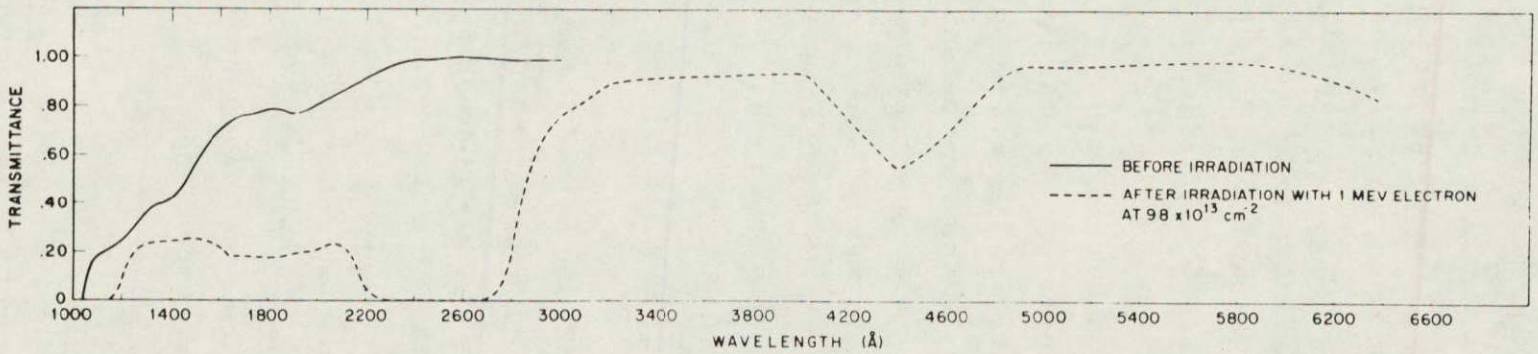

Figure 31. Transmittance of LiF Uvicon faceplate before and after irradiation.

transmittance between 1000 and 2200 Å. If the dosage is increased to 10^{14} electrons cm^{-2}, the transmittance is decreased to 10% of its original value in this spectral range. Since the optical degradation is energy dependent, since protons are also important in causing degradation, since degradation depends on wavelength as well as on radiation levels, and since the optical filters partially shield the LiF for U_1, U_2, and U_3, predicting degradation is very difficult. Davis and Gerard predicted about 40% loss of sensitivity in U_1, 20% in U_2, 7% in U_3, and 80% in U_4, based on the estimated dosage of electrons in the OAO of $\sim 5.6 \times 10^{11}$ electrons cm^{-2} per year (at a higher energy than 0.5 MeV). However, because the assumptions that went into this calculation were rather weak and conservative, these prelaunch predictions require reinterpretation on the basis of orbital data. Unfortunately, comparison of the predicted and the actual degradation is not easy, since the observed star data are greatly affected by decreases in Uvicon sensitivity caused by nonradiation effects. Although the sensitivity changes described in Chapter 2 of this report indicate that radiation damage in LiF was probably a minor contributor to the total sensitivity change, substitutes for LiF in space optics, such as MgF_2, are recommended whenever possible.

4.4 Residual Optical Sensitivity and Stray Light

As mentioned in Chapter 2, the Uvicon accumulates signal charges on the target if the Uvicon is left in the expose (XMO) mode for prolonged periods. The probable cause of the charge accumulation is direct generation of photoelectrons in the target material ("residual sensitivity"). Figure 32 pictures examples of these charge accumulations. The accumulated charge is more or less spread throughout the entire field of view, contrary to the one-side high-background of Lyman-α pictures. The camera 2 picture shows the results of target-material breakdown during the reading sequence. Camera 1 is not so sensitive as the other cameras; hence, the effect is not so large for it as for them.

Impact of the residual optical sensitivity on system design may be significant. The Celescope experiment does not include any movable mechanical parts, except latching relays, because of their potential unreliability in the space environment. To control the signal input to the Uvicon target, Celescope

uses an electronic shutter that controls photoelectrons created in the photocathode, rather than controlling the input of light itself. Once high voltages are off (electronic shutter closed), no accelerated photoelectrons reach the target to create signal charges. Because of residual optical sensitivity, however, the target is still accumulating signal charges. Since the electronic shutter has no control over this effect, Uvicon tubes are in continuous danger of overexposure and resulting target-material breakdown.

A similar problem in a future system can be avoided by: (a) installation of the mechanical shutter or (b) continuous erasure of the charges by proper beam scan. Each method has its advantages and disadvantages. Probably the best method is the combination of both: the mechanical shutter ensures the prevention of unwanted incoming light, and continuous erasure takes over only when the shutter fails to close. Since the continuous beam erasure requires additional power and also command capability, in addition to the possibility of accelerated fatigue of the target, it should be avoided in the normal mode of operation. If the mechanical shutter is designed to be open-failure rather close-failure (for instance, by jettison), this system will be a good compromise.

4.5 Effects of Geocorona

When orbital observations of Celescope were made at night, we expected a very dark sky, which was supposed to be much better than that seen from the ground. This proved to be true in the cases of U_1, U_2, and U_3. But in U_4, there was a very high background (see upper half of the picture in Figure 33). The background light was identified as Lyman-α emission from hydrogen atoms in the geocorona. The emission itself, the intensity of which was expected to be on the order of $2 \text{ to } 4 \times 10^{-3}$ erg cm^{-2} sterad^{-1} (Meier, 1969), is not really surprising. What is surprising is its apparent intensity in the television pictures. Because of this unexpectedly high background signal, useful observations by U_4 were limited.

The apparently high intensity of the Lyman-α emission (approximately 1216 Å) has several causes. The most obvious is the difference in instrument

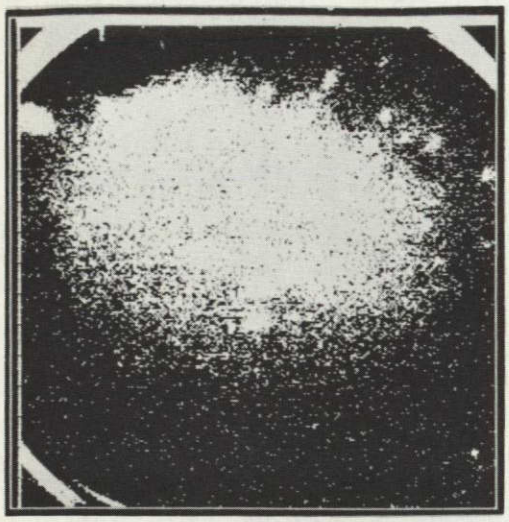

Camera 1

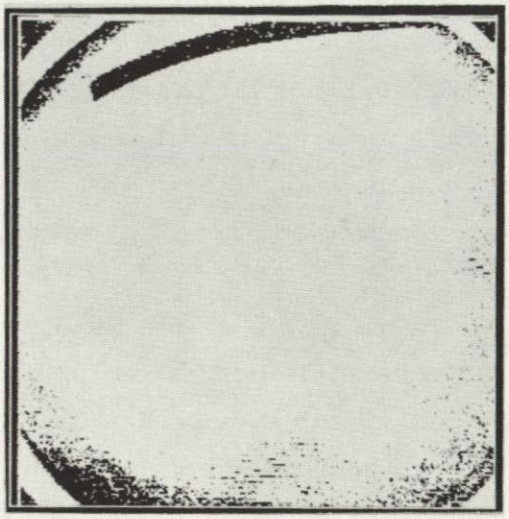

Camera 3

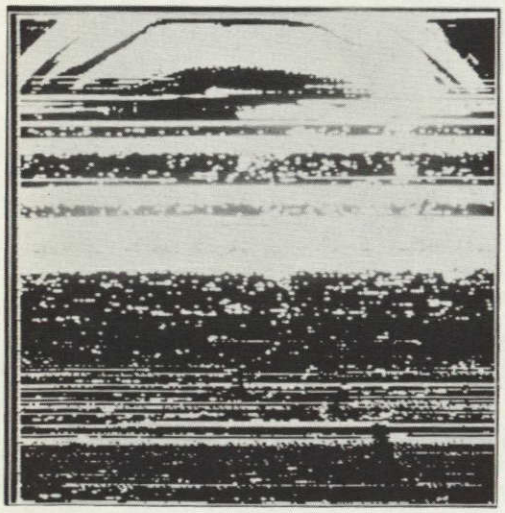

Camera 2

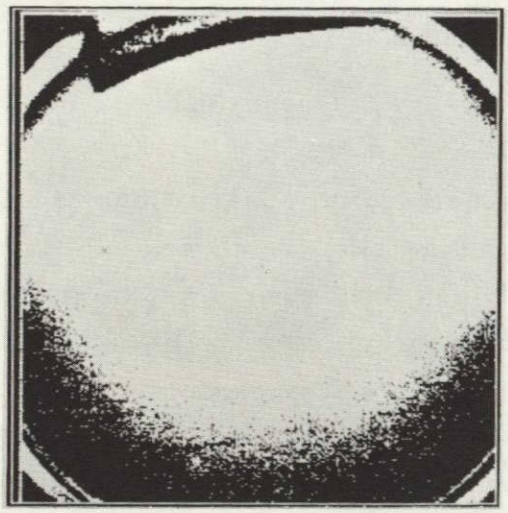

Camera 4

Figure 32. Charge accumulation due to residual sensitivity. Contact S262.

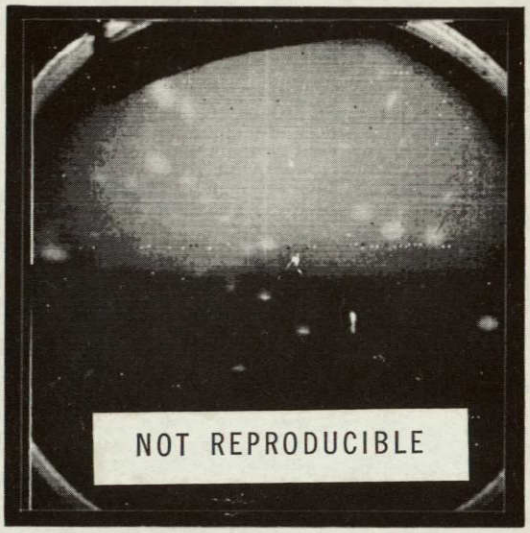

Figure 33. A television picture from camera 4. Upper half: U_4 with Lyman α; lower half: U_3.

characteristics for point sources (like stars) and for area sources (like the geocorona). In Celescope, a quantity called "Sigma," which is proportional to the amount of charge accumulated on the target and associated with a stellar input, was adopted as an output. Its adoption extended the dynamic range of the Uvicon television photometer. In the usual television signal, the amplitude of the readout current is taken as the output signal, with a dynamic range of the order of 10 to 100. But if we adopt the integral of the current rather than the amplitude of the current, the dynamic range becomes 1000 to 10,000. This extension is accomplished by the spread of image sizes. Once the amplitude of the readout current reaches a saturation level, the conventional signal can no longer distinguish the input levels. But the sizes, or widths, of readout current pulses are still increasing even after the amplitude reaches the saturation level. Therefore, Sigma, which is equivalent to the products of the amplitude and width of the readout current, will increase, even after amplitude saturation, as the input level increases. But this argument is correct only when the input light forms a near-point image. When the input is a point image, the readout current becomes pulse-like, and its width can be increased as the input level increases. When the input is an area-like image, then the readout current more closely resembles DC-level change, than it does pulses. That is, the dynamic range for an area-source input is the same as that for a conventional amplitude signal. For Celescope, the dynamic range of star input may reach as high as 10,000, but the dynamic range for the geocorona is still on the order of 100 at most. This is the reason that a 5-sec exposure creates a good picture in U_4, but a 60-sec exposure almost completely wipes out star images, despite a difference of only a factor of 12 in exposure time, far from the limit of the dynamic range of star image (see Figure 34).

The other causes of the apparently high Lyman-α background is the possibility of real Lyman α of unexpectedly high emission. Since the Celescope was calibrated for point sources only, an accurate value is not available yet.

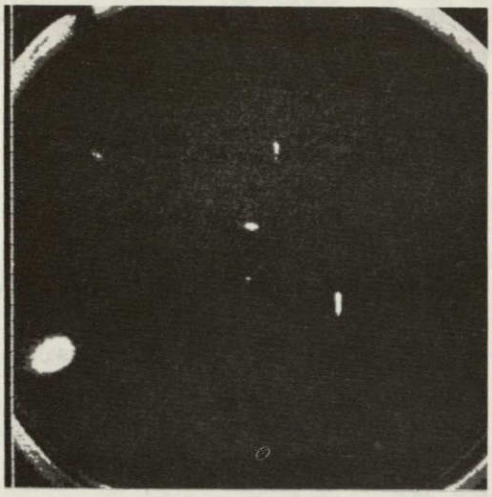

S702 – 5 sec

S688 – 15 sec

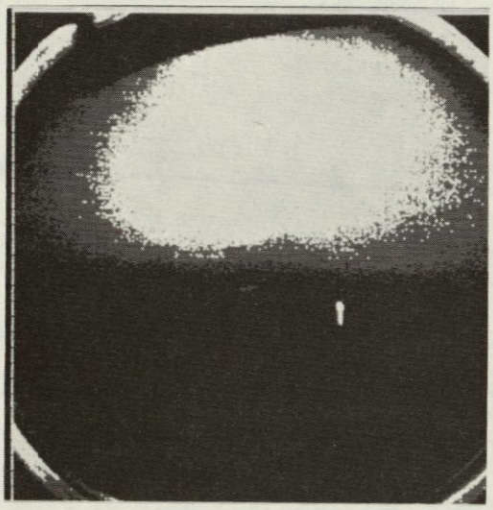

ϕ764 – 30 sec

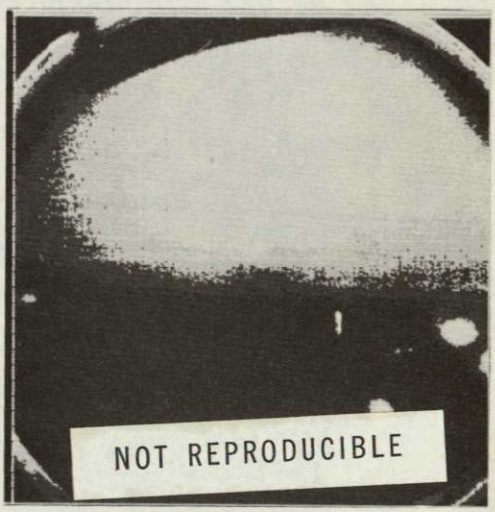

Q689 – 60 sec

Figure 34. Lyman-α pictures in different exposure time.

Since Celescope observed Lyman-α emission on many occasions, we can determine the relative intensity changes without determining the absolute intensity. On the basis of a preliminary study, the observed intensity of the Lyman-α emission can be expressed as

$$J = A \cdot t_{ex} \cdot e^{-cT} \cdot \theta^{d} \cdot \beta^{f} \cdot L^{g} \quad ,$$

where

- J intensity of Lyman-α emission, expressed as an increase of average background in selected areas of television pictures,
- t_{ex} exposure time (integration time in seconds),
- T temperature of the instrument (°K),
- θ solar zenith angle (limited to between 103° and 172°),
- β angle between sun and pointing direction of the instrument (limited to between 60° and 134°),
- L distance between instrument and intersecting point of earth-shadow cone and instrument line of sight (km),
- A 6.922×10^{4} (arbitrary unit, same as J),
- b 0.6168 (dimensionless),
- c 1.949×10^{-3} (1/°K),
- d -0.4284 (dimensionless),
- f -1.250 (dimensionless),
- g -4.841×10^{-2} (dimensionless).

The first two variables, exposure time and temperature, are correction factors for the measuring conditions and characteristic changes of the instrument. The last three variables suggest that the Lyman-α intensity becomes stronger for a smaller solar zenith angle, a smaller beta angle, and a shorter distance for illumination points. The spatial distribution of Lyman-α emission within the field of view of the Celescope experiment package can be determined if the details of the optical characteristics of the Celescope experiment package are understood. The observed intensity distribution in the television picture is not yet well understood. As seen in Figure 33, the peak intensity occurs

somewhere in the U_4 region. The location of the peak area varies from frame to frame. This suggests there are some kinds of change in Lyman-α distribution within the narrow cone of the field of view or simple changes in the reflection pattern of stray light. From calculations of the intensity distribution for the Schwarzschild telescope, the peak intensity area should be located along the middle of the U_4 region if all stray light and internal reflection are neglected. The calculations also assume the Lyman α intensity to be constant for any given air volume. Probably owing to these unrealistic assumptions, the observed intensity distribution and the calculated one are not in agreement. (This is another area where further study is needed.) Figure 35 shows the intensity distribution of Lyman α along a line perpendicular to the filter split line.

Implications of the Lyman-α emission for future space astronomy, especially for television astronomy, are very important. The existence of the geocorona may limit the detection threshold of stars in the spectral range. Also, the time for integrating the television photometer and the spectrophotometers may be limited by the background illumination of the geocorona emission. Of course, there are ways to get around this limitation, but they have to be devised beforehand. The avoidance of the Lyman-α limitation will be one of the most challenging problems of system design for future space astronomical television or other instruments.

4.6 Solarization*

The solarization of various optical or electro-optical components may cause changes in instrument sensitivity. These changes, if they occur, are expected in the following areas:

1. Deterioration of transmittance in the optical filters and faceplates.
2. Deterioration of the reflectance of the mirrors.
3. Deterioration of the photocathodes.
4. Deterioration of target sensitivity.

*Solarization, as used in this section, is defined as alteration of the optical characteristics of material that follows prolonged exposure to sunlight or other optical, infrared, or ultraviolet radiation.

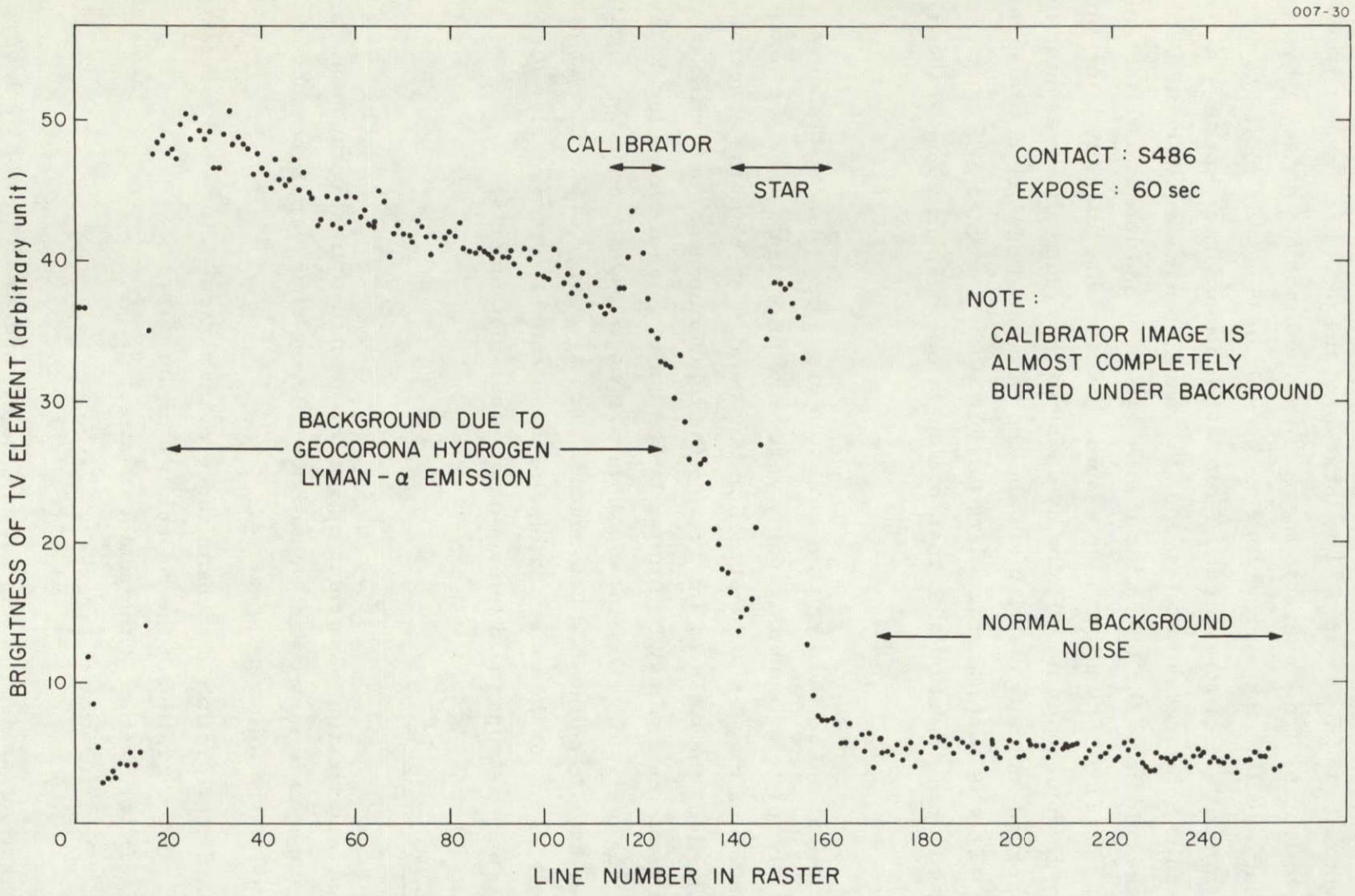

Figure 35. Brightness distribution along vertical center line of camera 4 picture.

At present, we have insufficient information to confirm or deny the effect of solarization on the above.

If detailed discussion on the solarization in the Celescope experiment package is necessary, it must be postponed until further studies of the observed data are completed.

4.7 Outgassing

Outgassing is one of the important problems in space optics, especially for the ultraviolet. Since almost every material outgasses in a vacuum, selection of material and choice of processing methods are very important. If outgassed material condenses on the optical surfaces, degradation of optical performance may be very severe in the ultraviolet regions. For the reader's interest, a brief history of the Celescope experiment package will be presented.

After careful selection of material, we completed the first Celescope experiment package (an engineering model). During the thermal-vacuum test, we experienced severe optical contamination on mirror surfaces. During low-temperature testing, we did not observe any deterioration. But when we opened the vacuum chamber, there was a heavy brown deposit on the mirror surface (see Figure 36). Infrared spectral analysis showed these deposits to be a mixture of black paint, which was used throughout the package, and diffusion pump oil. To avoid recurrence, we adopted the following approaches:

1. Selection of material based on the VCM index.
2. Improvement of the preparation of material, parts, and components.
3. Improvement of the assembling and handling procedures.
4. Stringent requirements for the test facility and procedures.

Generally speaking, outgassing of polymer material in a vacuum rapidly reaches a peak and then gradually decreases. Some of the outgassed material

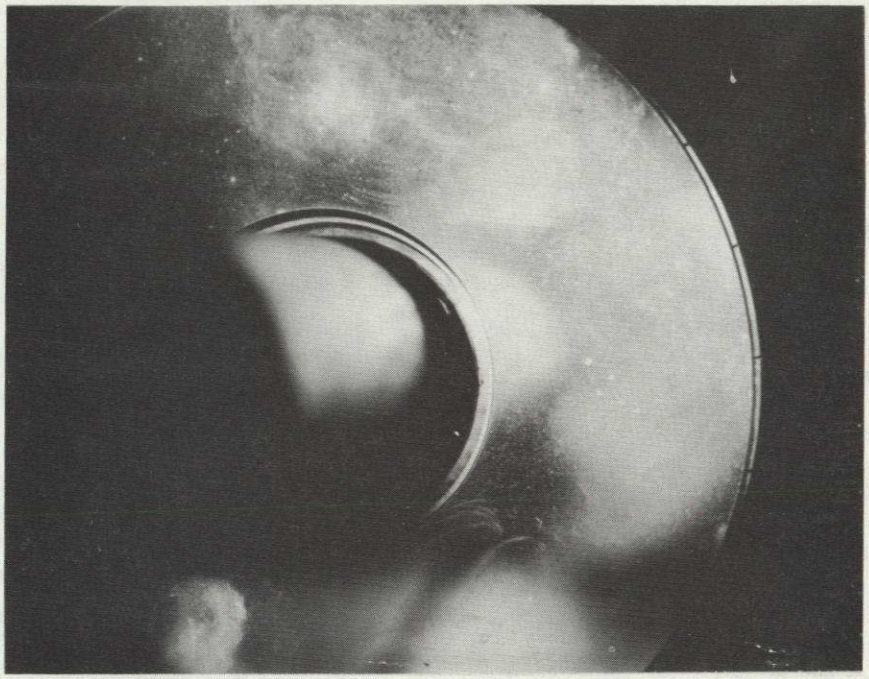

Figure 36. Contaminated mirror surface.

can condense on the surrounding surfaces where, depending on temperature and other conditions, it may remain or it may evaporate, or it may polymerize into a nonvolatile substance. As part of our program for controlling and preventing contamination of the Celescope optical elements, we used a quantity called the VCM index as a parameter for selection of materials to be used in the Celescope experiment. The VCM index is the ratio of the weight of volatile and condensable material to the total weight loss, determined by subjecting the material in question and an appropriate receiving surface to appropriate thermal-vacuum conditions and measuring the ratio of weight gained by the receiving surface to weight lost by the material sample. (Note: For a high-voltage power supply, the total amount of volatile material is more important than is the VCM.) Most of the actual measurements and related activities were performed at Stanford Research Institute.

We could not find a black paint that safely met our requirements. However, a study revealed that a sandblasted aluminum surface is sufficiently black in the ultraviolet region, thus eliminating the need for black paint on the internal surface of our experiment package.

To avoid other contaminants, particularly fingerprint oil, all manufacturing and handling were performed in a clean-room environment by personnel wearing plastic gloves. To minimize outgassing in space, all our parts were vacuum baked before being assembled into the system. The procedure for the thermal vacuum test follows:

1. The optical surface must never be the coldest spot in the chamber (the liquid-nitrogen shroud should always be cool). This is especially important during the warmup process.

2. The temperature gradient near the optical surface should be kept at a minimum.

3. During the warmup process, dry nitrogen should be introduced into the chamber while the optical surface is cold.

When these procedures were followed, we found no optical contamination during the numerous thermal-vacuum tests.

There is another phenomenon similar to optical contamination – dust on optical surfaces. During system testing, we observed considerable amounts of dust on mirror surfaces from time to time. This dust does not adhere to surfaces but is attached to them. It is difficult to remove it without disturbing system integrity. Therefore, it was left untouched. But this dust disappears during vacuuming. Therefore, it is possible that all dust particles were removed during the initial stages of orbital operations, and thus the apparent sensitivity of the instrument was increased. Sources of this dust are not evident, since the experiment package was kept in a clean-room environment. Probable sources are thermal blankets sheared during installation. The shearing of thermal blankets, commonly referred to as NRC, causes the generation of very fine particles that were usually impossible to remove.

A similar cleaning effect resulted from radiation on the optical filters during ground tests. Small amounts of radiation usually improve the transmission of optical filters. This radiation cleaning is another potential source of the initial sensitivity increase. (The initial sensitivity increase itself is not well established yet, since the effects of magnetic disturbance were so strong and also caused an increase in the apparent sensitivity of the instrument.)

In conclusion, we can say that contamination control procedures, which include design methods, material selection, handling procedures, operation and test procedures, etc., were satisfactory and produced the intended results.

4.8 High-Voltage Arcover

There is a danger of arcover (corona, flashover, sparking, etc.) in the space environment. In a high vacuum, arcover should not occur if the electrodes are properly spaced. Actually, almost all material will outgas to some extent in a vacuum. Therefore, outgassed vapor always exists locally, even in a high-vacuum environment, and contributes to arcover of high voltages.

In Celescope, we had a total of 12 high-voltage (above 200 V) power supplies (Table 23). This discussion will be limited to the 8000-V power supply since it was the most susceptible to arcover.

Three basic methods prevent arcover:

1. Venting.
2. Encapsulating.
3. Submerging in fluid (gas or oil).

Venting is the easiest to adopt if enough room is available and if the high-voltage point is located near the outside. This method was adopted in Celescope for connectors near high-voltage cables and for Uvicon faceplate areas. This method has some disadvantages, however — bulkiness, limited location, no mechanical protection, and no protection against contamination. We did not use the third method, since there were doubts as to the longevity of the seal in space and there was a danger of optical contamination. Our choice, then, for power supplies was the second method — encapsulation in solid dielectrics.

The potting material for encapsulation should have the following characteristics:

1. Compatibility with component surfaces.
2. Compatibility with thermal-expansion coefficient.
3. Low-temperature characteristics.
4. Transparency.

When we built the high-voltage power supplies the first time, some of them failed during the thermal-vacuum test. When we repeated the thermal vacuum test on the remaining units, all of them eventually failed in a similar environment. On analysis, we found that the potting compound separated from the component surface in cold temperatures and that the outgassed vapor trapped in this space provided arcover passage. After much testing and analyzing of various methods, we successfully developed a new method of manufacturing a high-voltage power supply that included

Table 23. High-voltage power supplies in Celescope.

Output level (V)	Number of units	Purpose
8000	4	Electrostatic lenses in Uvicon image section
3500	2	Xenon gas-discharge tubes
2500	2	Mercury gas-discharge tubes
500*	4	Readout gun in Uvicon

*Multilevel output power supplies -500, 200, 100, and -250 V.

1. Elimination of the printed-circuit board.
2. Special soldering technique.
3. Surface preparation before potting.
4. Conformal coating.
5. Testing at critical pressure (10^{-2} torr) through the temperature cycle.

Figure 37 shows a high-voltage power supply and its content (high-voltage divider portion). The special methods for mounting components and for bead soldering are clearly visible.

Since the potting compound adhered poorly to the commonly used fiberglass printed-circuit boards, we used instead solid polyurethane blocks, machined to fit the components. To avoid sharp points, which tend to initiate arcover and cause cracks in the potting compound, we used bead soldering. Then, to ensure proper adhesion of the potting material, we cleaned every surface thoroughly and dried it in a vacuum. A conformal coating was applied on each surface, and finally a potting compound was introduced. The preparation and curing procedures for the potting compound were both carefully controlled and were conducted without its ever being touched by human hands. Every completed power supply was then tested in the most critical environment to ensure that there was no possibility of arcover. Thereafter, we never allowed a system containing these high-voltage power supplies to be exposed to the critical environment. Whenever we had to go to vacuum in low temperatures, we waited at least 48 hr after the pressure in the vicinity of the high-voltage power supply fell below 10^{-5} torr before we applied input to the supply. This procedure ensured that no local high-pressure regions existed.

There is no direct method for detecting high-voltage arcover during orbital operations, since our high-voltage power supplies are designed to be arc proof. That is, our high-voltage power supplies would survive without any damage even though arcover occurred. The only possibility for detecting the arcover is based on a side effect that causes a very large transient surge current or voltage through the system. On the basis of the experience during ground test, once a high-voltage arcover happened, all commands were reset. In some instances, even the main power was cut off because of a transient surge.

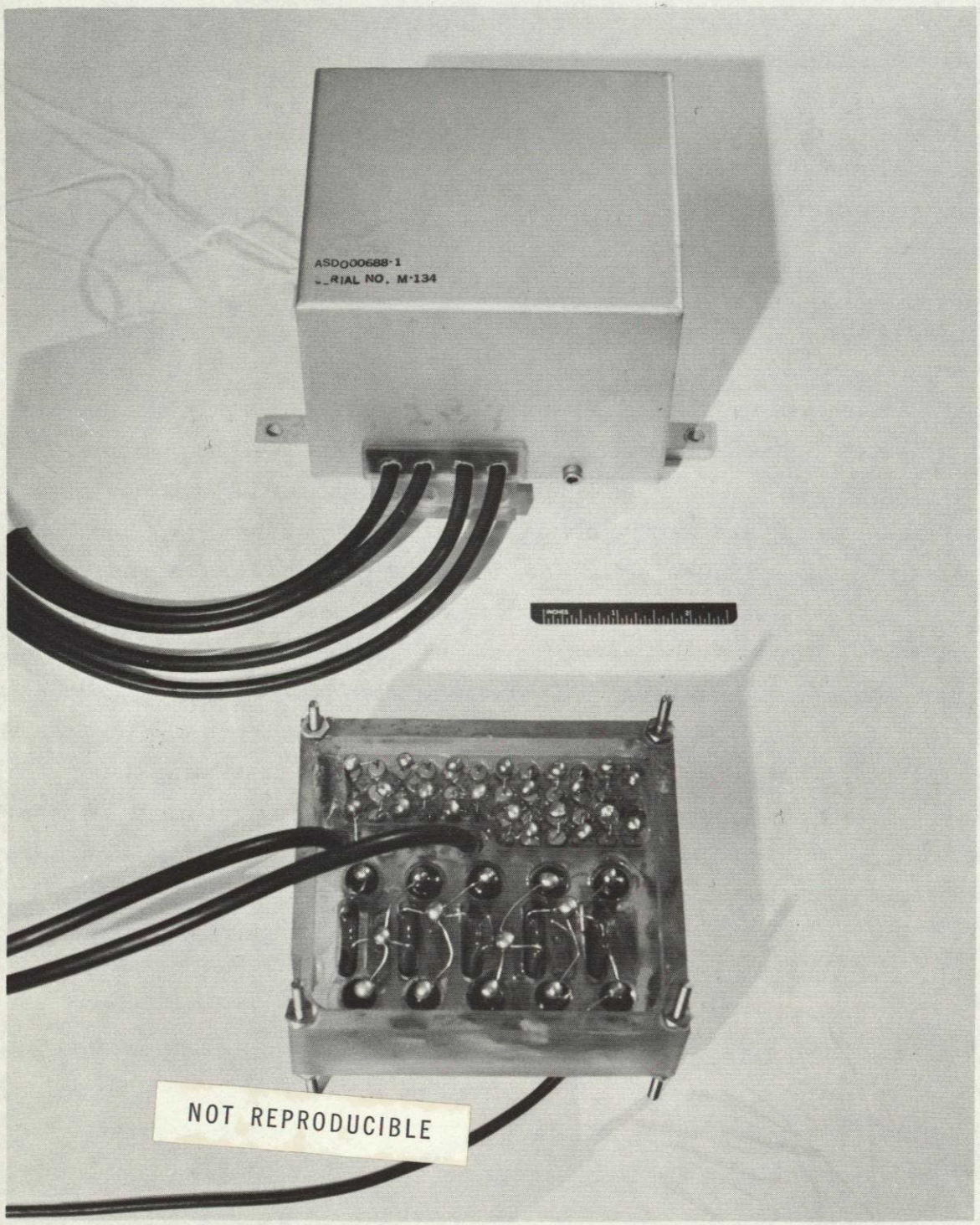

Figure 37. High-voltage power supply and part of its content.

On the basis of the above experiences, we can say that we did not find any evidence of high voltage arcover in the Celescope experiment throughout its entire operational life. This confirms the adequacy of the design and manufacturing methods and the adequacy of the initial waiting period between opening sunshade and the first high-voltage turn on. This waiting period, from orbit 87 through 102, was sufficient to allow for the escape of all outgassed material from the experiment cavity and to ensure safe operation of exposed high-voltage terminals (Uvicon flanges) in space.

4.9 Temperature Characteristics

It is not necessary to elaborate on the importance of the temperature control. Every part of the experiment package must be operated within the designed limitation on temperature. For instance, if Uvicon cameras were exposed to -85°C, the cameras would suffer irreversible damage.

Temperature variation during orbital operation (shown in Figure 38) is well within the expected range, and no abnormal temperature effects were observed.

4.10 Adjustment of Electronic Voltage Setup

As mentioned in the previous chapter, optimal adjustment of gun voltage setup is very difficult. General criteria used to select the actual adjustment level for the completed experiment package are the following:

1. Beam-level setup should be at the minimum allowed for safe operation.

2. Astigmatism and focus adjustment are selected at the middle point of the range of each — namely, astigmatism 4 and focus 2.

The purpose of these adjustments is to increase the useful life of the experiment when the initial settings of these voltages become undesirable for some reason. For instance, we observed changes in the beam current

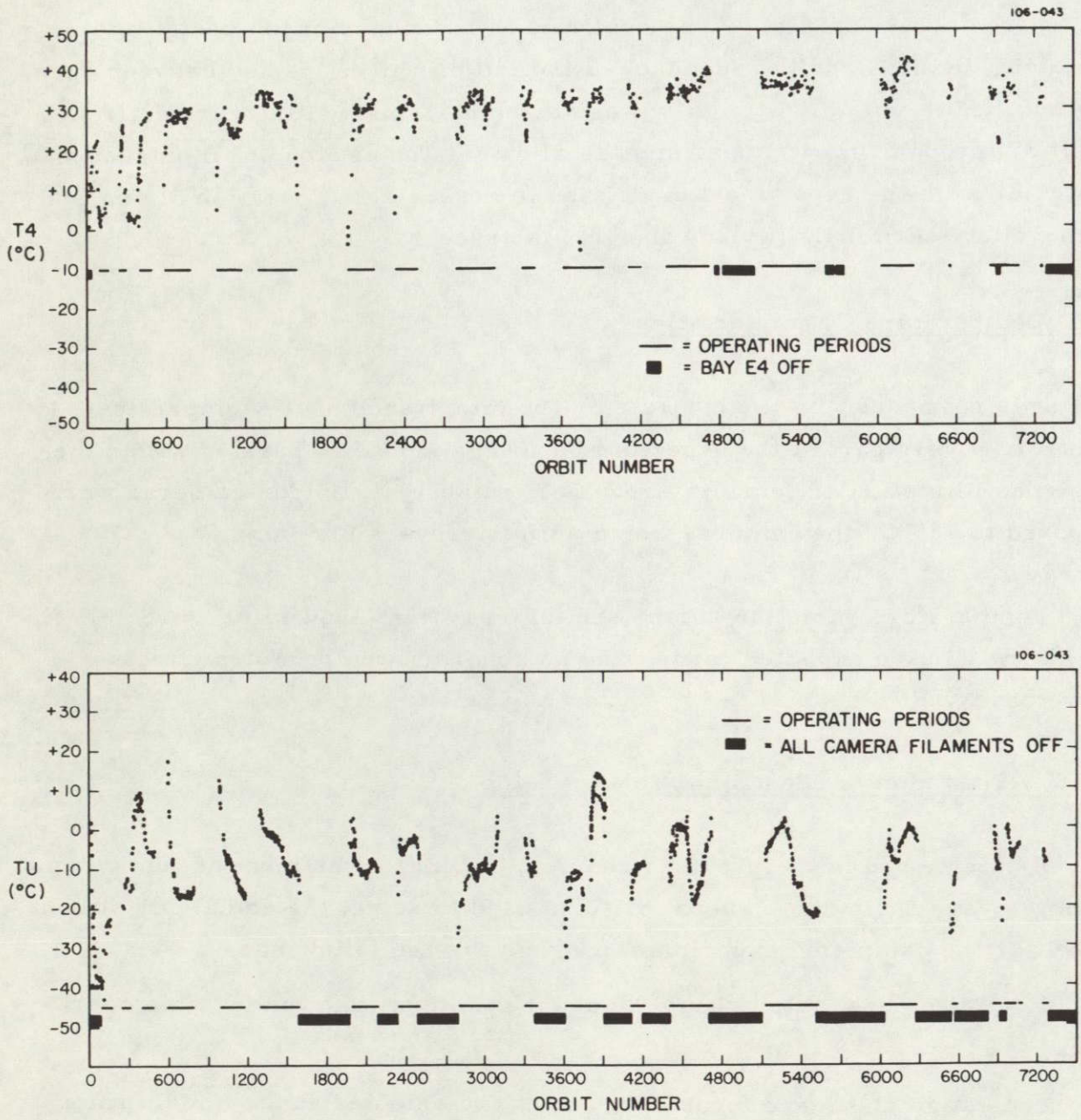

Figure 38. Temperatures in the Celescope package: (a) E-4 electronics package, (b) Uvicon temperatures; average temperatures of cameras 3 and 4.

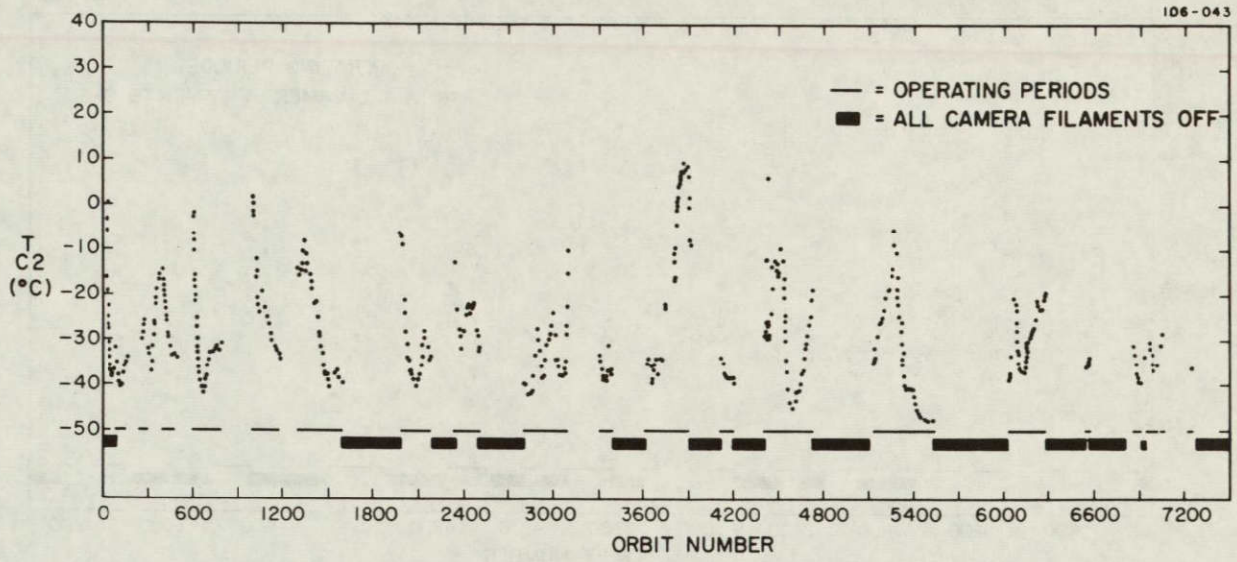

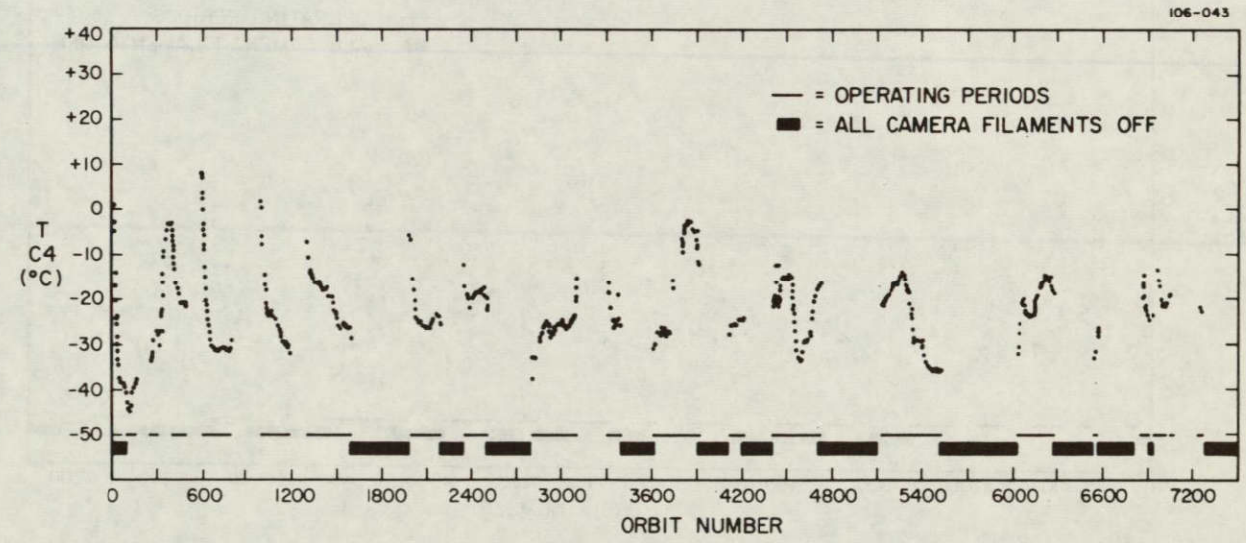

Figure 38 (Cont.). (c) Telescope temperatures at primary mirror of camera 2, (d) Telescope temperatures at primary mirror of camera 4.

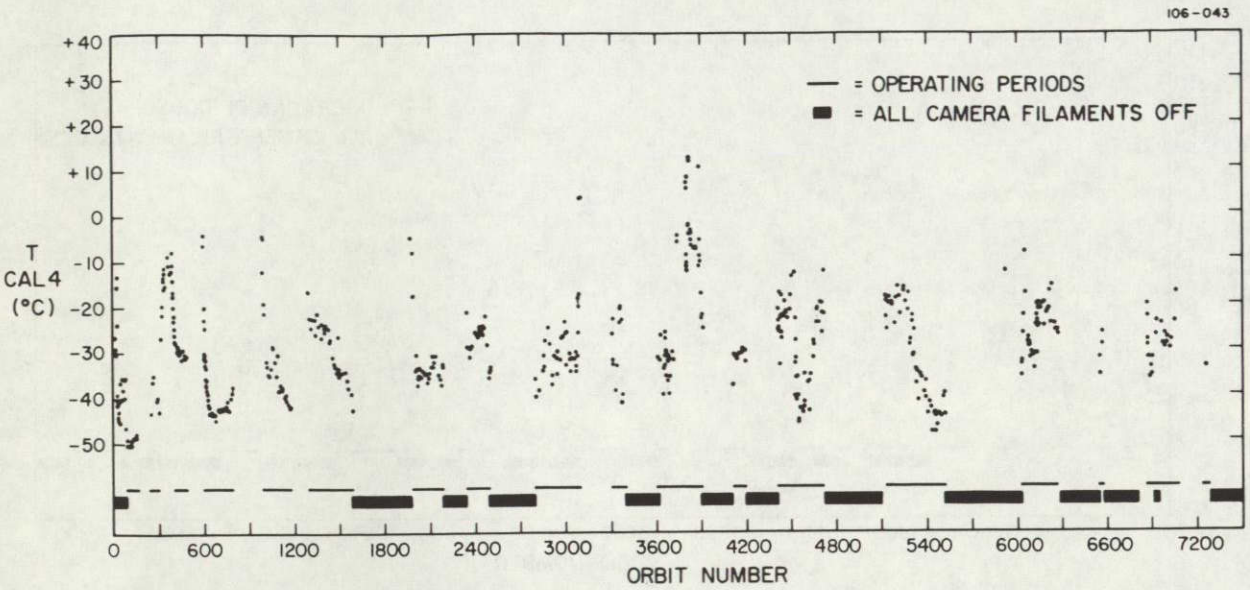

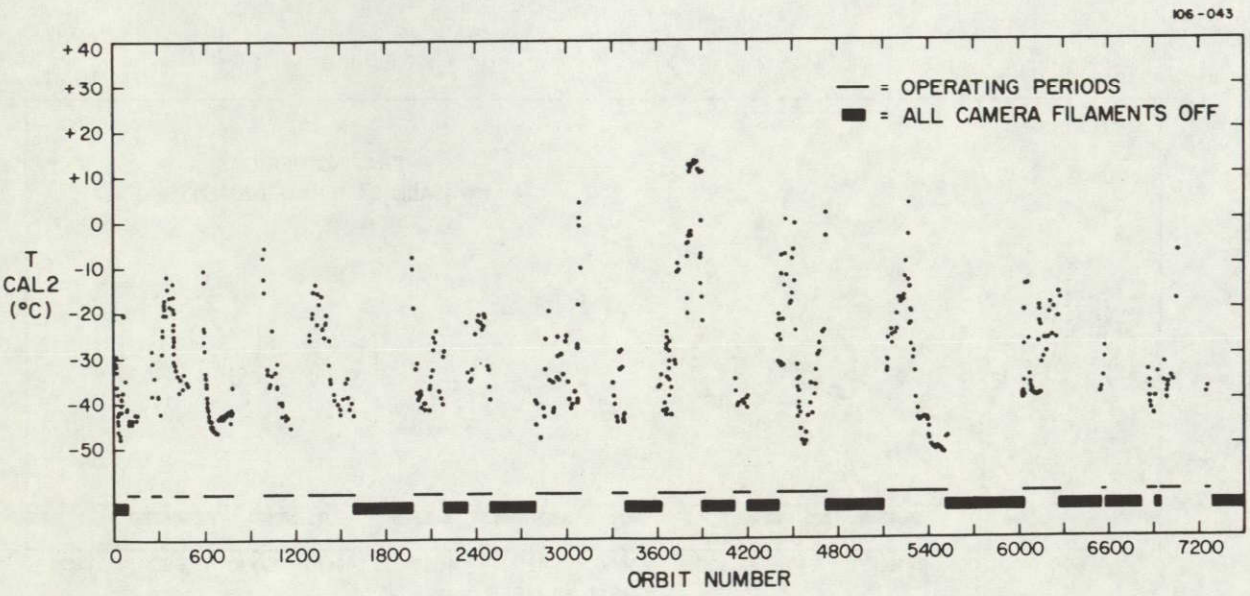

Figure 38 (Cont.). (e) Temperatures at calibration lamp 2. (f) Temperatures at calibration lamp 4.

after simulation of the launch environment during a very early phase of Uvicon development. Therefore, it is conceivable that the voltage settings change during launch or during orbital operations. If there are adjustable settings, we can extend the useful life of the experiment. In the case of beam-current adjustment, reduction of beam current as time elapses was anticipated. The readjustment of the beam-current setting would hopefully compensate for the reduction. Initial settings for beam current were all level 1, except for camera 3, which was at 3 (camera 3 could not be operated at less than level 3).

The beam level of camera 1 was changed to 2 during orbit 268. Later, it was increased to 3 during orbit 1030. Despite these two increases, beam current was not sufficient. Further increase to level 4 did not result in the intended increment of beam current. Rather, it caused a defocusing effect and made difficult the operation of the Uvicon.

We attempted to determine the optimal setting of astigmatism and focus by using orbital data. A result is shown in Figure 39. It indicates that proper settings are important since different settings produce different values of Sigma for the same object observed. Since no other settings were found to provide improved performance over that given by the original values, we retained the original settings for astigmatism and focus throughout the entire life of Celescope except during the brief period of experimentation.

On the basis of these experiences, we can say that (a) it is very difficult to determine the optimal setting from orbital observations of stars; (b) any change of the adjustment due to space or launch environment, if there is any, is also very difficult to observe; and (c) drifts in voltage levels in the gun section, if any, seem to have had a negligible effect on observed data, compared to other factors — for instance, fluctuation and deterioration of camera sensitivity — whereas when we tried changes in the adjustment settings we found significant changes in the instrument calibration. This also implies that the current design of the electron-gun section in the Uvicon is satisfactory for space application.

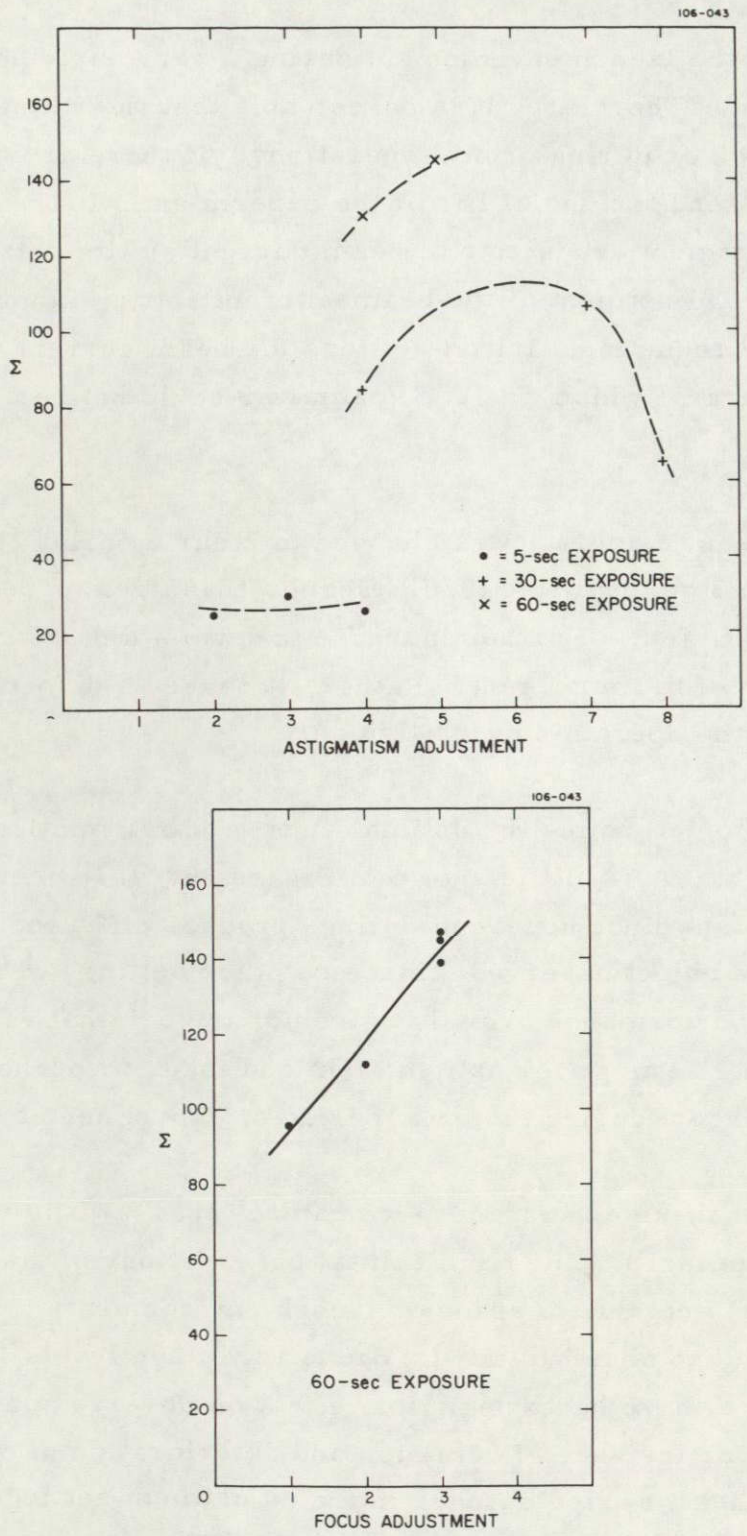

Figure 39. Change of Sigma due to adjustment level change. Orbital data, early 1300 series: (a) astigmatism, (b) focus.

4.11 Anomaly in Pictures

We observed abnormal pictures from time to time. Some of the pictures are explained easily, whereas a few have not yet been explained. Figures 40 through 43 show selected abnormal pictures and indicate the most probable cause of each type of anomaly illustrated.

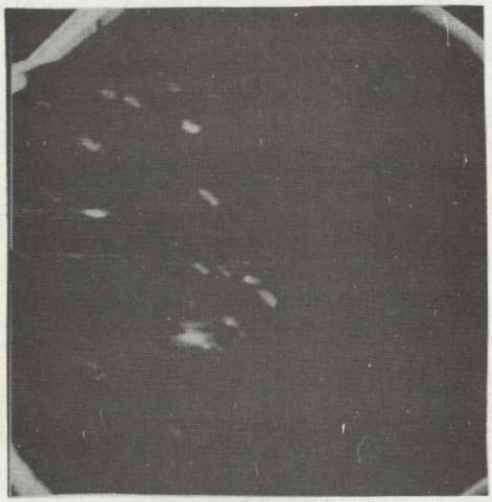

(a)
R141 – Camera 3
Effect of magnetic disturbance
on stars

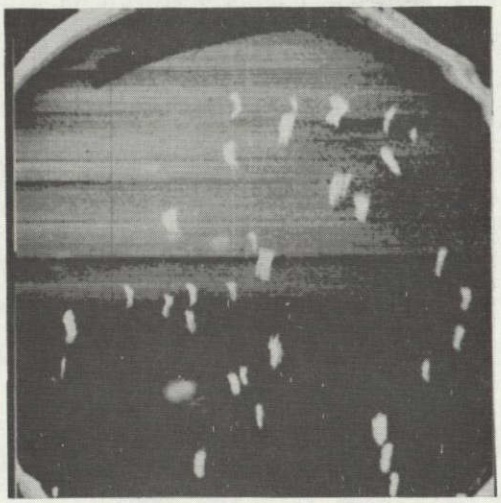

(b)
R141 – Camera 2
Effect of magnetic disturbance
on false stars

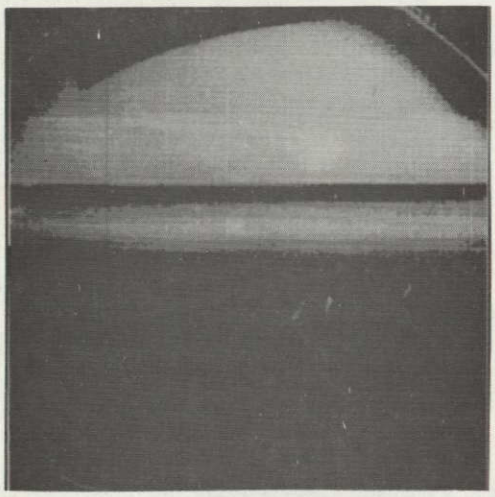

(c)
R141 – Camera 4
Effect of magnetic disturbance
on Lyman α

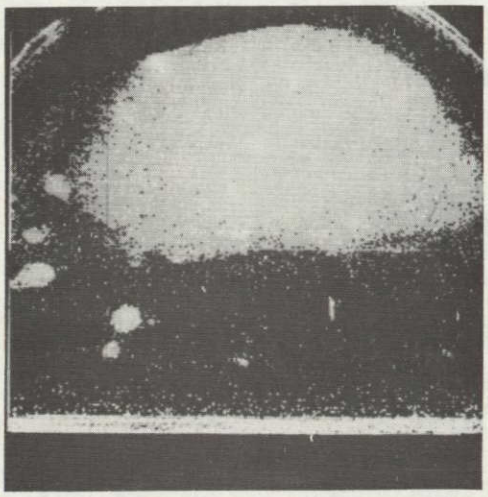

(d)
Q414 – Camera 4
Partial picture due to premature
termination of data transmission

Figure 40. Anomaly in picture 1.

(a)
S261 – Camera 1
Calibration lamp ghost
visible

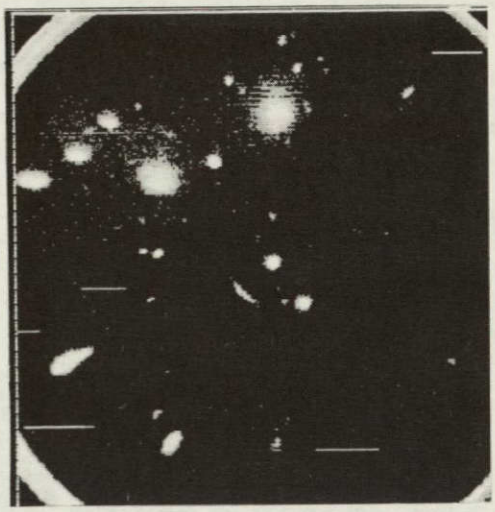

(b)
R256 – Camera 3
Calibration lamp ghost
visible

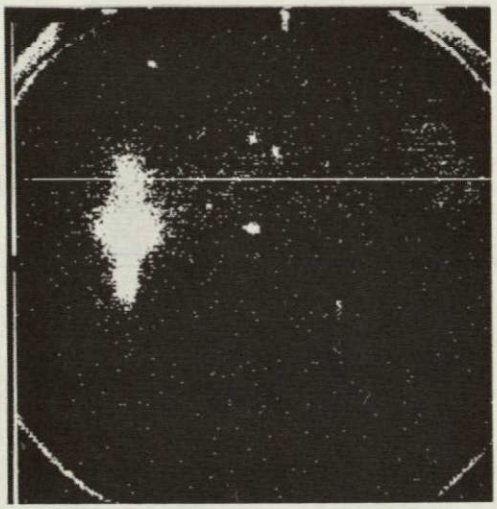

(c)
ϕ6085 – Camera 4
Star ghosts due to filter split
discontinuity

(d)
M2020 – Camera 3
Star ghost due to bright star

Figure 41. Anomaly in picture 2.

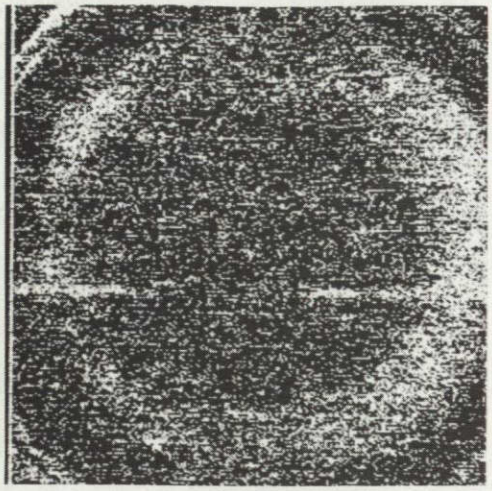

(a)
M6117 – Camera 3
Residual charge due to insufficient priming

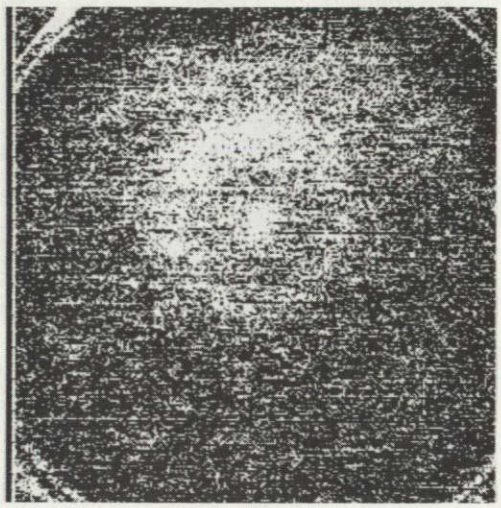

(b)
M4116 – Camera 3
Residual charge due to insufficient priming

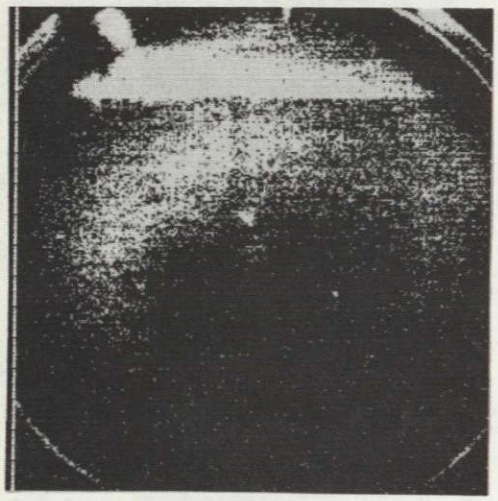

(c)
ϕ6086 – Camera 4
Residual charge due to insufficient priming

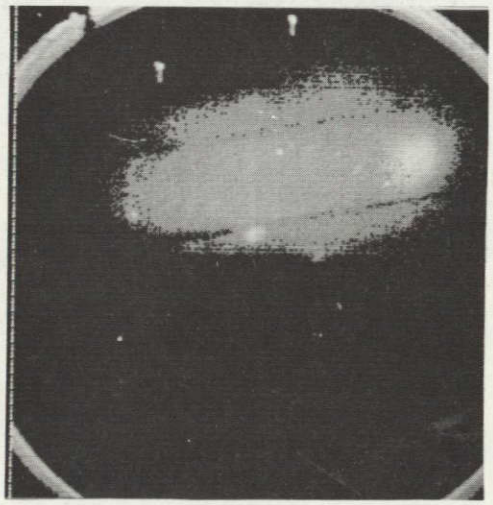

(d)
M2093 – Camera 4
Electronic noise in Lyman α

Figure 42. Anomaly in picture 3.

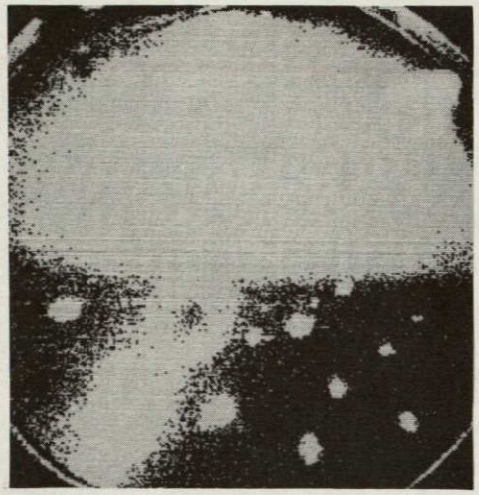

(a)
R5158 – Camera 4
Black area due to reflection

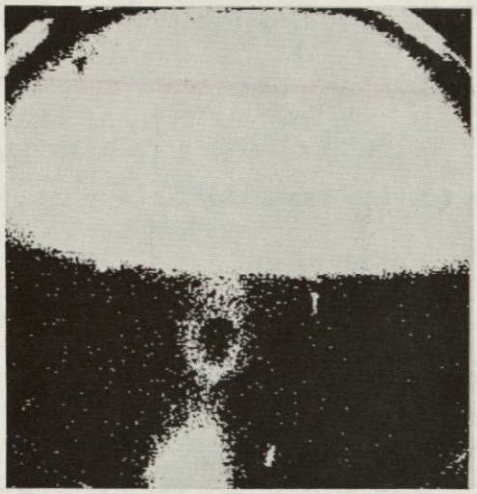

(b)
Q4658 – Camera 4
Black area due to reflection and overexposure

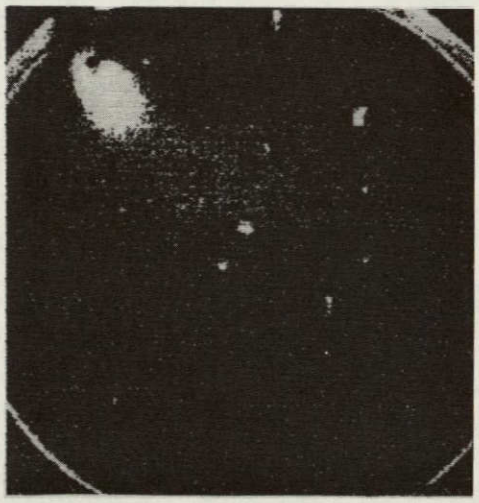

(c)
ϕ6113 – Camera 4
Probably due to intersection of shadow with star

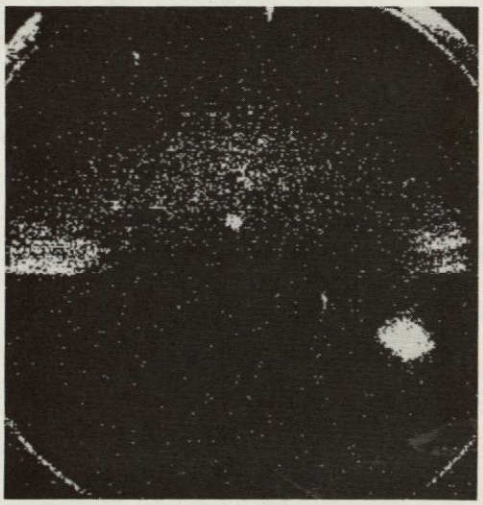

(d)
ϕ6114 – Camera 4
Probably due to leakage at filter split

Figure 43. Anomaly in picture 4.

4.12 Conclusions

The conclusions of this chapter are the following:

1. Daytime observation is possible in some limited circumstances.

2. Effects of space radiation are minimal, except possibly for a long-term one, the transmittance change in the lithium fluoride optical components.

3. Residual optical sensitivity is bothersome in some cases. The use of mechanical shutters should be considered for future flights.

4. Geocorona seriously interfered with Celescope measurements in the spectral band containing 1216 Å, especially for long exposure times.

5. Contamination control procedures during ground operations were fully successful.

6. The anti-arc design for high-voltage power supplies, ion traps, and related circuits worked perfectly.

7. Solarization has no observable effect on Celescope.

8. Thermal design of Celescope/OAO is satisfactory.

9. The ruggedized gun section of the Uvicon tube performed satisfactorily.

CHAPTER 5

SYSTEM CHANGES DURING ORBITAL OPERATION

5.1 Introduction

The characteristics of the Celescope experiment changed as time elapsed, as do most instruments. This chapter describes the nature of the changes and their probable causes. The most significant change encountered was a reduction of system sensitivity; degradation of other performance parameters was slight.

Each camera is equipped with a calibrator lamp. One indicator of Uvicon deterioration is the signal from the calibrator-lamp image. To obtain accurate knowledge of changes in Uvicon sensitivity, however, we need the additional information provided by the stellar observations themselves.

True deterioration of the Celescope experiment as a whole can be determined from the processed star observations. These results will be available when data processing is complete. Until such time, discussion of the deterioration will be limited to system deterioration deduced from apparent deterioration. Even when the processed star observations are available, determination of the mechanism of system deterioration will not be straightforward.

Deterioration of optical components, such as mirrors, filters, calibrator lenses, and faceplates, was determined from careful analyses of star observations and from deterioration of other components, since deterioration of optical components could not be observed directly.

Performance changes in electronics except gain reduction are more easily detected than any other type of deterioration. These changes cause malfunctions of logic that are easily observed.

System deterioration is in part affected by operating procedures. For example, the method that Celescope adopted to increase the safety margin for target-material breakdown was one of the major factors in the accelerated deterioration.

System deterioration that affects the detection threshold should not influence measurement accuracy, provided the proper compensation method for data processing is established. The proper method must be based on correct mathematical models derived from extensive study of the system deterioration mechanisms. Therefore, it is conceivable that processed star observations may be improved, once accurate knowledge of system deterioration becomes available.

5.2 Deterioration of Calibrator Lamps

Each telescope in the Celescope experiment has a calibrator lamp. There are two types of Uvicons, A and D, according to spectral sensitivity. Therefore, we had two matching types of calibrator lamps: mercury and xenon.

The former are pen-ray lamps manufactured by Ultra-violet Products, Inc. (Model 11 SC-2); they are low-pressure gas-discharge tubes enclosed in pure fused quartz. Major emission lines are 5770, 5461, 4358, 4047, 3650, 3125, and 2537 Å. More than 90% of the emission is concentrated at 2537 Å. Considering the effect of spectral sensitivity, more than 99% of the effective input to the A-type Uvicons from the mercury calibrator lamps is concentrated at 2537 Å. The average life of the tubes is 5000 hr, according to the manufacturer. The output intensity is sensitive to operating temperature, but the output level is remarkably stable in intensity if the temperature is stabilized at $\sim 40°$ to 45°C and if the voltage input to the power supply is controlled within narrow limits, according to the same source.

In Celescope, the mercury lamps were operated by specially designed power supplies in which the output current was carefully controlled. Furthermore, temperature control maintained the lamp temperature at ~70°C by use of lamp terminal voltage. Because of the temperature control, the mercury calibrator-lamp system required several minutes of warmup. Also, the temperature control system seemed to be a problem in the high-temperature vacuum environment that occurred during ground tests but not during actual orbital operations. Owing to the lack of air, which would provide convection cooling, and the lack of cold environment, which would provide radiation cooling, the mercury calibrators seem to overheat in such an environment. Generally speaking, the output intensity decreases as the temperature increases. Mercury calibrator lamps require about 800 V of starting voltage in normal circumstances but may fluctuate about 20%. When they are operated in the dark, according to the manufacturer, lamps may require as much as 1400 V to start. In Celescope, we furnished 2500 V for normal starting, thus guaranteeing the start of the lamp in any circumstances, especially cold temperature. Lamp current was controlled to 1 mA ± 4%. Expected output fluctuation due to variation of the input current is of the same order. Variation due to temperature can be estimated from Figure 44, which is based on similar mercury gas-discharge lamps (Model 11 SC-1). The expected deterioration of lamp output can be also estimated from Figure 45, which shows deterioration characteristics of similar types of mercury discharge lamps. It is worth mentioning that the calibrator lamps that equipped the Celescope experiment were manufactured by the same company that produced lamps No. 7 and No. 8.

An independent life test for the mercury calibrator using the actual flight calibrator and power supply demonstrated that the system can operate through 7900 cycles at 15 sec on and 15 sec off. The maximum change of flux detected was 2.5%. This is equivalent to 7900 frames of picture-taking cycles for on/off switching effects, and it is equal to a total of 32.9 hr of continuous operation. (The end of this test was defined as completion of 7900 cycles to demonstrate the required number of on/off cycles, and the real end of life was never determined.) It may be reasonably assumed that the life of the lamps is approximately proportional to the inverse of the operating current.

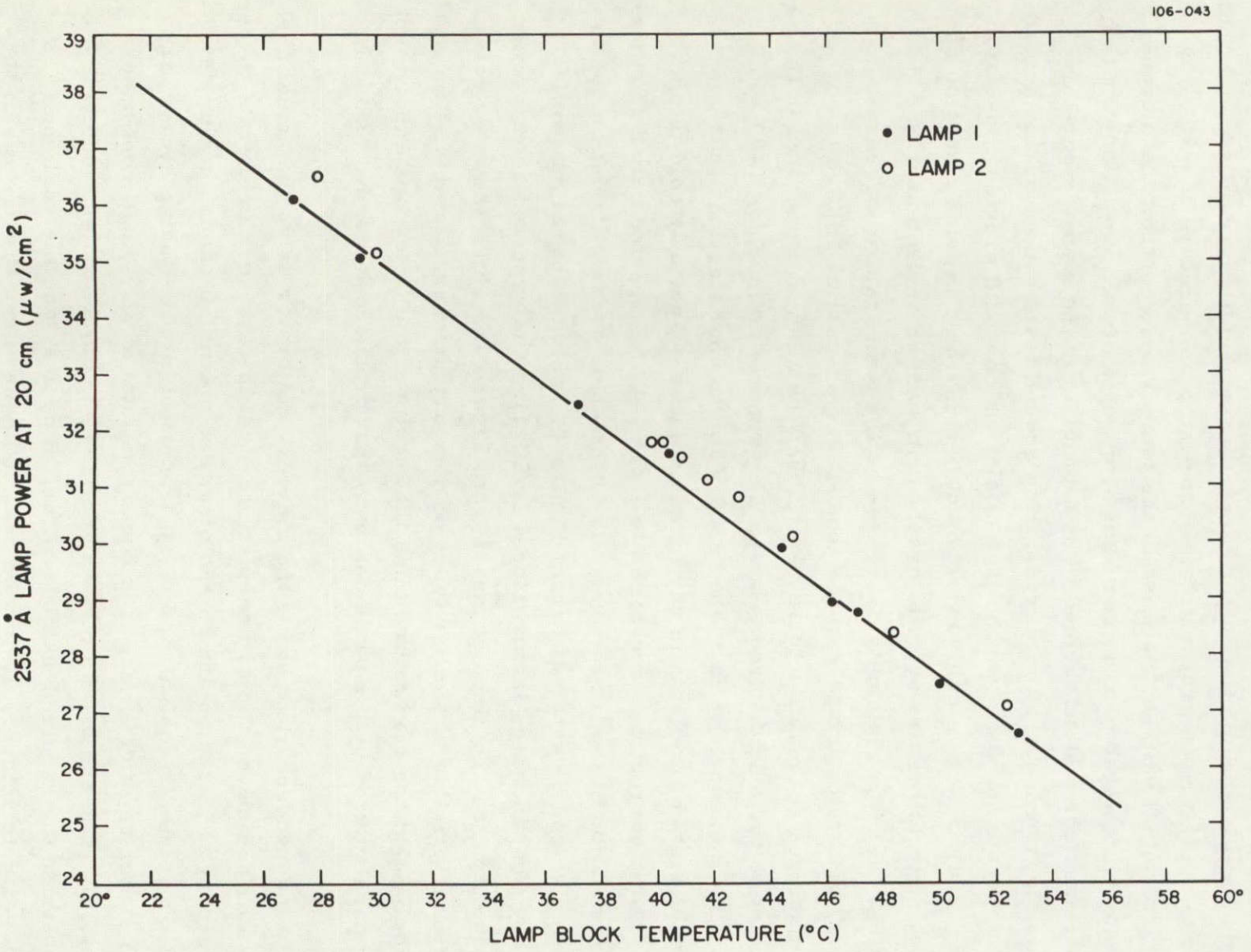

Figure 44. Temperature characteristics of mercury lamps.

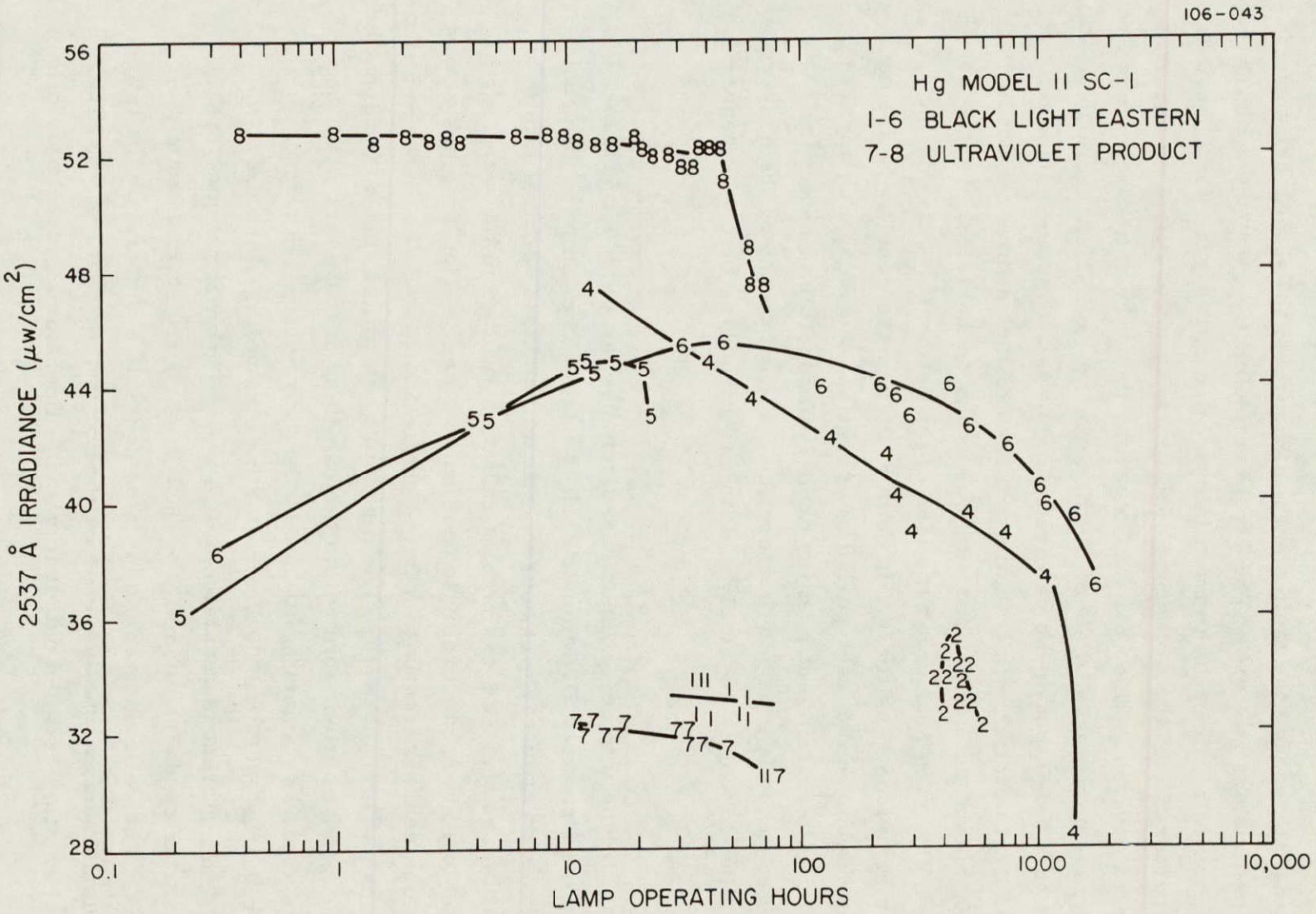

Figure 45. Irradiance at 2537 Å from OAO mercury lamp as a function of lamp operating time.

The operating current for the lamp shown in Figure 45 is 16 mA, and that of Celescope calibrators is 1 mA. The expected useful life as a standard source can be determined as about 40 hr from lamps 7 and 8 in Figure 45. Therefore the expected life of the Celescope calibrators is about $16 \times 40 = 640$ hr. The estimated operating times for the Celescope mercury calibrator lamps are about 370 hr for camera 1 and about 230 hr for camera 3 as shown in Table 24. We assume that the output of the calibrator lamps is a constant during the entire period of operation. In actuality, images of the calibrators became undetectable before the end of operation, as shown in Table 25. In the case of camera 1, the main reason for the loss of the calibrator image is the degradation of Uvicon sensitivity. In camera 3, camera sensitivity seemed to be adequate even in the later period of operation, but increased apparent background due to insufficient priming made it impossible to detect the calibrator images in the late period of operation. Figure 46 shows the Celescope mercury calibrator-lamp assembly and its gas-discharge tube with heater wires.

For the D-type Uvicon, a xenon gas-discharge lamp (Model 582) manufactured by the Princeton Division of EMR is used. The lamp is a ruggedized universal low-power ultraviolet source, and its principal spectral line is at 1470 A, with more than 90% of the total radiation emitted in the wavelength band of 1450 to 1600 A, according to the manufacturer. The lamp has a hard glass envelope sealed directly to a flat sapphire faceplate. The lamp is filled with xenon gas at low pressure. The manufacturer claims that a concentrated beam of energy is emitted from within the capillary of 0.050-in. diameter, and that the apparent radiant emittance of the source is ~ 4.5 mW/cm^2. The lamp requires 1000 to 2250 V for starting; the voltage then drops to $\sim$ 400 V and the current is regulated at 0.5 mA. The power supply for the xenon calibrator produces normally $\sim$ 3500 V to ensure starting in any circumstances. The calibrator assembly also contains a thermistor for temperature monitoring, since the xenon calibrator is temperature sensitive. The general relation between output flux and temperature is shown as follows:

$$F_1 = (T_0/T_1)^k \cdot F_0 \quad ,$$

where

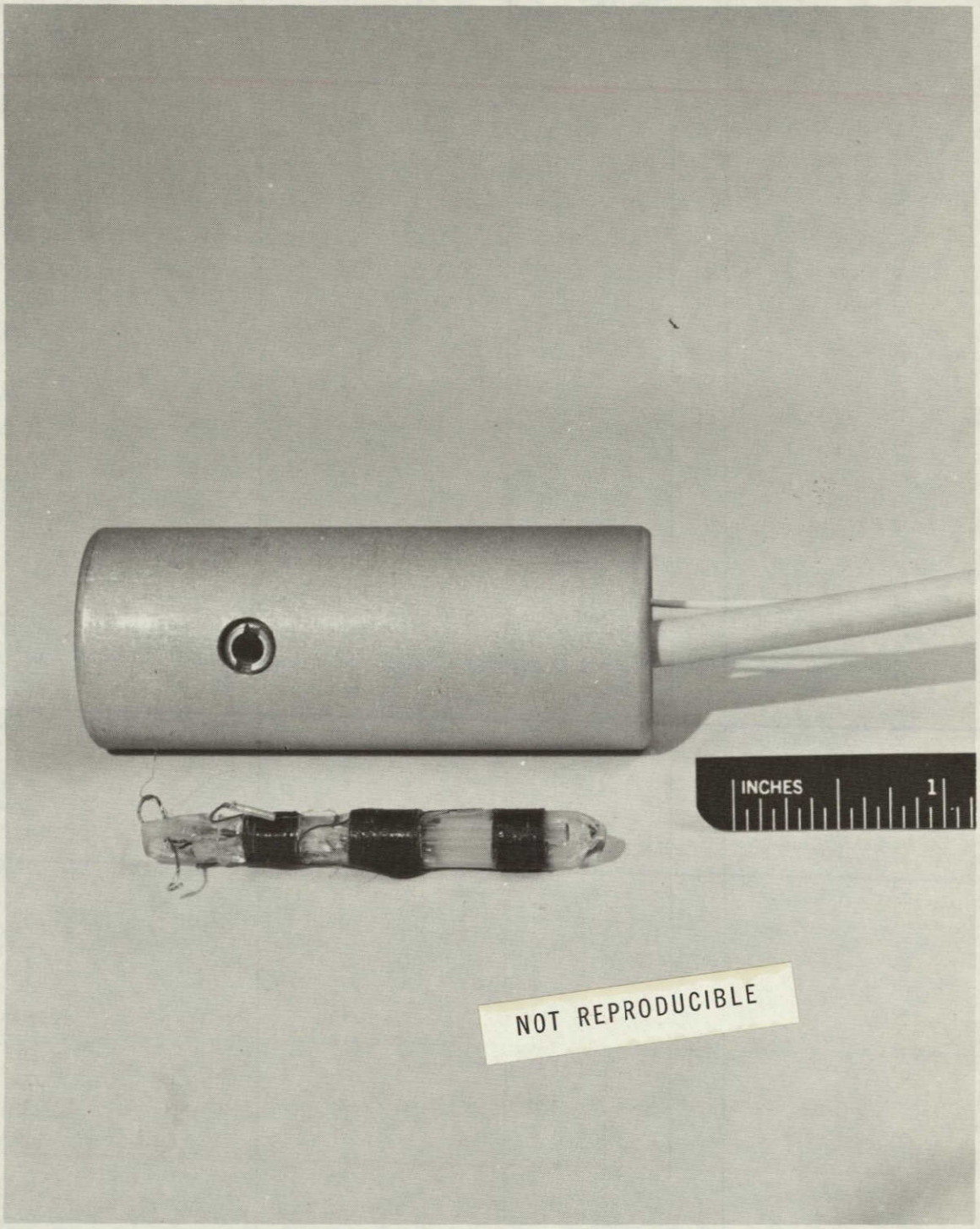

Figure 46. Celescope mercury calibrator assembly and its gas-discharge tube with heater wires.

Table 24. Estimated total operating time for mercury calibrators.

Camera	During ground test			In orbit				
	Estimated average on-time per exposure (sec)	Estimated number of exposures	Estimated operating time during ground tests	Estimated average warmup time per exposure (sec)	Estimated average exposure time (sec)	Estimated number of exposures	Estimated operating time in orbits	Estimated total operating time (hr)
1	360	500	18,000 sec = 300 min = 50 hr	300	48.9	3319	1,157,999.1 sec = 19,300.0 min = 321.7 hr	371.7
3	360	500	18,000 sec = 300 min = 50 hr	300	47.9	1826	635,265.4 sec = 10,587.7 min = 176.5 hr	226.5

Table 25. Calibrator-image detection in later orbits.

a) The last known calibrator images identified by the standard data-processing system

Camera	Contact	Estimated total operating time (hr)	K	L	Σ	I_p
1	M5240	231.8	155	136	19	12
3	R3364	166.7	143	141	64	17
4	R7261	90.2	130	127	174	13

b) The last known calibrator images recognizable by trained personnel

Camera	Contact	Estimated total operating time (hr)	K	L	Σ	I_p
1	R5510	241.2	162	136	13	8
3	O3700	178.4	144	133	29	13
4	R7261	90.2	130	127	174	13

F_1 = flux at temperature T_1 degree K,

F_0 = flux at temperature T_0 degree K,

k = a positive constant.

For Celescope, the values of k are reported as 0.63 and 0.39 for camera 2 and camera 4, respectively.

In the xenon calibrator lamps, the temperature is not controlled. Instead, the temperature is monitored by a thermistor temperature sensor. The true output flux for each observation is calculated from the measured temperature and the room temperature flux.

The expected change of the output flux from xenon calibrator lamps is negligible for at least 100 hr. Figure 47 shows the results of xenon-lamp life tests; Figure 48, the lamp assembly. The apparent change of output level is attributed to the degradation of the detector (photomultiplier) photocathode, rather than a change of output level. Independent studies of the output level with real calibrator lamps and power supplies indicate that apparent lamp degradation occurs only when the lamp is on and is in a vacuum system. Degradation will not occur at atmospheric pressure or in a vacuum with the lamp off. Furthermore, it appears likely that the window of the Uvicon that is being used as a photodiode is not being contaminated. This leads us to conclude that a charge condition exists on the front window of the lamp when it is on that causes it to attract contaminating particles when operated in a vacuum chamber.

Estimated operating time during Celescope operation for the xenon calibrator system is about 15 hr for camera 2 and about 90 hr for camera 4, as shown in Table 26. On the basis of the estimated operation time and deterioration characteristics, we may conclude that any apparent deterioration of calibrator output fluxes is caused by some other component deterioration — photocathode, target, optical transmittance, etc.

While on the subject, we will make some general comments about the calibrator lamps in the Celescope experiment. Their basic role is to relate ground-based calibration to orbital observation data and to determine the

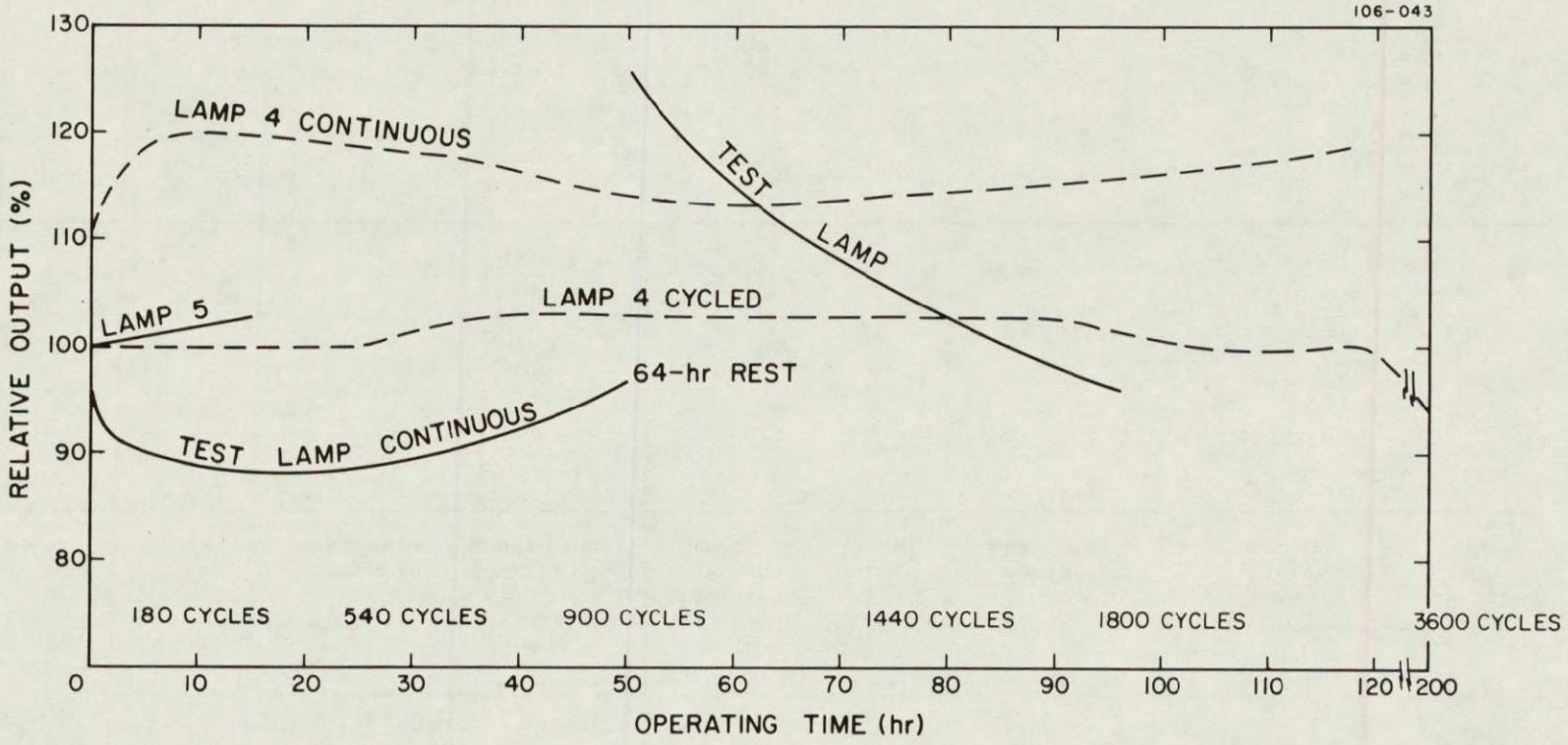

Figure 47. Relative output of xenon lamp as a function of operating time.

Table 26. Estimated total operating time for xenon calibrators.

Camera	During ground test			In orbit				
	Estimated average on-time per exposure (sec)	Estimated number of exposures	Estimated operating time during ground tests	Estimated average warmup time per exposure (sec)	Estimated average exposure time (sec)	Estimated number of exposures	Estimated operating time in orbits	Estimated total operating time (hr)
2	90	500	45,000 sec = 750 min = 12.5 hr	30	54.9	83	7,046.7 sec = 117.4 min = 1.96 hr	14.5
4	90	500	45,000 sec = 750 min = 12.5 hr	30	48.8	3535	278,558 sec = 4,642.6 min = 77.4 hr	89.9

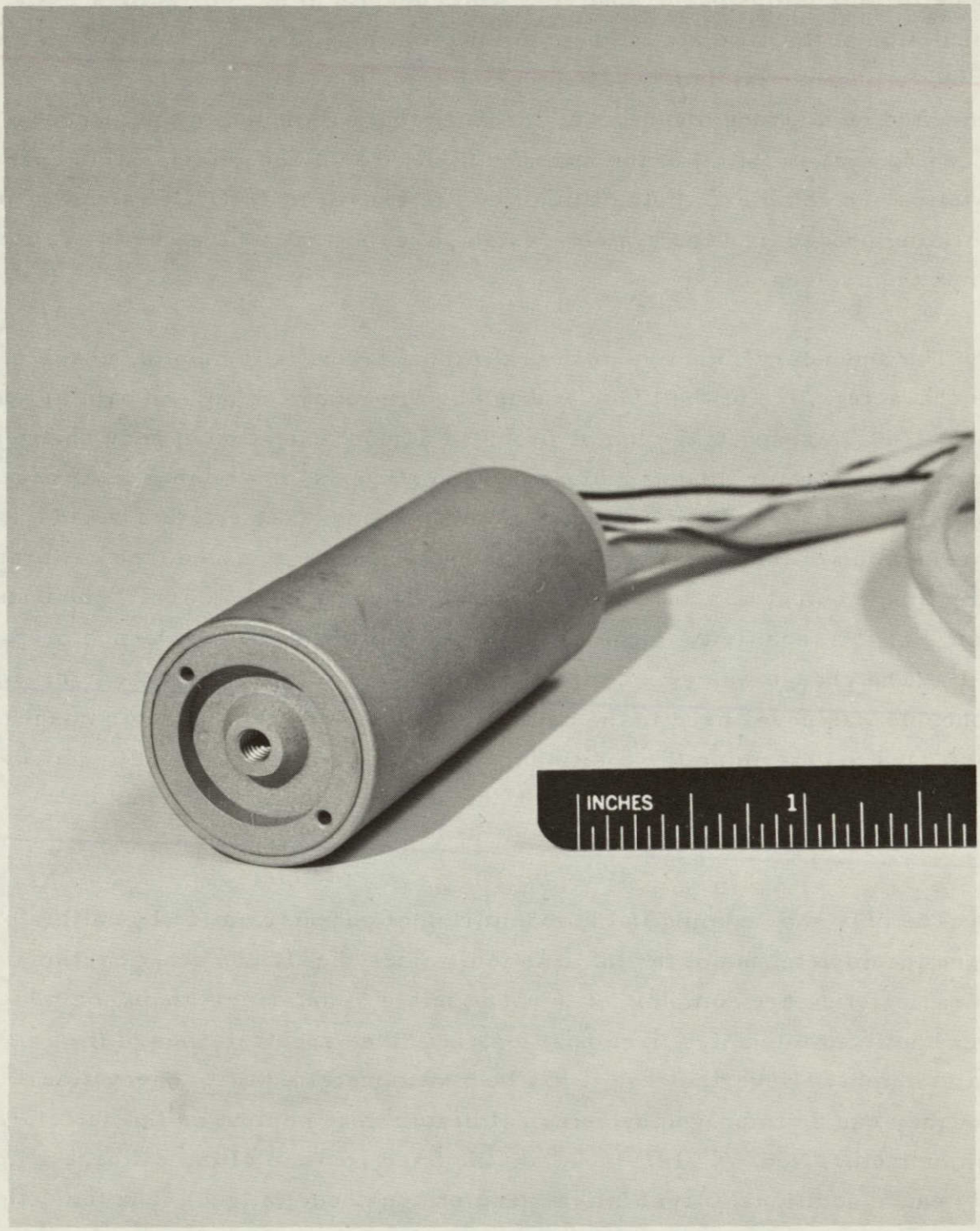

Figure 48. Celescope xenon calibrator lamp assembly.

absolute intensity (magnitude) of the observational data. In this respect, the calibrator lamps performed very well, despite minor difficulties in the calculation of the absolute intensity of observational data. These difficulties occurred because (a) data obtained during the initial operating period were contaminated by a strong magnetic disturbance that originated in the magnetic unloading system (MUS) of the spacecraft and (b) Uvicon deterioration characteristics are complex. Both difficulties are caused by OAO/Celescope system operating procedures and system-design philosphy rather than by the calibrator lamps themselves.

The secondary objective of the calibrator lamps is to monitor changes in the characteristics of the Uvicon tubes during ground testing and orbital operations. In this respect, the lamps provided a good indication of such changes. Output of calibrator images indicated the continuous, but slight, deterioration of the Uvicon sensitivity during ground testing and the rather rapid deterioration of the sensitivity during orbital operation. Also, the calibrator-lamp image output was successfully used to monitor and to correct the unusual change of the sensitivity in camera 4 during the last minute of launch preparation. (The change was self-corrected in orbital operation, and the correction technique was never used in the camera again.) And the calibrator images were used to determine the positional shifts of output images and to demonstrate possible methods of improving the accuracy of observational data (Nozawa, 1970).

The only shortcoming in the monitoring of characteristics by calibrators is the incompleteness of the information. Since the Uvicon deterioration characteristics are complex, it is not possible to determine them completely from the fixed intensity, fixed position, and fixed spectral lines of the calibrator lamps. Nevertheless, it has been demonstrated that observational accuracy can be improved by using calibrator image output as the deterioration indicator (Nozawa, 1969). Also, the fixed position of the calibrator image may cause additional target fatigue (and photocathode fatigue), and the deterioration of the calibrator image output may not be a good indicator for the Uvicon in general, especially for later operating period.

Problems associated with Celescope calibrator lamps are as follows:

1. Ghost images produced by calibrator lamps. These ghost images are believed to be caused mainly by imperfections of the pinhole mechanism in the lamp assembly. Some ghost may be caused by internal reflection of the calibrator light. Cameras 1 (see Figure 41a in Chapter 4) and 3 (see Figure 41b in Chapter 4) had calibrator-lamp ghosts.

2. Interference from Lyman-α emission. Since the calibrator lamps for the D-type Uvicons are located in the U_4 side of the faceplate, xenon calibrator images were contaminated by the background produced by the geocorona. Especially in longer exposure time, the calibrator image outputs become useless to determine changes in Uvicon characteristics.

3. Interference from electrical background. There is systematic electrical background noise in the output of camera 4. The noise is about 2 to 4 elements wide and runs vertically near the center of the picture (see Figure 33 in Chapter 4). Since the calibrator image of camera 4 is located approximately at the center of the picture (slightly upward), almost all calibrator images of camera 4 were contaminated by the vertical noise band. Because of problems 2 and 3, camera 4 calibrator images are much less valuable than expected.

In general, we can say that lamps made calibration possible in orbit and indicated the change of Uvicon characteristics, but were not sufficient to provide exact information on the time dependence of photometer response.

5.3 Deterioration of Optical Components

The effects of space radiation on the optical components were discussed in Section IV. If radiation damage had affected Celescope performance, the first evidence would have been a change in relative sensitivity of our U_1 and U_2 spectral regions induced by the characteristic wavelength-dependent change in transmittance of radiation-damaged lithium fluoride. The decay curves presented in Section IV indicate that this effect, if present at all, was a minor contributor to the total sensitivity change in the instrument.

Deterioration of optical surface quality is also possible in space. If it occurs, the general contrast in the picture decreases – that is, the background noise level increases. Electronic deterioration, which is also expected in space, can cause a similar increase of the background. Distinguishing between the two could pose a problem. However, since the general noise characteristics of the pictures did not change appreciably during the time the experiment was operated in orbit, we conclude that optical surface quality did not deteriorate in the space environment.

There are other forms of deterioration mechanisms, e.g., dimensional stability of the optics. If a structural member of the telescope shows dimensional instability, then the output image quality will be degraded. From observational data, we find no image-quality deterioration attributable to dimensional instability. One of the problems is the difficulty in separating optical image quality from electro-optical image quality. In general, we can say as far as we can determine, we cannot detect any optical-image deterioration.

5.4 Deterioration of the Electronics

Of the subsystems in the Celescope experiment, the electronics are the most unlikely to deteriorate. The reasons for this achievement are the following: (a) The mechanisms of deterioration in the electronic components are well understood, compared to those of other components. (b) The prime contractor, EMR, is an electronics-oriented company and has its "forte" in this area. (c) Major efforts were undertaken to design electronics of high reliability (Burkhalter, 1965).

The Celescope experiment package uses one of the first space-borne digital television systems. Failure of the logic circuits would be critical. Also, many commands had to be used for the operation of the experiment and for the onboard data-processing system coupled to the telemetry channels. Therefore, failure-proof design of the logic circuit was the greatest concern. To accomplish this goal, a special logic module was developed. The module was a quad-redundant transistor unit; a schematic is shown in Figure 49. The logic unit acts as a single transistor, but its calculated failure rate

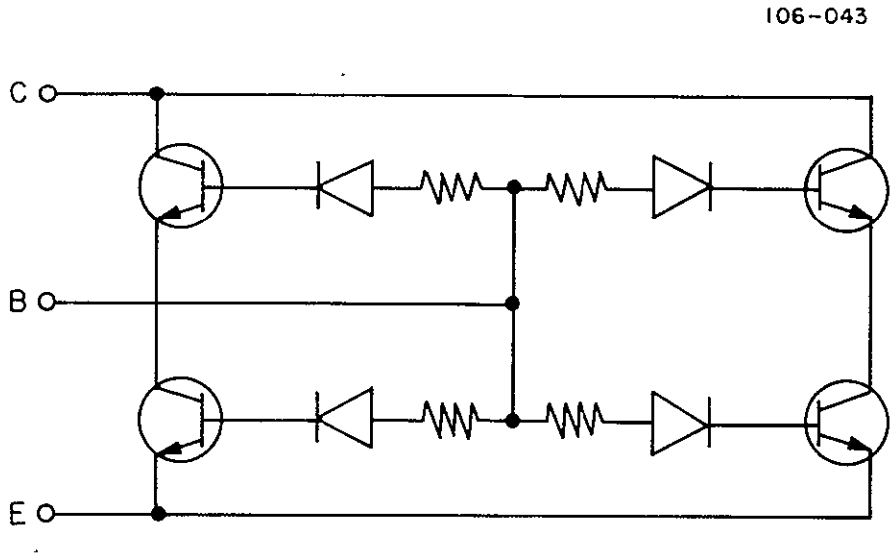

Figure 49. Schematic of basic logic unit used in the Celescope experiment.

reaches 2.46×10^{-9} by use of components with a failure rate of 5×10^{-8} to 1.7×10^{-7} (see Table 27). The other approach used in the Celescope experiment was a functional dual redundancy in the power supplies, camera chains, analog-to-digital converters, digital-sweep generators, output terminals, etc.

As far as we can determine, there has been no failure of the digital logic nor of the functional units. In the case of the dual-redundant functional units, we never needed to switch to a spare unit. Therefore, we can say that the reliability design of the electronics was a great success. Naturally, there were drawbacks:

1. Increased weight and volume,
2. Increased power consumption,
3. Reduced speed of unit, increased delay time,
4. Increased complexity of the experiment package,
5. Increased test and calibration time.

From orbital experience, the Celescope experiment electronics may be overdesigned compared to rest of the package.

The only known failure of the electronics was in the camera 2 video chain. The cause was target-material breakdown and resultant overloading of the video chain. The exact location of the failure was not determined, but only two locations seem possible: filament breakdown in the Uvicon or breakdown of the video preamplifier. If the former, it is still feasible to use the failed Uvicon tube as a photodetector for Lyman α (or for a similar very intense extended radiation source). However, investigation indicates that the failure is more probably in the preamplifier.

The change of gain in the electronics is not easily determined. This aspect is still being investigated and will be reported on later. Also, the increase of the background noise due to electronic deterioration is under investigation. Preliminary investigation indicates that there has been some increase of background noise as time elapsed; in particular, some kind of interference noise increased in the later orbits.

Table 27. Failure rates of logic unit used in Celescope.

Components	Projected failure rates
Transistor, small signal	1.7×10^{-7}
Resistor, metal film	5.0×10^{-8}
Diode, logic application	1.0×10^{-7}
If above three are combined as a logic unit	3.2×10^{-7}
Combined as quad-redundant basic Celescope logic unit	2.5×10^{-9}
Quad-redundant resistor unit	1.8×10^{-10}
If above two are combined as Celescope pulse inverter submodule	2.7×10^{-9}

In general, the effect of possible gain change and increase of background noise is minimal for the final accuracy of the measurements. Also, it is worthwhile to mention that the special scanning technique used in Celescope (superscan; see Chapter 2), performed its intended function perfectly, and there was no known failure. The pulse readout system, which is more popular now and which is more advantageous than superscan in some aspects, will be the method of future systems, but it should be noted that the superscan also had its advantages; slow scan rate with fast effective beam dwell time and without rapid switching of high voltages (beam-control voltages).

The conclusions of this section are the following: (a) The quad-redundance design in Celescope produced a reliable operation of the electronics package, at the cost of some power and weight, and (b) superscan readout performed well.

5.5 Deterioration of Uvicon Image Tubes

The most prominent system deterioration seems to be occurring in the Uvicon camera modules. The camera module consists of a Uvicon image tube, a preamplifier, deflection circuits, and a replaceable electronics package (REP), which has various resistors adjusted to match the common power supply to individual tubes. Also, optical filters are physically attached to the camera module. Deterioration outside the Uvicon tube, but still in the camera module, can be distinguished. (These results will be discussed in the pertinent sections.)

The Uvicon tube, which is a fairly complicated device, has many potential sources of deterioration: faceplate, photocathode, imaging section, target, readout beam current, and readout gun section. Almost every part of the Uvicon has a known or estimated mode of deterioration. Therefore, identification of the dominant mode of deterioration is very important for future evaluation of similar image tubes. The faceplate of the Uvicon, which is made of lithium fluoride, has been known to deteriorate from space radiation. Also, the photocathode may be damaged by intense input light. The imaging

section may show dimensional instability, which will cause defocusing. Or the imaging section may be influenced by surrounding structural material, which may be gradually magnetized over a long period of time. It is known that the target shows effects of fatigue in some circumstances, as well as the effects of aging.

Beam-current reduction is one of the most likely causes of Uvicon deterioration. Figure 50 shows the results of a life test for an electrostatic readout gun, very similar to the Uvicon gun. If we remember that the estimated operating time before launch is about 3000 hr for each Uvicon, the reason will be readily understood. Beam-current reduction and target aging will cause overall deterioration of the entire field of the output picture, in contrast to local deterioration of other types in the Uvicon.

Some aspects of Uvicon deterioration can be studied by using the calibrator-lamp output images. (Examples are shown in Figures 51 through 55.) To understand completely the deterioration characteristics of the Uvicon, all the observational data available must be studied. Since processing of star data is not yet complete, and since some of the deterioration studies are still continuing, the major analysis of this subject will be deferred to volume B of this report.

As a closing remark, it can be said that deterioration of the Uvicon is the most important parameter directly affecting the accuracy of Celescope measurements and that an understanding of the mechanisms involved is essential to an improvement of the accuracy. Since the basic characteristics of Uvicon are nonlinear and multi-parametric, deterioration of the Uvicon produces very complicated characteristics. Therefore, an understanding of basic mechanisms is not easy.

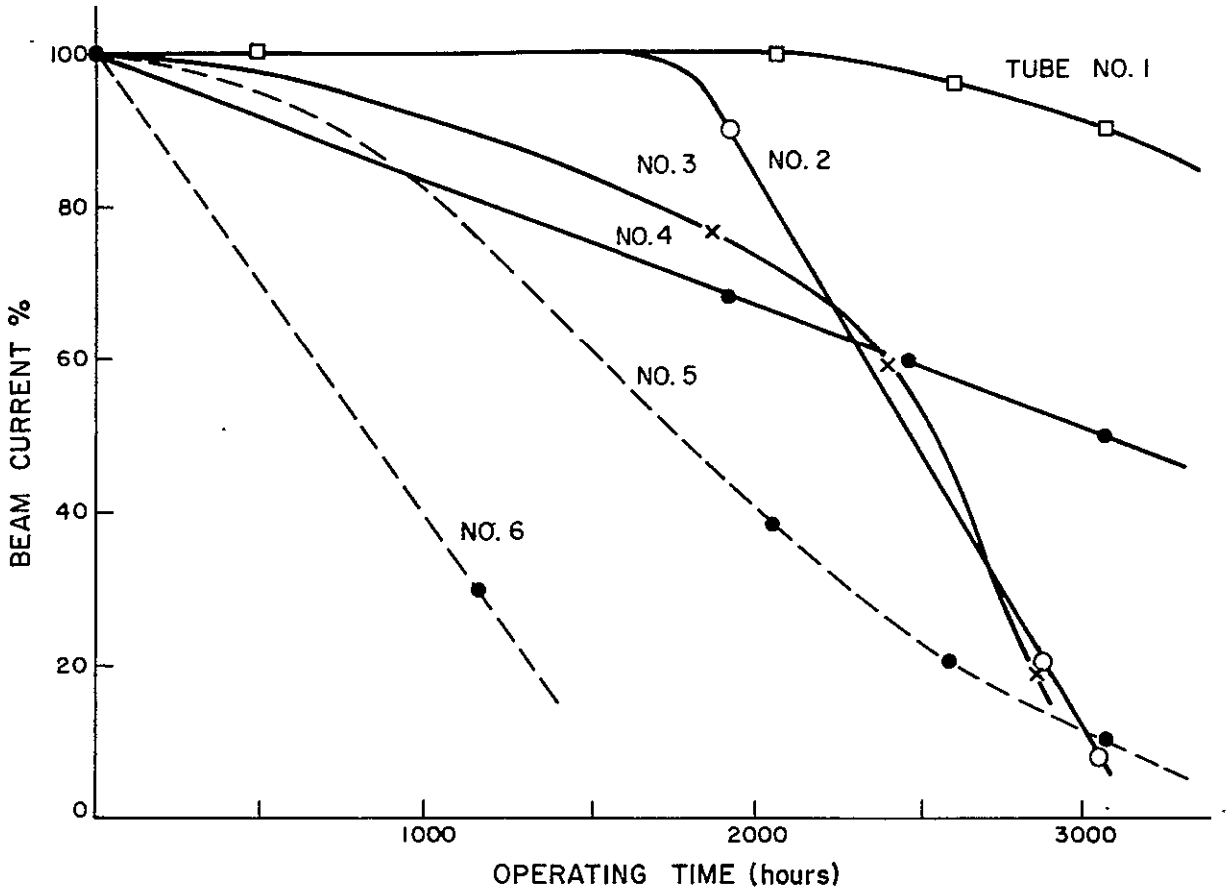

Figure 50. Difference of deterioration rates among Uvicon tubes.

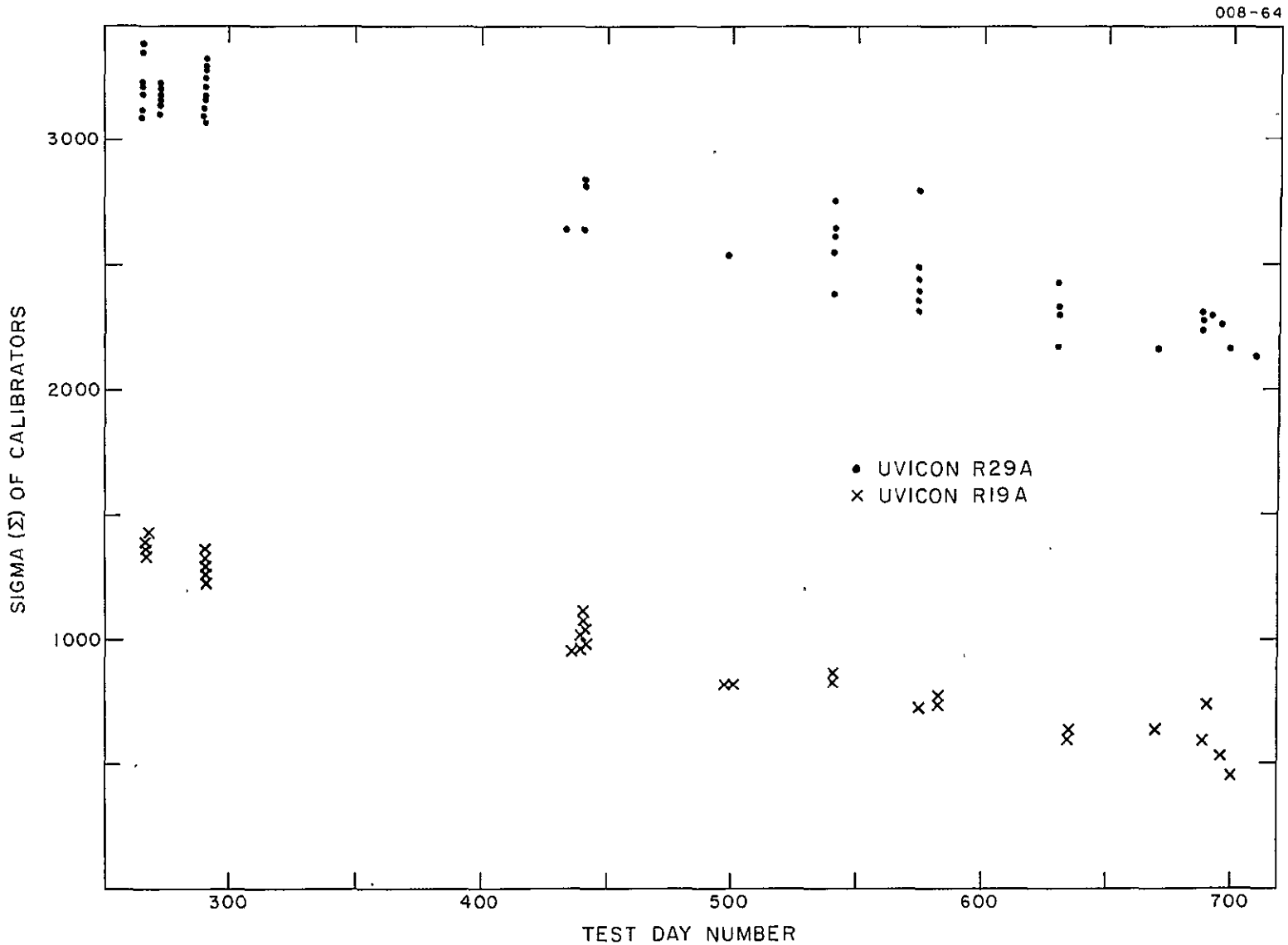

Figure 51. Changes of Sigma of calibrators during system test.

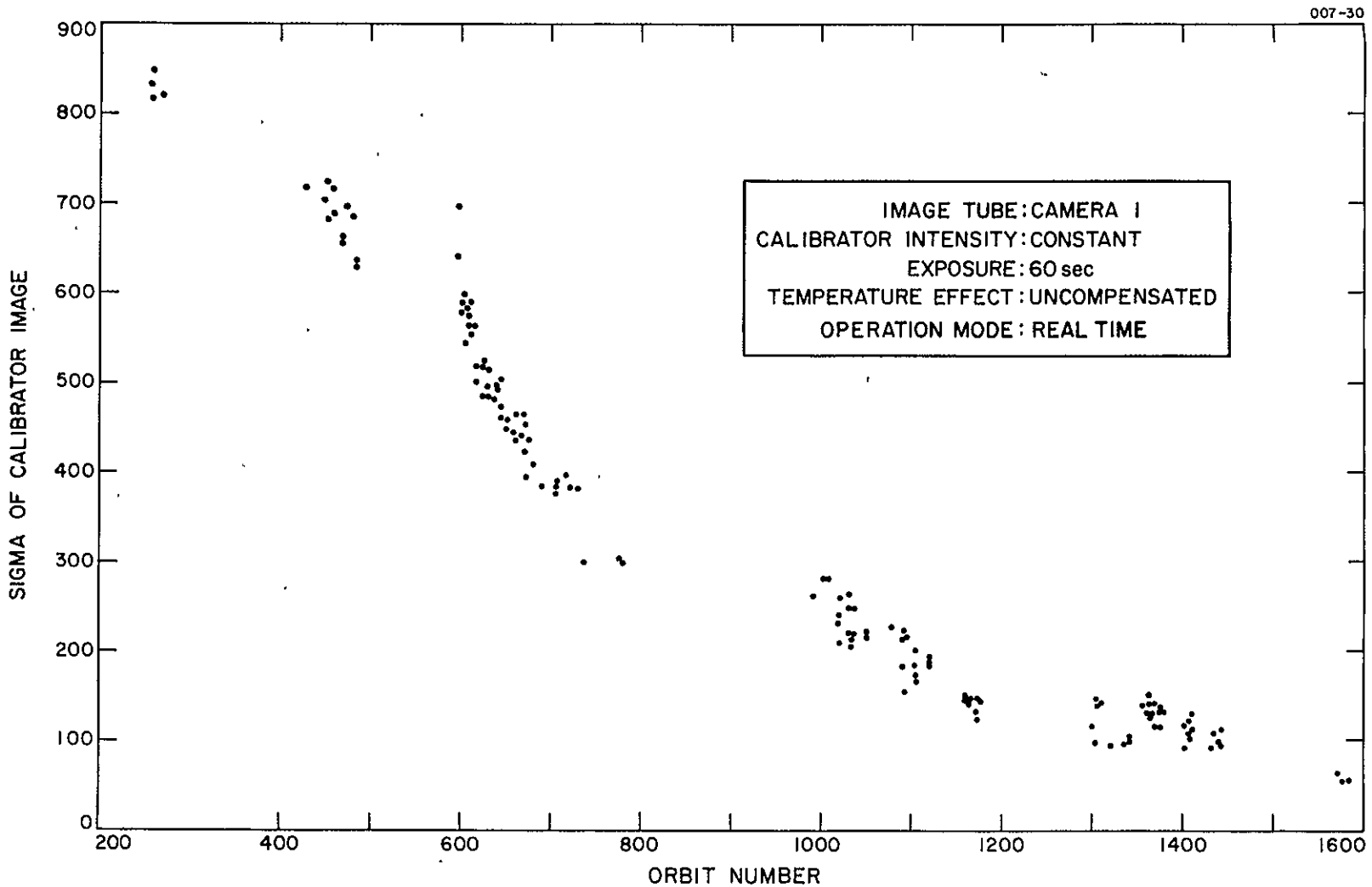

Figure 52. Deterioration of Uvicon sensitivity.

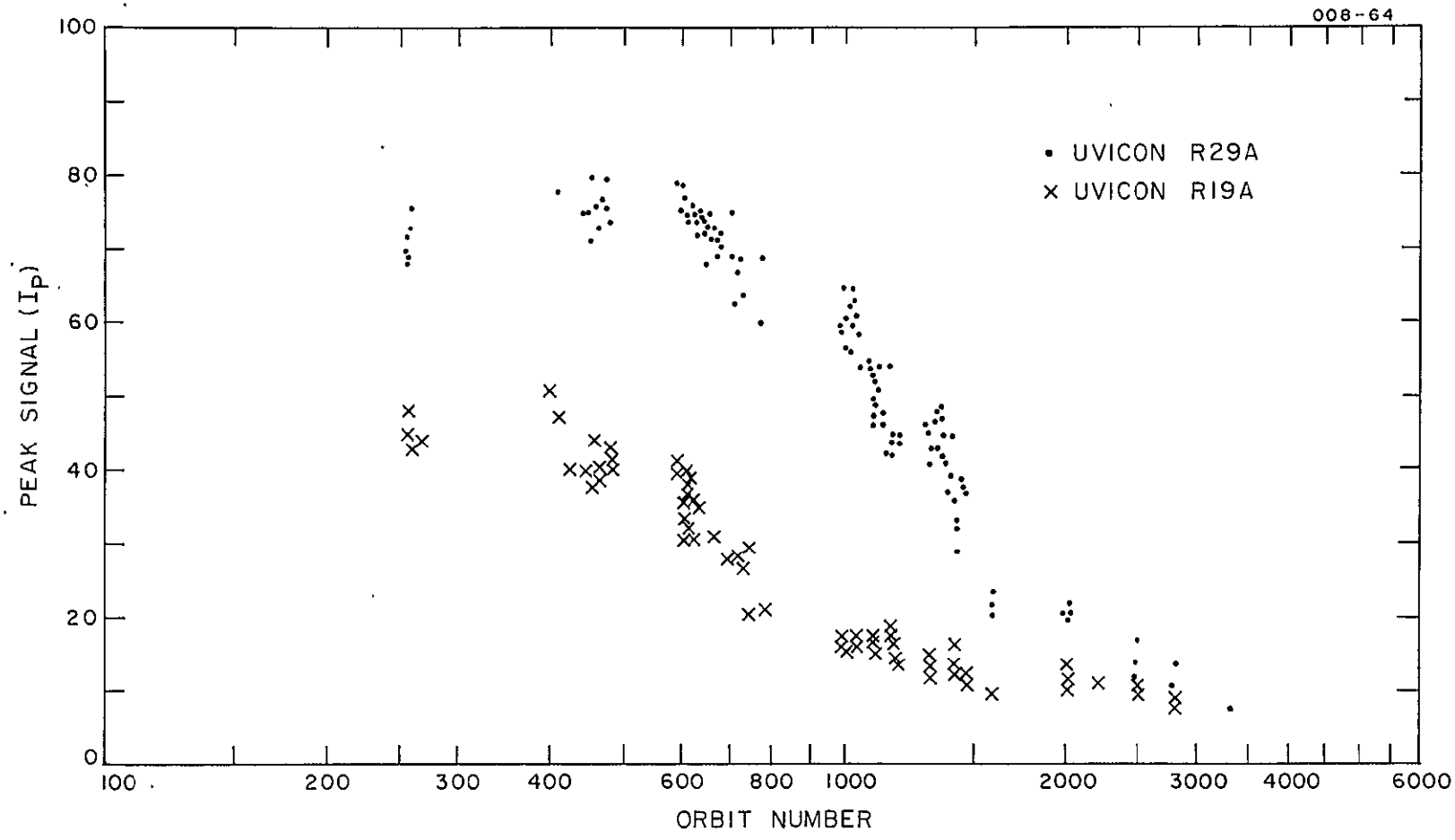

Figure 53. Changes of peak signal of calibrators.

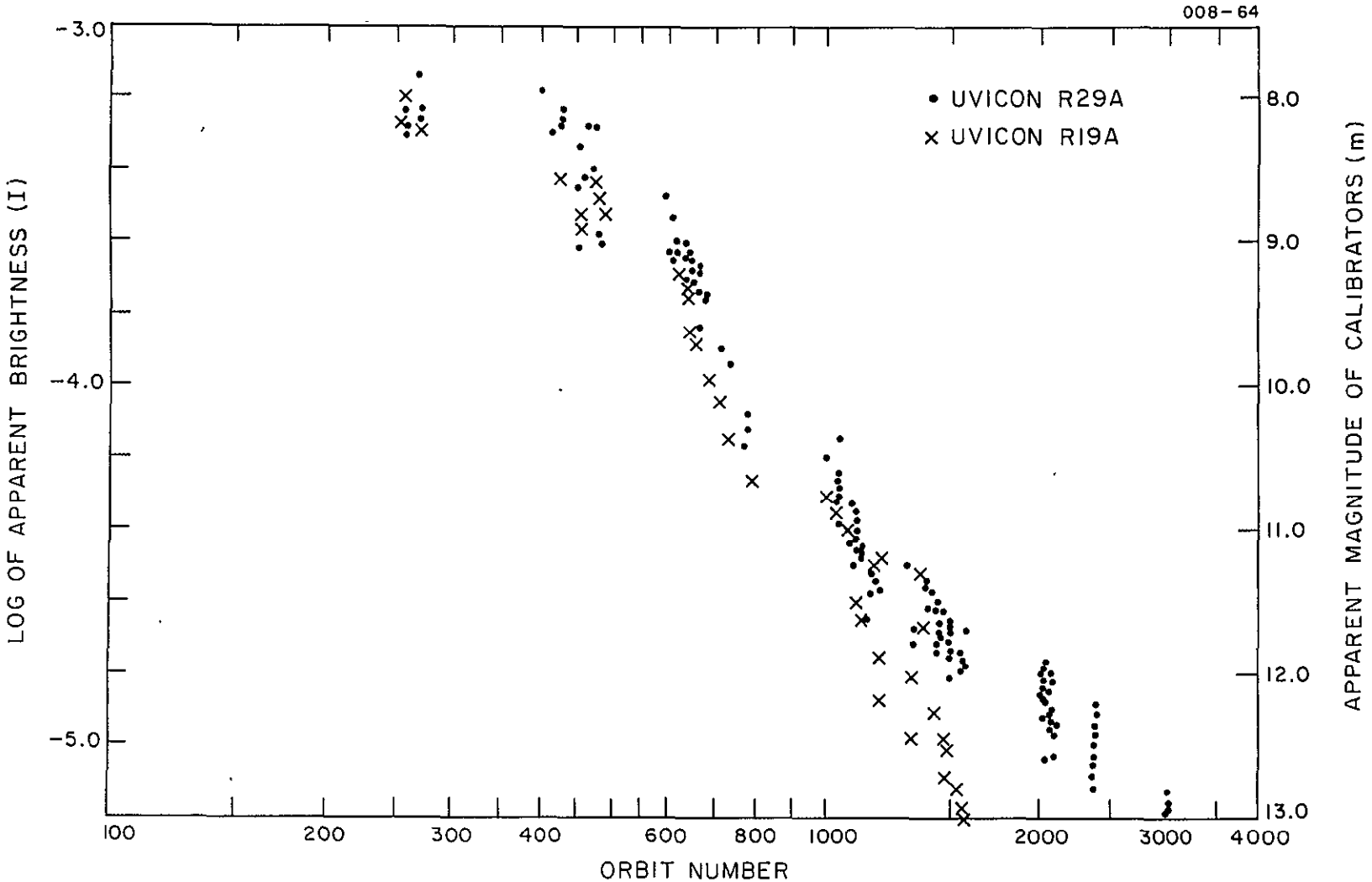

Figure 54. Changes of apparent brightness of calibrators.

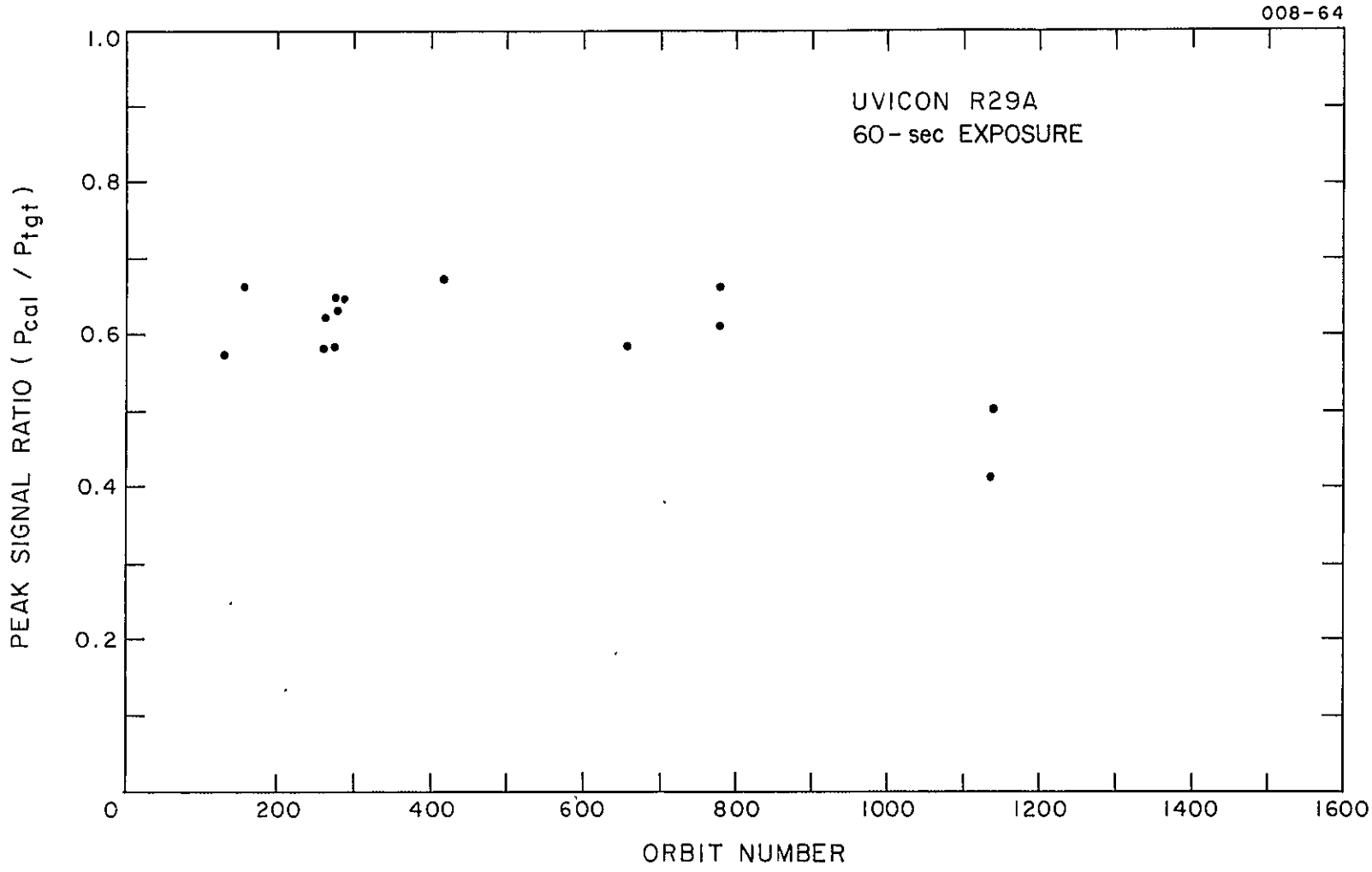

Figure 55. Change of peak ratio between target ring and calibrator images.

5.6 Conclusions

Although some subjects related to system deterioration are deferred to part B and to Section IV, the following conclusions can be reached:

1. Quad-redundancy design in Celescope produced a reliable operation of the electronic package, but at the cost of some increase of power and weight.

2. Superscan readout performed well.

3. Uvicon sensitivity during orbital operations decreased rather rapidly with time. Nevertheless, the useful life of the Celescope experiment significantly exceeded the prelaunch goal of 1 year in orbit for gathering scientific data.

4. The calibrator lamps proved to be valuable for providing a record of Celescope performance from the time the flight telescopes were first assembled, through all phases of subsystem and system testing, to well after launch.

5. The calibrator lamps carried initial calibration data into orbit but did not provide sufficient data for accurately establishing the time dependence of the photometer response.

REFERENCES

BEYER, R. R., and GOETZE, G. W.

1966. An optically scanned SEC camera tube. In Advances in Electronics and Electron Physics, vol. 22, ed. by J. D. McGee, D. McMullan, and E. Kahan, Academic Press, New York, pp. 241-250.

BOERIO, A. H., BEYER, R. R., and GOETZE, G. W.

1966. The SEC target. In Advances in Electronics and Electron Physics, vol. 22A, ed. by J. D. McGee, D. McMullan, and E. Kahan, Academic Press, New York, pp. 229-239.

BURKHALTER, W. R.

1965. A trade-off history for high reliability program. Journ. Elect. Div., ASQC, vol. 3, pp. 3-13.

DAVIS, R. J., and GODFREDSON, E. A.

1961. Optimum resolving power for an ultraviolet space telescope. Planet. Space Sci., vol. 5, pp. 207-212.

DOUGHTY, D. D.

1966. Ultra-violet sensitive camera tubes incorporating the SEC principle. In Advances in Electronics and Electron Physics, vol. 22A, ed. by J. D. McGee, D. McMullan, and E. Kahan, Academic Press, New York, pp. 261-271.

EMBERSON, D. L., TODKILL, A., and WILCOCK, W. L.

1962. Further work on image intensifiers with transmitted secondary electron multiplications. In Advances in Electronics and Electron Physics, vol. 16, ed. by J. D. McGee, W. L. Welcock, and L. Mandel, Academic Press, New York, pp. 127-139.

FILBY, R. S., MENDE, S. B., ROSENBLOOM, M. E., and TWIDDY, N. D.

1964. A new television camera, intended for scientific applications, having a very high sensitivity and good storage properties. Nature, vol. 201, pp. 801-802.

FILBY, R. S., MENDE, S. B., and TWIDDY, N. D.

1965. The detection of faint optical images by charge integration. II. A new television camera, intended for scientific applications, having a very high sensitivity and good storage properties. Intern. Journ. Electron., vol. 19, pp. 387-403.

1966. A television camera tube using a low density potassium chloride target. In Advances in Electronics and Electron Physics, vol. 22A, ed. by J. D. McGee, D. McMullan, and E. Kahan, Academic Press, New York, pp. 273-290.

GOETZE, G. W.

1962. Transmission secondary emission from low density deposits of insulators. In Advances in Electronic and Electron Physics, vol. 16, ed. by J. D. McGee, W. L. Wilcock, and L. Mandel, pp. 145-154.

1966. Secondary electron conduction (SEC) and its application to photoelectronic image devices. In Advances in Electronics and Electron Physics., vol. 22A, ed. by J. D. McGee, D. McMullan, and E. Kahan, Academic Press, New York, pp. 219-227.

GOETZE, G. W., and BOERIO, A. H.

1964. Secondary electron conduction (SEC) for signal amplification and and storage in camera tubes. Proc. IEEE, vol. 52, pp. 1007-1012.

GOETZE, G. W., BOERIO, A. H., and GREEN, M.

1964. Field-enhanced secondary electron emission from films of low density. Journ. Appl. Phys., vol. 35, pp. 482-489.

HEATH, D. F., and SACHER, P. A.

1965. Effects of a simulated high energy electron space environment on the ultraviolet transmittance of optical materials between 1050 and 3000 Å. NASA X-622-65-382, Goddard Space Flight Center, Greenbelt, Md.

LOWRANCE, J. L., and ZUCCHINO, P. M.

1961. Report on evaluation of television tubes for space astronomy. NASA Res. Cont. Rept. NSR 31-001-127.

MEIER, R. R.

1969. The hydrogen Lyman-α airglow. Astronaut. Aeronaut., vol. 7, pp. 68-75.

McMULLAN, D., and TOWLER, G. O.

1969. Some properties of SEC targets. In Advances in Electronics and Electron Physics, vol. 28A, ed. by J. D. McGee, D. McMullan E. Kahan, and B. L. Morgan, Academic Press, New York, pp. 173-188.

NOZAWA, Y.

1966. A digital television system for satellite-borne ultraviolet photometer. In Advances in Electronics and Electron Physics, vol. 22, ed. by J. D. McGee, D. McMullan, and E. Kahan, Academic Press, New York, pp. 865-874.

NOZAWA, Y.

1969. Overcoming system deterioration in a satellite-borne television photometer. 1969 Proc. Electro-Optical System Design Conf., pp. 585-593, Industrial and Scientific Conference Management, Inc., Chicago, Ill.

1970. Accuracy of an orbiting television photometer. 1970 Proc. Electro-Optical System Design Conf., pp. 905-920, Industrial and Scientific Conference Management, Inc., Chicago, Ill.

NOZAWA, Y., NEWMAN, P. A., and WALLGREN, K. R.

1970. Effects of space radiation on the SEC image tube. National Aerospace Electronic Conference (NAECON) Record, vol. 22, pp. 67-71, IEEE.

NOZAWA, Y., and TUCKER, B. J.

1966. Digital video data transmission system for photometric television. Supplement to the IEEE Transactions, Aerospace and Electronic System, vol. AES-2, pp. 388-391.

SCHNEEBERGER, R. J., SKORINKO, G., DOUGHTY, D. D., and FEIBELMAN, W. A.

1962. Electron bombardment induced conductivity including its application to ultra-violet imaging in the Schuman region, In Advances in Electronics and Electron Physics, vol. 16, ed. by J. D. McGee, W. L. Wilcock, and L. Mandel, Academic Press, New York, pp. 235-245.

SLARK, N. A., and WOOLGAR, A. J.

1962. A transmission secondary emission image intensifier. In Advances in Electronics and Electron Physics, vol. 16, ed. by J. D. McGee, W. L. Wilcock, and L. Mandel, Academic Press, New York, pp. 141-143.

WACHTEL, M. M., DOUGHTY, D. D., and ANDERSON, A. E.

1960. The transmission secondary emission image intensifier. In Advances in Electronics and Electron Physics, vol. 12, ed. by J. D. McGee and W. L. Wilcock, Academic Press, New York, pp. 59-71.

WACHTEL, M. M., DOUGHTY, D. D., GOETZE, G. W., ANDERSON, A. E., and STERNGLASS, E. J.

1960. Image intensification by transmission secondary electron emission. Rev. Sci. Instrum., vol. 31, pp. 576-578.

WILCOCK, W. L., EMBERSON, D. L., and WEEKLEY, B.

1960. Work at Imperial College (London) on image intensifiers with transmitted secondary electron multiplication. Proceedings of the Seventh Scintillation Counter Symposium, Trans. Inst. Radio Engings. Ns-7, No. 2-3, pp. 126-132.

SECTION III

DESCRIPTION OF CELESCOPE EXPERIMENT AND RECOMMENDED CHANGES FOR FUTURE EXPERIMENT

S. D. Bass and R. Davies

This article was prepared by Mr. S. D. Bass and Mr. R. Davies of the EMR Telemetry Division, Weston Instrument Inc., a Schlumberger Company. As key personnel of EMR, the prime contractor of the experiment package, both were heavily involved in the development of Celescope. The article presented here is not altered in any way except for minor editorial changes. Therefore, the opinions expressed here are not necessarily those of Smithsonian Astrophysical Observatory nor that of its Staff.

DESCRIPTION OF CELESCOPE EXPERIMENT AND RECOMMENDED CHANGES FOR FUTURE EXPERIMENT

1. EXPERIMENT DESCRIPTION

1.1 General

The Celescope experiment consists of two separate, but functionally integrated, major subassemblies: the Celescope Optical Package and the Bay E-4 Module Assembly. For purposes of describing its functional operation, however, the experiment may be more properly divided into basic subsystems: the optical and the electronic.

1.2 Optical Subsystem

1.2.1 Primary optical system

The optical subsystem consists of four Schwarzschild-configured telescopes, each having a diameter of 12.5 in. The secondary mirror obscures an area of 6.5-in. diameter of each aperture. The system is designed for point infinity; therefore, the incoming light flux is a parallel (collimated) light beam. The light is reflected by the primary mirror (hyperboloidal) and brought to focus at a point beyond the plane of the intercepting secondary mirror. The secondary mirror (oblate ellipsoidal) in conjunction with Uvicon faceplate lens, focuses the light at a surface coincident with the photocathode surface of the faceplate of the Uvicon camera tube.

The field of view of each telescope is determined by the active area of the image tube photocathodes and is nominally square with an equivalent angular subtense of $2° \times 2°$. Each telescope tube is designed to compensate passively for optical defocusing caused by thermal expansion and contraction.

The use of titanium as tube material, in conjunction with an aluminum alloy for the camera-tube housing, compensates for defocusing effects over a 100°C temperature change.

This wide temperature range required the development of a unique mounting system to prevent sinking of spacecraft heat, yet also to provide good shock and vibration isolation.

The field of view of each Uvicon is optically split into two areas of different sensitivity by mounting two different semicircular filters in the focal plane of the photocathode. The filter split line is oriented parallel to the direction of the television scanning lines and the Z_c axis of the OAO spacecraft. The calibration optical subsystem is oriented in such a manner that the filter split line does not intercept any light from the test source.

Further spectral selectivity is achieved by the use of two types of Uvicon: A and D. They differ only in their photoemissive surfaces. The type-A is sensitive between 1050 and 3200 Å, and the type-D between 1050 and 2000 Å. The resulting spectral responses can be seen in Figure 1.

This configuration of two tube types and split filters offers excellent redundancy since half the tubes (one A and one D) can supply full spectral data. Survival of any one camera would still supply one half of the desired data.

1.2.2 Calibration optical system

The calibration optics of the optical subsystem consist of a calibration lamp (with controlled and calibrated emission characteristics), apertures (to simulated star point sources of ultraviolet intensity), and a mirror and lens located in the aperture of the secondary mirror of each telescope. The point source of light from the calibration lamp and aperture is reflected by a mirror, 45° off the plane normal to the optical axis of the telescope, through a lens that brings the light from the simulated stars to focus at the plane of the faceplate lens.

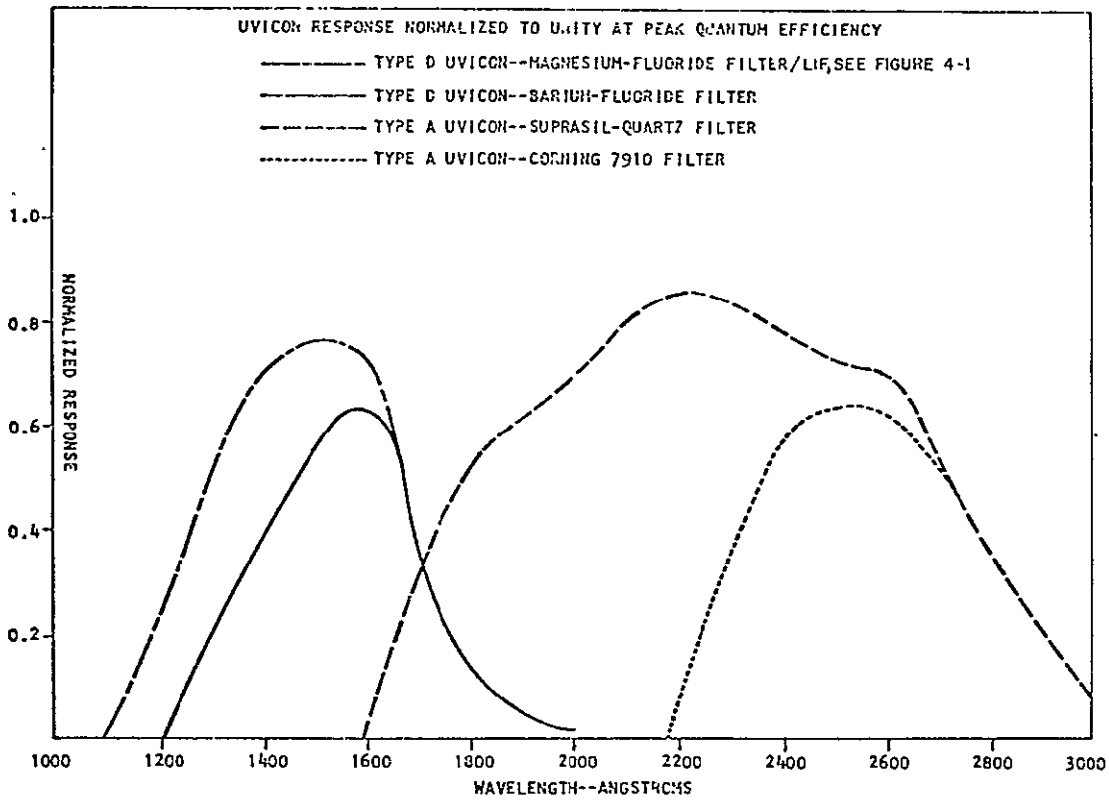

Figure 1. Typical spectral response characteristics of Uvicons.

The calibration optical subsystems operate from light sources that emit energy at either a 1470 or 2537 Å.

The 1470-Å xenon discharge lamps and associated components are used with type-D Uvicons. The 2537 Å mercury vapor discharge lamps and associated components are used with type-A Uvicons.

1.3 Electronic Subsystem

1.3.1 General

The electronic subsystem of the SAO experiment incorporates command and control functions for the operation of the SAO experiment. No command functions are incorporated into the system for mechanical adjustment or operation, as the design of the SAO experiment is such that the telescopes will remain in satisfactory focus under the anticipated environmental conditions. The television camera tubes are effectively exposed to ultraviolet energy only when high voltage is applied to the imaging section of the tube; thus, no mechanical shutter is required.

1.3.2 Uvicon camera*

In this system, exposure to ultraviolet light and scanning of the target are never performed simultaneously. As exposure is controlled by high-voltage on-off commands, the sensitivity of the system can be adjusted by varying the exposure time (the time during which high voltage is applied to each camera). The high-voltage commands energize three high-voltage potentials from 7 to 8 kV. These voltages are tailored for each Uvicon to produce optimum image-section focus.

*Unipotential, fixed-focus SEC Vidicons have been developed since the design of Celescope and have been incorporated into several digital TV systems.

Each camera module is provided with a high-voltage power supply (HVPS). The assembly techniques and materials technology used in the manufacture of this supply resulted in one of the significant developments of Project Celescope. The HVPS is reliable and virtually impervious to the hostile environments of space. The HVPS has demonstrated a capability of operating from sea level to high vacuum and during drastic temperature change (+25°C to -55°C).

As a result of this exposure, an electrical-charge (star-image) pattern is built up on the target of the Uvicon camera, each star image is represented by a small area on the target whose charge is a result of the product of the exposure time and the intensity of the flux imaged by the experiment optics onto the photocathode of the camera.

To convert the star image on the target into a video signal, the target must be scanned (read out) by an electron beam. The readout mechanism involves replacement of electrons on the charged areas of the target.

The target can be damaged and effectively destroyed, if the potential on the target exit surface (scanned surface) is allowed to increase indiscriminately. Certain conditions of operation can cause the emission from a target element of more electrons than they deposit crossover. This condition, if allowed to continue, will further increase the surface potential at discrete points on the target to the level where electrical breakdown will occur between the exit surface and the backplate of the target, and holes will be punctured into the target.

Various camera-operation techniques developed for this experiment virtually eliminate the possibility of destruction from crossover. Westinghouse Electric Company, pursuing this problem further, has since developed an SEC Vidicon employing a suppressor mesh that limits the exit-surface potential below crossover. The use of such a tube in the Celescope system would have eliminated complicated and time-consuming camera-operating techniques.

This replenishment of electrons is capacitively coupled to the target backplate. The video signal at this point is in the microampere region, and a video preamplifier is used to condition this signal for transmission outside the camera package. The video preamplifier provides low-noise high-gain amplification of direct Uvicon output signals. The unit is a transistor-type amplifier and has a gain of 1.7 mV per 1.0 na input adjusted for minimum noise with typical operating bandwidth of 60 to 80 kHz.

Further amplification of the video signal to a level necessary for digital encoding or synch mixing is accomplished in the video amplifier. It is a three-stage voltage amplifier with a 170 kHz bandwidth, producing a gain of 100 to 2000 (adjustable by trimming during manufacture) at a maximum output voltage of 8 V.

1.3.3 Operating modes

The scanning beam can be deflected either analog or digital. The analog scan is a 300-line raster with a 1.6-msec sweep duration and a total 0.48-sec scan time. The digitally swept beam is functionally more complex than the analog; however, the readout process at the target is the same. The digital deflection initiates a digitally indexed scanning beam equivalent to an element-by-element scan, 256 elements per line and 256 lines, and a scan time of 10.5 sec. The resultant dwell time per element (160 μsec) is excessive, causing beam pulling and resultant low peak-signal amplitude.

A unique unblanking technique known as superscan was employed in this experiment to eliminate these problems. The beam is positioned well into the previously readout area for all but the short period of time (less than 10 μsec) during which the video is being sampled.

It is to be noted, however, that the beam is always on. Should the previously readout area in which the beam is dwelling be above the first crossover point, this dwell will aggravate the condition. Analog operation is, therefore, an obviously safer operating mode.

More recent EMR-T digital TV systems have successfully employed beam blanking that eliminates dwell problems and allows ultraslow and asynchronous readout techniques.

The resultant video signal (in either mode) is then transferred to the Bay E-4 module assembly for processing in either ANALOG, PCM, or STORE mode before transmission (or storage) by the OAO spacecraft data-handling system.

In the ANALOG mode, the signal from the Uvicon is amplified and mixed with synchronization signals (resulting in a composite video output) for transmission. In both PCM and digital STORE modes, readout is accomplished in digital sweep mode in the Uvicons. In the PCM mode, the video output of the camera is sampled and encoded to 7-bit accuracy. Each line of data has a fixed sync code and the line (vertical position) number in the first 5 PCM words and 251 intensity words. The entire data train is transmitted in real time as PCM telemetry data. In the STORE mode, only data that exceed a preselected threshold are encoded. Each data word in this mode is comprised of 8 bits of horizontal (element) position data, 8 bits of vertical (line) position data, 7 bits of intensity data, and 2 zero bits. Whenever the intensity of a star exceeds the preselected threshold level, the experiment generates a Store Digital Data Word Command 1 (SDDWC1) transfer pulse, which is used to load each STORE-mode data word into the spacecraft PPDS.

2. CELESCOPE EXPERIMENT DESIGN

2.1 General

The basic approach selected for obtaining the experimental measurements was television photometry. Details of the experiment design have been given in SAO Special Report No. 110 and in the foregoing section. The Uvicon television sensors were developed and manufactured by Westinghouse Electric Corporation at Pittsburgh, Pennsylvania, and Elmira, New York. The

telescope optics were manufactured by Ferson Optics, Inc., Ocean Springs, Mississippi. The overall experiment designs, integration, and tests were performed by Electro-Mechanical Research, Inc., of Sarasota, Florida.

2.2 Significant Accomplishments

In addition to the collection and analysis of the experimental data, there were a number of significant accomplishments in the basic engineering, manufacturing, and testing of the hardware. A summary of these accomplishments follows. Detailed engineering reports for all project activities are on file at SAO.

2.2.1 Optical system manufacture and testing

The figuring and testing of the 12-in. Swhartzschild optical systems proved to be a formidable task. By careful matching of primary-secondary pairs and extensive photographic investigation of the focal plane of each instrument, the system was figured and adjusted to meet the experiment requirements.

2.2.2 Telescope structure design

A light-weight, thermally compensated, fixed-focus design was achieved by the use of a corrugated titanium tube for the outer structure and an aluminum sensor holding structure. This design met the experiment requirement over the temperature range of -70°C to +40°C. The titanium structure was epoxy bonded and foam filled between corrugations for vibration damping. A straight four-vane support for the secondary had a very high-of-torsional resonance but proved satisfactory. The only builtin optical adjustments were of the secondary location and the sensor location. The secondary adjustments were difficult but proved stable in the kinetic environment. The sensor adjustment was not a problem. The overall mechanical system stayed in good alignment through launch and for the life of the experiment.

2.2.3 The Uvicon sensor

The Uvicon developed for this experiment was the forerunner of the SEC Vidicons that have been used in many commercial and military applications. The chief advantage of these sensors over other types available were their excellent long-term integration properties and very good single-scan readout properties. These when added to the electron amplification of the high-voltage section of the tube, plus the optical collection system, yielded a very high information bandwidth and photon sensitivity factor for the overall experiment.

2.2.4 High-voltage technology

The design, fabrication, and test techniques used for the 8 to 10 kV high-voltage system are believed to be unique and were very successful on ground and in the space environment.

2.2.5 Electronic system

The experiment represented about the ultimate in discrete-part, solid-state electronics. Wide use was made of redundancy at the part level, at the subsystem level, and at the system level. Low power was also a major design factor. The excellent orbital operating history of the electronics proved the validity of the design concepts.

2.2.6 Noncontamination of optics

Through test failures and analyses, procedures were developed for achieving low outgassing of the experiment. The most significant factor was absolute minimization of polymeric-coated surface areas (especially black paint). A technique for sandblast finishing of metal surfaces was used to achieve ultraviolet black.

2.2.7 Digital TV

The use of digital scanning of the sensors (256 × 256 raster) and non-compressed serial PCM transmission of the video signal was the primary mode of operation. A special elemental scan technique termed "superscan" was developed to enhance the readout signal-to-noise ratio of the sensor. To avoid long strings of zeros in the PCM signal, alternate bits were complemented. The overall performance of digital TV in this experiment was highly satisfactory.

2.2.8 Optical calibration system

The mercury and xenon calibration systems operated satisfactorily throughout the experiment. The xenon-gas tube was especially designed for this experiment.

2.2.9 Data handling and experiment calibration

The data analysis and experiment calibration techniques developed by SAO must be listed as a major accomplishment. The data accuracy was improved many fold by these efforts.

2.3 Recommended Changes

In the event that a similar experiment is undertaken, the following changes in design concept should be considered.

2.3.1 Optical system

The Schwartzschild system was selected for its good image quality over a wide area in the focal plane and for its low sensitivity to element placement. The system, however, is difficult to figure and to adjust and is thus costly. In retrospect, the optical-image quality may have been somewhat better than the resolution characteristics of the Uvicon. It is believed that a tradeoff

study, with the sensor properties known, may show that a simpler, less expensive optical system would be adequate.

2.3.2 Telescope structure design

No particular structural changes are recommended — the design worked well. However, thermal design improvements are needed to keep the sensor and sensor electronics from getting as cold as they did in the Celescope design and to reduce open-end heat losses.

2.3.3 The Uvicon sensor

The basic problem in the Uvicon that must be corrected is the self-destruct mode known as crossover, which resulted in the destruction of one tube in orbit. New SEC devices employ an additional grid to protect the tube from this type of damage. Reduced cathode emission resulted in the premature loss (in 4 months) of one other tube in orbit. Improved beam-current measurement and control circuits are needed to overcome this problem. Consideration should be given to the use of ultraviolet-to-visible converter surface with visible sensors, as opposed to ultraviolet sensors as used in this experiment — costs could thus be considerably lowered.

2.3.4 High-voltage system

No particular changes are recommended in this area.

2.3.5 Electronic system

The size, weight, and cost of the Bay E-4 electronic module could be reduced by a factor of 5 to 10 with modern integrated circuits. In fact, it would be possible and desirable to integrate E-4 into the optical-subsystem structure. Subsystem and system redundancy of about the level employed in Celescope would still be required to maintain overall reliability.

In future designs, the command-system interface with the experiment should be simplified in terms of the number of wires. The wire and connector costs far exceeds those of today's integrated circuits.

Another significant simplification of the electronic system could be achieved by elimination of the analog-scan mode and the digital-store mode. These were seldom used.

The concept of one command for each experiment operation is highly flexible, but far too costly in number of commands. The use of fixed operation sequences in the experiment is recommended, with command selection of the desired sequence.

2.3.6 Noncontamination of optics

No particular changes are recommended here, except perhaps that project planning and administration should heavily stress the importance of a good anticontamination program.

2.3.7 Digital TV

The availability of microcircuits and microelectronic storage devices makes it desirable to consider the use of compressed TV in future experiments to reduce the time required for each picture sequence.

In addition, improved methods of remote operation are required so that the experiment can be operated throughout the orbit. Compression-improved data storage and improved command storage are required.

2.3.8 Optical calibration system

A calibration system that includes the primary and secondary optical surfaces should be considered. Also, it would be desirable to check more of the sensor field with the orbital calibration system.

2.3.8 Data handling and experiment calibration

It is believed that considerably greater emphasis must be placed on engineering a more accurate TV photometer for future experiments.

Three main areas require improvement:

1. Uniformity through the field,
2. Measurement repeatability,
3. Measurement temperature sensitivity.

SECTION IV

REVIEW OF CELESCOPE DATA-PROCESSING PROGRAMS AND CALIBRATION PROCEDURES

W. A. Deutschman

REVIEW OF CELESCOPE DATA-PROCESSING PROGRAMS AND CALIBRATION PROCEDURES

1. INTRODUCTION

This section of the performance evaluation report discusses the data-processing system and the associated orbital calibration data for the experiment. First, I will outline a number of conclusions that we were able to determine from the analysis of the data. Section 2 discusses our final data-processing system. The orbital calibration data are discussed in Section 3. Section 4 describes the way we used the data to calibrate the cameras. Finally, Section 5 discusses phenomena that affect the accuracy of the data. This section will not provide a detailed description of the programs nor will it delve into the theory of the calibration effort. Both these subjects will be covered elsewhere. From my analysis of the data, I was able to reach the following conclusions:

1. Calibration of the experiment in orbit was possible and necessary. We were able to reduce the weighted RMS magnitude deviation for all cameras to under 0.2 mag.

2. The photometric accuracy of a television system is satisfactory if proper attention is paid to the data-reduction system and the in situ calibration of the system.

3. The time-decay characteristics of the cameras were determined by repeatedly observing standard areas. A linear correction in observed magnitude was the best correction rather than a nonlinear correction to the beam current.

4. The choice of two filters for each camera provided necessary redundancy, but a significant amount of data in the center of the camera had a composite filter-transmission curve and were rejected for that reason.

5. The initial review and correlation of the data were unnecessarily complicated because all the pertinent data were not on the same data channel.

6. Calibration and data collection must be an integrated effort. Calibration data must be acquired during the initial operation phases.

Before discussing the main topics of this section, I should like to show some typical examples of our television pictures. One must remember that we are interested in photometry, not positional astronomy. The shape and size of the images are more than adequate for our purposes.

Figure 1 shows one of these pictures. Note the target ring in each corner of the picture; the shadow in the upper left corner; the calibration lamp just below the center of the picture; and its ghost slightly below and to the left. All other objects are stars. Each frame consists of 256 scan lines designated by the number k, with each line containing 251 pixels designated by the number ℓ, making a total of 64,256 intensity points $I(k, \ell)$. The frames are divided into two spectral regions by two filters: lines 1 to approximately 115 have one spectral range; lines 115-141 have a composite response from both filters; lines 142 to 256 have a different spectral range. Most pointings had exposures from three cameras. Figure 2 shows a montage of pictures from three cameras and a ground-based photograph. The stars in the television pictures range from 6 to 12 mag. The diffuse radiation in the U_4 filter of camera 4 is the Lyman-α radiation from the geocorona. Figure 3 shows an exposure of brighter stars in the Orion area. Note the larger image size caused by saturation in the target.

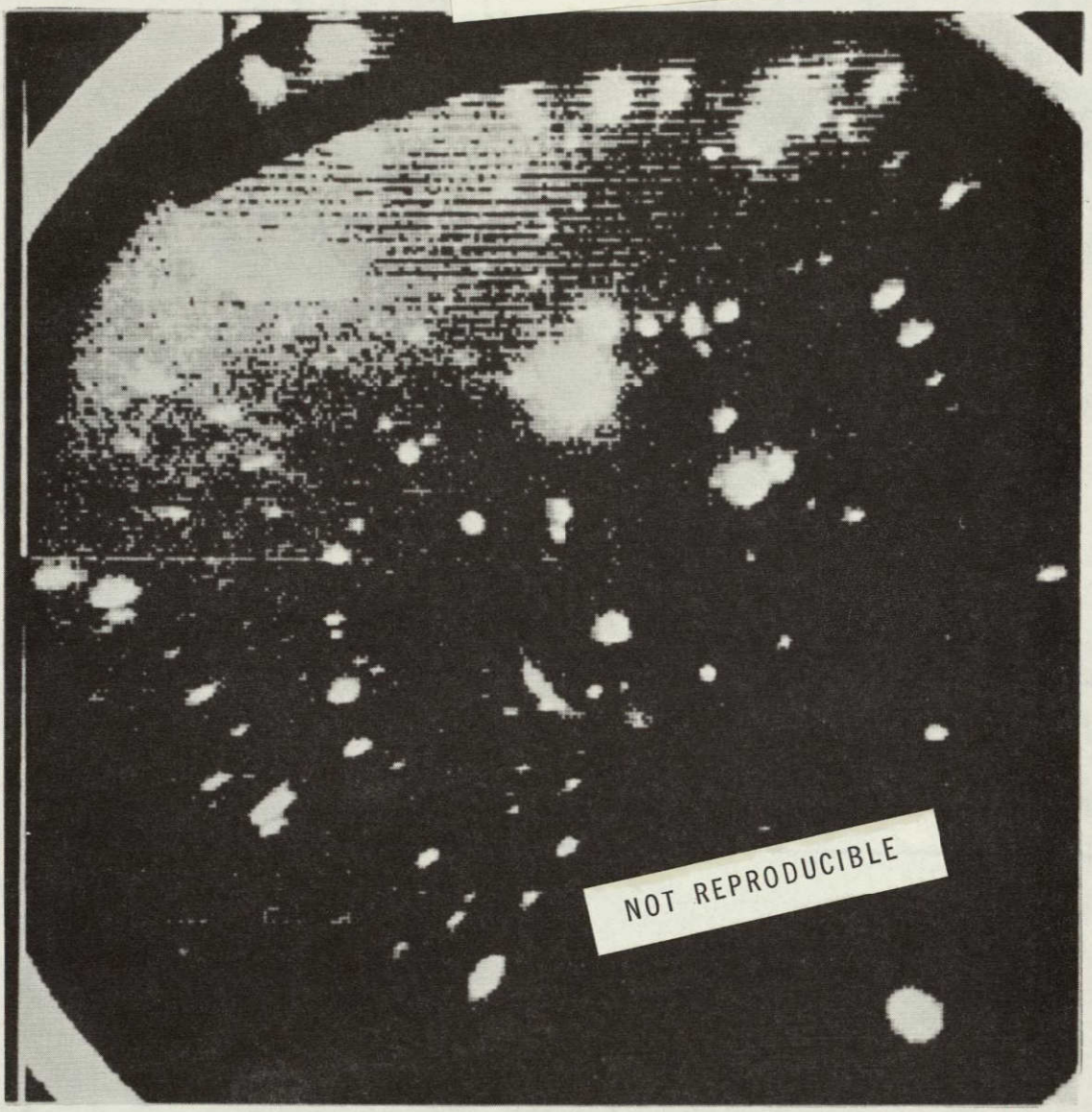

Figure 1. A sample camera 3 picture.

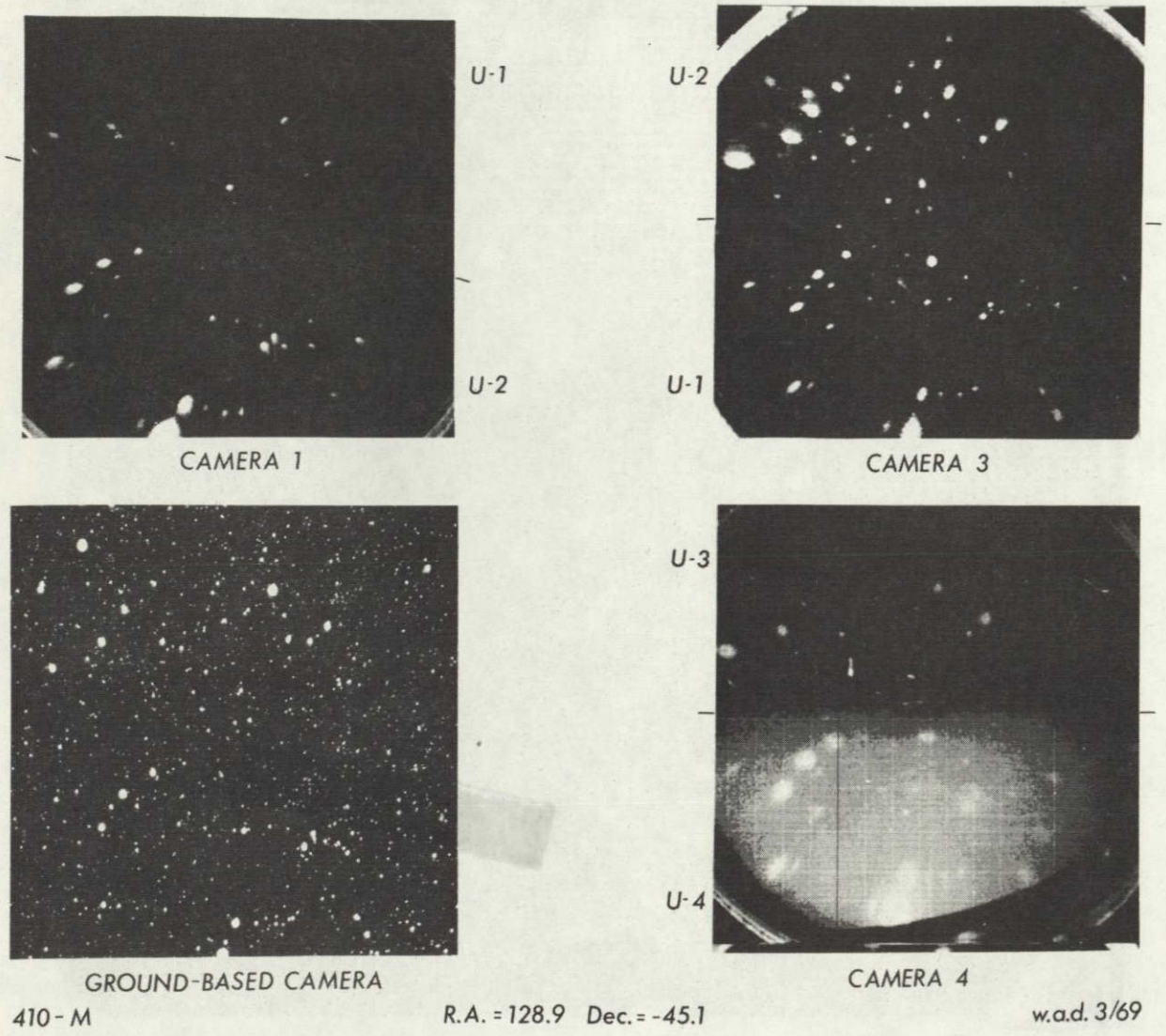

Figure 2. A composite picture in the Vela region.

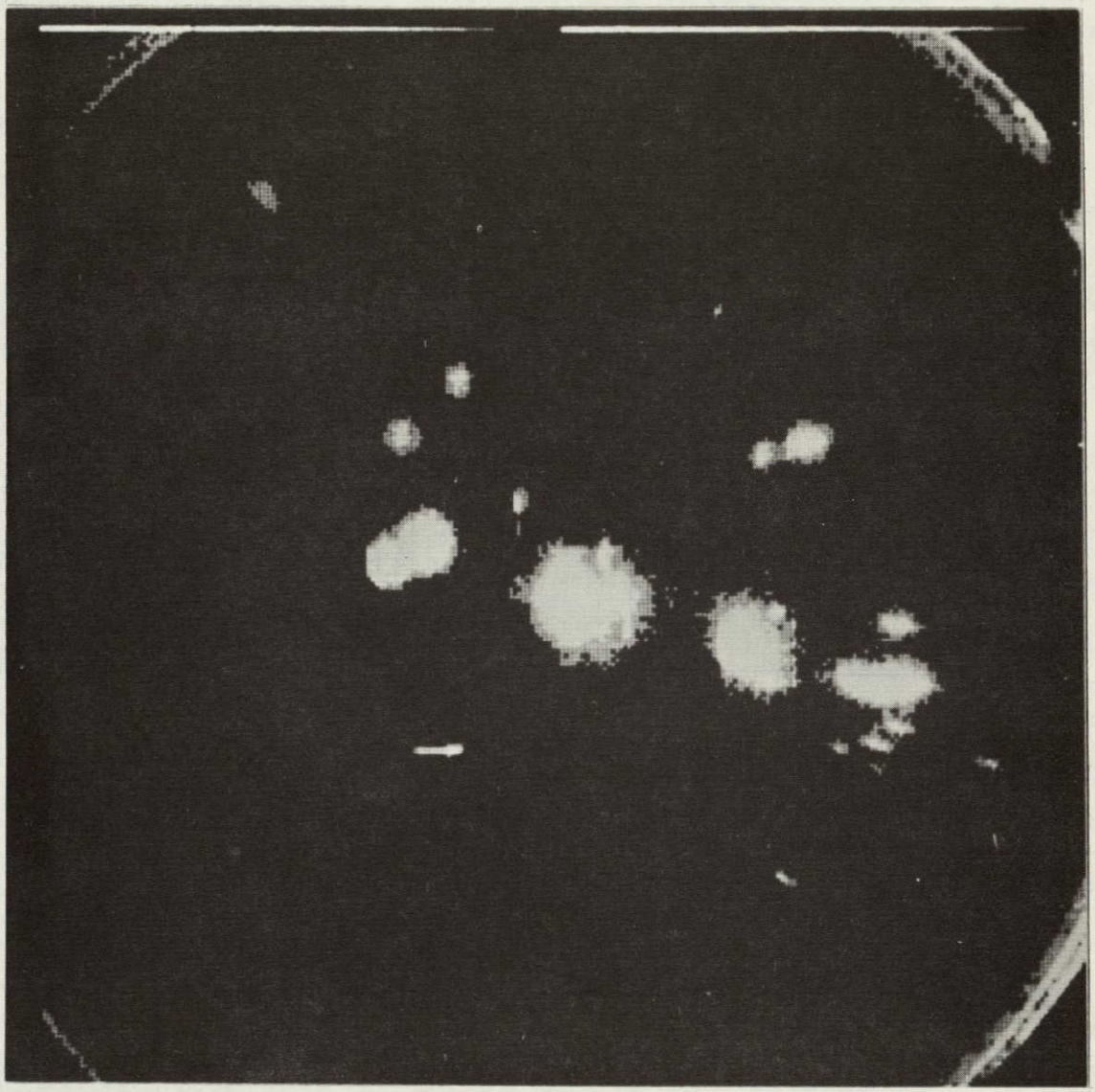

Figure 3. Stars in Orion.

2. DATA-REDUCTION SYSTEM

The data-processing system that evolved during the project deserves some philosophical comment. We thought we had the complete system ready before launch and would have only to reduce the data. However, we were not well prepared for noisy data (streaks, parity errors, and partial frames), nor were we able to handle the Lyman-α radiation in cameras 2 and 4. Both these problems required extensive modifications to the system. The moral is to expect problems and to be prepared to stop the system until they are solved, not to try to run some of the data through one system and some through another.

We received a large number of television pictures from the experiment. Some of them were of poor quality because of parity errors originating in the transmission link or in the data-handling equipment. We found that a quick and accurate quality check of the data was manditory. They were hand carried from the data-processing section to our operations team at the OAO Control Center and immediately evaluated. "Missing" or poor-quality data were then reprocessed before the tapes went into storage, thus cutting the time to reprocess the tapes from months to weeks. Even with these procedures, the data arrived at SAO at least 6 weeks after the experiment took the pictures.

The final data-reduction system has a feature that we consider worthy of special attention: a composite observation file, which consists of composite observations records. Each record contains space for all the information that we ever expect to know about an object.

Each object in a picture starts as an empty record with locations for all the information that the data system generates. Subsequent programs read the information from and add information to the record. Each piece of data has an existence bit that tells if the information is in the record; therefore, the availability of information in the record can be determined without unpacking all the data. Sufficient blank spaces are reserved for information that may

be added later. The advantages of common input and output routines are self-evident. In addition, the data can easily be used and sorted. We highly recommend this system.

The data system shown in Figure 4 consists of four main programs: Phases 0, 1, 3, and 5. (Phases 2, 4, 6, and 7 existed but have either been absorbed by the existing phases or were dropped.) The temperatures and pointing information are checked at the Phase 0 level. Some data were missing or incorrect on a significant number of the pictures because the necessary data were on four separate data channels and were merged after they were received at GSFC. Also, the camera number was not included with the picture data or with any other data. We strongly recommend that, if possible, future experiments include all data on one channel and that numbers identifying the cameras be incorporated into the television data.

At this stage, the pictures were also entered into the automatic bookkeeping system. (It is not a simple task to keep track of 10,000 frames of data in any one of 10 stages of processing.)

The frames then proceed to Phase 1, the heart of the data system. It is the program that finds all the stars in each frame and all the intensities $I(k, \ell)$ associated with each star. We assume that the stars are relatively sharp spikes on a smooth background and that we can fit a general cubic equation, $A + Bk^3 + Ck^2 + Dk + Ek^2 + Fk + Gk^2 + H + I^2 + J^3$, to the background. Any intensity points that are 2.5 standard deviations above the fitted background are regarded as parts of stars.

The program has three distinct parts: the first section fits the background; the second decides which points are signal and to which star they belong; and the third prints the output of the stars for any necessary manual review and creates an output tape for the remaining stages of processing.

The first section of the program computes a significance level for each filter half of the frame by using a least-squares technique to fit the background

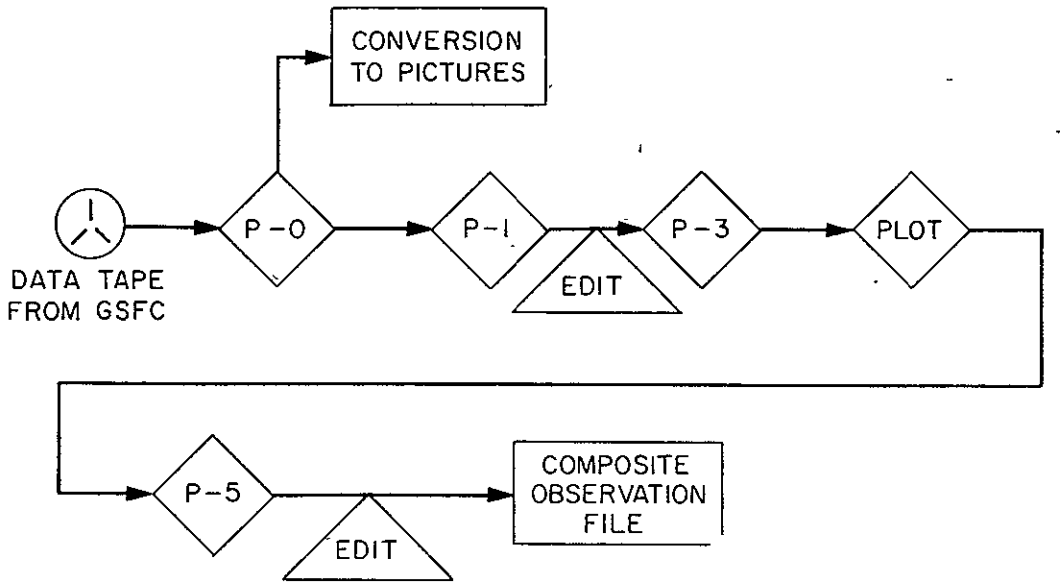

Figure 4. Schematic diagram of the data-processing system.

equation to every fifth intensity point on every fifth line. It iterates this step at least two times, eliminating any points that are more than 3 standard deviations from the fit, because we assume that these points are not part of the background but are signal points from stars that were chosen because of the regular grid. The iteration procedure continues until the standard deviation of the fit is changing by less than 0.2. This final equation is the background that the program uses for each half frame. Phase 1 then computes a significance level by adding 2.5 times the standard deviation of the fit to the background equation at each raster point. All intensities greater than or equal to the significance level are signal; all others are background noise. Figure 5 shows the significance level for every 16th point of the sample frame. Note the different levels for the upper and the lower portions of the frame.

The second section of Phase 1 groups into objects all contiguous points greater than or equal to the significance level. The program starts searching for objects in the upper left corner of the frame and works across and down until it finds a point above the significance level. The program finds all contiguous points above the significance level and then searches for the next star.

The third portion of the program calculates the center of intensity of the star, subtracts the calculated background from the individual points, and computes the sum of the net individual intensities (SIGMA). On the basis of the object's shape and density of points, the program then decides whether it is either a star; an object that may be either a star or noise; or just noise. If it is a star, the information is written on the output tape and printed. If it is a questionable object, Phase 1 only prints the information on the output page. If the object is noise, it is dropped. Figure 6 shows examples of the first two classes of objects; a star and a large spurious object. Note the message on the second object: THIS OBJECT IS NOT ON THE OUTPUT TAPE. The program then prints a symbol picture of all points above the significance level and numbers each star at its center of intensity so that we can easily find the star in the printed output. Figure 7 shows a portion of this printed picture for the sample frame.

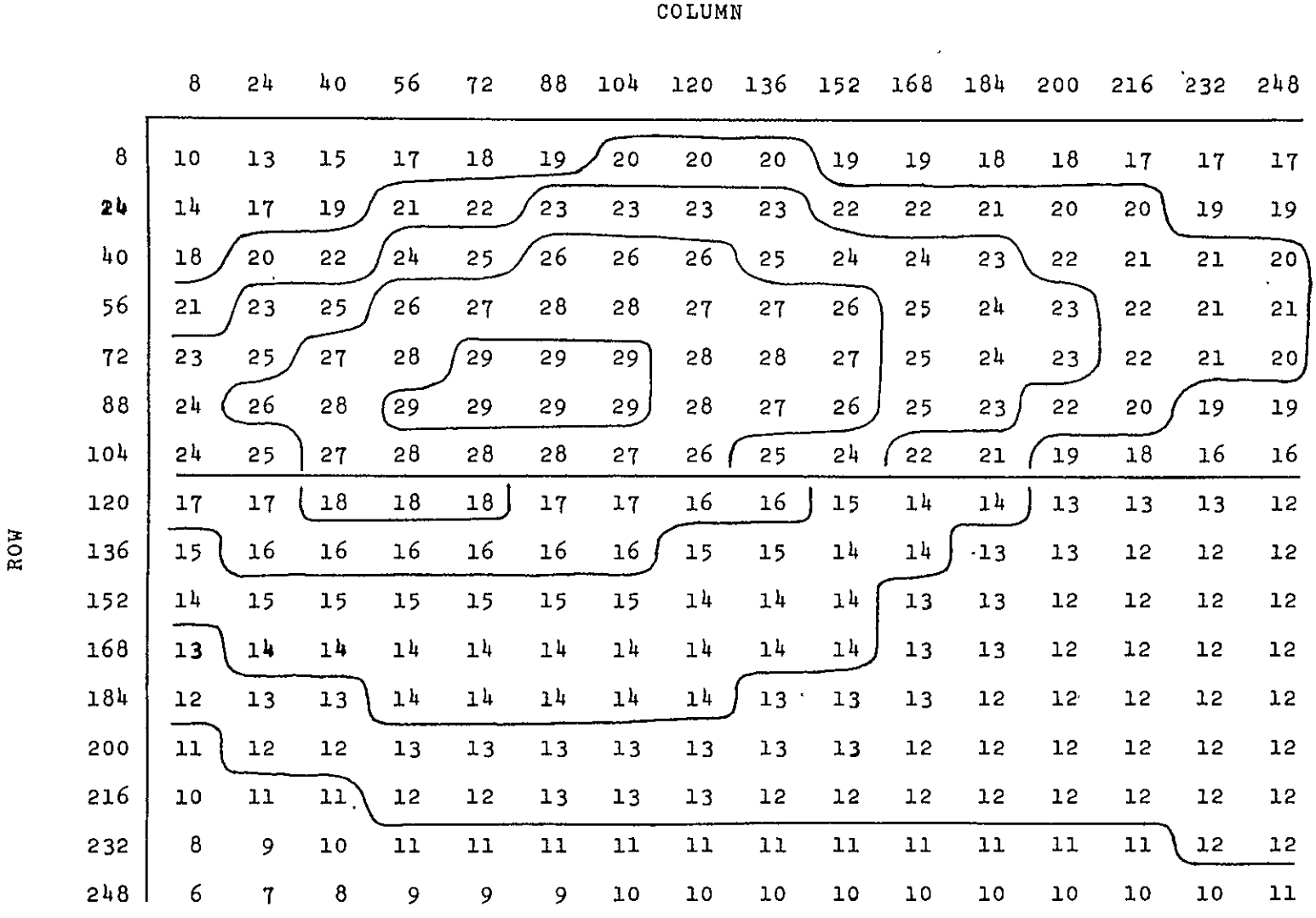

Figure 5. Significance level for camera 3, contact Rosman, orbit 413.

```
---------------------------------------------------------------------------------------

  Tape    FM  UPPER LEFT CORNER(ROW,COL)     CENTER  INTENSITY    N    LENGTH   FAC  SEQ.NUM
  TEST     2          118 109               121 112        727     31   6   7  2.50      59

BACKGROUND AVERAGE=    11.23     K,L AND RAW INTENSITY OF THE PEAK ARE  121 113   73

  0  0 19 24 22  0  0
  0 20 36 42 33 24  0
 17 24 42 68 64 40 19
  0 24 42 69 73 44 23
  0 17 35 58 63 33 18
  0  0 16 27 23 16  0

---------------------------------------------------------------------------------------

  TAPE    FM  UPPER LEFT CORNER(ROW,COL)     CENTER  INTESNITY    N    LENGTH  FAC  SEQ.NUM
  TEST     2          121  55               123  56        31      5    4  3  2.50      61

BACKGROUND AVERAGE=    12.07     K,L AND RAW INTENSITY OF THE PEAK ARE 124   55   20

  0 18  0
  0  0 18
  0 17  0
 20  0 18

 - THIS OBJECT IS NOT ON THE OUTPUT TAPE --

---------------------------------------------------------------------------------------
```

Figure 6. Output from the program that separates the stars from the background.

Figure 7. Example of printed picture for sample frame.

Phase 3, the intensity reduction program, uses the raw input intensity calculated by Phase 1, the instrument temperatures, and the calibration data to calculate the intensity of the star. It also eliminates the known positional distortion in the frame and calculates the angular position of each object relative to the center of the frame. To do this it needs to calculate the target gain at any position on the target.

Each camera was calibrated slightly differently: camera 1 had a 14-point grid; camera 3, a 17-point grid; and cameras 2 and 4, a 26-point grid. These grid points were in a regular pattern, not at the maximum, minimum or slope changes of the target-gain surfaces. Therefore, we needed a procedure for calculating the gain at any point on the target. We tried both interpolation and curve-fitting techniques. After evaluating both, we chose a second-order interpolator because a linear one would not work. Also, a new regular 9×9 array of grid points for each camera was defined for programing convenience and program efficiency. Our second-order interpolation scheme is best introduced by the short description of a first-order ruled-surface interpolator that follows. To find the value of the gain $G(k, \ell)$ shown in Figure 8, choose the surrounding four gain points $G_1(k_1, \ell_1)$, $G_2(k_2, \ell_2)$, $G_3(k_3, \ell_3)$ and $G_4(k_4, \ell_4)$ and draw straight lines through G_1 and G_2 and through G_3 and G_4 (the same value results if the pairing is G_1-G_4 and G_2-G_3). Then "roll" the line AA′ along the lines G_1G_2 and G_3G_4 such that the fractional distances along each line are equal ($G_4A/G_3G_4 = G_1A'/G_1G_2$). The gain $G(k, \ell)$ is defined when the line AA′ passes over the point. Our second-order ruled-surface interpolator uses an additional surrounding eight points and ensures that the slope of the surface is continuous.

106-043

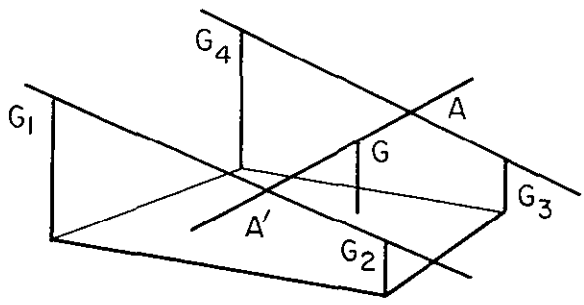

Figure 8. Schematic figure of the interpolation procedure.

This procedure was used to convert the existing points to the regular 9×9 grid needed by the programs and to interpolate values for the target gain for the reduction of the stellar data.

Phase 5 matches the stars in each frame with the Celescope catalog of stars, using a configuration match between the stars in the frame and those in the catalog. The program will correctly match the frame with the catalog even if the input center for the frame is 30 arcmin from the actual center. The automatic identification program worked satisfactorily for most of our data. The frame must be manually matched if there are fewer than four stars common to both the frame and the catalog. A review of all frames for correct star identification follows. At this stage, all the individual objects are compiled on one master tape. When the compilation is complete, the entire set of data is checked for consistency.

3. CALIBRATION DATA

Before we launched the experiment, we realized the need for in-orbit calibration and planned to take data for it. The least we could expect was a decay in sensitivity with time, but because of the 2 years between component calibration and the launch, we also planned to check the calibration in orbit. In addition, we felt strong pressure to fly a successful experiment and to acquire quickly a statistically significant amount of scientific data before a premature failure. The apparent conflict between the two goals of gathering calibration data and gathering scientific data in the initial orbits was not easy to resolve. In retrospect, we feel we turned the experiment on too quickly in an unknown environment. Camera 2 was damaged because of this haste. Furthermore, we pushed on to gather early scientific data at the expense of early calibration data. After the first month of operation, we began systematically to gather data for this task. They are listed below and are discussed in order.

1. A regular grid of stars or star fields; observations with a separation of 10 to 30 arcmin between pointings.

2. Repeated observations of the same stars at regular time intervals.

3. Multiple exposures at the same pointing with different exposure times.

4. Repeated observations at the beginning and at the end of every standard slew sequence.

5. Multiple exposures at the same pointing and exposure time.

In order to map the camera sensitivities, each camera observed a number of stars of different intensity with two or more exposure times at each of 40 positions. Whenever possible, we used areas containing many stars so that the frames contained many calibration stars at the same time.

We observed the first regular grid, which was a compromise between calibration and data collection, from orbits 400 to 490. During this period,

many stars were observed six times to obtain calibration data as well as scientific data. Later orbital periods were devoted entirely to this type of operation and they provided data for the calibration-improvement program. Data from these grids were essential for the calibration of the experiment.

The time decay of the system is most easily determined if the same stars are observed at the same positions on the target at regular intervals. Because of sun, power, and thermal constraints, this was impossible with our experiment, but we did observe a number of standard star fields as often as practical. Three star fields were used as primary calibration areas. We observed one as long as possible and then observed one of the other two fields as a standard until it was no longer available. Thus, we continually observed one of the three primary standard fields at least once during every operating period. These three areas, along with any chance repeat observations more than 20 orbits apart, provided the data that were used to determined the time decay for each camera-filter combination.

Multiple exposures at the same pointing but with different exposure times were used to test the calibration of the experiment. The one difference between these and the raster scans is the number of variables involved. Here, only the input energy to the target varies, so it is easier to isolate the target gain from the coupled effects of the filter, photocathode, and target gains.

Identical exposures test the repeatability of the instrument. Each of our standard 36-exposure patterns started and ended at the same point for a quick check on the stability of the instrument's sensitivity. Twice, we took approximately 10 consecutive exposures of several different stars to determine the repeatability of the observations. Magnitudes determined from these sets of observations varied by less than 0.2 mag.

4. USE OF THE CALIBRATION DATA

The calibration data were used to determine

1. An exposure time correction.
2. The decay characteristics of the cameras.
3. The change in the area sensitivity of the target gain from initial calibration until launch.

All the data require an exposure-time correction, but it is only important for short exposure times. The ground computer controlled the time between the expose-on and the expose-off commands (the exposure time) by counting a series of 1-sec pulses. It counted the first pulse after sending the expose-on commands as zero and then waited the required number of seconds before sending the expose-off commands. This counting technique created an unknown but constant increase in each exposure time.

We deduced the constant by determining the additional increment of time that gave the best agreement in magnitudes between consecutive exposures of 1, 5, 15, 30 and 60 sec of the same stars. A 2-sec increment gave the best fit. Table 1 lists this magnitude correction for each exposure time Note that only the short exposure times are affected and that 1-sec exposure times may have the least-accurate magnitudes.

Table 1. Magnitude correction for a 2-sec increase in exposure time.

Exposure time (sec)	Correction (mag)
60	0.036
30	0.068
15	0.136
5	0.365
1	1.193

The time-decay history of each camera-filter combination was determined by fitting a power series to the star data with a least-squares technique. Each star must have a unique magnitude at time zero. Its magnitude calculated from measurements at any other time will increase if the system decays. Magnitudes are defined as -2.5 log (power); hence, lower power signals have larger magnitudes. We therefore assumed that

$$M(t=0) = M(t_1) - \sum_{1}^{n} A_n t_1^n \quad .$$

If a star was observed twice,

$$M(t=0) = M(t_1) - \sum_{1}^{n} A_n t_1^n = M(t_2) - \sum_{1}^{n} A_n t_2^n$$

and hence the equation

$$M(t_1) - M(t_2) = \sum_{1}^{n} A_n (t_1^n - t_2^n)$$

when solved for all pairs of stars defines the coefficients A_n in the decay equation for the system.

Note that this is a linear correction; that is, every magnitude receives the same additive correction. This conflicts with the assumption that the primary decay mechanism was a diminishing readout beam current. A decaying beam current would show a nonlinear change because the target-gain curves are nonlinear. We attempted to compute the decay with a decaying beam current but were unsuccessful.

The standard calibration-area data and all chance repeats greater than 20 orbits apart were used in these fits. Other data were not used, because they reflect area sensitivity changes and isolated frame shifts rather than time decays. The curves determined with this program are shown in Figures 9 to 13. Each curve stops at the last reliable data point.

We used a Fletcher-Powell optimization technique to improve the target-gain curves. The input data were selected from the regular calibration grids and any other data that were appropriate. All marginal data and data that were contaminated by the filter discontinuity were eliminated from these runs.

The program uses pairs of stars observed at different positions on the target. It computes the required gain change for each grid point that will minimize the RMS magnitude deviation of all pairs of stars. Since we assume that reciprocity holds for our tubes, we also use data at different exposure times. A series of laboratory tests on similar tubes showed no reciprocity failure.

The procedure for calibration improvement went as follows. Each camera was treated separately, and the stars in one filter were not compared with the stars in the other. First, the decay program calculated a decay curve for each filter. These curves provided a first-order correction to the magnitude calibration, and then the optimization program improved the gain curves. These curves were then used to calculate new magnitudes. Next, we calculated a new set of decay curves. The iteration between these two techniques continued until the results converged. The resulting gain curves showed only slight variations from the curves determined from the preflight data.

A short comment about the amount of data is included here because insufficient data may produce misleading results. All the programs had sufficient data for a meaningful solution. The decay equation contained six coefficients for camera 1, and five for cameras 3 and 4. At least 320 data points were used for the least-squares fit. The gain-curve optimization program has 500 parameters and a minimum of 1500 data points.

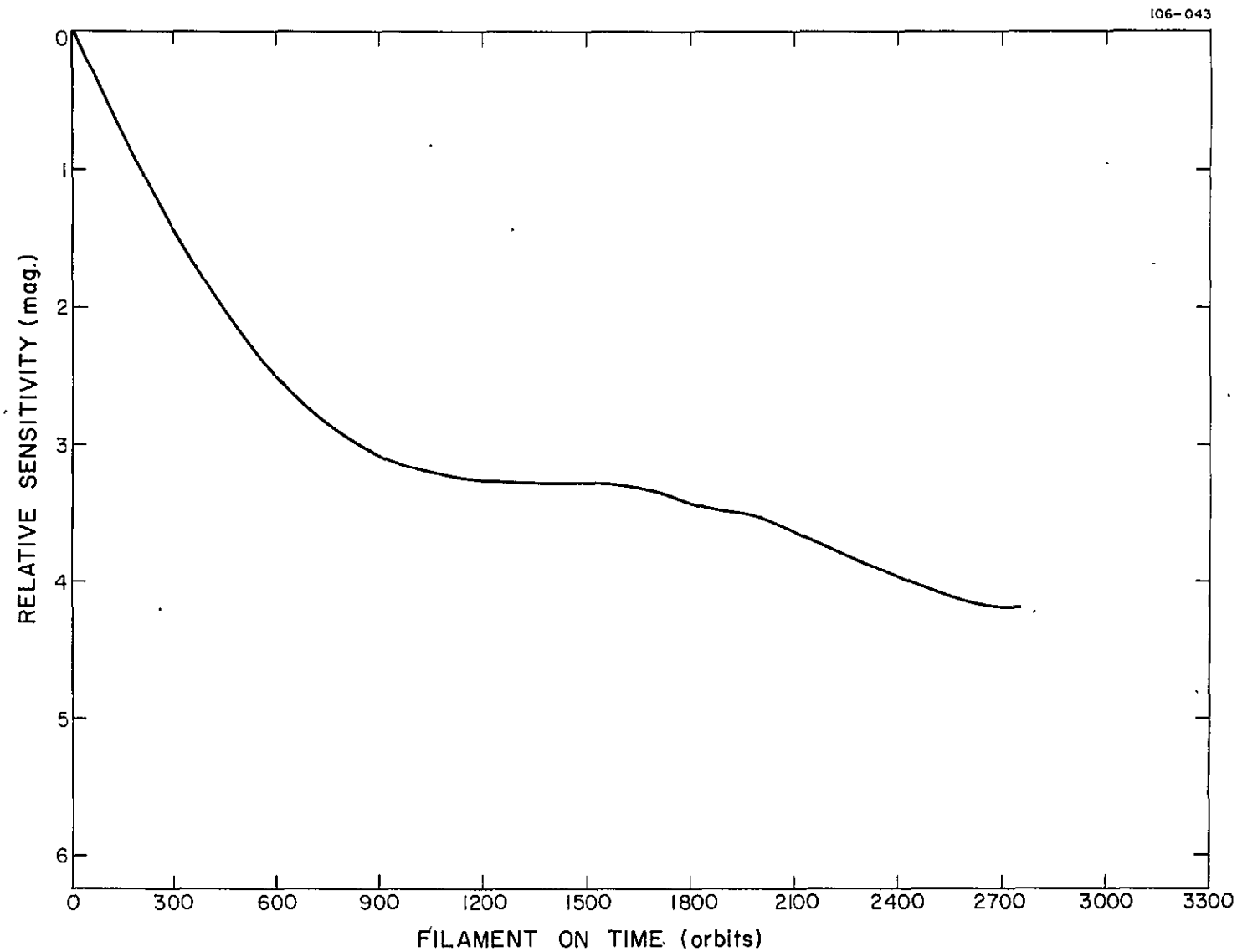

Figure 9. Camera 1 filter U_1 sensitivity curve.

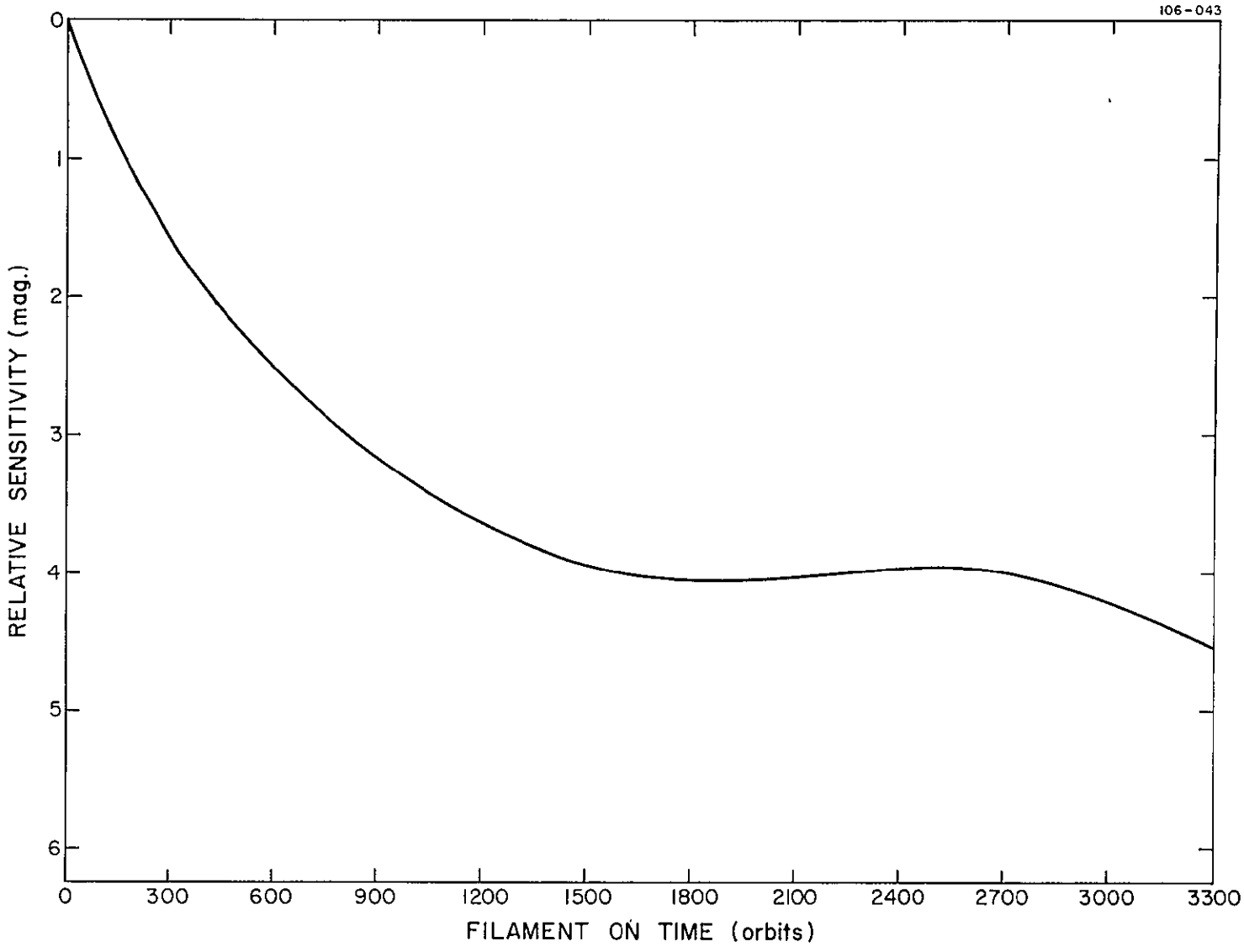

Figure 10. Camera 1 filter U_2 sensitivity curve.

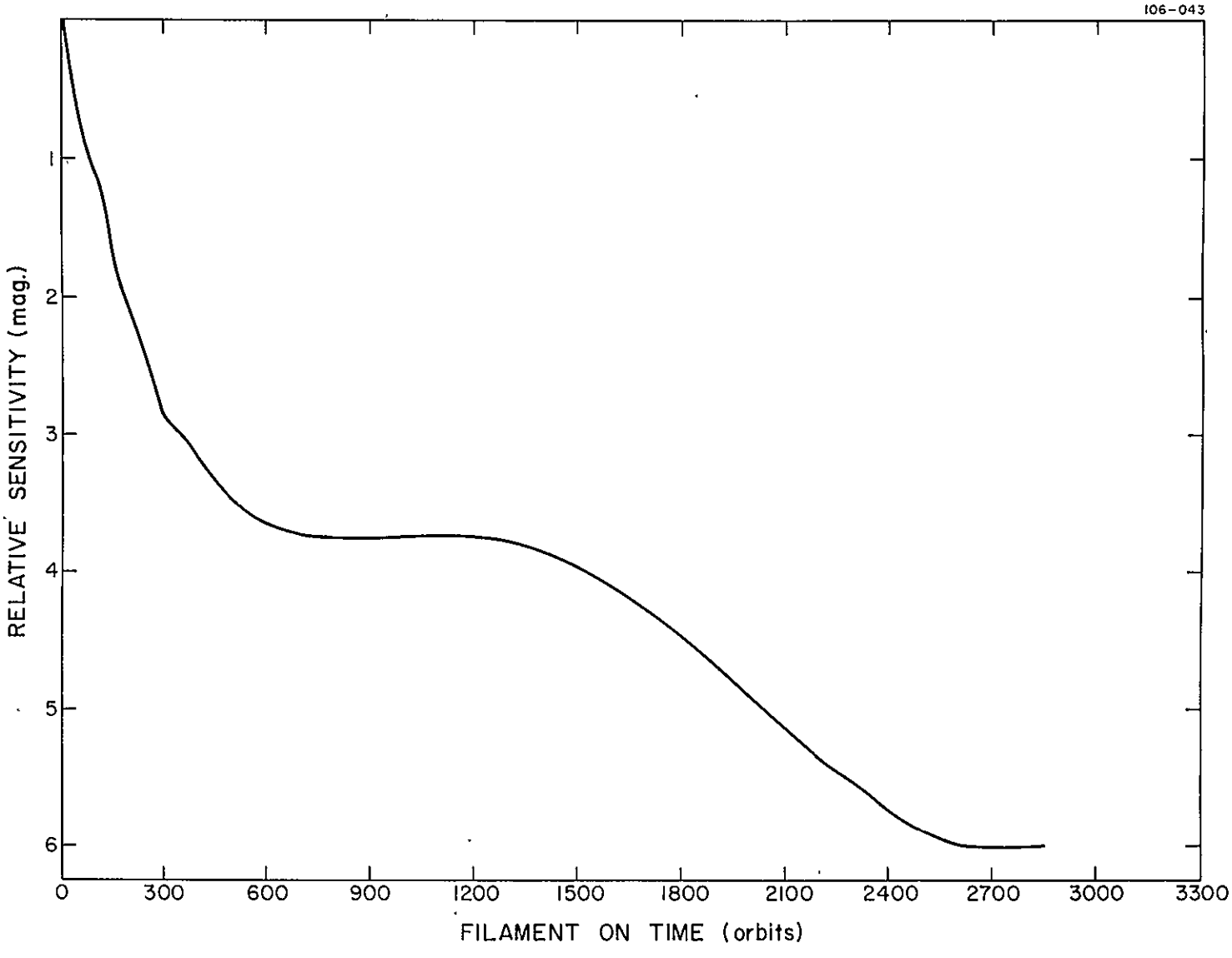

Figure 11. Camera 3 filter U_1 sensitivity curve.

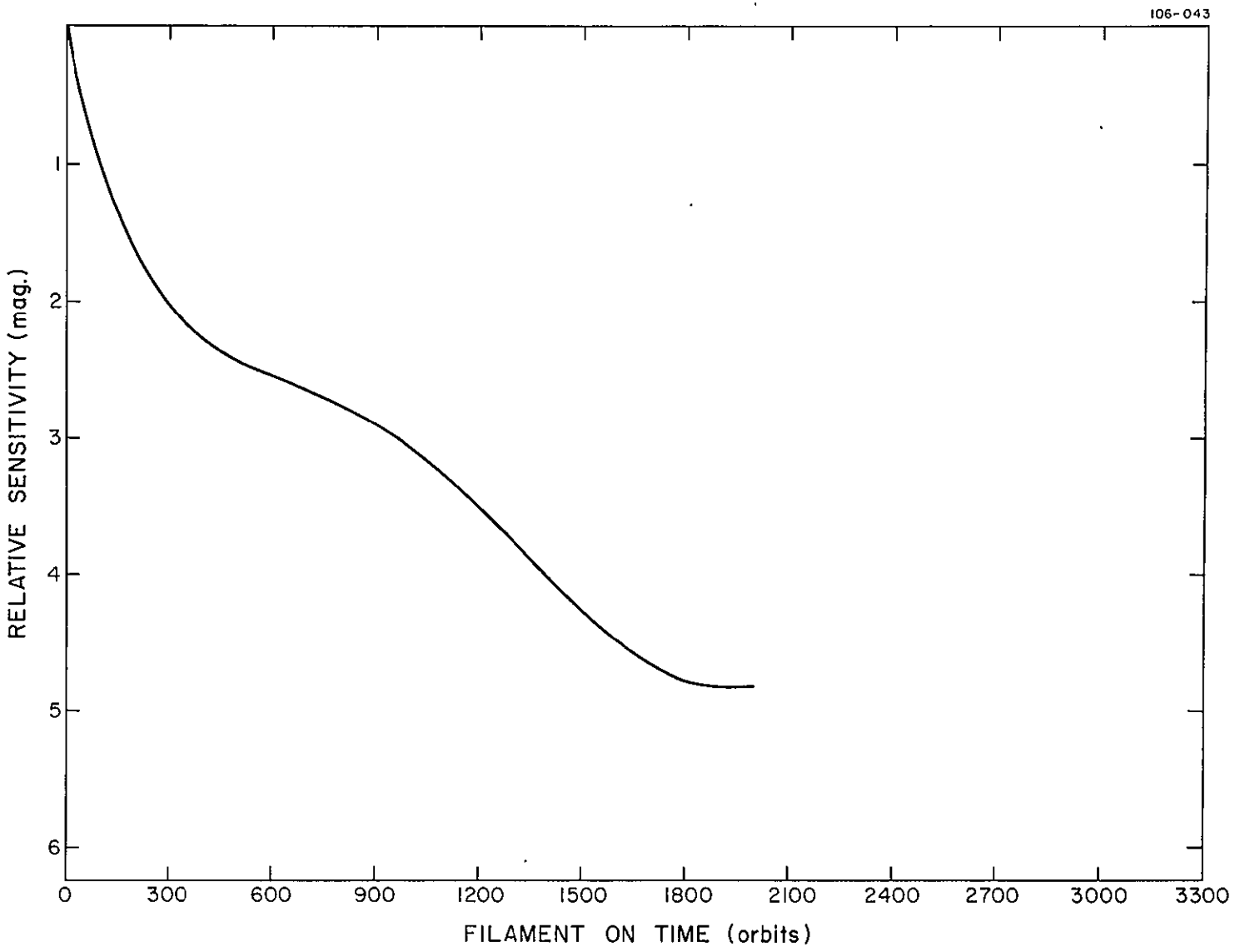

Figure 12. Camera 3 filter U_2 sensitivity curve.

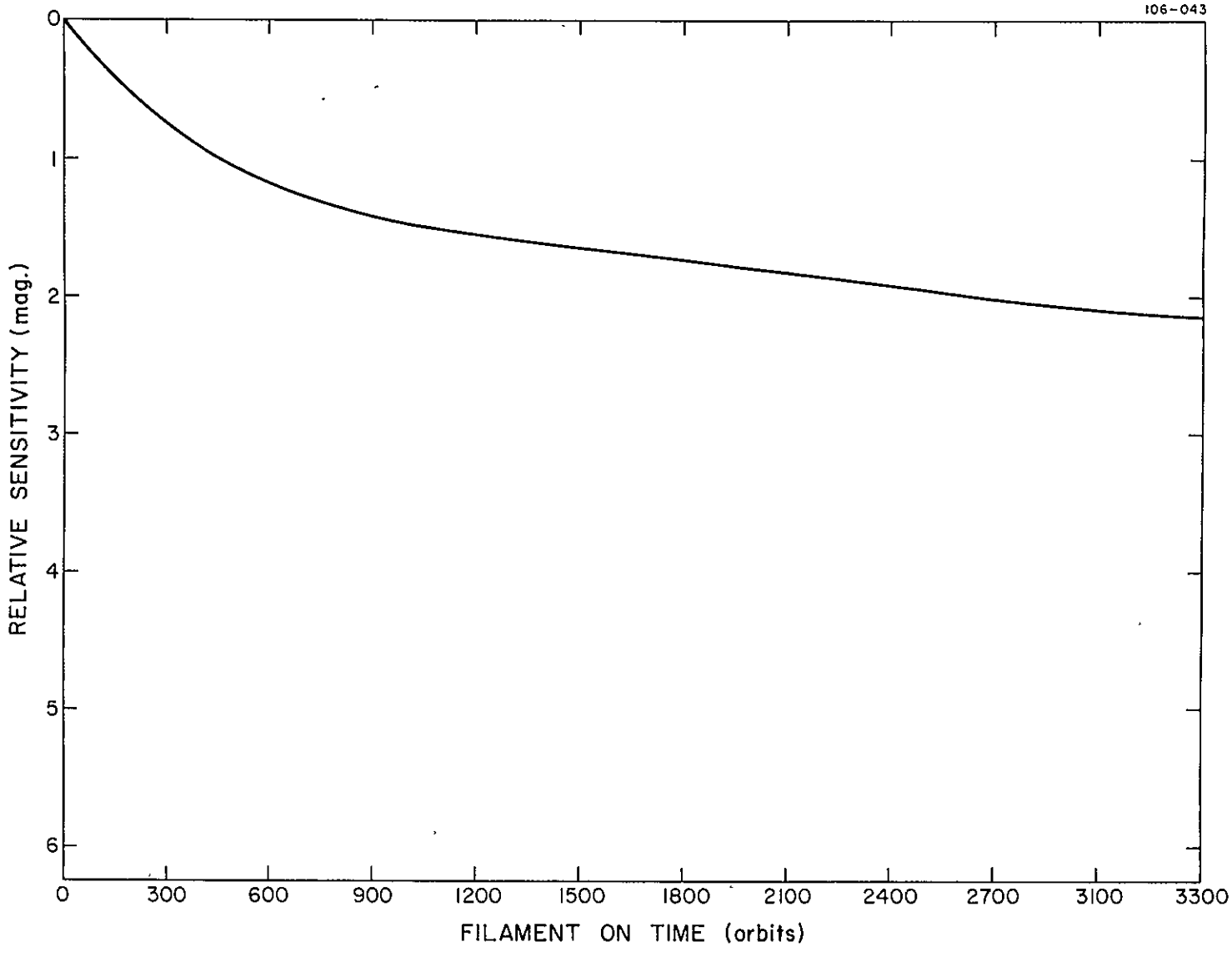

Figure 13. Camera 4 sensitivity curve.

Table 2 lists the final result of the magnitude-improvement procedure.

Table 2. Final RMS magnitude discrepancies.

Camera	RMS discrepancy (mag)
1	0.17
3	0.20
4	0.19

5. PHENOMENA THAT AFFECT THE ACCURACY OF THE DATA

A number of conditions that affect the data are discussed on a phenomenological basis in the following sections. Some of the effects were correctable; others resulted in rejection of the data. Most of these data were not used in the magnitude-improvement program. Each of the following effects is discussed in detail:

1. The discontinuity in the filter pass bands at the center of the Uvicon.
2. Merged objects.
3. Objects near target defects.
4. A high background from Lyman-α radiation.
5. Daylight observations.
6. Poor data.

Discontinuity in passbands. The choice of two filters for each Uvicon was based on the principle of redundancy for the experiment. If one camera failed, another camera still had each filter band for continued observation. This increased the reliability of the system, but it decreased the amount of accurate data that could be obtained.

The filter in any system should be placed far enough from the focal plane that local dust spots and transmission anomalies affect only a small portion of the beam. In our case, the beam was effectively 30 arcmin in diameter at the filter plane. That is, a star must be 15 arcmin away from the discontinuity between the filters before all the radiation passes through the same filter (see Figure 14). Hence, stars observed in the 30-arcmin band in the center of the Uvicon did not have a single filter pass band but a combination from the two filters. Furthermore, the position of the center had an uncertainty of ± 5 arcmin because of magnetic shifts in the imaging section. We resolved this problem by rejecting the magnitudes of any star within 5 arcmin of the predicted discontinuity. Stars within the range from 5 to 15 arcmin of the discontinuity are given lower weight in magnitude computations.

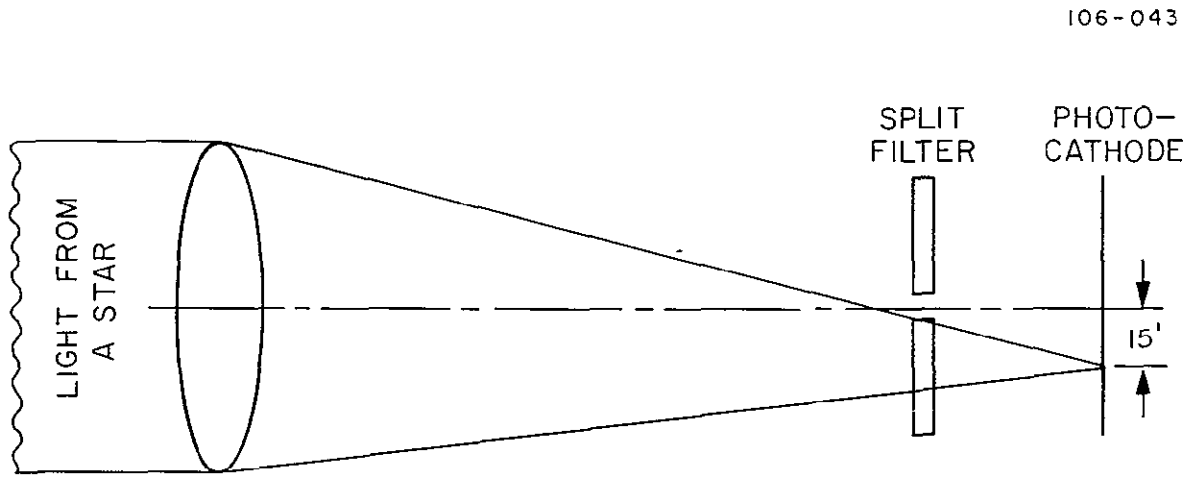

Figure 14. Schematic drawing of the geometry of the filter—light-cone interaction.

The net effect of this redundancy was fewer data because we took small slews from one exposure to the next so that each star would be in a good section of the filter pass band. This choice did provide the necessary redundancy in the shorter wavelength bands when camera 2 failed. However, for the next experiment, one filter for each camera should be seriously considered. The extra data-gathering capability may more than offset the lack of redundancy.

Merged objects. One characteristic of our Uvicons is the spreading of a saturated image. Many stars were close enough in angular separation that the images merged together. This merging can change the transfer function of the Uvicons because the combined image becomes more like an area source than a point source. It also caused us problems in trying to separate the merged stars. We use a number of procedures, ranging from simply dividing them manually to complicated programs that used a least-squares technique to fit elliptical Gaussian surfaces to the merged images and then computed the intensity in each object. The latter system was too complicated except for objects of extreme scientific importance. The remainder of the objects were divided into three subjective catagories:

1. Slightly merged images.
2. Moderately merged images.
3. Merged images that could not be separated.

We found that merged-image magnitudes are dependent on the degree of merging; this conclusion results from comparisons of the magnitudes of the same objects observed at shorter exposures. We therefore use moderately merged images with a lower weight and treat inseparable images as one combined star. In the case of an important star, shorter exposure times were used to obtain useful magnitudes.

Objects merged with or superimposed on target defects. Each camera has a few defects in its target. The calibration lamp is in this category because it can cover or merge with a star image. Each of these objects occupies a

very localized area and, because of our operation procedures of raster mapping, any stars under these defects would be in another area of the target at another exposure and could be measured there. In general, these defects were a minor nuisance that affected only a small portion of the target.

Lyman α. The problem of Lyman-α radiation from the geocorona was not easily resolved. Its intensity varied with the exposure time and with the position and pointing of the spacecraft. It was not detectable on 1- and 5-sec exposures. In some 15-sec exposures, there was no detectable Lyman-α background; in others it was apparent. All 30- and 60-sec exposures had a significant background from this source. We are as yet unable to reduce the magnitudes of stars observed in an area of high Lyman-α background. The net effect of this is to limit our U_4 magnitudes (the filter that includes 1216 Å) to those from exposures of 1 and 5 sec and some of 15 sec. This restricts the observations to bright stars because we are not able to observe faint stars through the geocorona. We did, however, observe a number of brighter stars and have accurate magnitudes for them.

Daylight observations. During the initial orbits, checkout operations in daylight were impossible. The background of scattered light would have caused the same problems as the Lyman-α background for the reduction system even had we made daylight observations. Later, we took some limited data during daylight. The spacecraft pointed away from the sun rather than toward it, and only the dark side of the earth was visible from the experiment. These pictures proved that we could gather accurate data under these conditions if we limited our maximum exposure time to 30 sec.

Poor data. A limited number of frames were rejected for various reasons. Pictures distorted because the magnetic unloading system (MUS) was mistakenly left on and high parity rates from some stations were the primary causes. These data are ~ 1% of the total, the distorted pictures were eliminated from the catalog. The frames with parity errors were used if possible. Single-line streaks in the data were eliminated by replacing them with the average of the lines above and below them. A partial picture was

reduced if at least one half of it was free from parity errors. Using these techniques, we were able to reduce nearly all poor data.

In conclusion, a number of phenomena affected the accuracy of some of the observations. We compensated for nearly all of them by operational techniques, data redundancy, and computer programs. We are, as yet, unable to compensate for the Lyman-α background in filter 4 for exposure times longer than 15 sec.

SECTION V

DRAMATIS PERSONAE

DRAMATIS PERSONAE

The general scientific planning that became the basis for Project Celescope originated in a series of meetings of the scientific staffs of the Smithsonian Astrophysical Observatory (SAO) and Harvard College Observatory in February 1958. Following these meetings, a committee consisting of Dr. R. J. Davis, Dr. K. G. Henize, Dr. R. E. McCrosky, Dr. G. F. Schilling, and Dr. C. A. Whitney made more detailed plans and wrote a proposal that eventually became the basis for the NASA grants and contracts that supported Project Celescope. Dr. F. L. Whipple and Dr. Davis were SAO's delegates to NASA's Working Group on Orbiting Astronomical Observatories (OAO), which developed the relative roles of spacecraft and experiment in the OAO. Celescope became an official project of SAO in 1959. The name was suggested by Dr. D. H. Menzel in 1960 as the winning entry in an informal contest for naming the project; the name implies that the Smithsonian Experiment is one of the first truly Celestial telescopes.

Since the beginning, Dr. Whipple has been Principal Investigator and Dr. Davis has been Coinvestigator and Project Scientist. From 1959 to 1961, engineering and administration were coordinated by Mr. F. R. Nitchie, Jr., Engineer-Administrator. In 1962, the title of this position was changed to Project Manager. Mr. G. K. Megerian served as Project Manager in 1962; Dr. C. A. Lundquist, as Acting Project Manager in 1963; Mr. J. J. Burke, as Project Manager in 1964-1968; Mr. J. J. Ainley, 1968-1970; Mr. R. T. Ayer, 1970-present. While Acting Project Manager, Dr. Lundquist was assisted for several months each by project administrators: Mr. L. McGrath, Mr. H. Rosenthal, and Mr. E. Kohn.

For the first few years, the major effort in Celescope was devoted to engineering. From 1959-1964, our engineering staff consisted of Dr. M. D. Grossi, Electronics Engineer; Mr. S. Sydor, Optical Specialist; and Mr. J. M. Franklin, Mechanical Specialist. From 1959-1962, Mr. H. Cobb

served as Mechanical Engineer. From 1964-present, Dr. Y. Nozawa has been Electronics Engineer, and special engineering needs have been covered by Mr. T. E. Hoffman and others from SAO's Engineering Department. In 1966, the post of Project Engineer was created; it has been filled since that time by Dr. Nozawa. A critical activity of the engineering section from 1965-1969 was field engineering during subsystem and system testing, launch preparation, and orbital operations. Dr. Nozawa was SAO's field engineer during that time.

Members of the SAO Field Engineering Team, which performed engineering tests, system acceptance tests, and launch preparation, were as follows: Mr. W. Peters (Manager, 1967-1968), Mr. J. Munier (Assistant Manager, 1964-1965), Mr. B. A. McLean (Supervisor from EMR, 1964), Mr. J. W. Kennedy (Supervisor from EMR, 1965), Mr. D. R. Nelson (Supervisor from EMR, 1967-1968), Mr. J. Brown (Member from EMR, 1964-1965), Mr. J. Faso (Member from EMR, 1964-1965), Mr. G. Komen (Member from EMR, 1964-1965), and others who became members of the Orbital Operation Group. The successful completion of acceptance tests and launch preparation of the Celescope experiment is heavily credited to the leadership, cooperation, and creativity of Mr. Peters, Mr. Nelson, Mr. L. Koshimeder from the test and integration division of Goddard Space Flight Center, and Mr. R. A. White from the OAO project office.

During 1968, 1969, and 1970, the major effort in Celescope was orbital operations; Dr. W. A. Deutschman was in charge of that activity. The success of the Celescope mission during orbital operations was in large measure the result of the efforts by him and his team in planning, computer programing, controlling, and reviewing the operating requirements and procedures. Special recognition is due Mr. J. Thorp and Mr. J. Latimer for representing Celescope as Field Managers during this round-the-clock operation; Mr. J. Block, as EMR Field Manager; and Mr. T. Omara and Mr. D. Moyer of Grumman Aircraft Corp., who acted as Project Operations Controllers for the OAO satellite.

During the summer and fall of 1970, a data-processing-improvement group consisting of Dr. C. Lundquist, Dr. R. Davis, Dr. W. Deutschman, Dr. E. Averet, Dr. E. Gaposchkin, Dr. S. Ross, Dr. E. Young, Dr. C. Gaposchkin, Dr. Y. Nozawa, Mrs. K. Haramundanis, Mr. R. Ayer, Mr. J. Thorp, and Mr. R. Loeser met every week to discuss the best way to use the calibration data. Many other individuals in the Observatory also contributed to this effort.

Since 1969, a major effort in Celescope has been data reduction, of which Mrs. K. L. Haramundanis has been in charge. Mrs. Haramundanis was responsible for the major portion of the work involved in converting the Celescope's general data-reduction requirements into a system involving both computer operations and manual review. She participated heavily in the identification of the stars observed by Celescope. Her data-reduction section was responsible not only for handling the vast amount of data involved in analyzing over 8000 Celescope pictures but also for keeping track of the source, location, and status of the individual data items. The creation of a star catalog from this vast body of Celescope data is in large measure the result of her efforts and those of her section.

During the entire life of the project, computer programing support has been important. From 1959-1963, Mr. G. Szabo was in charge of that activity. Since then, the programing effort has been headed by Mrs. Havelock (1963-1964), Mrs. B. (Feit) Nair (1964-1965), Mr. P. Conklin (1965), Mr. J. D. de Clercq Zubli (1966-1970), Mr. R. Loeser (1970), and Mrs. L. Kirschner (1966-present).

Since 1970, Dr. Deutschman has been Deputy Project Scientist, in charge of coordinating the activities of the various sections in Celescope. He has overall responsibility for Celescope data processing.

From 1959-1969, Celescope maintained a spectrophotometric standards laboratory for calibrating the optical and spectrophotometric characteristics of Celescope's optical elements, calibration lamps, and Uvicons. From

1959-1960, Dr. A. V. Baez headed this laboratory. From 1960-1962, it was headed by Dr. O. P. Rustgi. In 1963, and other times on a temporary basis, Mr. C. Miles was in charge.

In 1964, scientific activities of the laboratory were supervised by Dr. J. Marsh and Dr. I. Simon under subcontract to A. D. Little, Inc. From 1965-1969, Mr. H. O'Brien was manager of the spectrophotometric standards laboratory; he had been one of the laboratory assistants during 1963-1964. In 1966, under subcontract again, A. D. Little, Inc., furnished the services for Dr. P. von Thüna for scientific supervision of the activity required for recalibrating the primary laboratory standards against a black thermocouple standard. During the entire lifetime of the laboratory, 1959-1969, Mr. P. J. Hoffman performed ably as a physical-science aide.

During the 13 years that Project Celescope has operated, the above Project Staff has been ably supported by a number of devoted employees, as follows:

Physical-Science Aides: Mrs. G. Wald, Dr. E. Godfredsen, Mr. F. Ahern, Mrs. A. Renshaw, Mr. J. Gallagher, Miss M. Drugan, Mr. J. Black, Mr. I. A. Ahmad, Mrs. E. Green, and S. Strom, D. Cunnold, E. Gerard, A. J. Malaise, and N. Reghavan.

Programers: Miss V. Kan, Mr. R. Taylor, Mr. M. Patenaude, Mr. P. Collins, Mrs. D. Hills, Mrs. O. Johonnot, Mr. G. Bullock, and Mr. B. Welch.

Assisting Engineers: Mr. E. Arazi, Mr. S. Asano, Mr. W. Ng, Mr. A. Goldstein, Mr. W. Grim, and Mr. S. Shell.

Laboratory Technicians: Mr. R. Beckett, Mr. F. Licata, Mr. M. Kalish, Mr. T. Lee, Mr. P. Griffiths, Mr. A. Bardos, Mr. D. Frost, Mr. E. A. Monash, and Mr. J. Munier.

Data-Analyst Clerks: Mr. P. Sylvester, Mr. G. Westgate, Mrs. L. Cannell, Mr. R. Jarvis, Mr. R. van der Ley, Mr. W. Persons, Miss A. Ballard, Miss C. Jones, Mr. A. Kallai, Miss A. Brownlee, Mrs. S. Yeh, Mrs. Z. Gallagher, Mr. R. Palleschi, Mr. C. Sprangers, Mr. J. Orman, and Mr. A. Girnius.

Astronomers: Prof. C. Payne-Gaposchkin and Mrs. K. (Hebb) O'Neill.

Administrative Assistants: Mr. J. Taylor and Mr. E. Shenton.

Orbital Operations. SAO: Mr. J. Thorp (Field Manager), Mr. J. Latimer, Mr. J. Luce, Mr. L. Greenhouse, Mr. T. Cram, Mr. A. Oakes, and Mr. W. Munn. EMR: Mr. J. Block, Mr. L. O'Connor, Mr. O. Brown, Mr. P. Scoles, Mr. C. Sloan, Mr. K. Leilich, and Mr. T. Dennison.

Secretaries: Mrs. H. M. Beattie, Mrs. B. Hicks, Mrs. P. (Kluge) McMullen, Mrs. P. Januszkiewicz, Mrs. M. deJoie, Mrs. A. Green, Mrs. B. Millar, Mrs. M. V. Flaherty, Mrs. C. Williams, Miss E. Shipe, and Mrs. L. (Poireir) Jordan.

Assistance from other Departments: Mr. M. N. Malec (Contracts), Dr. E. M. Gaposchkin (Satellite Geodesy), Mr. C. Tillinghast (Administration), Mr. L. Campbell (Administration), Mr. G. Woron (Contracts), Miss E. Collins (Ed. & Pub.), Mr. E. N. Hayes (Ed. & Pub.), Mrs. A. Omundsen (Ed. & Pub.), Mrs. C. Wong (Ed. & Pub.), Mr. C. Hansen (Ed. & Pub.), and Mr. R. Martin (Computer).

Scientific advice and interpretation were provided by many other members of the Observatory staff, including the following: Dr. E. H. Avrett, Dr. J. G. Baker, Mr. D. F. Carbon, Dr. N. P. Carleton, Dr. G. G. Fazio, Dr. F. A. Franklin, Dr. O. J. Gingerich, Dr. P. W. Hodge, Dr. W. Kalkofen, Mr. R. L. Kurucz, Dr. D. W. Latham, Dr. R. W. Noyes, Dr. E. Peytremann, Dr. W. W. Salisbury, and Dr. R. E. Schild.

In addition to the above employees of the Smithsonian Astrophysical Observatory, we wish to acknowledge the support of many staff members at the Smithsonian Institution in Washington, D. C. Especially important were the support and encouragement given by Dr. Leonard Carmichael, Secretary of the Smithsonian Institution until 1964, and by Dr. S. Dillon Ripley, Secretary since that time. Mr. James Bradley, Assistant Secretary, helped in a number of ways, especially in negotiating contracts between the Smithsonian Institution and EMR, Westinghouse, and the National Aeronautics and Space Administration.

Almost all the detailed design, fabrication, and testing of the Celescope hardware were performed by subcontractors. Among the most important were the EMR Telemetry Division of Weston Instruments, Inc. (formerly known as Electro-Mechanical Research, Inc.); the Research Laboratories of the Westinghouse Electric Corp.; the Harshaw Chemical Co.; Astro-Data, Inc., and A. D. Little, Inc. EMR was prime contractor to SAO for the payload and ground-support systems; they had important subcontracts with Westinghouse, Harshaw, and the Ferson Optical Co. Westinghouse was responsible to SAO for development and fabrication of the Uvicon camera tubes; later that responsibility was changed to become a subcontract through EMR and in 1965 the effort was transferred from the Research Laboratories to the tube division. The raw materials for all the barium fluoride and lithium fluoride optical elements used in the Celescope paylaod were provided by the Harshaw Chemical Company — some directly under contract to SAO, some under subcontract to EMR, and some under subcontract to Westinghouse. The Ferson Optical Co. fabricated the Schwarzschild telescopes and the Corning and Suprasil filters. They had an important subcontract with Saffran Engineering Company for manufacture of the titanium structural components of these telescopes. Astro-Data designed and fabricated the data-handling equipment that Celescope used to record selected television pictures at Goddard Spaceflight Center and to reformat those pictures for analysis on the CDC-6400 computer at SAO. In addition to the spectrophotometric assistance described above, A. D. Little, Inc. performed a number of special engineering analyses for Celescope, including thermal and vibration analyses.

Key subcontractor personnel involved in the Celescope effort were Mr. S. D. Bass, Project Manager for Celescope at EMR; Mr. B. J. Tucker, Project Engineer for Celescope at EMR; Dr. J. P. Magnin, first as head of the Advanced Development Department at EMR and later as General Manager of the Telemetry Division and finally as President of EMR; Dr. G. Goetze, Mr. R. Schneeberger, Mr. A. E. Anderson, Mr. D. D. Doughty, and Mr. H. Alting-Mees of Westinghouse; Mr. F. Ferson and Dr. A. Schatzel of Ferson.

The Orbiting Astronomical Observatory Project was operated by the Goddard Space Flight Center of the National Aeronautics and Space Administration. The most important single factor contributing to the success of the OAO and its experiments was the support provided by GSFC. The OAO Program Office provided the money for the Celescope Project at SAO, the spacecraft, the test facilities, and the guidance necessary for SAO to produce a reliable experiment. The Data and Analysis Branch transformed the raw data received from the tracking stations into magnetic tapes that could be processed by SAO's CDC-6400 computer. The Tracking and Data Acquisition Branch provided the logistic support required for communicating with the OAO and with the Celescope experiment. Key personnel included Mr. R. Ziemer, Project Manager of the OAO Project, 1961-1965; Mr. J. Purcell, Project Manager since 1965; Mr. R. Stroup, Experiment Systems Manager; Mr. J. J. Ainley, Assistant Experiment Systems Manager; Mr. R. White, SAO Experiment Coordinator; Mr. W. White, Experiment Systems Manager since 1967; Mr. D. Parker, Data-Processing Engineer; Dr. J. E. Jupperian, Project Scientist for OAO; Mr. S. Osler, Mission Operations Manager, Mr. T. Omara of Grumman Aircraft Corp., Project Operations Controller; Mr. D. Moyer of GAC, Project Operations Controller; Mr. E. Light of GAC, and the other members of the Grumman Operations Crew; Mr. L. Koshimider, Experiment Test Manager; Mr. J. Stucker, Experiment Coordinator; and Mr. S. Socia, SCPS Manager.

The OAO Program Office at NASA Headquarters provided financial, administrative, policy, and scientific support to Goddard Space Flight Center, without which the OAO Project could not have occurred. Especially helpful in supporting the OAO and Project Celescope were Dr. N. G. Roman, Head of Astronomy; Mr. C. D. Ashworth; and Mr. E. Ott.

APPENDIX A

BRIEF DESCRIPTION OF OAO A2

Goddard Space Flight Center

BRIEF DESCRIPTION OF OAO A2

1. INTRODUCTION

The National Aeronautics and Space Administration's Orbiting Astronomical Observatory (OAO) is the heaviest and most automated unmanned satellite the United States has launched. Its basic mission is to extend man's knowledge of the origin and development of the universe by observing celestial bodies from above the atmosphere. OAO A2 contains two experiments: the Celescope of the Smithsonian Astrophysical Observatory and the University of Wisconsin Experiment. Both were intended to observe extremely young hot stars in ultraviolet, as well as other interesting objects, such as the planets, nebulae, interstellar matter, etc.

Possibly the most significant feature of OAO A2 is the pointing precision required to keep its telescope aimed at a star. It has a high-performance, coarse-pointing accuracy of 1 arcmin. This accurate pointing is accomplished by using active stabilization with six star trackers onboard.

The following description, with minor editorial changes, is from NASA's operation plan.*

The OAO A2 is a precisely stabilized observatory, weighing 4400 lb, that is capable of supporting a variety of astronomical experiments. The spacecraft is an 8-sided structure with a central tube, 4 ft in diameter, that carries 1000 lb of astronomical observing equipment. This structure is 10 ft long and 7 ft wide.

*Goddard Space Flight Center, X-513-68-301, Operation Plan 1-68, Orbiting Astronomical Observatory (OAO A2), August 1968.

Eight solar-cell paddles are arranged on opposite sides of the spacecraft in a plane making an angle of 33.75° with its longitudinal axis. Eight equally spaced radial trusses, extending the entire length of the spacecraft, protrude from the cylinder to form the corners of the octagon. The annular space between the inner structural tube and the outer octagon is divided into six bays by shelves fitted between the trusses to form continuous bulkheads around the central tube.

Inside the central tube, at the location of the third shelf from the separation plane or base of the spacecraft, are four equally spaced lugs for mounting the OAO experiment container. The eight radial trusses terminate in eight separate feet on an 80-in. diameter at the separation plane. These eight feet are fashioned to accommodate a Marmon-type separation clamp that fastens the spacecraft to its adapter on the launch vehicle for the transmission of axial and lateral loads.

Thin nonstructural aluminum, coated with aluminum oxide, covers the entire spacecraft except the opening for the optical equipment. This covering is a part of the spacecraft's thermal control subsystem.

The spacecraft is made up of five basic subsystems:

- Communications
- Data processing and instrumentation
- Power supply
- Thermal control
- Stabilization

Each of these subsystems is described briefly in the following.

2. COMMUNICATIONS SUBSYSTEM

The communications subsystem of the OAO contains the spacecraft equipment provided for receiving command signals from the ground and for

transmitting tracking signals, command-verification signals, and spacecraft and experiment data. The communications equipment consists of four radio links:

- Radio PCM/(NRZ) FSK/AM command (148.260 MHz)
- Wide-band PCM/NRZ or split-phase/FM telemetry (400.550 MHz)
- Narrow-band PCM/PM telemetry (136.260 MHz)
- Radio tracking beacon (136.440 MHz).

3. DATA-PROCESSING SUBSYSTEM

The onboard data-processing subsystem provides the circuitry and storage capabilities necessary to verify, decode, store, and distribute digital spacecraft-control and experiment commands. Timing signals for internal synchronization of the data-processing subsystem and for use by the experiment and spacecraft instruments are also part of this system. It has the capability of converting spacecraft and experiment analog data to digital data and of assembling data into a format suitable for storage or real-time transmission to the ground.

The command subassembly portion of the data-processing subsystem contains the circuitry for decoding, distributing, and storing the commands received from the ground command station via the radio command receiver system. The command decoder is capable of handling real-time and stored commands. Real-time commands are those to be executed immediately after being verified in the spacecraft from a bit-by-bit comparison of the command with its complement as received from the ground station. Stored commands are those placed in storage for execution at a later time. Stored commands are programable between 0 and 1023 spacecraft-equivalent min (62.9 sec equal 1 spacecraft-equivalent min) and can be executed in 15-sec increments. If two or more commands have the same execution time code, they will be executed in the same order in which they are stored.

4. THERMAL CONTROL

External surface temperature of the spacecraft in orbit is determined by a heat balance between the vehicle and its environment, which includes the following sources: (a) radiation from the sun and earth, and (b) solar radiation reflected from the earth.

The magnitude of the incident radiation and the temperature of the spacecraft depend on the orientation of the spacecraft and the percentage of the oribtal period that the spacecraft will be in sunlight. To compensate for the incident radiation, the spacecraft skins are fabricated of sheet aluminum having a high coefficient of thermal conductivity.

The experiment packages and the OAO A2 internal structure are maintained at the equilibrium temperature levels specified by the experimenters. To isolate thermally the OAO A2 structure from heat sinks and sources, titanium, nylon, and fiberglas are used as connecting members to minimize heat conduction to or from the structure. Aluminized mylar is wrapped around various members to control radiant heat transfer. Decreasing the insulation between electronic equipment and the structure increases the equilibrium temperature of the structure. Thus, the various insulators act as valves controlling the influx of heat from various sources to the structure. The spacecraft structure gains heat internally from three distinct sources: (a) Radiation of heat from equipment to structure through super-insulation, (b) Conduction of heat from equipment to structure through gold-coated fiberglas fittings, and (c) External fittings directly attached to the structure radiating to, and receiving heat from, the space environment.

Seventy-seven thermistors are located throughout the spacecraft to sample the temperature of the electronic equipment, spacecraft structure, and solar paddles. Critical components such as batteries and PPDS have two or three thermistors per unit; other black boxes usually have one thermistor. Thermistors are also mounted at various points on the structure to indicate operational temperatures.

5. POWER SUPPLY

The power supply must furnish properly regulated electrical power to the spacecraft during both the light and the dark portions of each orbit for the projected lifetime of the spacecraft. The following major equipment comprises the OAO power supply:

- Solar-cell array
- Batteries
- Power-control unit and power-regulator unit
- Regulator-converter
- Inverter
- State-of-charge unit (SOCU)

6. STABILIZATION AND ATTITUDE-CONTROL SUBSYSTEM

The operational requirements imposed on the spacecraft's stabilization and attitude-control subsystem were evolved to achieve the accuracy and stability that the scientific missions demand from the observational equipment. The system permits determination of the absolute direction of the optical axis of the spacecraft to an accuracy of 1 arcmin (rms circular error) and of the roll orientation of the optical axis to 1 arcmin rms with respect to a known reference. The control system also permits an ultimate pointing accuracy of 0.1 arcsec. The error signal for this fine control is generated in the experiment's prime optical system.

The major functions of the attitude-control subsystem are to

- Stabilize the spacecraft after booster separation and achieve a known attitude with the required precision
- Slew the spacecraft to any desired attitude, as dictated by the scientific objectives of the mission
- Maintain the spacecraft in a given attitude within the required accuracy for long periods of time

To perform the foregoing functions, the spacecraft is equipped with several types of sensors and actuation mechanisms. The major components of the stabilization and attitude control subsystem are listed below:

- Solar sensing optics
- Rate gynoscopes
- Pneumatric system
- Sensor signal processors
- Fine-wheel and jet controller
- High-torque controller
- Momentum wheels
- Gimbaled star tracker
- Digitized logic unit
- Star-tracker signal processor
- Magnetic unloading system
- Coarse-wheel controller
- Boresighted star tracker
- Rate and position sensor (RAPS)
- Programer star-tracker signal controller
- Restabilization reset generator (RRG)
- Undervoltage reset generator.

Two experiments were carried aboard the OAO A2 spacecraft. These experiments occupy opposite ends of the central experiment tube. Each one is briefly described below.

7. WISCONSIN EXPERIMENT PACKAGE

The primary function of the Wisconsin Experiment Package (WEP) is to gather information on the spectral energy distribution of selected stars and nebulae in the ultraviolet range of 1000 to 4000 Å. As a secondary function, WEP measures the time-varying spectral intensity of particular stars. This second function requires that repetitive measurements be made of the same object.

7.1 WEP Observation Instruments

The WEP contains seven observation instruments. These are:

1. Four stellar photometers, each covering a spectral band of approximately 1000 Å with partial overlap. Each photometer is equipped with a programable filter device to subdivide the coverage into 250 Å bands.

2. Two scanning spectrometers to provide backup for the stellar photometers. Once covers the range from 1000 to 2000 Å, and the other, from 2000 to 4000 Å. The spectrometers can be cycled 100 steps, thereby yielding a spectral resolution of about 10 Å.

3. One nebula photometer capable of measuring spectral intensity of nebulae as observed through five programable filters, each covering approximately 600 Å. Total coverage capabilities range from 1500 to 3000 Å.

During the mission, the instrument package is housed in the center cylindrical portion of the OAO A2 forward end.

The WEP instrument package is controlled by an electronic package housed in Bay E-5 of the spacecraft. The electronic control package consists of the circuitry and electronic components necessary to operate the prime instruments. The electrical power required is nearly constant at 9 w.

8. SAO EXPERIMENT (PROJECT CELESCOPE)

Project Celescope is one of the major scientific experiments to be conducted by SAO. The scientific objective of this project is to measure the brightness of approximately 25,000 stars and other celestial bodies in four separate ultraviolet spectral bands ranging between 1100 and 3000 Å. From these measurements, curves of the spectral energy distribution of different types and classifications of stars will be determined. Smithsonian and NASA scientists hope to employ the data to extend the existing knowledge of the composition of interstellar dust, the atmosphere of hot stars, and planetary nebulae.

8.1 SAO Equipment

The SAO experiment consists of two major integrated packages: The Celescope Optical Package (COP) and the Bay E-4 module assembly.

The COP contains four 12-inch Schwarzschild-configured telescopes, each of which images a star field onto the ultraviolet-sensitive photocathode of a special-purpose image tube. In turn, the photoelectrons emitted by the photocathode are imaged on a target where the image is integrated and stored as an electrical-charge pattern for readout at the desired time. The video signal developed by the readout of the image tubes is amplified and applied to an electronic data-processing system (Bay E-4 module assembly) for data processing in the manner prescribed by a preselected operating mode.

The data-processing system contained in the Bay E-4 module assembly is capable of operating in three discrete modes: analog, PCM, and store. In the analog mode, the analog video signal from each telescope camera is transmitted sequentially to the ground station via the wide-band transmitter. In the PCM mode, the digitally produced video signals are encoded into serial PCM which is then transmitted to the ground in real-time. In the store mode, the video signal is encoded and assembled with digital position data into 25-bit digital words, which are stored in the spacecraft storage unit of the experimenters' data-handling equipment (EDHE) for later transmission to ground. Only star signals greater than a selected threshold level are stored.

50

APPENDIX B

INTERNAL REPORTS FOR PROJECT CELESCOPE

INTERNAL REPORTS FOR PROJECT CELESCOPE

The internal reports dealt with here are loosely defined as any technical documents, except letters, prepared for project Celescope and distributed to other organizations. These reports can, for convenience, be classified as follows: periodical reports, serialized documents, and nonserialized reports.

1. Periodical Reports

   a. Celescope Monthly Progress Reports, prepared by SAO.
   b. EMR Monthly Progress Reports, prepared by EMR.
   c. Monthly Reports for product improvement, manufacturing, and testing of Uvicon tubes, prepared by WEC.

2. Serialized Documents (see Table 1). The majority of these documents are specifications, work statements, test plans, and test reports prepared for each subunit of the experiment; they contain detailed information on each subunit, test, or task, and they are of little value for general engineering reference, except as background material. Documents of general usefulness are the CCR and CER series (see Tables 2 and 3).

3. Nonserialized Reports. These are reports prepared for special studies or special tasks. The ones listed are especially useful for future reference. Table 4 lists these reports according to issuing organizations.

Table 1. List of serialized documents in project Celescope.

Designation of series	Issued by	First issue	Last issue	Contents
CCL	SAO	CCL-100	CCL-121	Celescope Command List
CCP	SAO	CCP-100	CCP-105	Celescope Calibration Plan
CCR	SAO	CCR-100	CCR-183	Celescope Calibration Report
CDL	SAO	CDL-98	CDL-105	Celescope Documentation for Data-Processing System and Identification Catalog
CEL	SAO	CEL-100	CEL-106	Celescope Engineering Specifications
CER	EMR	CER-1	CER-154	Celescope Engineering Report
CES	EMR	CES-111	CES-153	Celescope Engineering Specifications
CESR	SAO	CESR-1	CESR-1	Celescope Engineering Status Report
CFR	EMR	CFR-1	CFR-44	Celescope Failure Report
CQAP	EMR	CQAP-100	CQAP-113	Celescope Quality Assurance Procedure
CTP	EMR	CTP-100	CTP-22	Celescope Test Plan
CTR	EMR	CTR-100	CTR-573	Celescope Test Report
CWS	EMR	CWS-100	CWS-289	Celescope Work Statement
EM	SAO	EM-001	EM-049	Engineering Operation Procedure
ETP	SAO	ETP-100	ETP-101	Celescope Engineering Test Plan
FEM	EMR(FST)	CEL-FEM-001	FEM-022	Field Engineering Memorandum
LR	SAO	LR-1	LR-122	Optics Laboratory Report
QTP	SAO	QTP-100	QTP-105	Qualification Test Plan
QTR	SAO	QTR-100	QTR-100	Qualification Test Report
RS	EMR	RS-100	RS-114	Celescope Reliability Specification

Table 2. Celescope calibration report (CCR).

CCR-101	Prototype 2537 Å Calibrator System Camera C-2, Telescope Subassembly S/N 5
CCR-102	Photoionization Efficiency of Nitric Oxide at 1216 Å
CCR-103	Photoelectric Quantum Efficiency of Tungsten Photocathodes W-1 and W-2 at 1216 Å
CCR-104	Calibration and Intercomparison of Mercury-Lamp and Photomultiplier Standards at 2537 Å
CCR-105	Relative Spectral Sensitivity of Sodium Salicylate Fluorescent Detectors
CCR-106	Absolute Photodiode Quantum Efficiency of ASCOP Photomultiplier, Type 541F, Serial No. 3030
CCR-107	Photoelectric Quantum Efficiency of Metallic Photocathodes between 900 and 1600 Å
CCR-108	Time Degradation of SAO Standard Mercury-Lamp Assemblies at 2537 Å
CCR-109	Photoelectric Quantum Efficiency of Tungsten Photodiode between 900 to 1800 Å
CCR-110	Photoelectric Quantum Efficiency of Metallic Photocathode between 900 to 1800 Å
CCR-111	Spectral Sensitivity of Sodium Salicylate Fluorescent Detectors
CCR-112	Calibration of Photodiode Sensitivity of ASCOP Photomultiplier, Type 541F, Serial No. 3030
CCR-113	Calibration of Monochromatic Irradiance from SAO Standard Mercury-Lamp Assemblies at 2537 Å
CCR-114	Calibration of ASCOP Photomultiplier, Type 541F, Serial No. 3030
CCR-115A	Calibration of ASCOP Photomultiplier, Type 541F, Serial No. 5536
CCR-116A	Calibration of ASCOP Photomultiplier, Type 541G, Serial No. 4650
CCR-117	Calibration of ASCOP Photomultiplier, Type 541F, Serial No. 206, Operated as Photodiode
CCR-118A	Calibration of ASCOP Photomultiplier, Type 541F, Serial No. 4907
CCR-119	Transmittance of Filter 1C1
CCR-120	Reflectance of Mirror Sample X1BL1
CCR-121	Calibration of Calibrator System C-107 with ASCOP Photomultiplier, Type 541F, Serial No. 4907

Table 2. (Cont.)

CCR-122	Calibration of Uvicon R19A
CCR-123A	Calibration of Corning 7910 Filter C-7 and of Suprasil Quartz Filter S-1
CCR-124A	Calibration of Uvicon 65-36-050D
CCR-125A	Calibration of Lithium Fluoride Filter L-2 and of Transmittance Sample 3L1
CCR-126A	Calibration of Barium Fluoride Filter B-8 and of Transmittance Sample 8B2
CCR-127A	Calibration of Uvicon R29A
CCR-128	Calibration of Corning 7910 Filter C-8 and of Suprasil Quartz Filter S-21
CCR-129	Calibration of Uvicon R42D
CCR-130A	Calibration of Lithium Fluoride Filter L-6 and of Sample 1L1
CCR-131A	Calibration of Barium Fluoride Filter B-10 and of Transmittance Sample 9B1
CCR-132	Calibration of Uvicon R37D
CCR-133A	Calibration of Lithium Fluoride Filter L-5 and of Transmittance Sample 1L6
CCR-134A	Calibration of Barium Fluoride Filter B-2 and of Transmittance Sample 7B6
CCR-135A	Calibration of Corning 7910 Filter C-5 and of Suprasil Quartz Filter S-3
CCR-136B	Reflectance of Mirror Samples 6FP-4-OCL-2, 2DP2F2, and X-110-GSFC
CCR-137	Effect of Temperature on the Transmittance of Celescope Filters
CCR-138	Calibration of Uvicon R23A
CCR-139	Calibration of Barium Fluoride Filter B-3
CCR-140A	Calibration of Lithium Fluoride Filter L-1 and of Transmittance Sample 1L5
CCR-141	Calibration of Magnesium Fluoride Transmitter Sample 2M1
CCR-142	Calibration of Reflector Sample X-1-BL-2
CCR-143	Calibration of Reflector Sample 1GP-1-OCL6
CCR-144	Calibration of Reflector Sample 1GS-1-OCL5
CCR-145	Calibration of Reflector Sample 5FS-3-BL5
CCR-146	Calibration of Reflector Sample 6FS-4-CL4
CCR-147	Calibration of Uvicon R30A
CCR-148	Calibration of Uvicon S31A

Table 2. (Cont.)

CCR-149	Calibration of Uvicon 65-44-001A
CCR-150	Calibration of Uvicon 65-40-031A
CCR-151	Calibration of Uvicon 66-22-043D
CCR-152	Calibration of Uvicon 66-08-063A
CCR-153	Calibration of Uvicon 66-13-079D
CCR-154	Calibration of Uvicon 65-48-090A
CCR-155	Calibration of Uvicon 65-48-102D
CCR-156	Calibration of Uvicon 66-17-107D
CCR-157	Calibration of Uvicon 65-52-154D
CCR-158	Calibration of Uvicon 65-40-155D
CCR-159	Calibration of Primary and Secondary Mirror Coating Spare Telescope No. S-1
CCR-160	Calibration of Barium Fluoride Transmittance Samples 10B1, 10B3, 10B10, and of Barium Fluoride Filter from Aerobee Rocket Payload
CCR-161	Calibration of Magnesium Fluoride Transmittance Samples
CCR-162	Calibration of Primary and Secondary Mirror Coatings Flight Telescope No. F-1
CCR-163	Calibration of Primary and Secondary Mirror Coatings Flight Telescope No. F-2
CCR-164	Calibration of Primary and Secondary Mirror Coatings Flight Telescope No. F-3
CCR-165	Calibration of Primary and Secondary Mirror Coatings Flight Telescope No. F-4
CCR-166	Calibration of Primary and Secondary Mirror Coatings Space Telescope No. S-2
CCR-167	Calibration of BaF2 Filter B-9 and of Transmittance Samples 9B1
CCR-168	Calibration of Uvicon 65-44-007A
CCR-169	Calibration of Uvicon 65-52-034A
CCR-170	Calibration of Reflectance Samples 7FS-4-RS6, 225-4-RS7, and 4FP-4-RS8
CCR-171	Calibration of Uvicon 66-08-088A
CCR-172	Calibration of RCA Photomultiplier, Type 6199, Serial No. 763
CCR-173	Calibration of Filter BX-1, BX-2, BX-3, and BX-4
CCR-174	Calibration of Barium Fluoride Filter B-7

Table 2. (Cont.)

CCR-175	Calibration of Lithium Fluoride Sample 6L1, Magnesium Fluoride Samples 3M2, 3M11, 3M12, 4M1, and 4M2, and Barium Fluoride Sample 10B6
CCR-179	Calibration of Thermal Effects on the Quantum Efficiencies of Uvicons
CCR-180	Calibration of Effect of Environmental Exposure During Testing of the Celescope Prototype Experiment in NASA/GSFC's 12 × 15 ft Thermal-Vacuum Chamber, on the Transmittances of the Optical Filters
CCR-181	Calibration of EMI Photomultiplier, Type 9661B, Serial No. 5958
CCR-183	Calibration of Uvicon 66-22-044D
CCR-184	Calibration of the Celescope experiment

Table 3. Celescope Engineering Reports.

CER-1	Relocation of Uvicon Electronics
CER-2	Bay E-4 Weight Status
CER-3	Thermal Tracking Analysis and Test of Telescope
CER-4	Thermal Vacuum Tests on S43D Uvicon Assembly
CER-5	Results of Incoming Acceptance Tests for Uvicon S126A
CER-6	Inspection and Testing of Celescope Mirrors: Prototype Telescope
CER-7	Crossover Protection of the Uvicon Target
CER-8	Evaluation of Qualification Test Procedures for Mercury Calibration Lamp T1ML
CER-9	Reticle Positioning on the Xenon Calibration Lamp Assembly
CER-10	Analysis of Thermal-Vacuum Chamber Optical Window
CER-11	Prototype Observatory Weight Status
CER-12	Prototype Telescope Tube Concentricity Data
CER-13	Optical Instrumentation for Thermal-Vacuum Chamber Functional Tests
CER-14	Bay E-4 Spacecraft Interface Test Results
CER-15	A Transmissibility Test of an Encapsulated Uvicon Subject to Sinusoidal Vibration
CER-16	(Void)
CER-17	(Void)
CER-18	Random Vibration Effects on Bay E-4 Modules
CER-19	Celescope Thermal Analysis
CER-20	Vibration Test on the Celescope Prototype Experiment Container
CER-21	(Void)
CER-22	Analysis of the Celescope Optical System
CER-23C	Qualification Test Status for Celescope Assemblies
CER-24A	Celescope Electronic Component Burn in Summary Supplement 1 through 6
CER-25	Status of Acceptance Testing on Modules and Subassemblies for the Prototype Celescope Package
CER-26	Alignment of Celescope Experiment Package

Table 3. (Cont.)

CER-27	Resistor X-Ray Inspection Report
CER-28	Mercury Calibration Lamps
CER-29A	Investigation of Crossover Prevention Techniques
CER-30	(Void)
CER-31	Celescope Balance Report
CER-32	Bay E-4 Electronics Package Shock and Vibration Test Report
CER-33	Evaluation of Analog-Mode Uvicon Performance with Crossover Prevention Operating Procedures
CER-34	Image-Tube Replacement for Uvicon
CER-35	Determination of Vibration Levels for Testing Uvicons
CER-36	A Performance Test and Evaluation of an Isolator Mounted Telescope
CER-37	Celescope Magnetic Materials List
CER-38	Acceptance Test Report Status — Bay E-4 Modules and Observatory Electronics Modules
CER-39	Ion Trap Analysis
CER-40	Interface Documentation
CER-41	Power Summary for the Celescope Experiment
CER-42	Actual Weight of Prototype Experiment Package and Bay E-4 Electronics Package
CER-43	Effect of Filter Thickness on Optical System Focus
CER-44	Photometric Response of the Prototype Payload
CER-45	Summary of R-Series Uvicon Transfer Functions
CER-46	Magnetic Moment Measurement Report
CER-47	Summary of Flight Calibration Data
CER-48	Alignment of Flight Telescope D1
CER-49	Alignment of Flight Telescope A1
CER-50	Celescope End Item Status Report
CER-51	Recommended Components for Celescope Balloon Experiment
CER-52	(Void)
CER-53	(Void)
CER-54	Uvicon Camera R30A Noise Study
CER-55	Alignment of Flight Telescope A2

Table 3. (Cont.)

CER-56	Telescope and Camera Interchangeability Study on Flight Camera Optical Package
CER-57A	Bay E-4 Flight Space-Module Status
CER-58	Celescope High-Voltage Power Supplies
CER-59	(Void)
CER-60	Review of Celescope Primary Technical Problems
CER-61	Celescope Optical Package Contamination Study
CER-62	Evaluation of Erie High-Voltage Capacitors for Use in Celescope High-Voltage Power Supply
CER-63	Electric Field Considerations Applied to High-Voltage Power-Supply Design
CER-64	Celescope Contamination Test Program: Interim Test Report
CER-65	Preliminary Magnetic Moment and Stray Field Test Report for the Bay E-4 Electronics Package
CER-66	Status Indicator Interface
CER-67	Bay E-4 Electronics Package – Phase I Testing Report
CER-68	Telescope Vibration and Optical Stability Test
CER-69	Medium-Voltage Power-Supply Evaluation
CER-70	Power Summary Celescope Payload Electronics
CER-71	Trip Report – Static Load Test for OAO/SAO Celescope
CER-72	High-Voltage Power-Supply Design for Operation in the Critical Gas-Pressure Regions and at Low Temperatures
CER-73	Study of Requirements for Experiment Calibration
CER-74	(Void)
CER-75	High-Voltage Power-Supply Qualification Program
CER-76	Nonredundant Interface Modules
CER-77	Sample and Hold Module
CER-78	Sync Mixer Module Redesign
CER-79	(Void)
CER-80	(Void)
CER-81	High-Voltage Power-Supply Divider Stability
CER-82	End of Frame Generation

Table 3. (Cont.)

CER-83	E-4 Sweep Mode Select
CER-84	Alignment of Qualification Telescope S-1
CER-85	Transfer Pulse Interface
CER-86	E-4 Corrective Action Plan
CER-87	Phase II System Test Report
CER-88	Celescope System Turnon Transient
CER-89	Bay E-4 Temperature Test
CER-90	E-4 Temperature Limit
CER-91	MVPS on/off Switch
CER-92	Evaluation of Telescope Methods under Vibration ADL Modification
CER-93	Target and G5 Voltage Control
CER-94	Magnetic Moment Test Report for SAO Telescope Subassembly, Video Amp and Calibration Lamp Power Supply
CER-95	Resonant Frequency and Transmissibility Test of Telescope Vibration Fixture
CER-96	(Void)
CER-97A	Weight Chart for Flight Telescope
CER-98A	Weight Chart for Flight Experiment Container
CER-99	Infrared Emittance Measurement of Some Metallic Surface
CER-100C	Flight Bay E-4 Weight Chart
CER-101B	Alignment of Flight Telescope F-1
CER-102	Inverter Amplifier Redesign
CER-103	-250 V Regulator
CER-104C	Weight Report Summary
CER-105A	Alignment of Flight Telescope F-2
CER-106	Magnetic Moment Test Final Report
CER-107A	Alignment of Flight Telescope F-3
CER-108	(Void)
CER-109	Effects of New Telescope Qualification Vibration Levels on the Uvicon and Camera
CER-110	(Void)
CER-111	Report on Trip to Astrodata

Table 3. (Cont.)

CER-112	Summary Report of Uvicon Vibration and Celescope Thermal Investigation
CER-113	Evaluation of 3M Instrumentation Tape on the Ampex FR-1800H Tape Transport
CER-114A	Alignment of Flight Telescope F-4
CER-115	Engineering Evaluation of NASA Suggested Telescope Qualification Shock and Vibration Level
CER-116	COP Alignment Report
CER-117	Ambient and Thermal-Vacuum Calibration Test Report 050D
CER-118	A Method for Preventing Beam-Relay Lockup Modes
CER-119	An Investigation of Methods for Preventing Spacecraft Storage of Target Ring
CER-120	Uvicon Monitor Mirror Test Report
CER-121A	Bay E-4 Calibration Test Report
CER-122	Ambient and Thermal-Vacuum Calibration Test Report: R19A Camera
CER-123	Ambient and Thermal-Vacuum Calibration Test Report: R42D
CER-124	Celescope Balance Report
CER-125	Flight E-4 Rework
CER-126	Uvicon Parametric Response Study
CER-127	Alignment of Flight Telescope S-2
CER-128	Open Collimator Ambient Calibration Test Report R29A Camera (F-3 Telescope Assembly)
CER-129	Derivation of Equation Relating Telescope Deflection Angle to Test Fixture Measurement
CER-130A	Position Calibration Test Report: F-1 Telescope Assembly (R19A)
CER-131	Position Calibration Test Report: F-2 Telescope Assembly (050D)
CER-132	Position Calibration Test Report: F-3 Telescope Assembly (R29A)
CER-133	Position Calibration Test Report: F-4 Telescope Assembly (R42D)
CER-134	Calibration of Digital Test Set Video Gain (G_{TS})
CER-135	Thermal-Vacuum Calibration Test Report: F-1 Telescope (R19A Camera)

Table 3. (Cont.)

CER-136	Thermal-Vacuum Calibration Test Report F-2 Telescope (050D Camera)
CER-137	Thermal-Vacuum Calibration Test Report F-3 Telescope (R29A Camera)
CER-138	Thermal-Vacuum Calibration Test Report F-4 Telescope (R42D Camera)
CER-139	Beam-Control Failure
CER-140	Typical Sequences for Celescope Orbital Operations
CER-141	Thermal Tracking of Optical Components
CER-142	Ambient and Thermal-Vacuum Calibration Test Report 65-40-031A Camera
CER-143	Ambient and Thermal-Vacuum Calibration Test Report 66-17-107D Camera
CER-144	Ambient and Thermal-Vacuum Calibration Test Report 66-22-122D Camera
CER-145	Ambient and Thermal-Vacuum Calibration Test Report 65-44-007A Camera
CER-146	Position Calibration Test Report, S-2 Telescope Assembly (031A)
CER-147	Telescope Plasma Test Report
CER-148	Thermal-Vacuum Calibration Test Report S-2 Telescope (65-40-031A Camera)
CER-149	Ambient and Thermal-Vacuum Calibration Test Report R37D Camera Rebuilt Configuration
CER-150	Thermal-Vacuum Calibration Test Report S-1 Telescope (R37D Camera Refur.)
CER-151	Plasma Test No. 2 Test Report
CER-152	Circuit Design and Pulse Backfeed Analysis of -250 V Regulator
CER-153	Electrical Stress and Reliability of -250 V Regulator.
CER-154	Position Calibration Test Report S-1 Telescope Assembly (R37D Rebuilt)

Table 4. List of nonserialized reports.

ADL (Reports for study subcontracts)

1 C-66285, Celescope Vibration Study, A Review of Celescope Design Changes, 4/9/64.

2 C-67216, Celescope Vibration Study, Analysis of 2/65 Experiment Package Vibration Test, 4/5/65.

3 Technical Memorandum #1, Computation of Environmental Thermal Input, Project Celescope, 1/28/65.

4 ADL-C-67918, Thermal Design of Celescope, A Review to EMR Final Report, 3/15/66.

5 ADL-C-66145, Celescope Vibration Study, 1/24/64.

6 ADL-C-66856 and C-66427, Final Report on Calibration of Celescope Components, 6/65.

7 ADL-67898, A Thermocouple System as a Standard of Intensity in the Vacuum Ultraviolet, 5/66.

8 Technical Memorandum #2, Discussion of Thermal Test Plan, 2/11/65.

9 Technical Memorandum #3, Discussion of Thermal Test Results SAO Experiment, 5/5/65.

EMR General

1 Project Celescope Technical Manual Smithsonian OAO Experiment.

2 Instruction Manual, Ground-Support Equipment Storage Display Unit.

3 Instruction Manual, Ground-Support Equipment Binary Accumulator.

4 Instruction Manual, Ground-Support Equipment Spacecraft Simulator.

5 Instruction Manual, Ground-Support Equipment Observatory Simulator.

6 Instruction Manual, Ground-Support Equipment Status Indicator.

7 Instruction Manual, Ground-Support Equipment Display/Accumulator Test Set.

EMR Reliability (Failure) Analysis Report

1 RA-072, Failure of Magnetic Latching Relays During Life Test.

2 RA-042, High-Voltage Arc in Xenon Calibration Power Supply.

3 RA-073, High-Voltage Arc in High-Voltage Power Supply.

Table 4. (Cont.)

EMR Reliability (Failure) Analysis Report (Cont.)

4 RA-107, Shorted Termashield Ferrule.

5 RA-114, +6 VPS.

6 RA-131, Technipower Power Supply.

7 RA-143, Uvicon Heater Power Supply.

8 RA-162, Celescope -250 V Regulator Module.

EMR RE — Reliability Engineering Report

1 RE-116, Reliability Assessment of the Smithsonian Experiment Package (SEP).

2 RE-123, Effect on Reliability Assessment of the SEP due to Delayed launch of Payload.

3 RE-127, Relay Life Test Project Celescope.

4 RE-125, Additional Studies to Determine the Effect of a Delayed Launch on Project Celescope Equipment Reliability Phase 1.

5 RE-132, Reliability Statement Medium-Voltage Power-Supply Magnetic Latching Relay.

6 RE-147, Reliability of HVPS.

7 RE-148, Supplement 1 — Celescope Burn-in Data Summary.

8 RE-152, Celescope Optical Package Cable.

NASA Celescope Test Report

1 MR No. 66-2-1, OAO-SAO Thermal-Vacuum Engineering Development Test, by W. W. Auer, 7/28/65.

2 MR No. 651-5, Engineering Development Vibration Test of Prototype SAO Celescope Optical Package, by E. F. Schokey, 3/30/65.

3 Structural Qualification Vibration Test of OAO-SAO Celescope Optical Package with Vibration Isolator Telescope, 9/21/66.

4 Static Load Test of SAO Celescope Experiment Container, 2/11/66.

5 Memo 641-4, Vibration Survey of SAO Partial Prototype Experiment, 1/29/64.

6 Memo 671-155, Vibration Acceptance Test of Three OAO Uvicon Tubes S/N S125A, S126A, and S128A, 6/18/63.

Table 4. (Cont.)

NASA Celescope Test Report (Cont.)

7 DIRS 01281-I-2-MR-157-215-181, Results of the OAO-A2 Experiment Thermal-Vacuum Test, by K. A. Davis, 5/20/68.

8 Memo Report No. 681-8, DIRS-11176, Final Report on the SAO-WEP Prime Experiment Package Flight Acceptance Vibration Test, by C. S. Moutoux, 5/6/68.

SAO

1 Special Report No. 110, Project Celescope, An Astronomical Reconnaissance Satellite.

2 Special Report No. 282, The Celescope Experiment.

3 CTB-9, Problems of Electrical Connectors in the Celescope Payload.

4 CTB-10, Celescope Power-Supply System and Related Problems.

5 CTB-11, The Effects of Filter Thickness and of Optical Dispersion on the Alignment of D-type Telescopes.

6 CTB-12, Results of Reflectivity Measurements Performed on Samples of Celescope Structural Surface Finishes.

7 CTB-13, Power Requirements for the SAO Experiment (Celescope)

8 CTB-14, The Radiation Environment for the Orbit of the OAO A2 Satellite, and its Effects on the Celescope Optical System

9 CTB-15, Status Report on Celescope Calibration.

10 CTB-16, Celescope Power Consumption.

11 CTB-17, SAO Operational Constraints.

12 CTB-18, Results of an Experiment to Evaluate the Effects of Earthlight and Sunlight on the Operation of the Celescope Instrument.

WESTINGHOUSE Reports for Uvicon Contracts

1 WRL Research Report 912-J902-R1, Research and Development of a Family of Ultra-violet Sensitive Camera Tubes.

2 WRL 64-912-248-R1, Product Design Report for Product Design, Manufacture and Test of Uvicon Tubes.

3 WRL Fabrication of Uvicon Tube, Contract Sp-22-12 EMR Final Report.

4 WRL 64-9527-248-R1, A Method of Safe Uvicon Operation.